36801

National Library of Canada / Bibliothèque nationale du Canada

CANADIAN THESES ON MICROFICHE / THÈSES CANADIENNES SUR MICROFICHE

NAME OF AUTHOR/NOM DE L'AUTEUR ROSSITER, JAMES RANDELL

TITLE OF THESIS/TITRE DE LA THÈSE INTERPRETATION OF RADIO INTERFEROMETRY DEPTH SOUNDING, WITH EMPHASIS ON RANDOM SCATTERING FROM TEMPERATE GLACIERS AND THE LUNAR SURFACE.

UNIVERSITY/UNIVERSITÉ TORONTO

DEGREE FOR WHICH THESIS WAS PRESENTED/GRADE POUR LEQUEL CETTE THÈSE FUT PRÉSENTÉE Ph.D.

YEAR THIS DEGREE CONFERRED/ANNÉE D'OBTENTION DE CE GRADE 1977

NAME OF SUPERVISOR/NOM DU DIRECTEUR DE THÈSE DAVID W. STRANGWAY.

Permission is hereby granted to the NATIONAL LIBRARY OF CANADA to microfilm this thesis and to lend or sell copies of the film.

The author reserves other publication rights, and neither the thesis nor extensive extracts from it may be printed or otherwise reproduced without the author's written permission.

L'autorisation est, par la présente, accordée à la BIBLIOTHÈQUE NATIONALE DU CANADA de microfilmer cette thèse et de prêter ou de vendre des exemplaires du film.

L'auteur se réserve les autres droits de publication; ni la thèse ni de longs extraits de celle-ci ne doivent être imprimés ou autrement reproduits sans l'autorisation écrite de l'auteur.

DATED/DATÉ Oct 7/77 SIGNED/SIGNÉ Jane Rossiter

PERMANENT ADDRESS/RÉSIDENCE FIXÉ 2 TESSIER'S LANE.
ST JOHN'S, NEWFOUNDLAND
CANADA A1C 5S7

NL-91 (3-74)

National Library of Canada

Cataloguing Branch
Canadian Theses Division

Ottawa, Canada
K1A 0N4

Bibliothèque nationale du Canada

Direction du catalogage
Division des thèses canadiennes

NOTICE

The quality of this microfiche is heavily dependent upon the quality of the original thesis submitted for microfilming. Every effort has been made to ensure the highest quality of reproduction possible.

If pages are missing, contact the university which granted the degree.

Some pages may have indistinct print especially if the original pages were typed with a poor typewriter ribbon or if the university sent us a poor photocopy.

Previously copyrighted materials (journal articles, published tests, etc.) are not filmed.

Reproduction in full or in part of this film is governed by the Canadian Copyright Act, R.S.C. 1970, c. C-30. Please read the authorization forms which accompany this thesis.

THIS DISSERTATION
HAS BEEN MICROFILMED
EXACTLY AS RECEIVED

AVIS

La qualité de cette microfiche dépend grandement de la qualité de la thèse soumise au microfilmage. Nous avons tout fait pour assurer une qualité supérieure de reproduction.

S'il manque des pages, veuillez communiquer avec l'université qui a conféré le grade.

La qualité d'impression de certaines pages peut laisser à désirer, surtout si les pages originales ont été dactylographiées à l'aide d'un ruban usé ou si l'université nous a fait parvenir une photocopie de mauvaise qualité.

Les documents qui font déjà l'objet d'un droit d'auteur (articles de revue, examens publiés, etc.) ne sont pas microfilmés.

La reproduction, même partielle, de ce microfilm est soumise à la Loi canadienne sur le droit d'auteur, SRC 1970, c. C-30. Veuillez prendre connaissance des formules d'autorisation qui accompagnent cette thèse.

LA THÈSE A ÉTÉ
MICROFILMÉE TELLE QUE
NOUS L'AVONS REÇUE

THE UNIVERSITY OF TORONTO LIBRARY

MANUSCRIPT THESIS

AUTHORITY TO DISTRIBUTE

NOTE: The AUTHOR will sign in one of the two places indicated. It is the intention of the University that there be NO RESTRICTION on the distribution of the publication of theses save in exceptional cases.

(a) Immediate publication in microform by the National Library is authorized.

Author's signature ..... Date .....

or

(b) Publication by the National Library is to be postponed until ..... 19.. (normal maximum delay is two years). Meanwhile this thesis may not be consulted in the University Library except with written permission on each occasion from me.

Author's signature ..... Date .....

This restriction is authorized for reasons which seem to me, as Head of the Graduate Department of ..... , to be sufficient.

Signature of Graduate Department Head .....

Date .....

BORROWERS undertake to give proper credit for any use made of the thesis, and to obtain the consent of the author if it is proposed to make extensive quotations, or to reproduce the thesis in whole or in part.

Signature of borrower	Address	Date

P02 A

REVISED AUGUST 1973

UNIVERSITY OF TORONTO

SCHOOL OF GRADUATE STUDIES

PROGRAM OF THE FINAL ORAL EXAMINATION

FOR THE DEGREE OF DOCTOR OF PHILOSOPHY

OF

JAMES RANDELL ROSSITER

11:00 a.m., Friday, October 7, 1977

Room 309, 63 St. George Street

INTERPRETATION OF RADIO INTERFEROMETRY DEPTH SOUNDING, WITH EMPHASIS ON RANDOM SCATTERING FROM TEMPERATE GLACIERS AND THE LUNAR SURFACE

Committee in Charge:

Professor D. Basmadjian, Chairman
Professor R.N. Edwards
Professor A.W. England, External Examiner
Professor R.M. Farquhar
Professor W.R. Peltier
Professor J.-C. Roegiers
Professor D. Strangway, Supervisor
Professor D. York

JAMES RANDELL ROSSITER

Biography

1947	Born, London, Ontario.
1969	B.Sc., University of Western Ontario.
1971	M.Sc., University of Toronto.
1969-77	School of Graduate Studies, University of Toronto.

GRADUATE STUDY

Major Field:

Geotectonics - Prof. G.D. Garland

Minor Fields:

Numerical Methods for Engineers - Prof. R.A. Mathon

Geophysics Laboratory - Prof. R.A. Wiggins

Inversion Theory - Prof. R.A. Wiggins

Low Temperature, Oriented & Non-Equilibrium States - Prof. J.M. Daniels

Topics of Current Interests in Nuclear Physics - Prof. A.E. Litherland

Publications and Theses

Strangway, D.W., Annan, A.P., Redman, J.D., Rossiter, J.R., and Watts, R.D., "Electrical Structure at Taurus-Littrow", in preparation, 1977.

Rossiter, James R., "Interpretation of Radio Interferometry Depth Sounding, with Emphasis on Random Scattering from Temperate Glaciers and the Lunar Surface", Ph.D. Thesis, University of Toronto, Department of Physics, to be submitted September 1977.

Rossiter, James R., and Gustajtis, K. Andrew, "Iceberg Sounding by Impulse Radar", submitted to Nature, July 1977.

Rossiter, J.R., Strangway, D.W., Koziar, A., Wong, J., and Olhoeft, G.R., "Electromagnetic Sounding of Permafrost, N.W.T., Canada, in Summer and Winter", Proceedings of the Third International Conference on Permafrost, Edmonton, July 10-13, 1978, accepted July 1977.

Rossiter, James R., Langhorne, P., Ridings, T., and Allan, A.J., "Study of Sea Ice Using Impulse Radar", Proceedings of the Fourth International Conference on Port and Ocean Engineering under Arctic Conditions, St. John's Sept. 26-30, 1977, accepted August 1977.

Wong, J., Rossiter, J.R., Olhoeft, G.R., and Strangway, D.W., "Permafrost: Electrical Properties of the Active Layer Measured In Situ", Can. J. Earth Sci., vol. 14, pp. 582-586, 1977.

Rossiter, J.R., Strangway, D.W., Annan, A.P., Watts, R.D., and Redman, J.D., "Detection of Thin Layers by Radio Interferometry", Geophysics, vol. 40, pp. 299-308, 1975.

Annan, A.P., Waller, W.M., Strangway, D.W., Rossiter, J.R., and Redman, J.D., "The Electromagnetic Response of a low-loss, 2-layer, Dielectric Earth for Horizontal Electric Dipole Excitation", Geophysics, vol. 40, pp. 285-298, 1975.

Strangway, D.W., Simmons, G., LaTorraca, G., Watts, R., Bannister, L., Baker, R., Redman, J.D., and Rossiter, J.R., "Radio-frequency Interferometry - A New Technique for Studying Glaciers", J. Glaciol., vol. 13, pp. 123-132, 1974.

Simmons, G., Strangway, D., Annan, P., Baker, R., Bannister, L., Brown, R., Cooper, W., Cubley, D., deBettencourt, J., England, A., Groener, J., Kong, J., LaTorraca, G., Meyer, J., Nanda, V., Redman, D., Rossiter, J., Tsang, L., Urner, J., and Watts, R., "Surface Electrical Properties Experiment", Apollo 17 Preliminary Science Report, NASA SP-330, Washington, pp. 15-1 - 15-14, 1973.

Rossiter, James R., LaTorraca, Gerald A., Annan, A. Peter, Strangway, D.W., and Simmons, Gene, "Radio Interferometry Depth Sounding: Part II - Experimental Results", Geophysics, vol. 38, pp. 581-599, 1973.

Rossiter, James R., "Interferometry Depth Sounding of the Athabasca Glacier - Development of the interferometry technique for lunar Exploration", M.Sc. Thesis, University of Toronto, Department of Physics, 1971.

Rossiter, James R., "A Description of a Model Simulating Electromagnetic Geophysical Surveys", B.Sc. Thesis, University of British Columbia, Department of Geophysics and Astronomy, 1968.

INTERPRETATION OF
RADIO INTERFEROMETRY DEPTH SOUNDING,
WITH EMPHASIS ON RANDOM SCATTERING
FROM TEMPERATE GLACIERS AND THE LUNAR SURFACE

BY

James Randell Rossiter

Department of Physics
University of Toronto
Toronto, Ontario
Canada M5S 1A7

A Thesis submitted in conformity
with the requirements for the Degree of
Doctor of Philosophy
in the University of Toronto

© James R. Rossiter 1977

October 1977

ABSTRACT

Radio interferometry sounding data have now been collected, at frequencies from 1 to 32 MHz, from two temperate glacial regions, the Taurus-Littrow valley of the Moon (Apollo 17 site), a permafrost region, and a frozen lake. In order to interpret these data, studies were made in a laboratory-size analogue scale model, operating at 5.9 GHz. Automated interpretation procedures were developed using the scale model results as a guide, and were applied to field data.

The dielectric constant, loss tangent, and thickness of a two-layer, low-loss earth can be determined from the envelopes of the interference curves and maximum entropy spectral analyses. The tilt of a sub-surface reflector can also be obtained if up- and down-dip traverses are available. The two-layer interpretations presented are consistent with previous estimates.

The level of random scattering was obtained at each site. Inhomogeneities are ineffective scatterers unless they are larger than 0.3 wavelengths in size. Larger objects are slightly more effective scatterers, but the overall scattering level increases primarily with scatterer density. The result is that for radio frequencies above the scattering threshold, scattering is essentially frequency-independent.

Data from a permafrost area near Tuktoyaktuk, N.W.T., and from a frozen lake near Sudbury, Ontario, show that these regions were too conductive to be amenable to the interferometry technique. Therefore the scattering levels are low, and give non-scattering baseline levels.

Data from the two temperate glacial regions both show very high levels of scattering above about 8 MHz. On the Athabasca Glacier, Alberta, the scattering is partly from surface crevasses. However, the scattering level is also high from the Juneau Icefield, Alaska, where there were few surface crevasses. Therefore, the majority of the scattering effects are attributed to water-filled cavities within these glaciers, with dimensions on the order of 3 to 6 m, and typical separations of 10 to 30m. There appear to be differences between glacial regions, and these deserve further study.

Data from the Apollo 17 site show relatively low scattering up to 32 MHz, indicating that there are few scatterers larger than about 2 m on or near the lunar surface. It is shown that many of the radar results from the moon are compatible with a two-layer lunar model: a regolith with a dielectric constant of 2 and a thickness of several meters, overlying rock with a dielectric constant of about 7. The results are relatively insensitive to losses, and are therefore not greatly affected by scattering, which may be more important at frequencies above 32 MHz.

In addition, a theoretical model of low-level scattering in a two-dimensional waveguide was examined using perturbation theory. The results have not been experimentally confirmed, but indicate that the effective loss tangent and dielectric constant of a randomly scattering dielectric layer will increase above their mean values. This result is in basic agreement with previous work.

ACKNOWLEDGEMENTS

I wish to thank my supervisor, Dr. David Strangway, for suggesting the topic and for consistently aiding me to pursue it. The many Saturday afternoons that we spent, discussing matters both scientific and non, were very important to me.

I would also like to thank the other members of my supervisory committee, Dr. Richard Peltier and Dr. Nigel Edwards, for helping to keep my ideas focused. Dr. Peltier was instrumental in guiding me through the theoretical section.

This work evolved out of a team project, the Apollo Lunar Surface Electrical Properties (SEP) Experiment, in which I participated. Several of the ideas presented here had their beginnings during discussions that took place over a period of several years, amongst team members; in particular, with Peter Annan Gary Olhoeft, David Redman, and Ray Watts. In addition, field data from the Athabasca Glacier, Juneau Icefield , and the moon, and some of the early scale model data, were collected by the team as a whole, which included personnel from the University of Toronto, Massachusetts Institute of Technology, and NASA's Manned Spacecraft Center in Houston.

More recent field data from northern Ontario and the Arctic were collected with very able assistance from David Redman, who designed and built the hardware modifications, kept equipment operational under severe conditions, and aided the data collection. He also assisted in operation of the data acquisition system for scale model and field results.

Others who assisted me were: Jeff Proctor and John Rylaarsdam, who taught me the intricacies of using IBM computers; Joe Wong, who volunteered to go to the Arctic in March; and Khadar Khan, who always responded calmly and successfully to my urgent requests for drafting and photographic work.

Financial assistance was provided by a University of Toronto Open Fellowship, an Ontario Graduate Scholarship, and a Research Assistantship. The work was funded primarily by Energy, Mines and Resources Research Agreement 1135-D13-4-16/73. Arctic logistics were provided by Polar Continental Shelf Project. Loan of the SEP hardware by NASA was greatly appreciated.

I am grateful to my employer, the Centre for Cold Ocean Resources Engineering at Memorial University of Newfoundland, for granting me leave to write the final manuscript, and I thank the staff for considerable assistance in its preparation.

Finally, I owe a vast amount to my wife, Amy, who endured my bouts of procrastination and industry equally,with both support and patience.

TABLE OF CONTENTS

		Page
ABSTRACT		ii
ACKNOWLEDGEMENTS		v
TABLE OF CONTENTS		
CHAPTER 1:	INTRODUCTION	
1.1	Background	1
1.2	Radio interferometry depth sounding	4
1.3	Thesis outline	10
CHAPTER 2:	SCALE MODEL STUDIES	
2.1	Introduction to scale model studies	11
2.2	Two-layer case: horizontal layers	13
2.3	Two-layer case: tilting reflector	33
2.4	Single scattering object	42
2.5	Many scattering objects	52
2.6	Summary of scale model results	65
CHAPTER 3:	THEORETICAL FORMULATION OF VOLUME SCATTERING	
3.1	Introduction to volume scattering	67
3.2	Perturbation theory	70
3.3	Homogeneously-filled waveguide	73
3.4	Inhomogeneously-filled waveguide	81
3.5	Numerical evaluation	85
3.6	Discussion of theoretical results	90
CHAPTER 4:	INTERPRETATION OF INTERFEROMETRY FIELD DATA	
4.1	Introduction and interpretation procedure	94
4.2	Athabasca Glacier	102
4.3	Juneau Icefield	114
4.4	Taurus-Littrow valley of the Moon	124
4.5	Conductive regions	133
4.6	Summary of scattering results	137

Page

CHAPTER 5: CONCLUSIONS

5.1 Scattering in temperate glaciers 144

5.2 Scattering from the lunar surface 150

5.3 Overall summary 159

REFERENCES 162

APPENDIX 1: ANALOGUE SCALE MODEL 170

APPENDIX 2: $r^{-\alpha}$ DECAY PARAMETER 177

APPENDIX 3: OFF-AXIS TRAVERSES 183

APPENDIX 4: PLOTS OF RADIO INTERFEROMETRY FIELD DATA 185

CHAPTER 1

INTRODUCTION

1.1 Background

This thesis is concerned with the geophysical depth sounding technique of radio interferometry. The method was primarily developed to probe the surface layers of the moon, and was successfully flown on Apollo 17 as the Surface Electrical Properties (SEP) Experiment. However, the technique has also been used to sound a number of terrestrial environments -- two distinct temperate glacier regions, a permafrost region, and a frozen lake.

The work presented here is aimed at estimating and interpreting the effects of random scattering in radio interferometry data. Previous work, both theoretical and experimental, dealt with the technique as applied to plane layered models (Annan, 1973; Rossiter et al., 1973; Tsang et al., 1973; Strangway et al., 1974; SEP Team , 1973; Kong et al., 1974; Annan et al., 1975; and, Rossiter et al., 1975), and this work has been extended. However, even if a plane layered model is a good approximation to the real earth, the boundaries of the real earth are not necessarily smooth, nor the layers homogeneous. In several geological environments these limitations are of interest.

The roughness or inhomogeneity in the real earth has two distinct aspects. First, one would like to know when the models one has chosen are no longer realistic approximations to the real earth for the measurement being made. And secondly, if in fact the earth

is closely approximated by the chosen model, but exhibits small perturbations as a function of space, one wonders if anything can be said about the perturbations themselves. In some cases estimates of the perturbations may be the most useful information to be obtained.

For example, in almost all of the radio inferometry data collected on temperate ice sheets and glaciers, there is a marked difference between data collected at 1, 2, and 4 MHz, and data collected at 8, 16, and 32 MHz. At the lower frequencies there is a drop of about 10 to 20 dB between the maximum-coupled and minimum-coupled components (assuming a plane layered structure). However, at the higher frequencies, the two sets of components are essentially indistinguishable in power level. Strangway et al.(1974) attributed this behaviour to random scattering by pockets, probably water-filled, within the ice. The success of Watts and England (1976) in using low frequency (centre frequency below 4 MHz) electromagnetic (EM) pulse sounders on temperate ice is consistent with this idea. Therefore it is of glaciological interest to try to say something more about the scatterers themselves.

The topic of random scatterers is also of interest in lunar and planetary studies (e.g. Hagfors, 1970), in order to be able to use results from the Surface Electrical Properties Experiment to calibrate results determined by earth-and satellite-based radar. An understanding of scattering is essential to successful interpretation of these types of data, particularly as radar studies are applied to

more distant planets.

In the following work a plane layer geometry has been taken as the basic model, and the effects of random scattering are seen as perturbations on it. Two types of scattering are discussed. First, "surface scattering" will mean distortion of the received signal due to scattering by roughness in the boundaries between layers. Secondly, "volume scattering" will be that caused by scattering from inhomogeneities within the layers themselves. The overall scattering is the sum of the two.

In this work the scattering bodies or roughness features are generally assumed to be small with respect to the wavelength being used, although the limiting values of this assumption are also examined. Moreover, they are assumed to be randomly distributed in space -- i.e. the effects of particular spatial distributions are not examined, but the cumulative effect of a group of scattering bodies as a statistical ensemble is studied.

The basic pattern of the work is as follows. Data were collected using a scale model experiment, in a two-layer geometry, both with, and without, scatterers of various types in place. These results were used to develop techniques for separating scattering information from the response to the layered structure. These tools were then applied to field data from the several regions studied, in order to estimate the nature of scattering in each region.

1.2 Radio interferometry depth sounding

The radio interferometry concept and application has been described at some length elsewhere (for example Annan, 1970; Rossiter, 1971; Simmons et al., 1972; Annan, 1973; Rossiter et al., 1973) so the current description will be brief. In simple terms, a radio transmitting antenna is laid out on the surface to be probed, and a receiver makes measurements of field strength as a function of distance from the transmitter.

Waves travel directly from the transmitter to the receiver above the surface. In addition, if the sub-surface material is sufficiently transparent at the frequency being used, waves travelling through the sub-surface material will also arrive at the receiver, and will interfere with the direct wave (see Fig. 1-1). Therefore, a plot of received field strength vs range shows the field decaying with distance, but also shows a complicated interference pattern as various waves from the sub-surface constructively and destructively interfere with the direct wave (Fig. 1-2). This pattern is indicative of the electrical properties and the geometry of the sub-surface.

The experiment, as configured for the lunar experiment, and as used in most of the terrestrial experiments to date, is as follows (see Fig. 1-3). The transmitter operates at six frequencies: 1, 2, 4, 8, 16, and 32 MHz, and powers each of two perpendicular horizontal electric dipole antennas, at each frequency, in succession. Each antenna is powered for sufficiently long that the experiment can be considered continuous wave (i.e. all transients have died out). The receiver, which is usually mounted on some sort of

RADIO INTERFEROMETRY

HALF - SPACE CASE

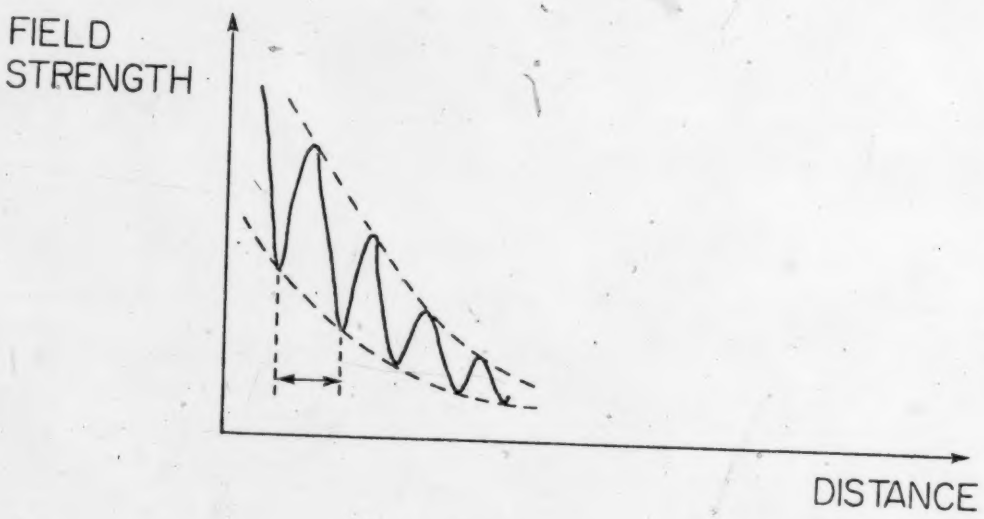

Figure 1-1.

RADIO INTERFEROMETRY

TWO LAYER CASE

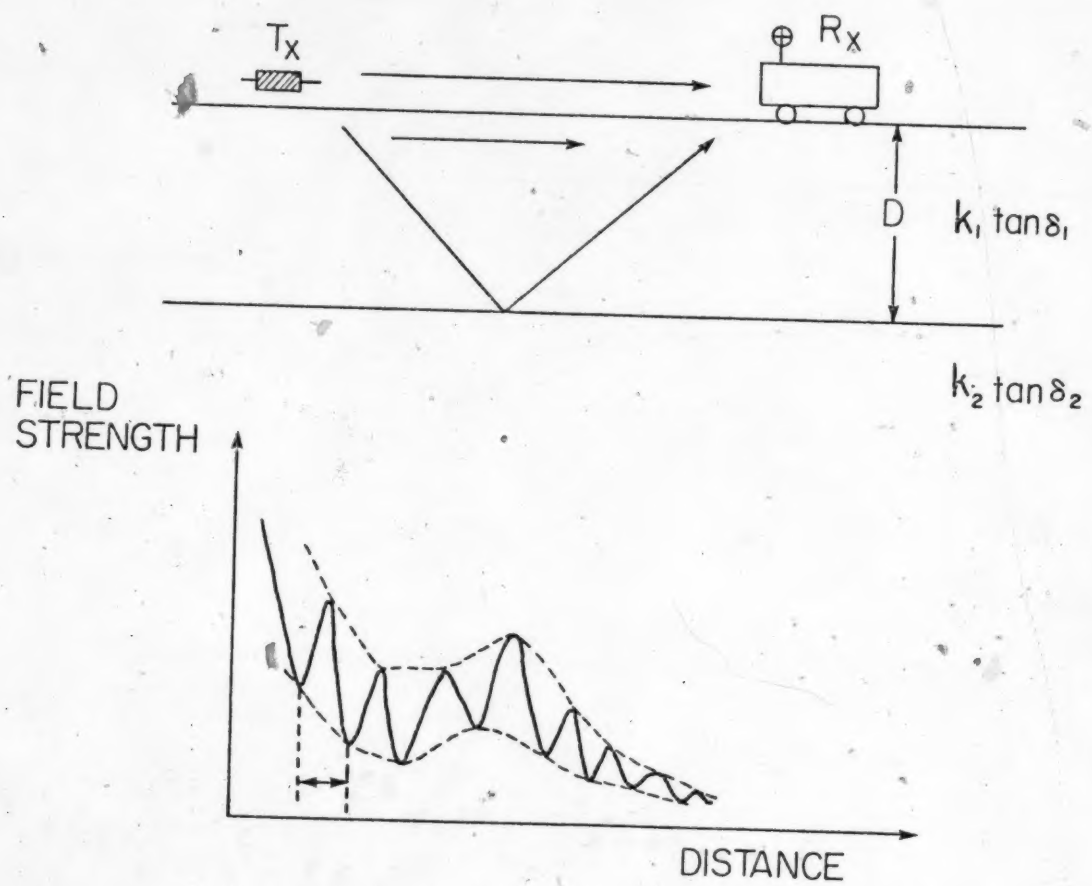

Figure 1-2.

RADIO INTERFEROMETRY

Plan View -- Field Configuration

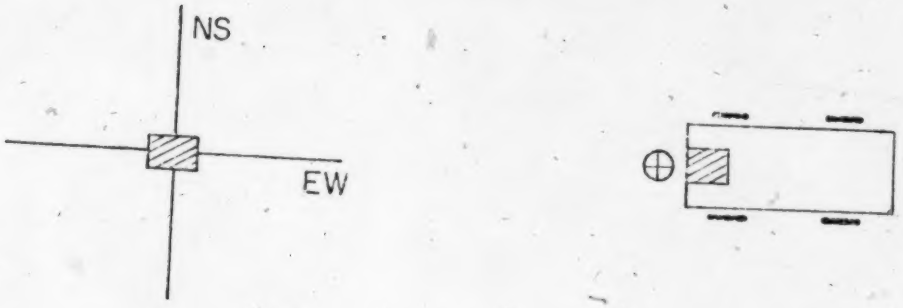

Transmitter
2 horizontal electric
half-wave dipoles

Receiver
3 orthogonal loops

6 frequencies: 1, 2, 4, 8, 16, and 32 MHz

6 components:

3 endfire (EW transmitting antenna powered)

H_ρ (radial) - minimum-coupled
H_ϕ (tangential) - maximum-coupled
H_z (vertical) - minimum-coupled

3 broadside (NS transmitting antenna powered)

H_ρ (radial) - maximum-coupled
H_ϕ (tangential) - minimum-coupled
H_z (vertical) - maximum-coupled

6 x 6 = 36 independent measurements made as a function of distance between transmitter and receiver.

Figure 1-3

vehicle, takes measurements from each of three orthogonal magnetic dipole antennas, for each combination of transmitted frequency and antenna. Therefore 6 x 2 x 3 = 36 independent measurements are made as a function of distance for each run. Unfortunately, no phase information is recorded.

A scale model experiment was also designed to make measurements in the laboratory. This was operated primarily at a frequency of 5.9 GHz, so that the free space wavelength was scaled from tens or hundreds of meters to 5.08 cm. Both the transmitter and receiver in the model were horizontal electric half-wave dipole antennas. A two-layer configuration, consisting of a variable-depth layer of low-loss transformer oil over an aluminum plate, was used for most experiments.

Because of the complexity of the interference patterns that are received from anything other than quite simple geometries, the redundancy of information obtained by measuring six different components for each of six frequencies is essential to be able to successfully interpret the data. In order to simulate various freqeuncies in the scale model, the size of structures is varied. Although this procedure is adequate to model different geometries, it is not possible to represent frequency-dependent electrical parameters easily.

In order to study more general two-layer, theoretical formulations for the EM fields were developed. Theoretical calculation programs were tested against scale model results, and

then used to calculate curves for other sets of parameters (Annan et al., 1975). Interpretation of the data measured in the field was then accomplished by comparison to computed curves for plane layered geometries of arbitrary electrical parameters.

1.3 Thesis outline

In Chapter 2, baseline data from the scale model will be given, and an interpretation of two-layer results presented. Scattering effects from both a single scatterer and from distributions of many scatterers will be shown. A way in which the effects of scattering can be separated from the interferometry response will be given. Chapter 3 will contain a theoretical model based on perturbations to the normal modes propagating in a two-dimensional waveguide. In Chapter 4 field data from four different geological regions will be presented. Layered structure interpretations will be given, and scattering effects will be isolated from the data using the results of Chapters 2 and 3. Finally, in Chapter 5, the estimated effects of scattering seen in the field data from each of the regions will be examined, and the implications will be considered in terms of the geological nature of each region.

CHAPTER 2

SCALE MODEL STUDIES

2.1 Introduction to scale model studies

Although a theoretical basis for certain types of random scattering is presented in Chapter 3, it is far easier to study a large number of physically realistic cases by using an analogue scale model. Data collected using such a controlled environment (described in Chapter 1, in Appendix 1, and by Annan et al., 1975, and in unpublished reports such as Waller, 1973) are presented here. First the simple two-layer geometry will be examined, then several different types of perturbations on the basic structure by random scatterers will be discussed. Hence it will be possible to follow the transition from no scattering to considerable random scattering.

At the same time the processing applied to the data will be presented, and the results shown. There are several problems in extracting scattering information from radio interferometry data. First, it is not clear a priori what the effect of any given distribution of scatterers might be on a particular interference curve. Secondly, interferometry measurements, by their very nature, tend to be highly sensitive to small changes in parameters. Therefore it is necessary to isolate some essential features from the data that are fairly indicative of the large-scale geometry, and then to determine the effects of perturbations.

The general approach that I have taken to reduce the high sensitivity is to examine interferometry data in the wavenumber domain,

i.e. to take a power spectrum of an interference curve using Fourier Transform methods. The rationale behind this approach is that for a given geometry several sets of waves are set up that interfere with each other. The resulting interference pattern contains various spatial-frequency components, and these are more consistent than the absolute size or position of any particular interference peak or null. One feature of this approach is that it leads naturally to various filtering techniques to enhance or to reject particular spatial frequencies.

The remainder of this chapter will examine the two-layer case (dielectric over a perfect reflector): first, with no scattering, with the bottom reflector both horizontal and tilted slightly; the effects of a single scatterer; and, finally, the effects of many scatterers. The effects of scatterers within the dielectric itself are dealt with theoretically in Chapter 3.

2.2 Two-layer case: horizontal layers

As mentioned earlier, a two-layer geometry will be the basic structure used: a dielectric layer overlying a nearly perfect reflector, represented by transformer oil over an aluminum sheet. Therefore, given a set of data from a region that reasonably approximates this geometry, one would initially like to be able to determine (a) the electrical properties (dielectric constant and loss tangent) of the upper layer, and (b) the thickness of the upper layer. We will postpone to the next section the situation of a dipping reflector.

A set of scale model data, collected with various thicknesses of oil, are shown in Fig. 2-1, plotted on a logarithmic (dB) scale. Theoretical curves for the typical electrical properties of transformer oils (dielectric constant = 2.16, loss tangent = 0.002) are also shown in Fig. 2-1 (computed using programs written by A.P. Annan). Previous interpretations of field data have been made by comparing the field results to extensive sets of theoretical curves. However, if the properties are not known reasonably well, this approach can become intractable, since the number of possible comparisons that needs to be made can become prohibitively large. Also, the resulting interpretation may not be unambiguous. It would be preferable to be able to estimate the required parameters analytically from the data.

Rossiter et al. (1973) showed that if there is significant interference between waves travelling directly from the transmitter to the receiver, both above and below the air-earth interface, they

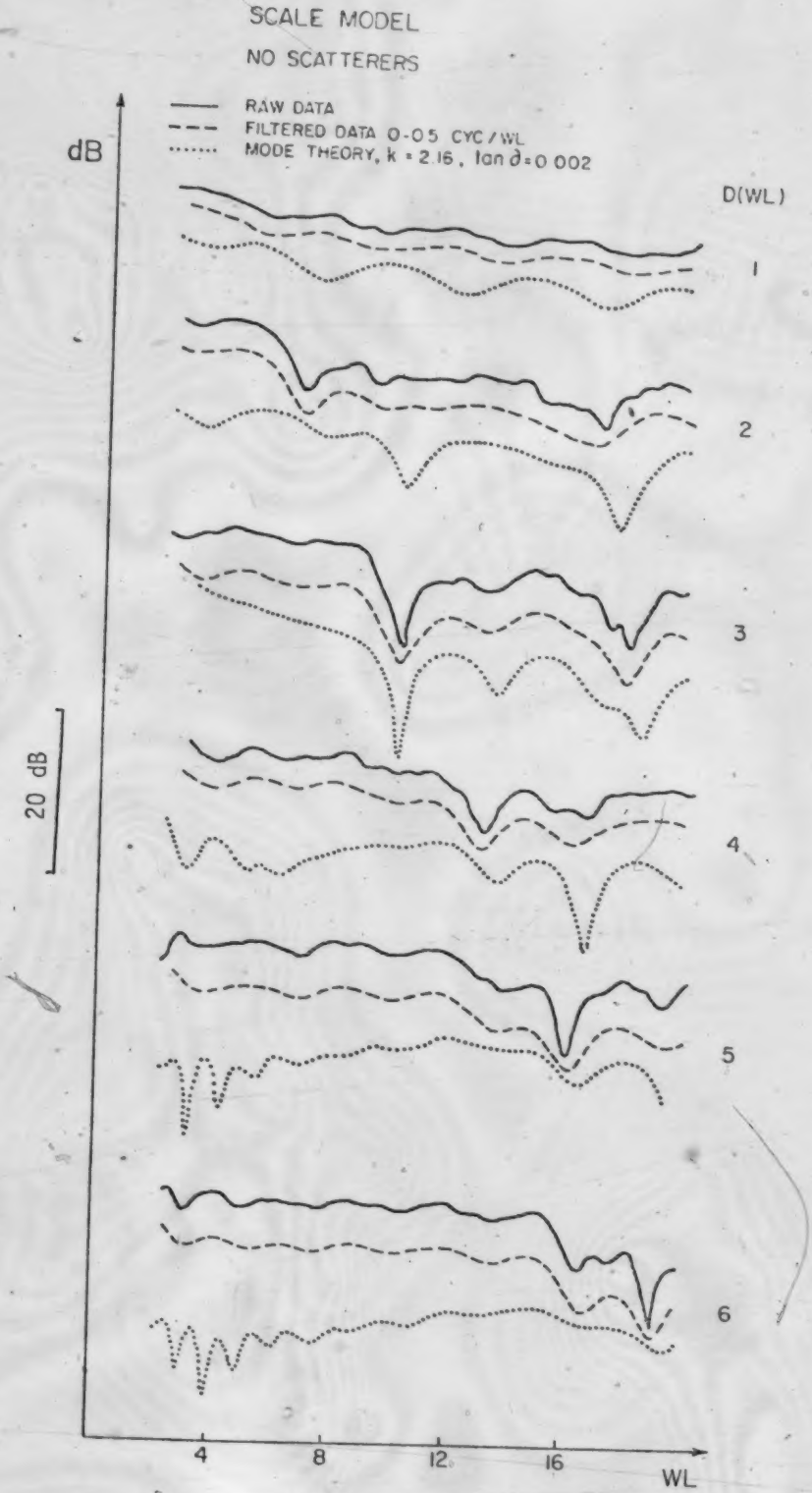

Figure 2-1. Accuracy of scale model is ± 1 dB (see appendix 1).

should beat with a frequency given by

$$f_k = k_1^{\frac{1}{2}} - 1 \qquad (1)$$

where f_k is the beating frequency in cycles per free-space wavelength (wl), and k_1 is the relative dielectric constant of the earth. Hence,

$$k_1 = (f_k + 1)^2 \qquad (2)$$

Equation (2) suggests that if the surface wave beating were strong, frequency f_k would show up in a spectral analysis of the interference curve, and k_1 could be calculated.

Power spectra of the curves shown in Fig. 2-1 are shown in Fig. 2-2. To compute each spectrum, the raw curve from Fig. 2-1 was put into the linear domain, i.e. field-strength instead of dB, which reduces the effects of the very sharp nulls endemic to the logarithmic curves. Then a power law fit of the form $r^{-\alpha}$ was subtracted, where r is distance from the transmitter, and α is determined from the data by a least-squares fit to all points in the linear curve (See Appendix 2). This procedure is essentially a pre-whitening that removes the strong decay in field-strength away from the transmitter. The power spectrum was then computed using a one-dimensional Fast Fourier Transform (FFT).

It is clear that the bulk of the energy is well below the Nyquist frequency of 5 cycles/wl, and is largely below 0.5 cycles/wl. For thicker layers -- greater than 3 wl -- there are two main spectral peaks. The lower frequency is attributed to a large reflection from the sub-surface reflector, which is discussed in more detail below. The high frequency is associated with the beating of the surface waves. For thicknesses of 2 to 3 wl, several distinct modes are able to

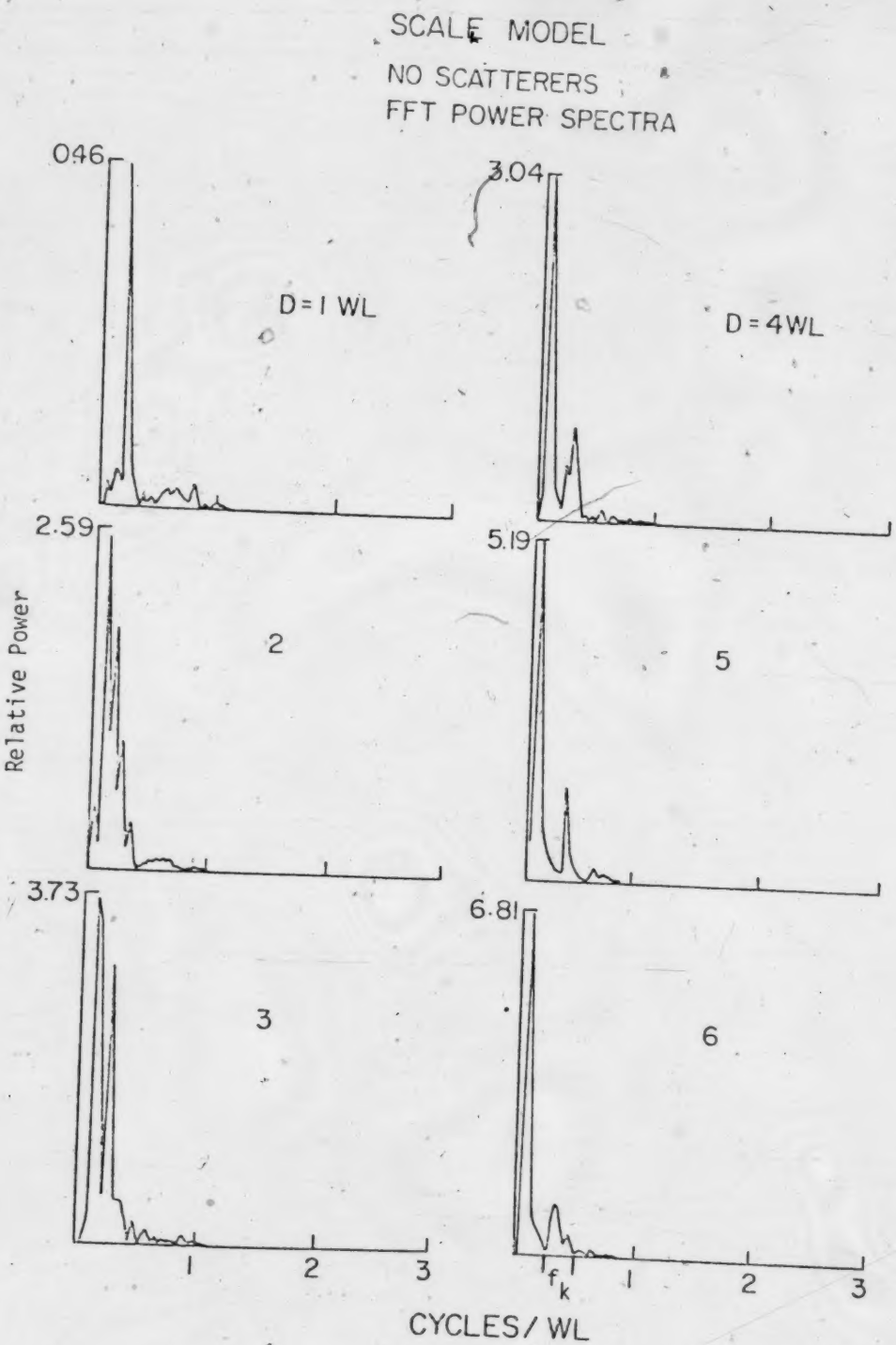
SCALE MODEL
NO SCATTERERS
FFT POWER SPECTRA
0.46
D = 1 WL
3.04
D = 4 WL
2.59
2
5.19
5
Relative Power
3.73
3
6.81
6
1
2
3
f_k
1
2
3
CYCLES / WL

Figure 2-2.

propagate with little attenuation in the dielectric layer, and these interfere with each other to give several spectral peaks. For a depth of 1 wl, two modes predominate (and then only relatively weakly).

Also apparent on the spectral curves (Fig. 2-2) are the small amounts of energy between frequencies of 0.5 and 1.0 cycles/wl. These are attributed to reflections from the walls of the tank, and to standing waves set up between the transmitter and receiver, and are apparent as small ripples on the raw curves in Fig. 2-1 (See Appendix 1). These ripples have been removed from the filtered curves, shown in Fig. 2-1, by suppressing all frequencies above 0.5 cycles/wl. As can be seen, there is no phase shift in the filtered curves, although some of the sharp nulls are slightly smoothed. Filtering was done by removing high spectral components in the wavenumber domain and re-transforming back to the space domain.

The frequency of immediate interest, f_k, is between 0.25 and 0.50 cycles/wl (Fig. 2-2). These values, using equation (2), give an apparent dielectric constant of 1.90 ± 0.35. Although the assumed dielectric constant, 2.16, is within this spread, the mid-value is somewhat low. One possible explanation is that the frequency, f_k, given by equation (1) is the highest frequency possible if two plane waves, travelling in the same direction, interact. Therefore the high edge of the spectral peak may be more indicative of the true dielectric constant than its peak value.

In order to more accurately estimated the exact position of

spectral peaks, maximum entropy (or "autoregressive") power spectral density curves were also calculated (Fig. 2-3). Although this method of computing spectra is still somewhat controversial because its usefulness depends on the choice of prediction operator, it appears to give the positions of spectral peaks from short data series with far greater resolution than standard Fourier methods (see Ulrych and Bishop, 1975; Wiggins and Miller, 1972, for descriptions of this method). However, the relative power in any peak is not accurate, and since variance estimates are not available, these relative intensities were ignored. The spectral estimates were calculated from the raw interference curves in the same way as for the FFT spectra, with the exception that the maximum entropy method was used in the final step (using a routine written by S.W. Dunbar), with a prediction error operator length of 40% of the data length.

Using the highest spectral peaks, as obtained with the maximum entropy method, shown in Fig. 2-3, the dielectric constant of the oil was estimated with equation (2). The results are given in Table 2-1. The estimated dielectric constant, 1.7 ± 0.3 is still considerably lower than the expected value of 2.16, and we will return to this point later in the section.

If the interaction between the super- and sub-surface waves are almost entirely represented in the 0.25 to 0.50 cycles/wl frequency band, it should be possible, at least in principle, to determine the loss tangent of the dielectric from the decay of this frequency component with distance from the transmitter.

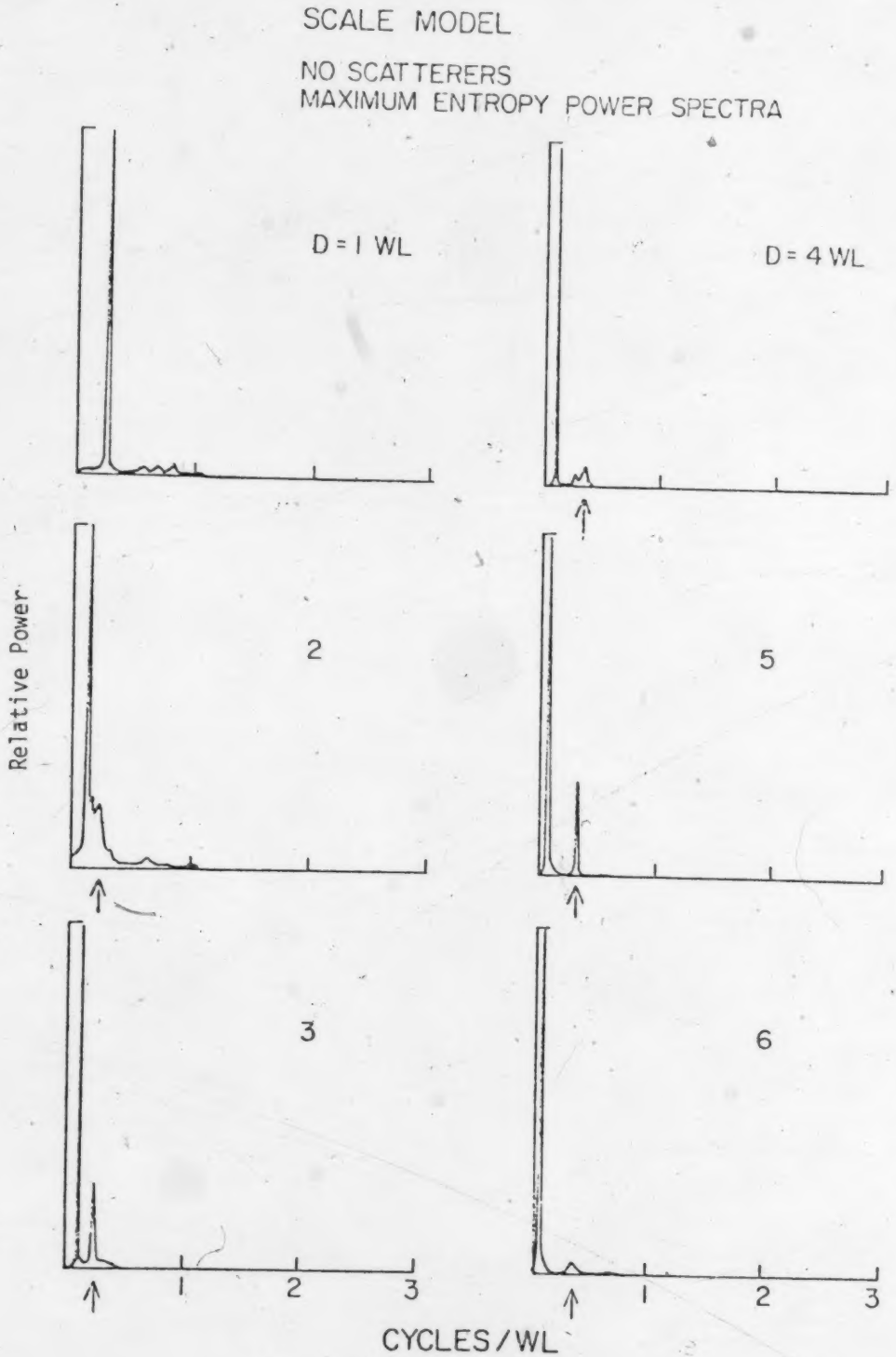

Figure 2-3. Arrow indicates dielectric constant interference frequency, f_k. Each spectrum is normalized to its largest peak. Amplitudes of peaks are not significant.

Table 2-1: Scale Model Dielectric Constant and Depth Estimates; Horizontal Reflector

Oil Thickness (wl)	f_k (1) (cycles/wl)	Dielectric Constant (k_1) (2)	Peak Position (wl) (3)	Depth Estimate (wl) (4)
2.0	0.24 (.17-.30)	1.54 (1.37-1.69)	---	---
3.0	0.24 (.20-.28)	1.54 (1.44-1.64)	8.15 ± 0.5	3.0 (2.3-3.6)
4.0	0.35 (.17-.37)	1.82 (1.37-1.88)	8.55	3.9 (2.7-3.6)
5.0	0.33 (.30-.35)	1.77 (1.69-1.82)	11.4	5.0 (4.5-5.4)
6.0	0.33 (.26-.39)	1.77 (1.59-1.93)	14.1	6.2 (5.2-7.0)

(1) Figure 2-3

(2) Equation 2-2

(3) Figures 2-6, 2-7

(4) Equation 2-12

If two waves on the boundary of the half-space interfere with each other, the wave above the surface will decay as 1/r (spherical wave spreading), and the wave below the surface will decay, not only with 1/r dependence, but also with an exp(-cr) attenuation loss in the earth. Here c is a loss factor that is directly related to the loss tangent, tan δ .

Then, when the waves are in-phase, a curve formed by joining the peaks, R_s, is an estimate of the in-phase summation of the two waves, and the curve formed by joining the nulls, R_d, the out-of-phase difference between the two:

$$R_s(r) = \frac{a}{r} + \frac{b}{r} e^{-cr} \tag{3}$$

and,

$$R_d(r) = \frac{a}{r} - \frac{b}{r} e^{-cr} \tag{4}$$

where a and b are the initial field-strengths of the air and earth waves respectively. The difference of (3) and (4) gives:

$$\left[R_s(r) - R_d(r)\right] \cdot r = 2be^{-cr} \tag{5}$$

Taking logarithms,

$$\ln \left[R_s(r) \cdot r - R_d(r) \cdot r\right] = \ln (2b) - cr \tag{6}$$

Hence, the decay of the envelope around the peaks and nulls should give an estimate of c. The attenuation factor, c, is related to the loss tangent by (von Hippel, 1954, p.28):

$$c = 2\pi\left[(\tfrac{1}{2})k_1(\sqrt{1 + \tan^2 \delta} - 1)\right]^{\frac{1}{2}} \tag{7}$$

or,

$$c = \pi \sqrt{k_1} \tan \delta \tag{8}$$

for very low losses. Distance is in free-space wavelengths.

An envelope was calculated by manually picking the peaks and troughs on an interference curve in the linear domain. A piecewise cubic spline was fitted to the peaks to obtain $R_s(r)$, and to the

nulls, to obtain $R_d(r)$. Each of these resultant curves was multiplied by the distance factor r, and their difference computed. By then taking logarithms, the attenuation factor, c, can be computed using equation (6). The loss tangent was calculated using equation (8).

In Fig. 2-4 the envelopes calculated for the curves shown in Fig. 2-1 are presented for spatial frequencies between 0.25 and 0.50 cycles/wl (the curve for D = 1 wl was too weak in this frequency band to be useful). As can be seen, the envelopes do not show a smooth decay, but have a bulge that moves out with depth to the reflector and is attributed to an increase in energy coming from the reflecting plate. Of course, the position of the bulge is not given accurately in Fig. 2-4 because of the narrow bandwidth used.

The difficulty of estimating the loss tangent of the oil is compounded by its very low electrical loss ($\tan\delta \approx 0.002$). Therefore, sub-surface waves are not greatly attenuated, and the decay of the envelope is not expected to be large. Using the envelope decay away from the bulge (Fig. 2-4) for the D = 3 wl case, and equations (6) and (8), gives $\tan\delta \approx 0.002$. The same procedure for D = 2 wl gives $\tan\delta \approx 0.02$. However, it is clear that virtually any value below 0.02 could be obtained by choosing a different section of the envelope. It appears that although the technique of examining the rate of decay of the envelope curves shows promise theoretically for estimating the loss tangent, it must be used with some care because of the unwanted effects from reflections.

It is also of interest to be able to determine the depth to the reflector. One approach to this problem is suggested by the peaks in the envelopes, which are due to energy reflecting from the plate.

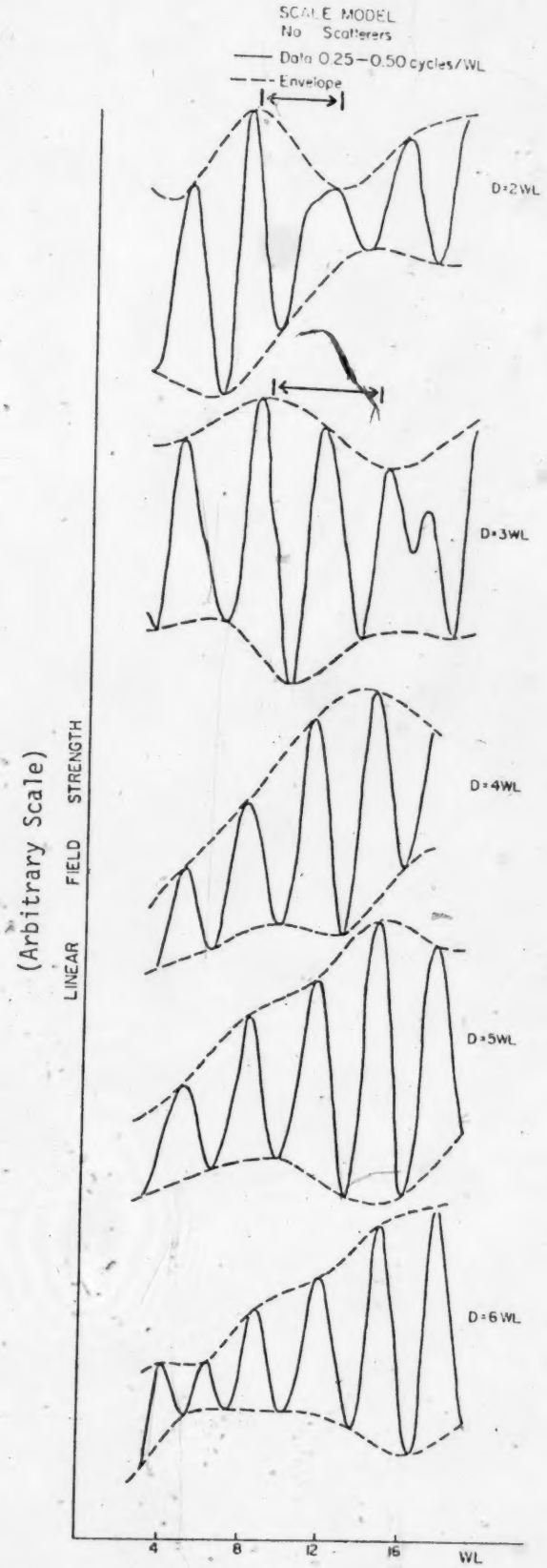

Figure 2-4. Each curve is normalized in amplitude. Regions used for loss tangent estimates are shown.

The radiation pattern of a horizontal electric dipole on the surface of a two-layer dielectric earth, has been examined in some detail by Annan (1970, 1973), Cooper (1971), Kong (1972), LaTorraca (1972), Tsang et al. (1973), Kong et al. (1974), Tsang and Kong (1974), Tsang et al. (1974), Annan et al, (1975), and Chan et al. (1976). A typical pattern is shown in Fig. 2-5. The feature of interest is the large lobe directed into the lower layer, which is essentially created by critically refracted waves entering the sub-surface at the interface. The direction of the lobe depends on the dielectric constant of the lower layer, k_1 (assuming the upper layer to be free space, and the lower layer losses to be negligible). The angle from the vertical (the "critical angle") is given by:

$$\theta = \sin^{-1} \left(\frac{1}{k_1}\right)^{\frac{1}{2}} \tag{9}$$

in the plane broadside to the electric dipole. For the endfire orientation, the angle is given by:

$$\theta = \sin^{-1} \left(\frac{2}{1 + k_1}\right)^{\frac{1}{2}} \tag{10}$$

(although the relative energy in this direction is much smaller).

The lobate pattern therefore directs a substantial fraction of radiated power into a fairly narrow solid angle. Hence, by measuring the position of the peak in the envelope, knowing the dielectric constant of the upper layer, and assuming a horizontal reflector, it should be possible to estimate the thickness of the top layer. For a horizontal reflector it is easily shown that the distance

BROADSIDE RADIATION PATTERN

$k_1 = 2.16$

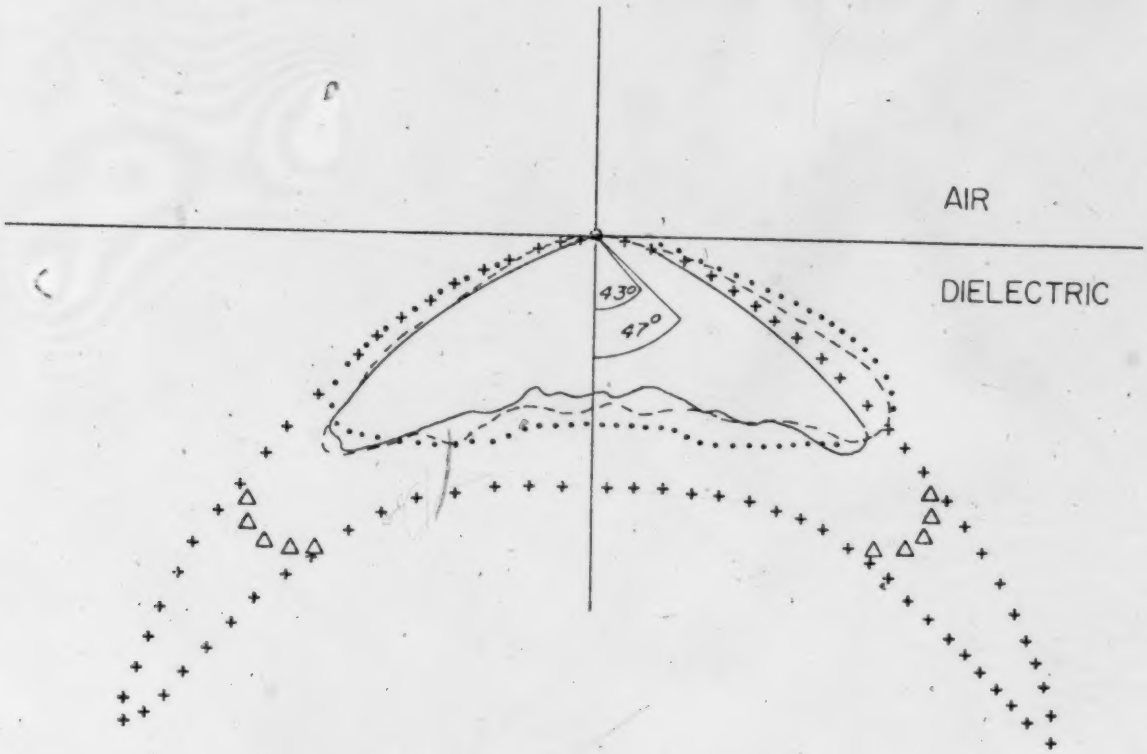

\+ THEORETICAL (COOPER, 1971)
△ FINITE DISTANCE APPROXIMATION
• SCALE MODEL, 3.0 WL RADIUS
-- " " 4.5 " "
— " " 6.0 " "

Figure 2-5.

from the transmitter at which the peak energy will be received is:

$$\rho = 2D \tan\theta \qquad (11)$$

where ρ is the distance of peak received power (from the transmitter),

D is the depth to the reflector, and,

θ is the angle of greatest radiated power (from the vertical).

Substituting equations (9) and 10) into (11),

$$D = \frac{\rho}{2} \left(k_1 - 1\right)^{\frac{1}{2}} \qquad (12)$$

for broadside transmitting antenna, and,

$$D = \frac{\rho}{2} \left(k_1 - 1\right)^{\frac{1}{2}} \qquad (13)$$

for an endfire antenna.

The envelopes for the curves shown in Fig. 2-1, with no filtering, are given in Fig. 2-6 (plotted on a linear, not dB scale). There is a clearly visible peak in the envelope, which moves out smoothly with reflector depth, for depths greater than about 3 wl (Fig. 2-7, inset). However, for a thinner upper layer there is no clear peak. It is at about this thickness that the radiation pattern becomes greatly distorted by the presence of the reflector. It is not surprising, then, that at this depth the geometrical optics theoretical solutions break down (Annan et al., 1975). It is also at this depth that the clear splitting of the spectra into a reflected component and a dielectric constant interference component is no longer seen (Figs. 2-2 and 2-3).

Substituting the positions of the peak, determined in Figs. 2-6

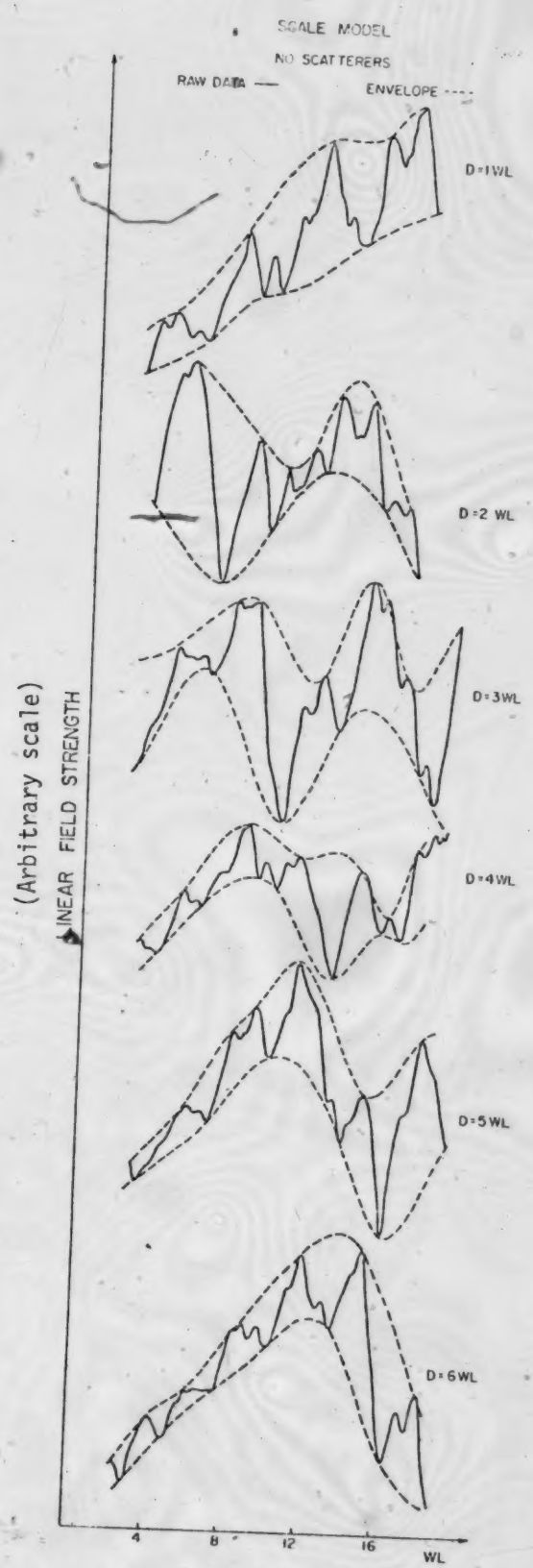

Figure 2-6. Each curve is normalized in amplitude.

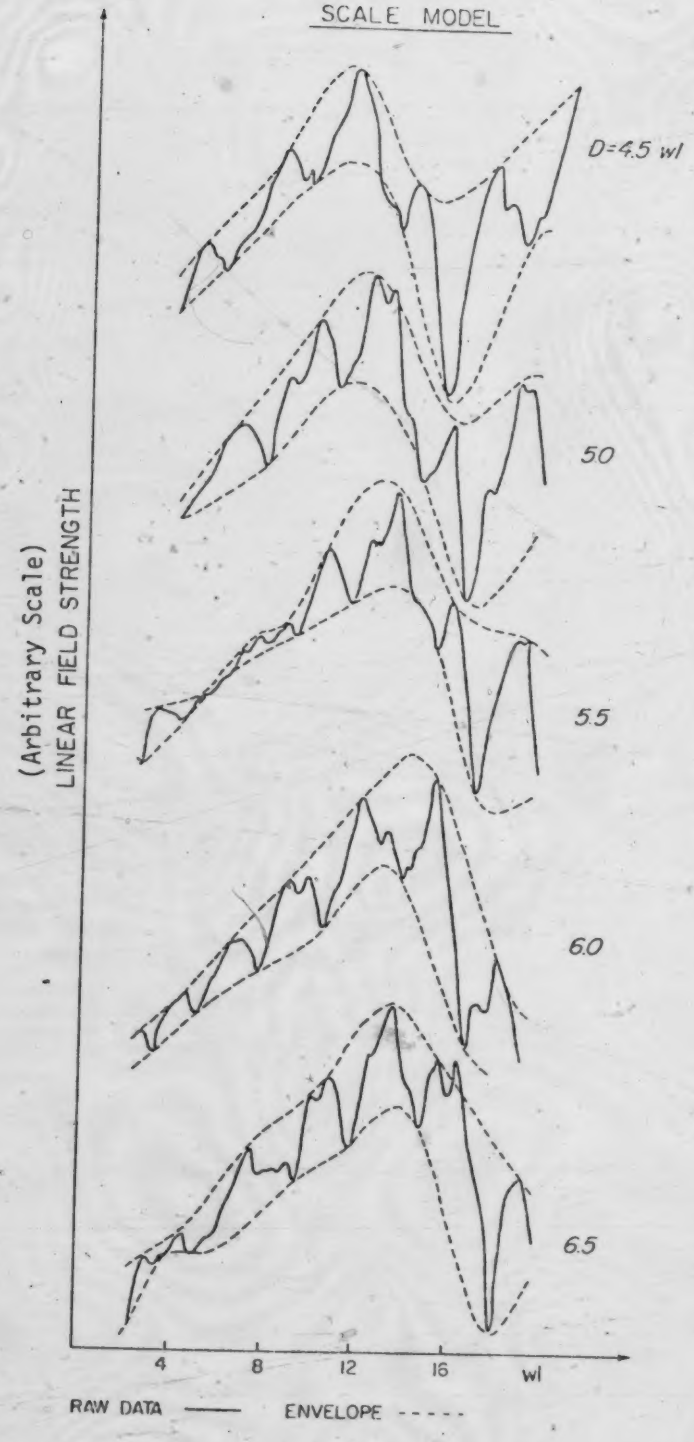

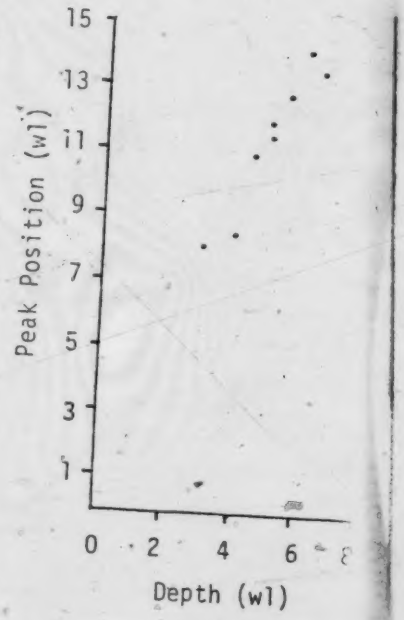

Figure 2-7. Each curve is normalized in amplitude.

and 2-7 into equation (12), the reflector depths determined using the assumed dielectric constant of 2.16 are consistently overestimated. This result implies that the radiation lobe in the model is shifted somewhat toward the horizontal plane, as is seen in scale model measurements of the radiation pattern (Fig. 2-5). The theoretical pattern is calculated for an infinite distance from the transmitter, and, as shown in Fig. 2-5, as this distance increases, the measurements do approach the theoretical pattern.

However, using the dielectric constant estimated using maximum entropy spectra, much better depth estimates, given in Table 2-1, are obtained. The internal consistency of the results, in spite of relatively large possible errors in making the estimates, suggests that the dielectric constant of the oil is somewhat lower than originally thought. Although the value was independently measured while the scale model was in Houston, a different oil was used in Toronto, and it is possible that the latter had, in fact, a lower dielectric constant.

The component discussed so far in this section is that measured with both the transmitting and receiving dipoles perpendicular to the traverse direction (i.e. E_ϕ broadside compenent). Clearly by turning the receiver 90°, so that it is parallel to the traverse, a minimum-coupled response will be obtained. A set of raw data from this component and the respective power spectra are shown in Fig. 2-8. This component essentially illustrates the effective background noise level in the model environment, and the spectra are understandably

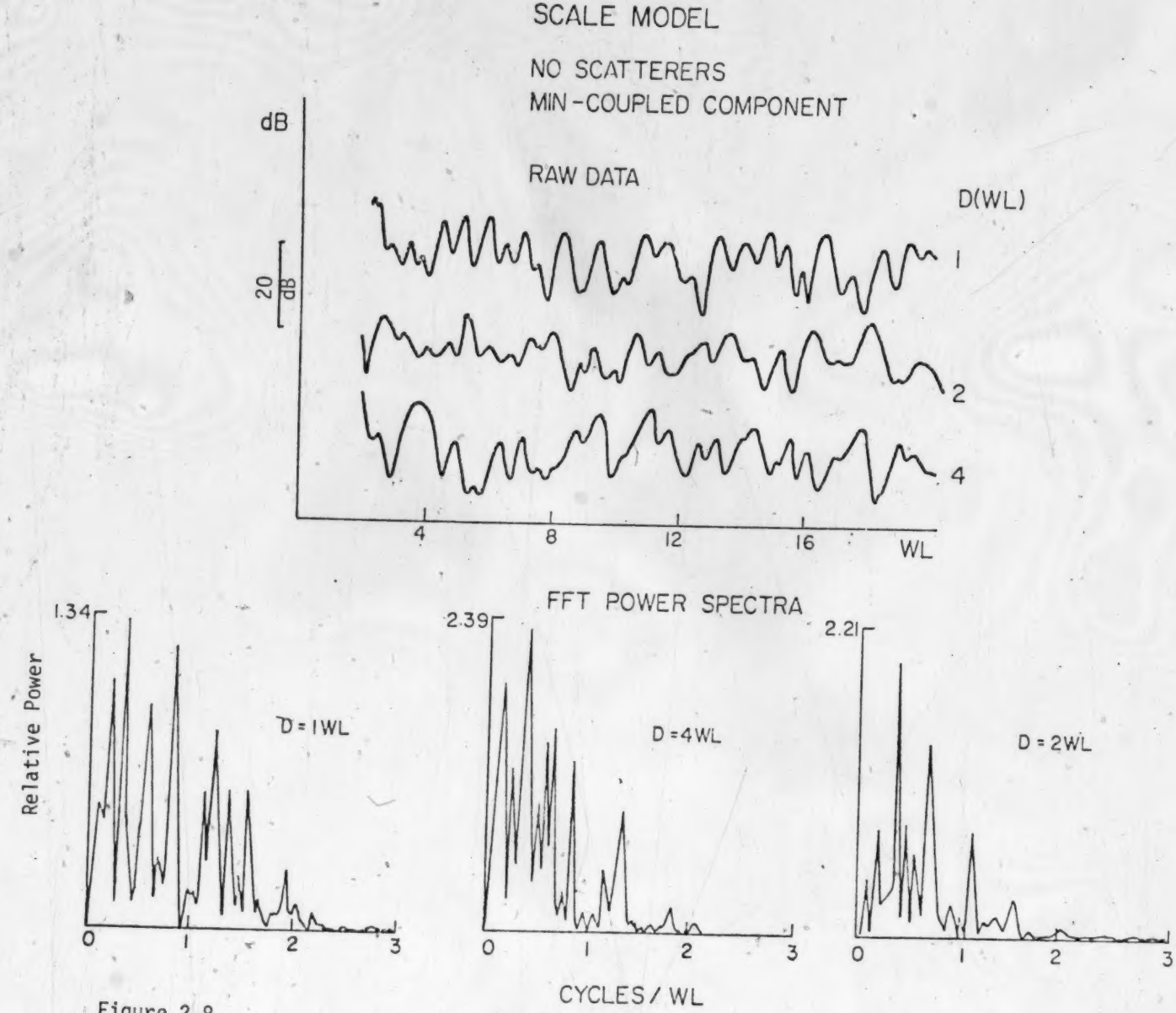
SCALE MODEL
NO SCATTERERS
MIN-COUPLED COMPONENT
RAW DATA
dB
20 dB
D(WL)
1
2
4
4
8
12
16
WL
FFT POWER SPECTRA
Relative Power
1.34
D = 1WL
2.39
D = 4WL
2.21
D = 2WL
0
1
2
3
CYCLES / WL

Figure 2-8

random. A $r^{-\alpha}$ function was fitted to these in exactly the same way as for the maximum-coupled component. By comparing the intercepts of the fits from the components, a measure of the relative level of the two was obtained (See Appendix 2). Over depths from 1 to 6 wl, the two sets of components were separated by an average of 41 dB.

The importance of this component is that if scattering were large, energy would be expected to transfer from the maximum-coupled component to the minimum-coupled component as the coherent waves became randomized. Further, since the coupling is implicitly for a plane layered geometry, the separation will also decrease in the presence of lateral inhomogeneities.

In the field situation, as described in Chapter 1, six components are collected at each frequency, three maximum- and three minimum-coupled. Unfortunately the field components are not directly analagous to the scale model measurements, except that the H_z broadside field component is proportional to the E_ϕ broadside model component (Annan, 1970). However, relative behaviour of the maximum and minimum components can still be deduced from the scale model in a qualitative way.

In summary, this section has developed ways in which the properties of a two-layer structure can be interpreted directly from interferometry data. The dielectric constant of the upper layer can be estimated using the highest spatial frequency spectral lines and using maximum entropy analysis for greater resolution. The envelope around the interference peaks and troughs can possibly be used to

estimate the loss tangent of the upper layer by the rate at which the envelope decays. The depth to the reflector can be estimated by picking the peak of the return energy in the envelope curve. Although it is difficult to assign accuracies to these estimates, the results from the scale model are, at least, internally consistent. Finally, a minimum-coupled component can be used as a background reference to the maximum-coupled signal.

2.3 Two-layer case: tilting reflector

The formulas given above for the thickness of the upper layer, equations (12) and (13), are obviously only applicable for a horizontal reflector. The situation may occur in which the thickness of the dielectric layer increases or decreases fairly constantly along the traverse. Then the arrival of the energy peak will be further from, or closer to, the transmitter, respectively.

The geometry is shown in Fig.2-9, in which the critical angle is θ, the depth to the reflector is D, directly below the transmitter, and D^1, at the point of reflection. The tilt of the reflecting plane is α, positive for increasing thickness along the traverse. ρ_1 and ρ_2, shown, are distances along the surface. Then, clearly

$$\rho_1 = D^1 \tan\theta \tag{14}$$

$$\rho_2 = D^1 \tan(\theta + 2\alpha) = D^1 \tan\gamma \tag{15}$$

$$\rho = \rho_1 + \rho_2 = D^1(\tan\theta + \tan\gamma). \tag{16}$$

Hence,

$$D^1 = \frac{\rho}{\tan\theta + \tan\gamma} \tag{17}$$

$$D = D^1 - \rho_1 \tan\gamma \tag{18}$$

$$= D^1 - D^1 \tan\theta \tan\alpha = \frac{\rho(1 - \tan\theta \tan\alpha)}{\tan\theta + \tan\gamma} \tag{19}$$

When there is no tilt, $\gamma = 0$, and equation (19) reduces to equation (11). It gives a means of determining the layer thickness, even if the lower reflector is sloping, if the tilt can be estimated. The tilt might be determined, for example, from other

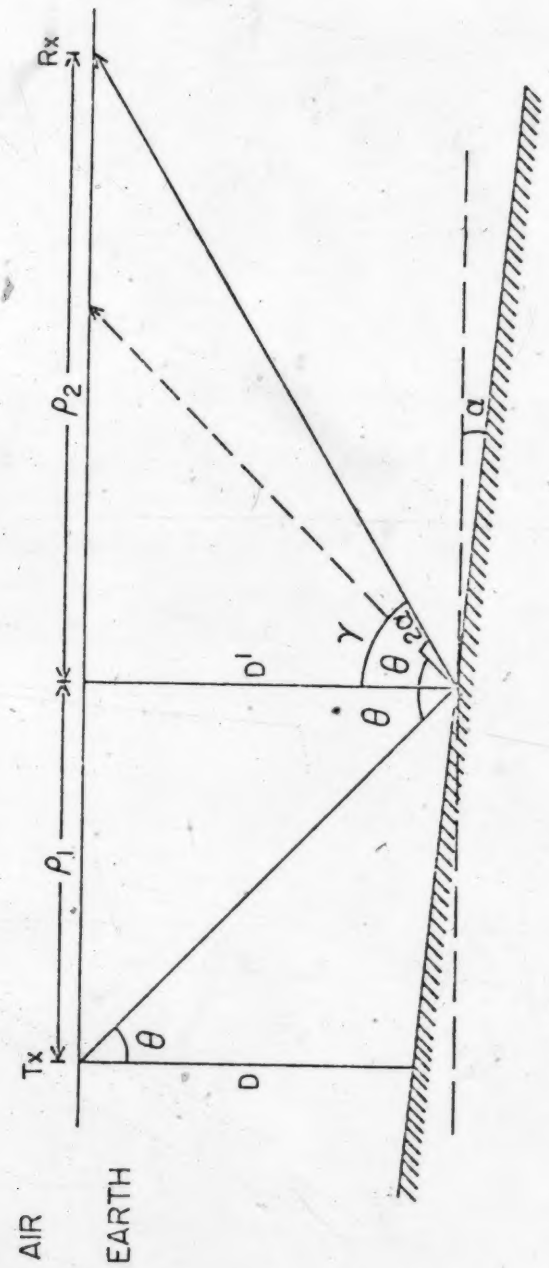

TILTING INTERFACE GEOMETRY

Figure 2-9

geological evidence, or by traverses made both up- and down-dip, as discussed below. Equation (19) also applies to a traverse up-slope, since γ will then be negative.

A number of cases with a tilting reflector were run in the scale model, and the results are presented in Figs. 2-10 and 2-11. The estimated depths at the transmitter, using the positions of the peak, equation (19), and an effective dielectric constant of 1.7 ± 0.3, do not agree with the actual depths as well as for a horizontal reflector (Table 2-2). If the maximum entropy spectral peaks are used, as before, to estimate the appropriate effective dielectric constant, the results are even worse, since the spectral peak shows a systematic shift to lower spatial frequencies as the tilt increases (layer becoming thicker along the traverse), and to higher spatial frequencies when the tilt is negative (Fig. 2-12).

However, the fact that the spectral line shifts in a reasonably uniform way with the tilt of the reflector (Fig. 2-12a) indicates that the shift could be used to estimate the dip. Examination of the apparent angle of the lobe of the reflection radiation pattern implied by the shifted spectral peaks, shows that it varies by about twice the tilt angle of the sub-surface reflector. This suggests that the lateral waves, initially propagating at close to the critical angle, are reflected, and hence given a new effective angle of propagation if the reflector is dipping..

Therefore, although the physical mechanism is not clearly described, a rough rule of thumb can be developed, based empirically

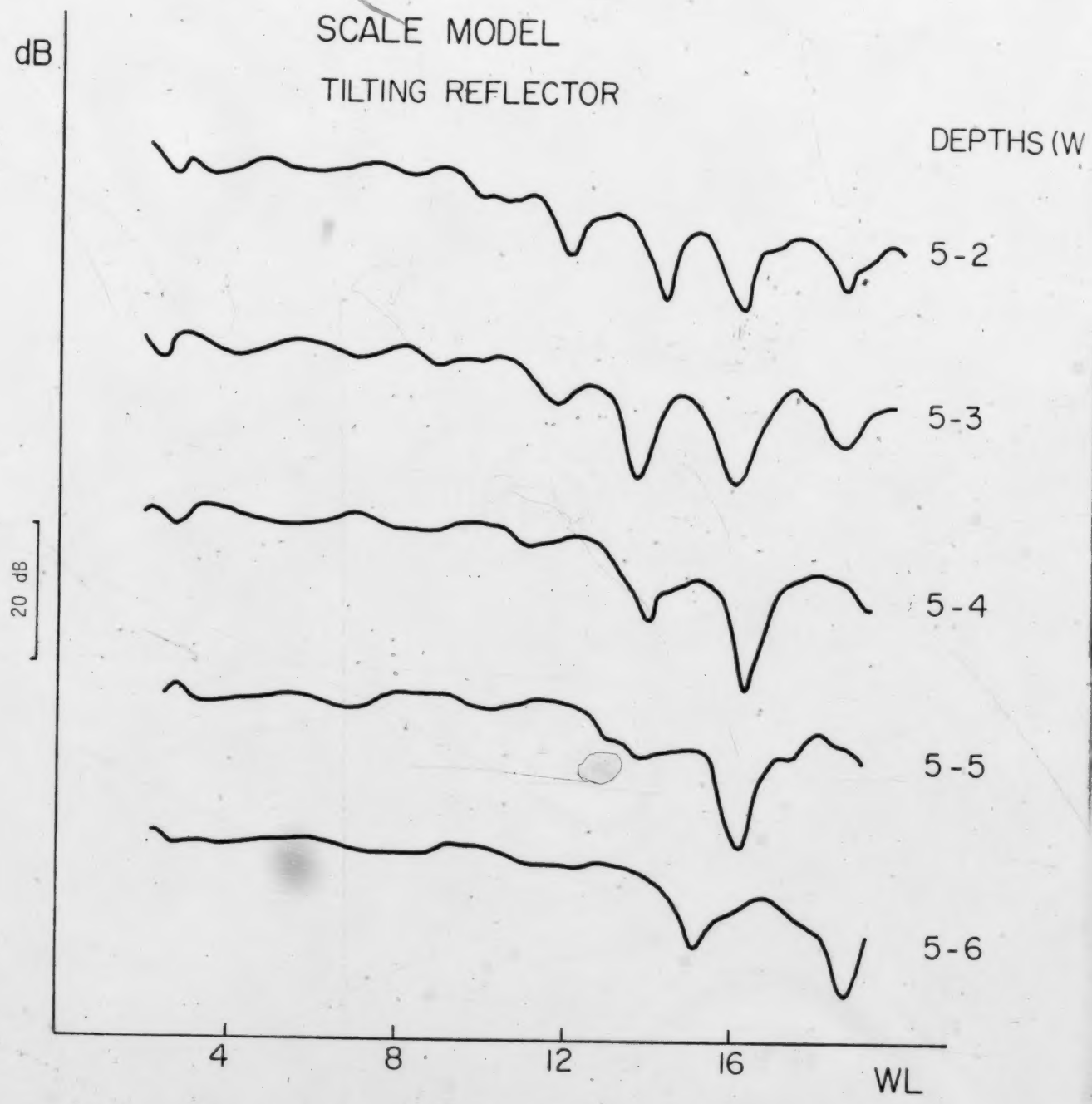
SCALE MODEL
TILTING REFLECTOR
dB
DEPTHS (W
5-2
5-3
5-4
5-5
5-6
20 dB
4
8
12
16
WL

Figure 2-10.

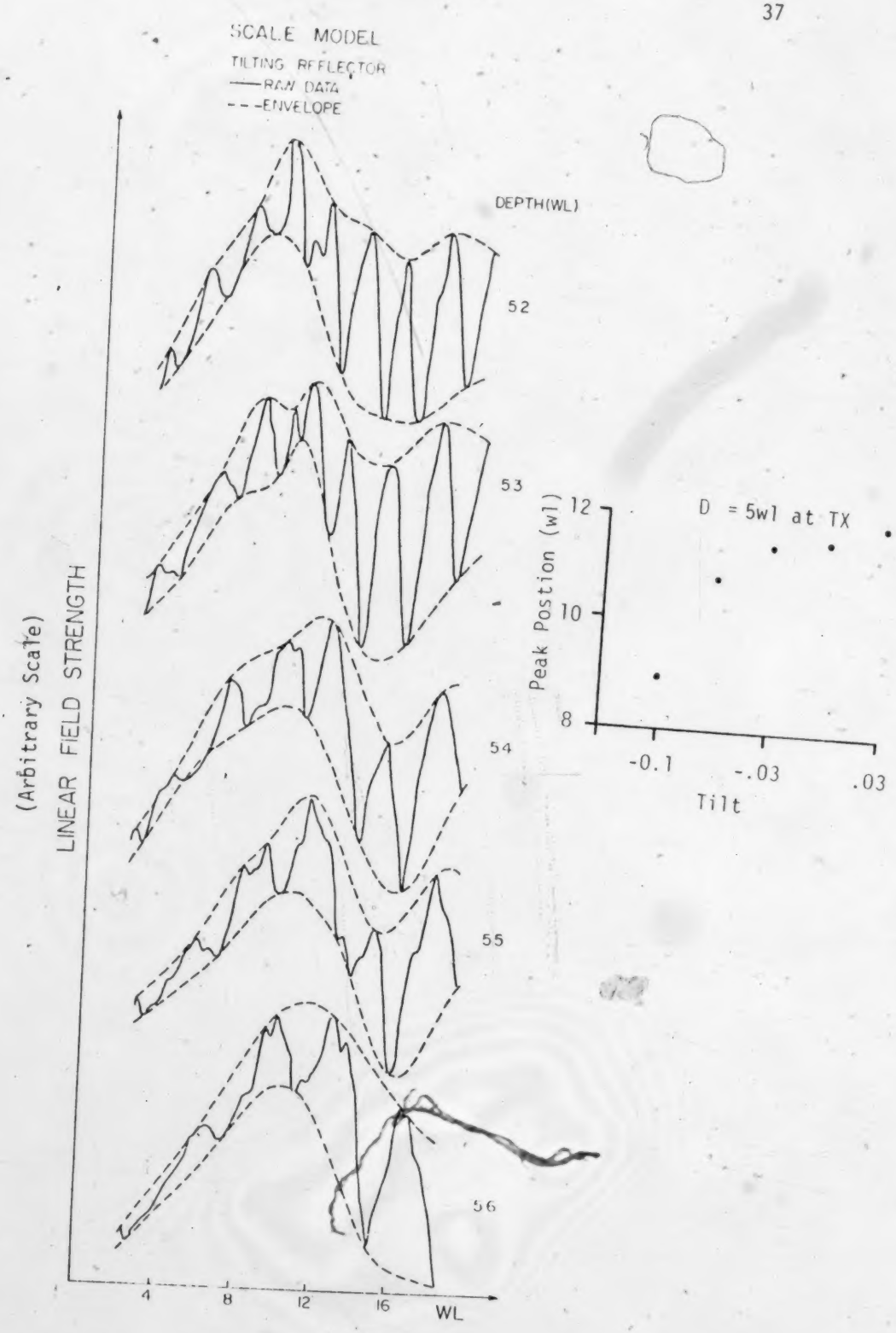

Figure 2-11

Each curve is normalized in amplitude.

Table 2-2: Depth estimates for tilting reflector (scale model)

Depth at Transmitter (wl)	Depth at far end of tank (wl)	Tilt	Estimate of Depth at Transmitter (1) $k_1 = 1.7 \pm 0.3$	Frequency of Spectral peak (2) (cycles/wl)
3	2	-0.033	3.1 ± 0.8	0.28 ± 0.03
3	3	0	2.6	0.26
3	4	0.033	2.2	0.22
3	5	0.067	2.6	0.20
3	6	0.100	2.2	0.16
4	2	-0.067	4.2	0.37
4	3	-0.033	3.8	0.35
4	4	0	3.7	0.30
4	5	0.033	3.7	0.26
4	6	0.067	3.2	0.24
5	2	-0.100	5.1	0.46
5	3	-0.067	5.4	0.43
5	4	-0.033	5.2	0.38
5	5	0	4.8	0.33
5	6	0.033	4.2	0.28

(1) Equation 2-19

(2) From maximum entropy spectra and equation 2-2

SCALE MODEL

TILTING REFLECTOR
MAXIMUM ENTROPY SPECTRA

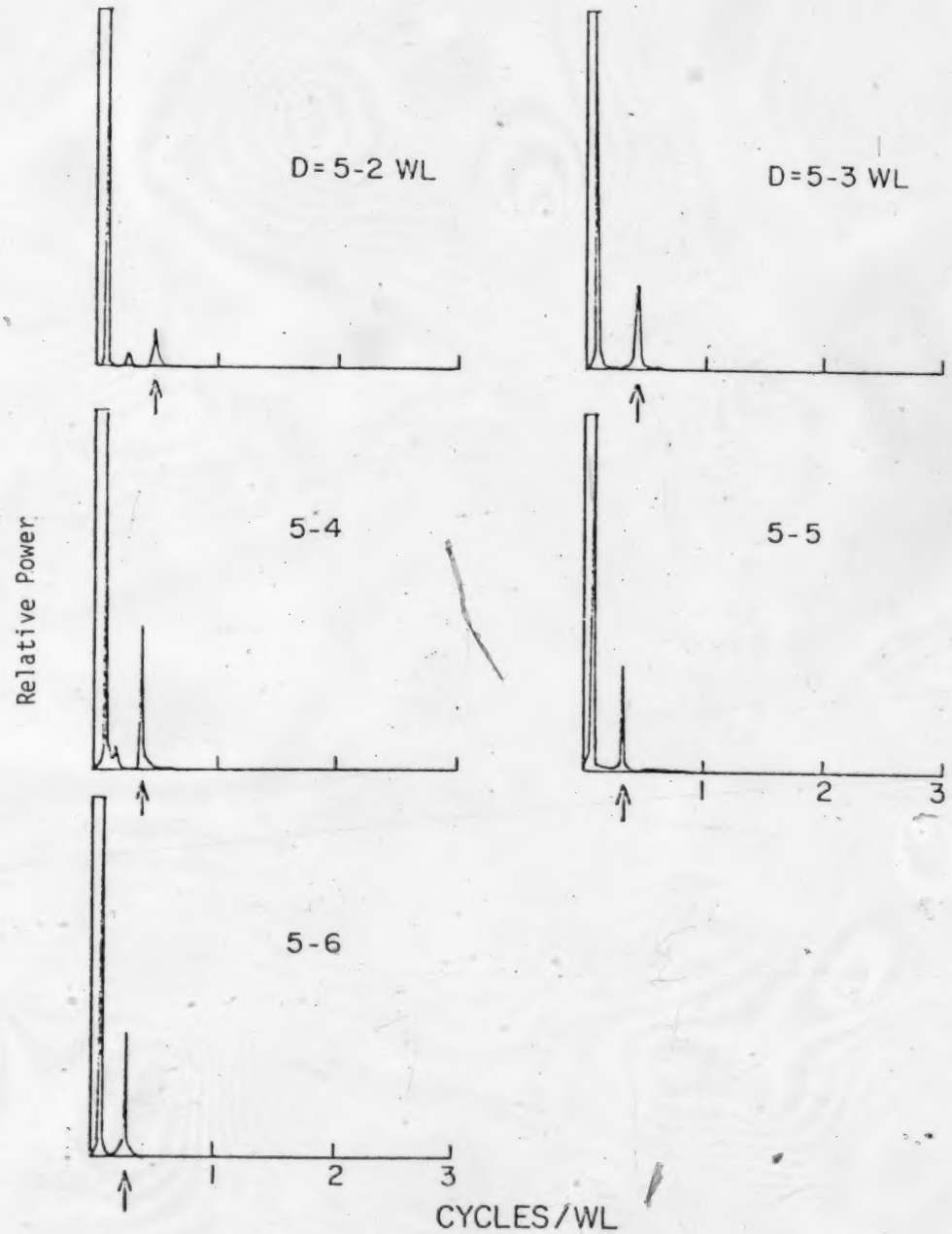

Figure 2-12.

Note shift of higher spatial frequencies peak (arrow) as tilt increases
Each curve is normalized to its peak value; amplitudes are not significant.

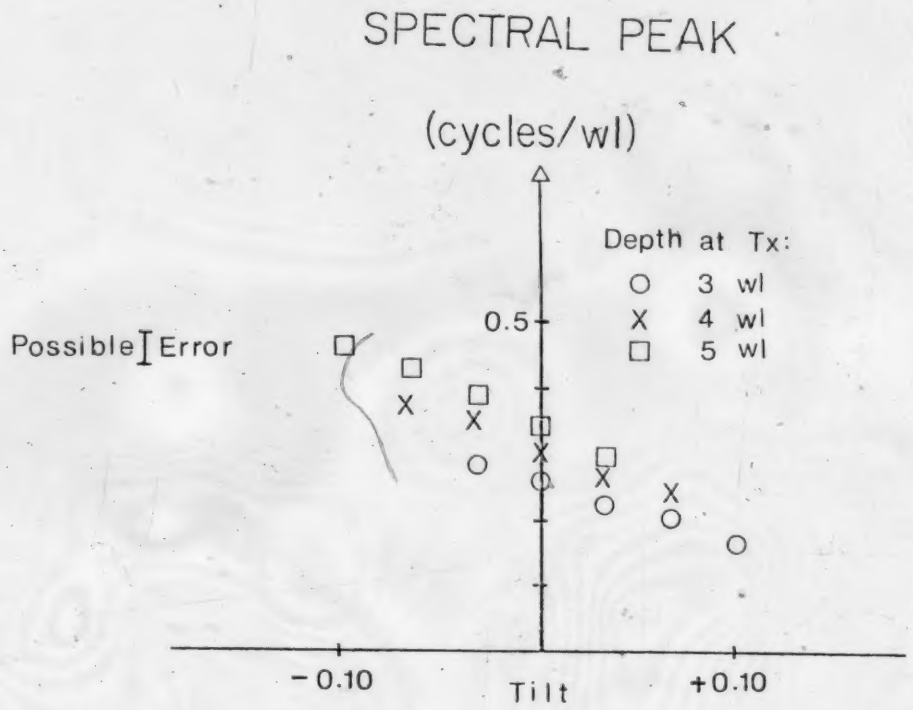

Fig. 12-a: Shift of spectral peak with tilt of subsurface reflector.

on the scale model results; i.e. that the spectral shift (cycles/wl) is approximately equal to minus the tilt. This relationship is sketched in Fig. 2-12a, and the fit has a slope of -1.0 ± 0.4. Hence, by analyzing runs that have been made both up- and down-dip, it should be possible to estimate both the effective dielectric constant and the sub-surface dip independently.

2.4 Single scattering object

Although the primary aim of this thesis is to examine the effects of random distributions of scatterers, it is worthwhile initially to look at the effects of a single scatterer. This approach is a bridge between geometries containing no scatterers, and those containing many scatterers, by indicating the minimum properties that are required for a scatterer to be effective. It may also show ways of isolating the effects of a single significant scatterer from an otherwise non-scattering environment.

Initial data were collected while the scale model was in Houston, and are catalogued in a report by Waller (1973). Although no analytical work was done on the results, a number of different scattering objects were used, with various shapes, sizes, and positions within the tank. The general conclusion reached was that the major effect of a single scatterer is to increase the local rate of beating seen in the interference curve near the scattering object, but to otherwise leave the interference curve unchanged. The shape, and the position of the scatterer along the traverse, or its depth within the oil layer, make little difference. However, the effect decreases with distance of the scatterer from the traverse path.

In order to quantify these preliminary results, and, in particular, to discover the minimum effective scatterer size, a number of further experiments were made. The scattering objects used were hexagonal machine nuts. These were chosen because they

were easy to obtain in various sizes and in large numbers, and because they could be used in two separate orientations. (Small dielectric spheres were also used, with rather limited success, as reported at the end of Chapter 3.)

The basic experimental procedure was to place a single machine nut upright on the surface of the reflecting plate. Various sizes of nuts were used, varying from 3/8 inch (0.28 wavelength in the dielectric, abbreviated wl_d), to 3/4 inch, or 0.55 wl_d. The objects were placed both directly under the traverse path, and offset from it. Runs were made with both the broad face of the nut perpendicular (tangential), and parallel (radial), to the traverse path. The maximum-coupled E-phi broadside component was measured for all configurations, and the minimum-coupled E-rho broadside component was measured for comparison in many cases.

A typical curve is shown in Fig.2-13. A single 0.32 wl_d nut was placed tangentially under the traverse path at a distance of 10 wl from the transmitter. There is a clear signature of rapid oscillations near the scatterer and deep null behind the scatterer, followed by a resumption to undisturbed behaviour. The rapid oscillation has been enhanced in Fig.2-13 by passing the data through a 1.0 to 2.0 cycles/wl pass-band filter. Filtering was done by transforming the interference curve into the wavenumber domain, eliminating all but the frequencies of interest, and re-transforming. The rapid oscillation then stands out as a wavelet several times larger than the background signal. This

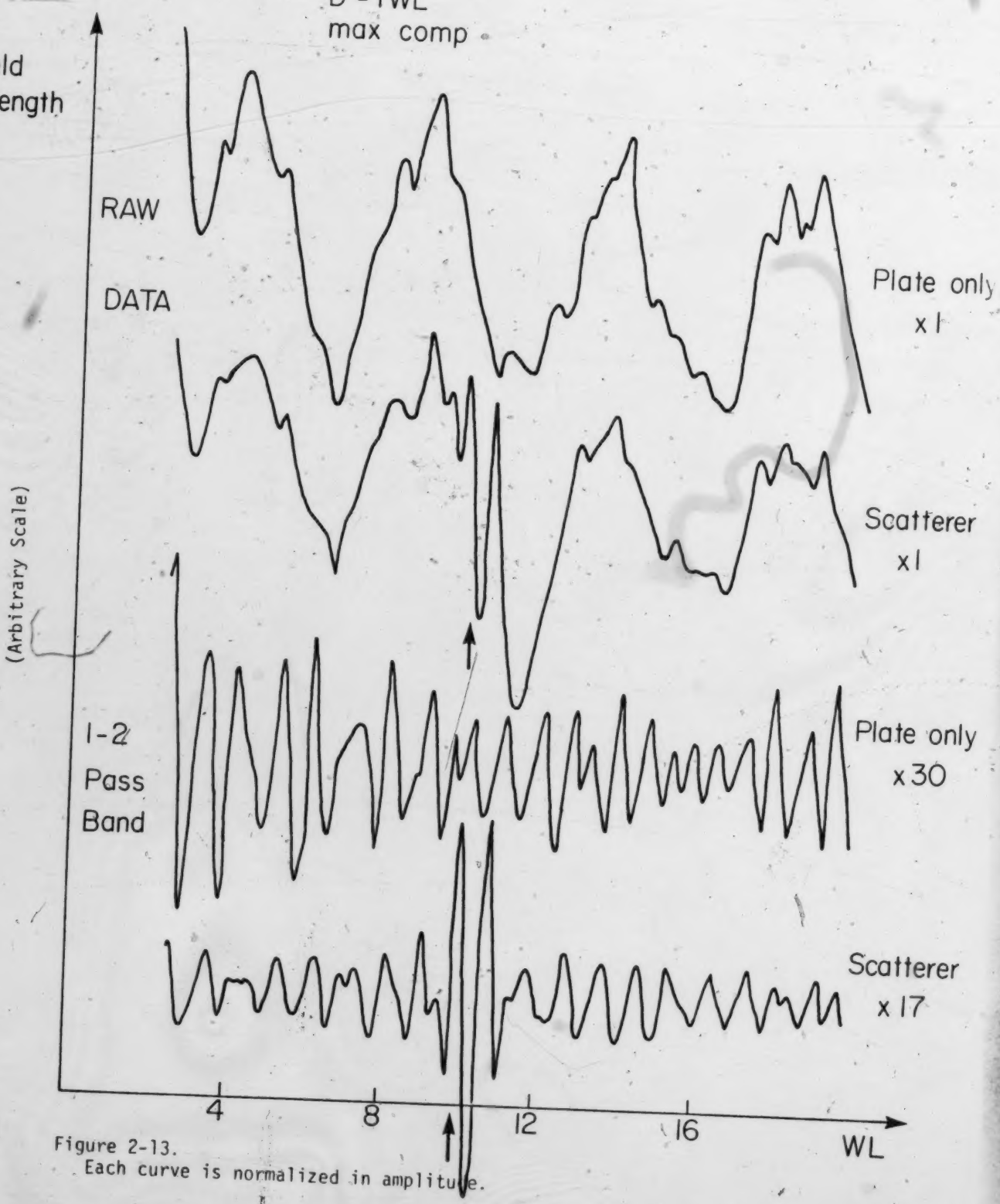

Figure 2-13.
Each curve is normalized in amplitude.

oscillation is due mostly to a doubled beating rate as waves reflected from the scatterer interfere with direct waves. The null behind the scatterer is due to shadowing.

The increased beating rate is clearly shown by taking maximum entropy spectra for various sizes of scatterers (Fig.2-14). Interference curves from 2.5 to 8.5 wl from the transmitter were analyzed, with the scatterer at 8.0 wl. It can be seen that a new spectral line develops at about 1 cycle/wl as the scatterer increases in size. The spatial frequency of the new peak also shifts to slightly lower spatial frequencies as the scatterer becomes larger, mostly because the width of the null behind the scattering object becomes larger.

Taking the spectral peaks in Fig. 2-14 as a guide, the data were band-pass filtered to show only the spatial frequencies enhanced by the scatterer. A typical set of curves for increasing size of scatterer (H) is shown in Fig. 2-15. In each case, a single tangential machine nut is at 8 wl from the transmitter, as indicated by the arrow. The curves that are shown are in the linear domain, after filtering. As can be seen, the amplitude of the scattering wavelet generally increases with the height of the scatterer. Scatterers less than 0.3 wl_d are not detectable in the data, even with the enhancement of filtering. Large scatterers show effects that are not restricted to the locality of the scatterer.

The amplitude of the interference curve in the linear domain after filtering is used as a measure of the scattering level, and

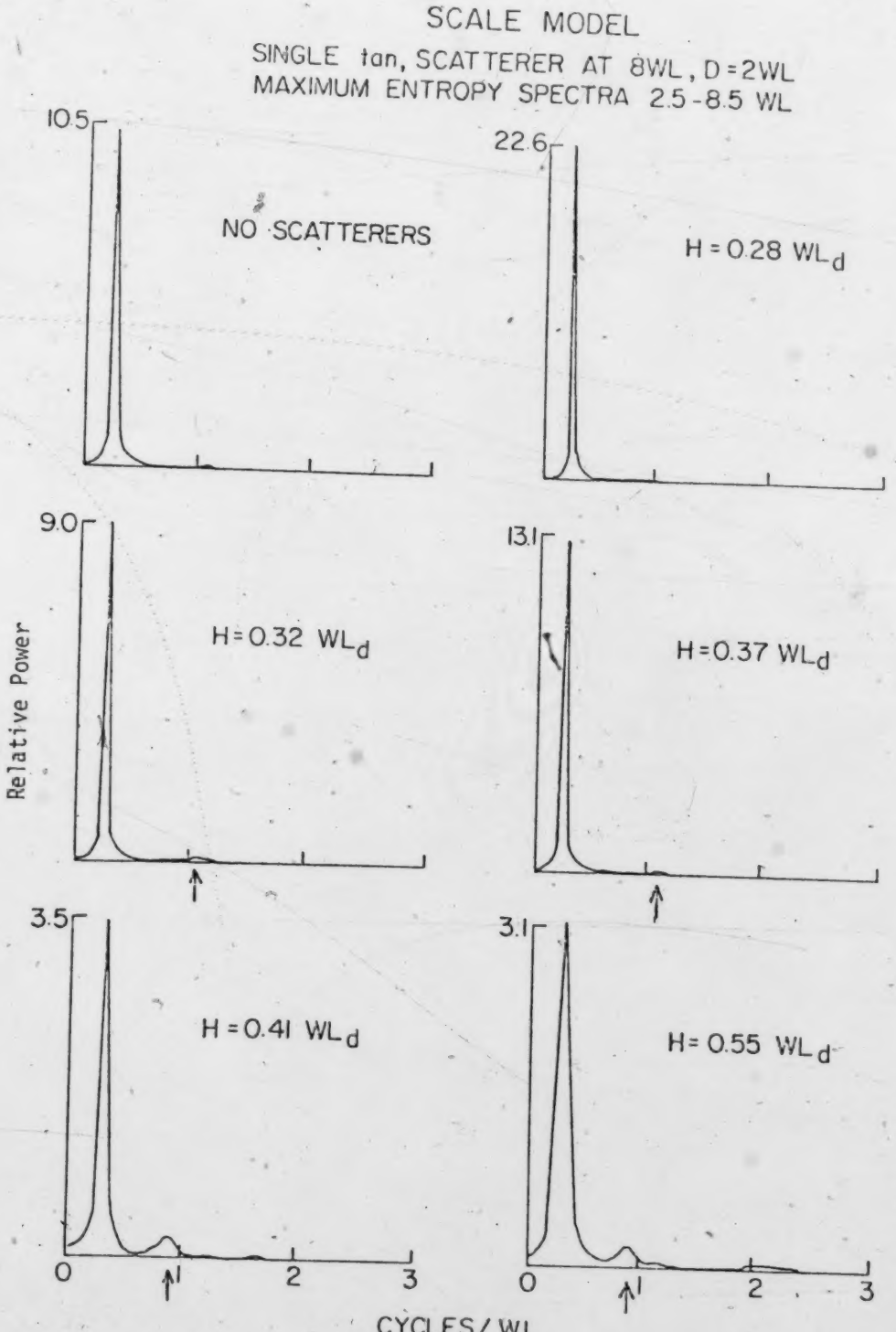

Figure 2-14.

Note increasing higher spatial frequencies for large scatterers
Each curve is normalixed to its peak value; amplitudes are not significant.

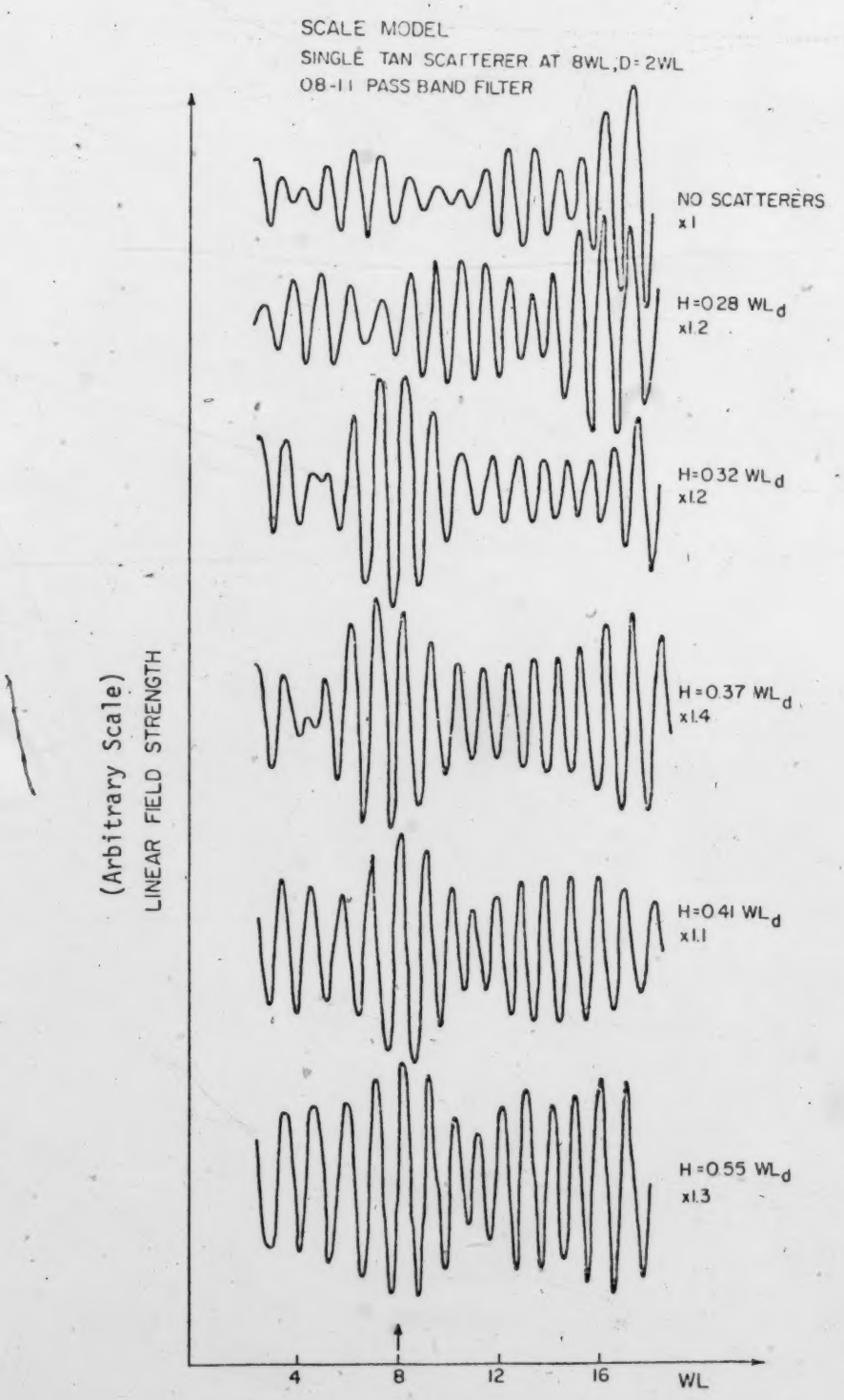

Figure 2-15. Each curve is normalized in amplitude.

is called the "scattering amplitude". Since it is referenced implicitly by the interferometry technique to the amplitude of the coherent signal, this amplitude is comparable from one set of data to another, although the units are arbitrary. In Fig.2-16 several scattering amplitudes have been plotted, for two filter bands, and for a number of different sizes and positions of a single scatterer. In all cases the scattering level is small until the scatterer is about 0.3 wl_d in height. Large scatterers do not scatter much more effectively.

As shown in Fig. 2-16, the effect of an off-traverse scatterer is considerably weaker than from one that is directly under the path of the receiver, and there is also less shadowing. However, substantial effects are measurable from scatterers that are offset as much as 2 wl_d, if the scatterers are reasonably large. The radial orientation of the machine nuts show lower scattering levels than the tangential orientation, but otherwise the response is similar.

The mechanism of a scatterer altering an interference curve is to reflect waves back toward the transmitter. These "incoherent" waves can then interfere with the direct "coherent" waves, and set up standing waves with spatial frequencies double that of the original set. Since the waves are travelling down the waveguide, the position of the scatterer from the surface makes little difference. However, the effect does fall off with distance from the traverse path. Once a scattering body is large enough to re-radiate a

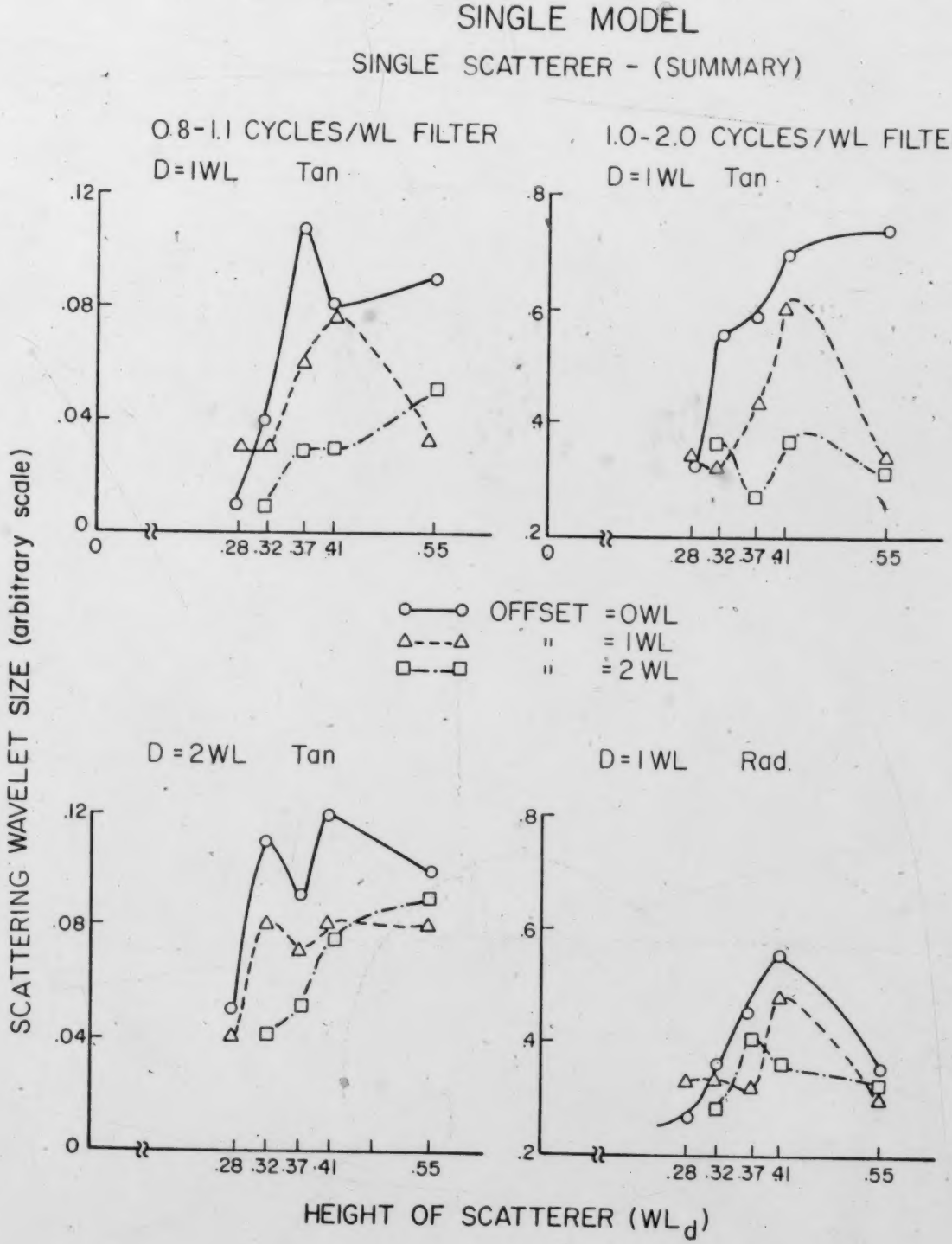

Figure 2-16. Error is estimated at ± 25% of the value

significant amount of energy back its size does not greatly affect the interference curves, except that there is a slightly greater shadowing effect behind larger scatterers.

Results from the minimum-coupled component are not shown, but in general the interference curve is very random, and no discernable change was seen when a single scattering object was added.

In order to try to detect a priori a single scatterer from radio interferometry field data, one might spectrally analyze a data curve section by section. This kind of procedure could be fairly tedious, and, given the irregular nature of interferometry curves, one might not be too confident of a scatterer location unless several runs were made over a given region. A better approach might be some sort of predictive filtering method, such as that suggested by Wiggins and Miller (1972) to pick out the sudden bursts of anomalous energy.

In conclusion, the effects of a single scatterer on interferometry data have been shown. The primary effect is an increase in the spatial frequencies that are present in the interference curve, due to increased interference from backscattered waves. This effect can be enhanced by removing the lower spatial frequencies with band-pass filters, and this process leads to a semi-quantitative measure of the overall level of scattering. A scatterer with dimensions smaller than 0.3 wl_d does not appear to effectively backscatter; larger objects do, but with little increase in

effectiveness with large size. The effect from a single scatterer is fairly local, but can be seen even when the scatterer is several wavelengths away from the traverse path. Position of the scatterer, either along the traverse or within the oil, is not significant.

2.5 Many scattering objects

In this section we will examine scale model results in which many scatterers are placed on the reflecting plate. Hence, the plate is a rough surface, and can reflect energy into many directions. The subject of scattering by random rough surfaces has been studied by other authors (see, for example, Beckmann and Spizzichino, 1963, for a good review), but typically there are theoretical solutions only for surfaces with roughness that has dimensions much smaller than a wavelength, or for very well-defined shapes. However, as shown in the previous section, scatterers much smaller than a wavelength do not have much effect on radio interferometry data.

Hexagonal machine nuts were again used as scattering objects; placed on the surface of the aluminum plate they simulated a smooth reflector covered with random bumps. The following parameters were varied (see Fig. 2-17):

(a) component -- maximum-coupled E-phi broadside (Rx_1) and minimum-coupled E-rho broadside (Rx_2);

(b) depth (D) -- 1, 2, and 4 wl thickness of oil layer:

(c) scatterer size (H) -- nuts of 0.28, 0.32, 0.37, and 0.55 wl_d diameter;

(d) scatterer spacing (L) -- mean separation between the nuts of 4, 2, and 1 wl_d (i.e. increasing number of scatterers);

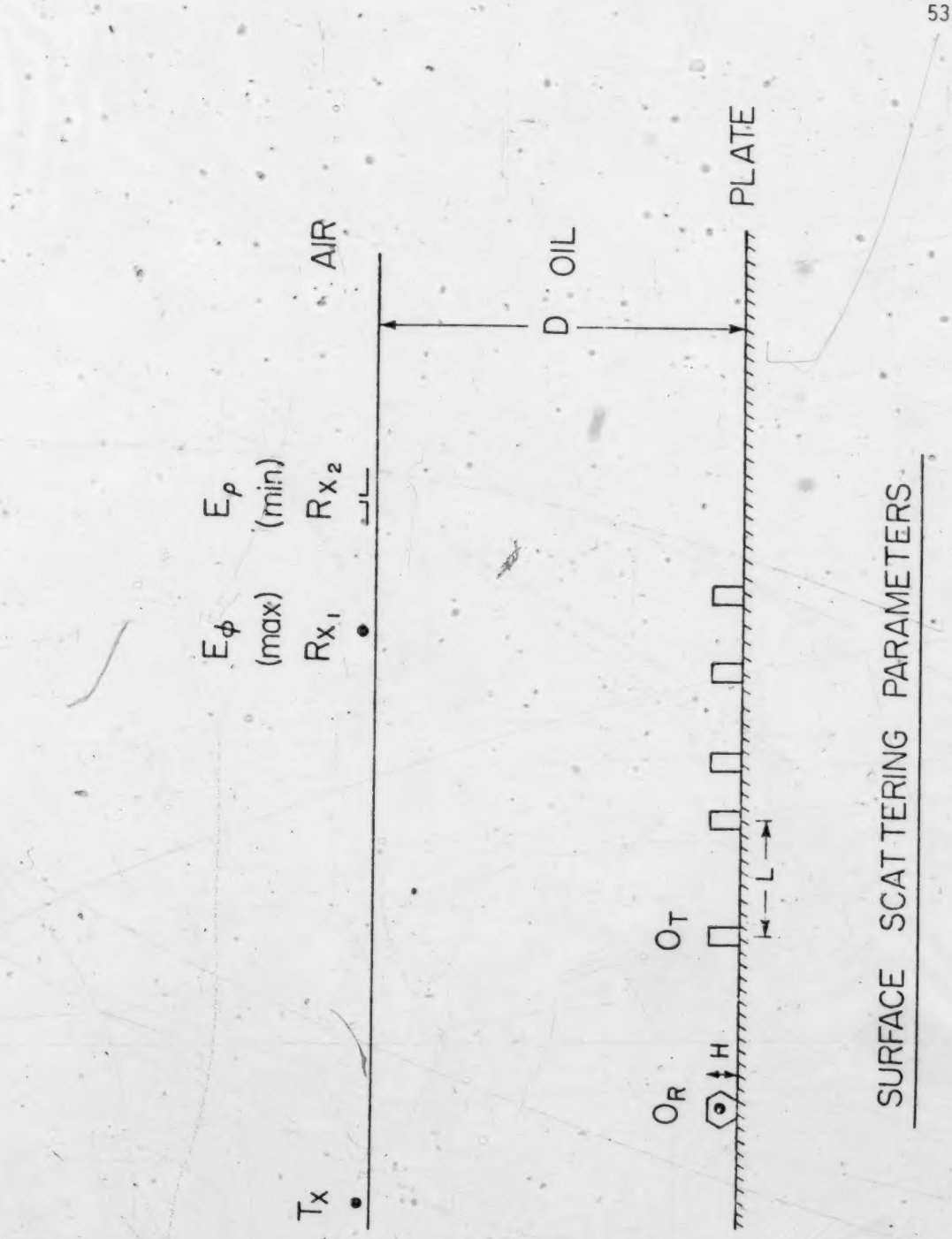

Figure 2-17. Scale Model Studies of Random Scattering

(e) scatterer orientation -- radial (O_R) and tangential (O_T) orientations of the scatterers.

Two typical curves for smaller scatterers are shown in Fig. 2-18. It is apparent that when the scatterers are less than about 0.30 wl_d in size, they are not effective, even if there are many of them. However, as the size increases above 0.30 wl_d the scatterers do become effective, and a low-amplitude, high-frequency, ripple is added to the interference curves. This ripple is apparently due to interference between the main "coherent" waves (discussed in Section 2.2) and "incoherent" waves backscattered in a more or less random way by the scatterers. Spectra of the curves, shown in Fig. 2-19, indicate that the scattering effects are mostly in the spatial frequencies above 1 cycle/wl. When these frequencies are filtered out by a low-pass filter, the curves are very similar (Fig. 2-20).

As the size of scatterer or the number of scatterers per unit area increased, the effects of scattering also increase. In order to relate scattering effects to the types of scatterer, spatial frequencies above 1 cycle/wl were isolated from the data by a high-pass filter, as before, so that the amplitude of the signal that remains is then a measure of total scattering. Curves of this "scattering amplitude" are shown in Figs. 2-21 and 2-22 for various parameters. As can be seen, scattering increases as a function of scatterer size (H) and number of scatterers (L^{-1}). Although a thin

SCALE MODEL

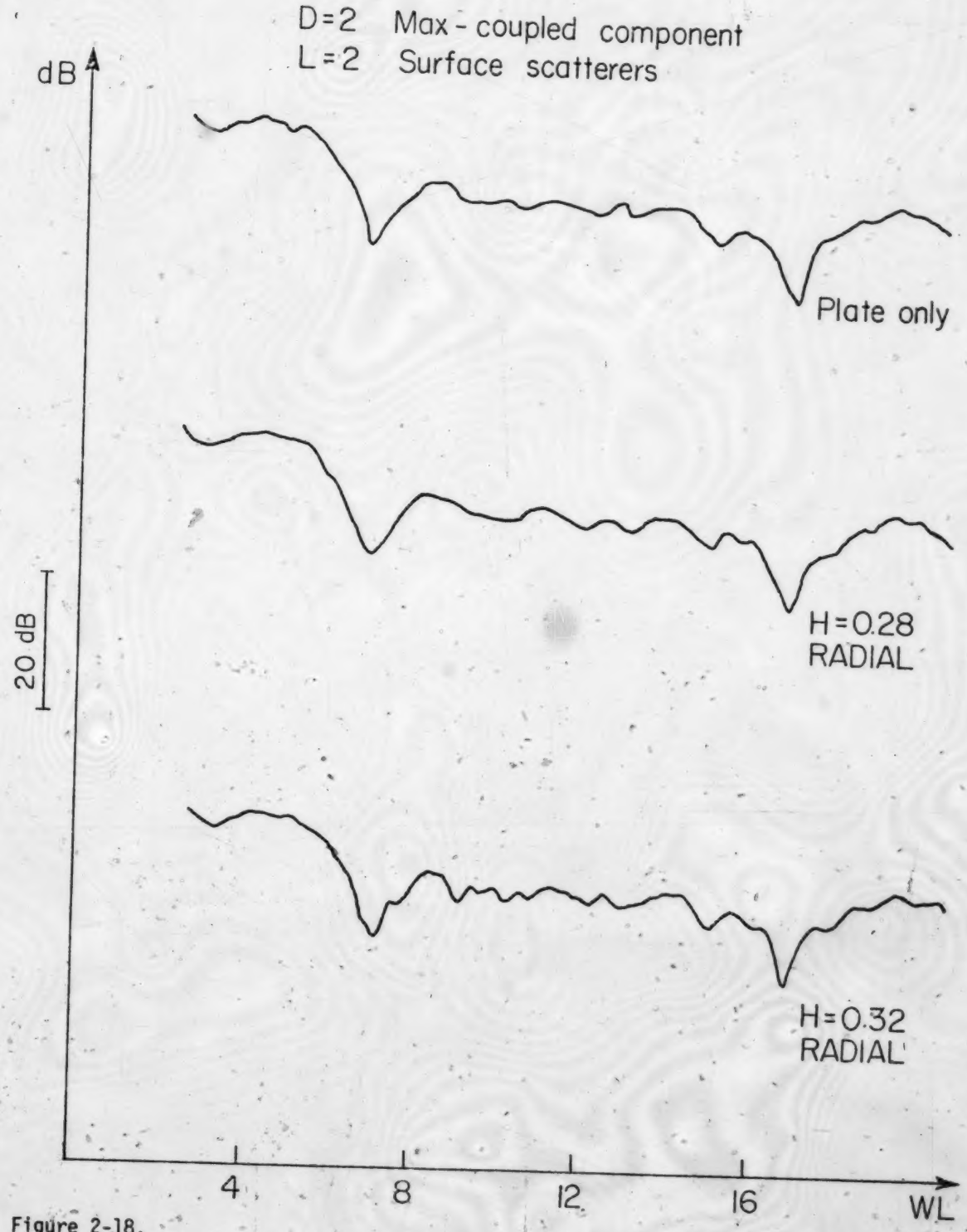

Figure 2-18.

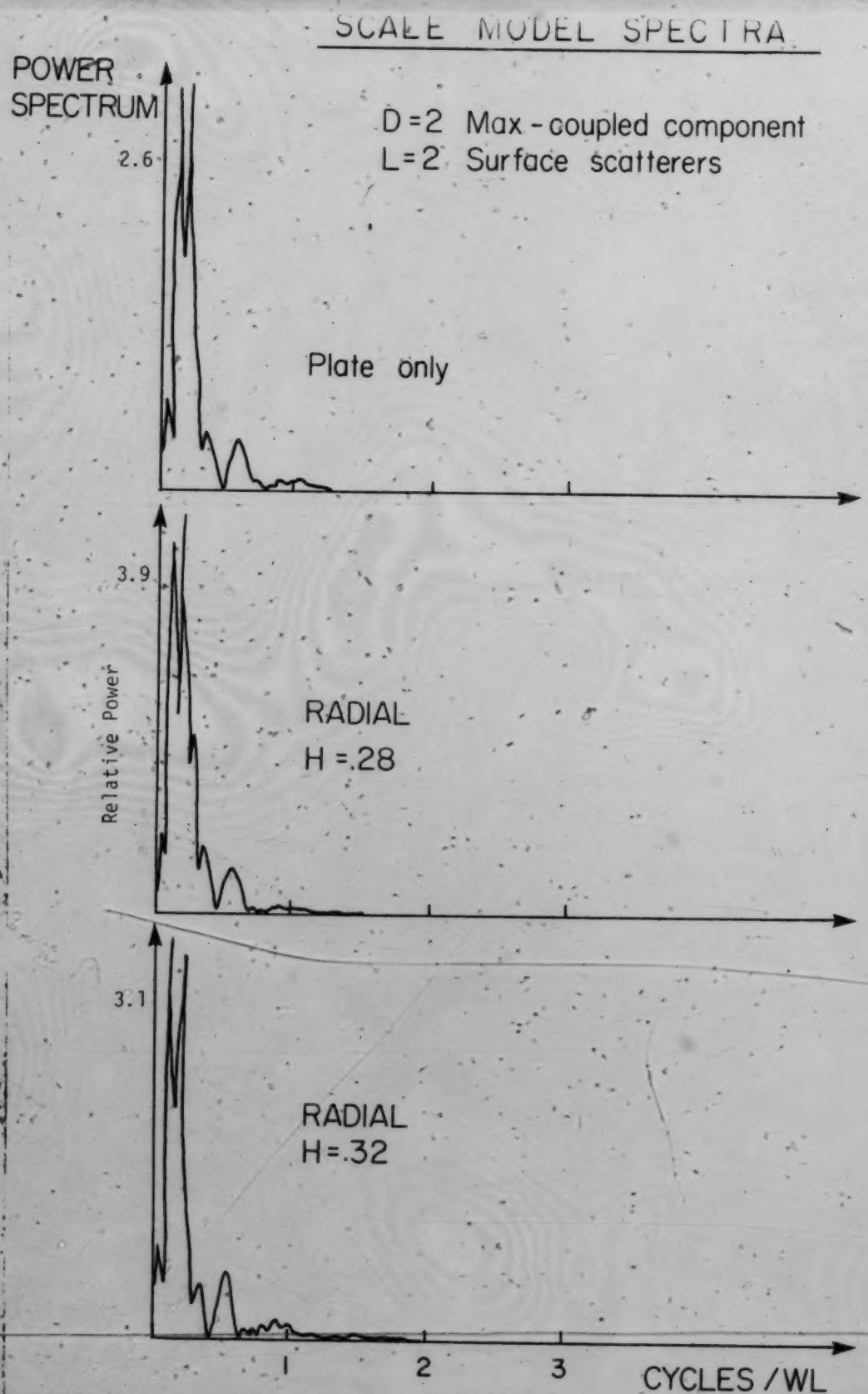

Figure 2-19. Low-level scattering, FFT Spectra. Note slightly increased level above 1 cycle/wl in lowest curve. Each curve is normalized to its peak value.

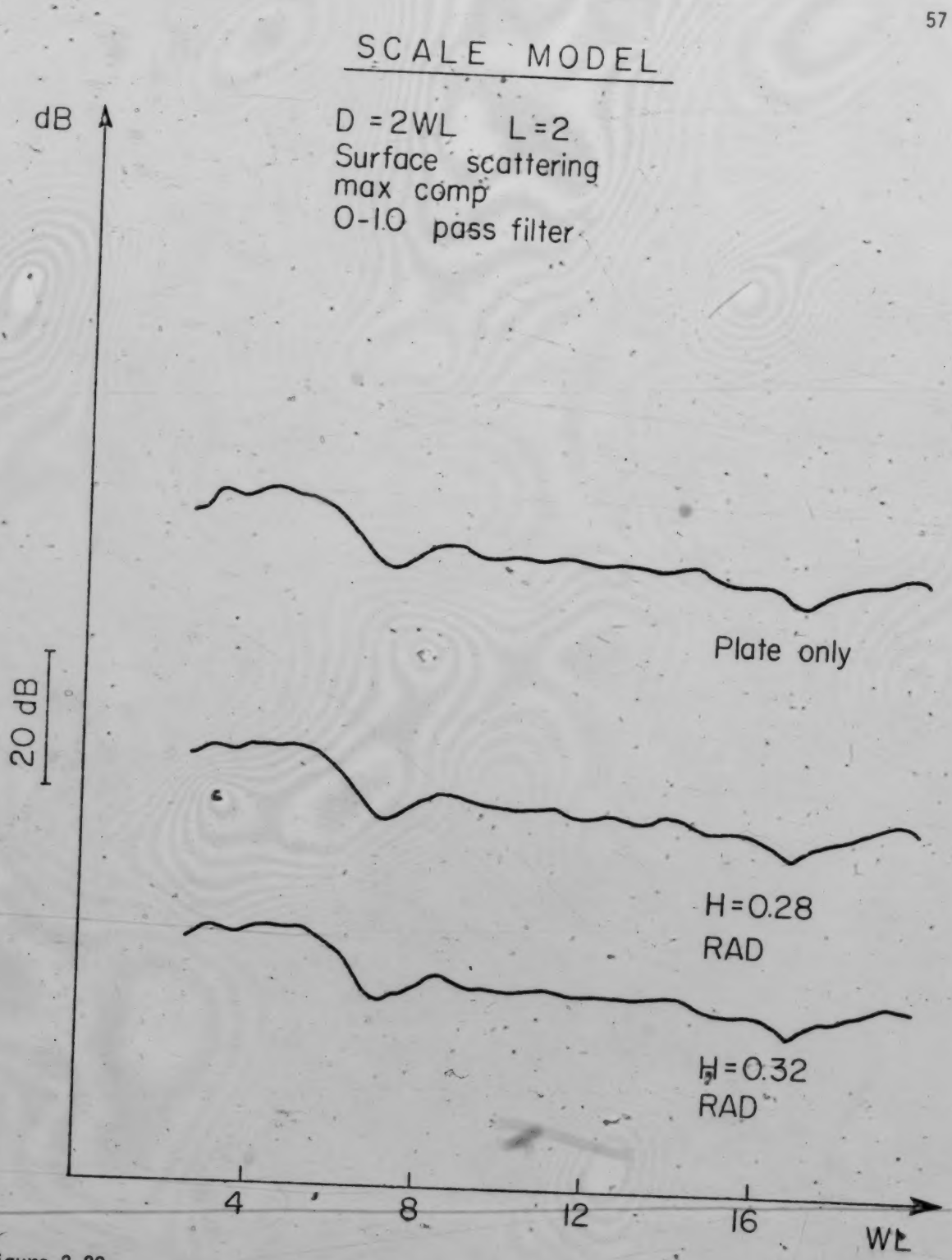
SCALE MODEL
D = 2WL L = 2
Surface scattering
max comp
0-1.0 pass filter
dB
20 dB
Plate only
H = 0.28
RAD
H = 0.32
RAD
4
8
12
16
WL

Figure 2-20.

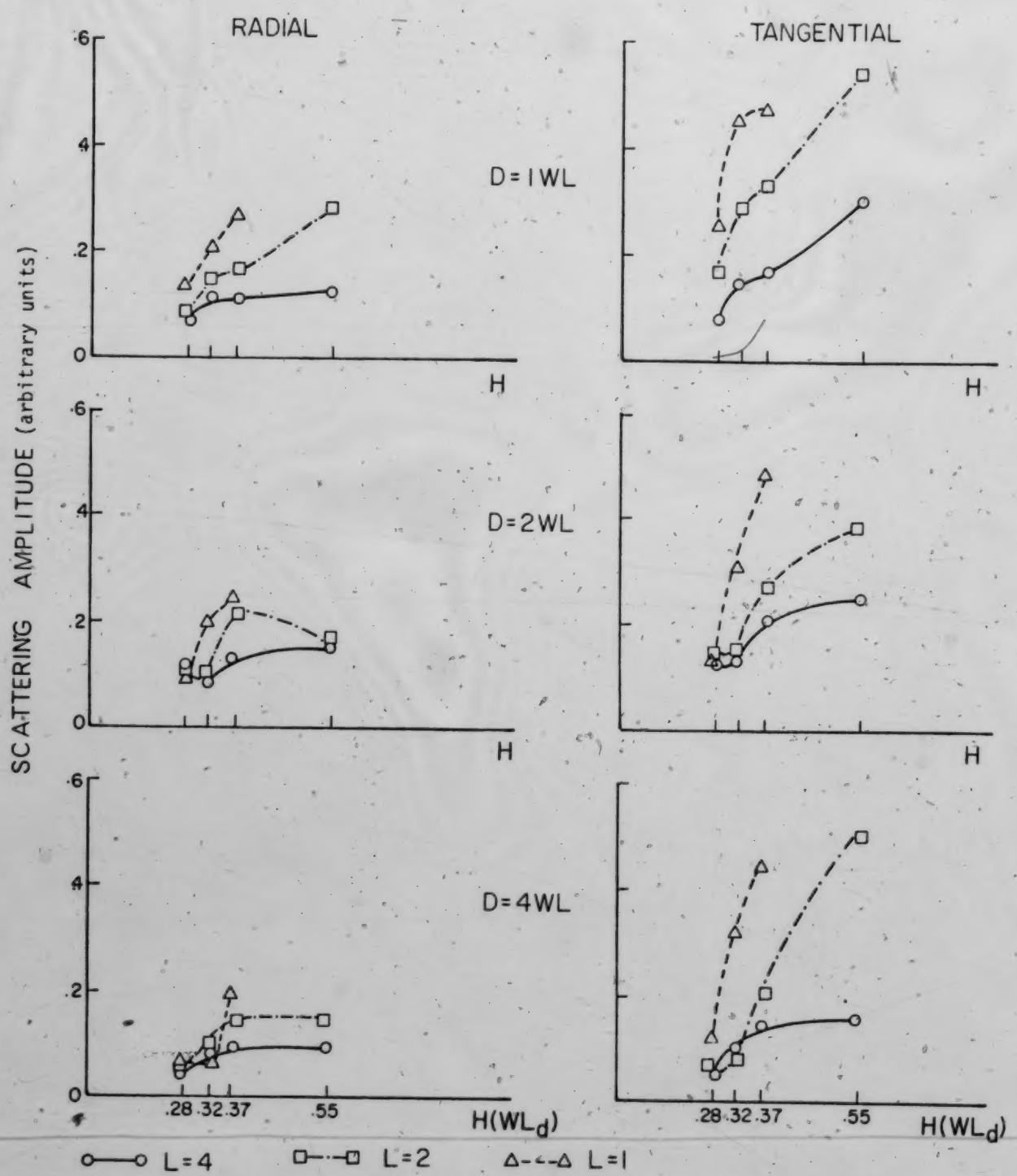

Figure 2-21.

Scattering amplitude vs scatterer size.
Error estimated at ± 25% of each value.

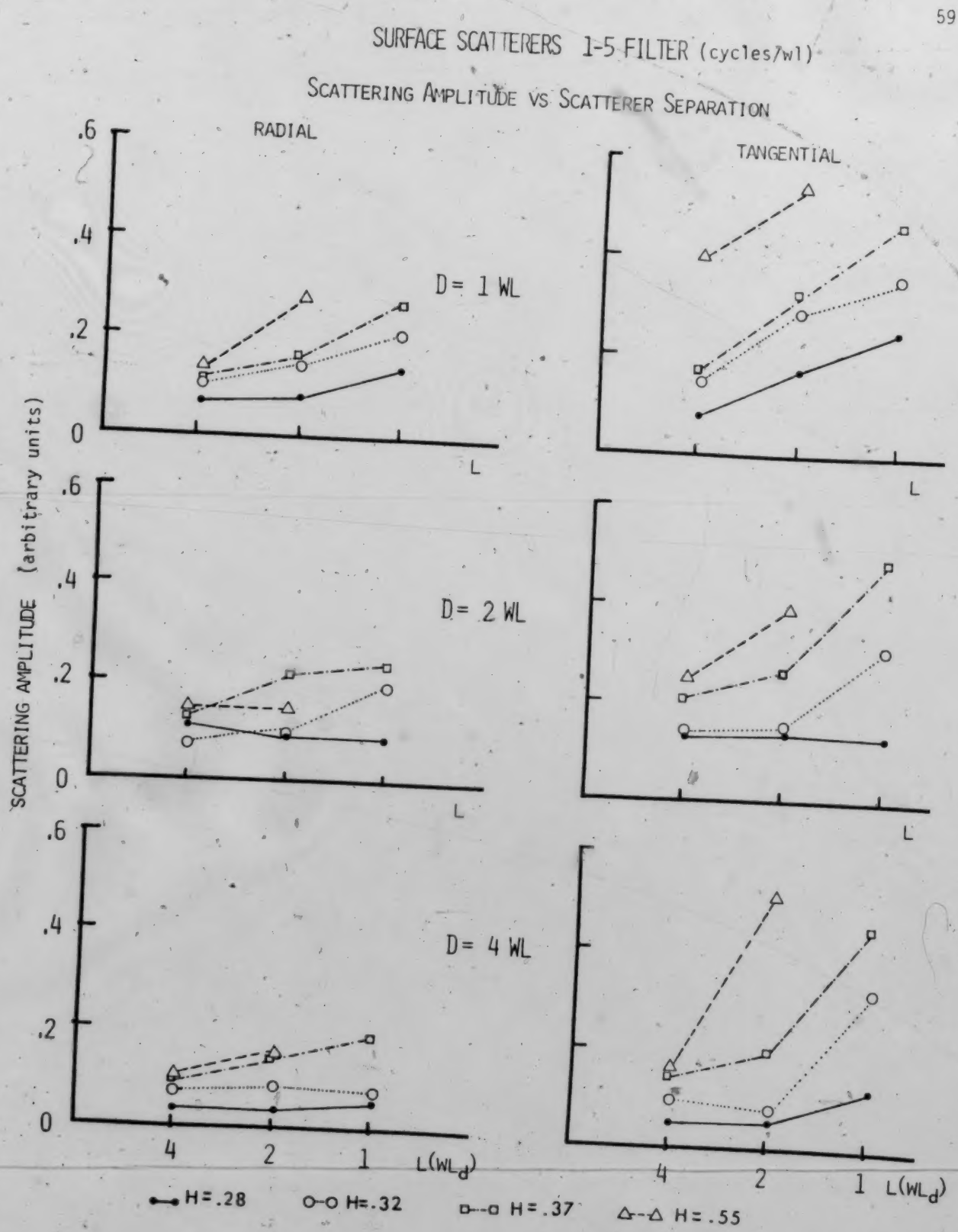

Figure 2-22.
Error estimated at ± 25% of each value

dielectric layer is slightly more sensitive to scatterers than a thicker one, there is not much difference between the results. And, not unexpectedly, the tangential scatterers, about twice as wide as the radial ones, scatter about twice as effectively.

The data of Figs. 2-21 and 2-22 are re-plotted in Fig.2-23 so that scattering amplitude is given as a function of a non-dimensional roughness parameter L/H. As can be seen, except for the H = 0.28 wl_d points, scattering amplitude increases smoothly with roughness (decreasing L/H). As shown, there is very little dependence on the waveguide thickness, D. The H = 0.28 wl_d points are all low on Fig. 2-23, indicating once again that those scatterers are not large enough to be effective, while the H = 0.32 wl_d scatterers are.

The fact that the points in Fig.2-24 increase reasonably smoothly indicates that once the critical amplitude, H, has been reached, scattering is approximately frequency-independent. As the radio frequency used increases, parameter L/H will not change: the scatterers will become bigger, but further apart.

Another effect of random scattering is the general trend of the minimum-coupled component increasing while the maximum-coupled component decreases. Essentially more coherent energy is scattered into incoherent directions. Therefore the relative power levels of the two sets of components were measured by fitting each curve to an $r^{-\alpha}$ decay, and comparing the intercepts. As scattering increases the two sets of components begin to merge in level (Fig.2-25).

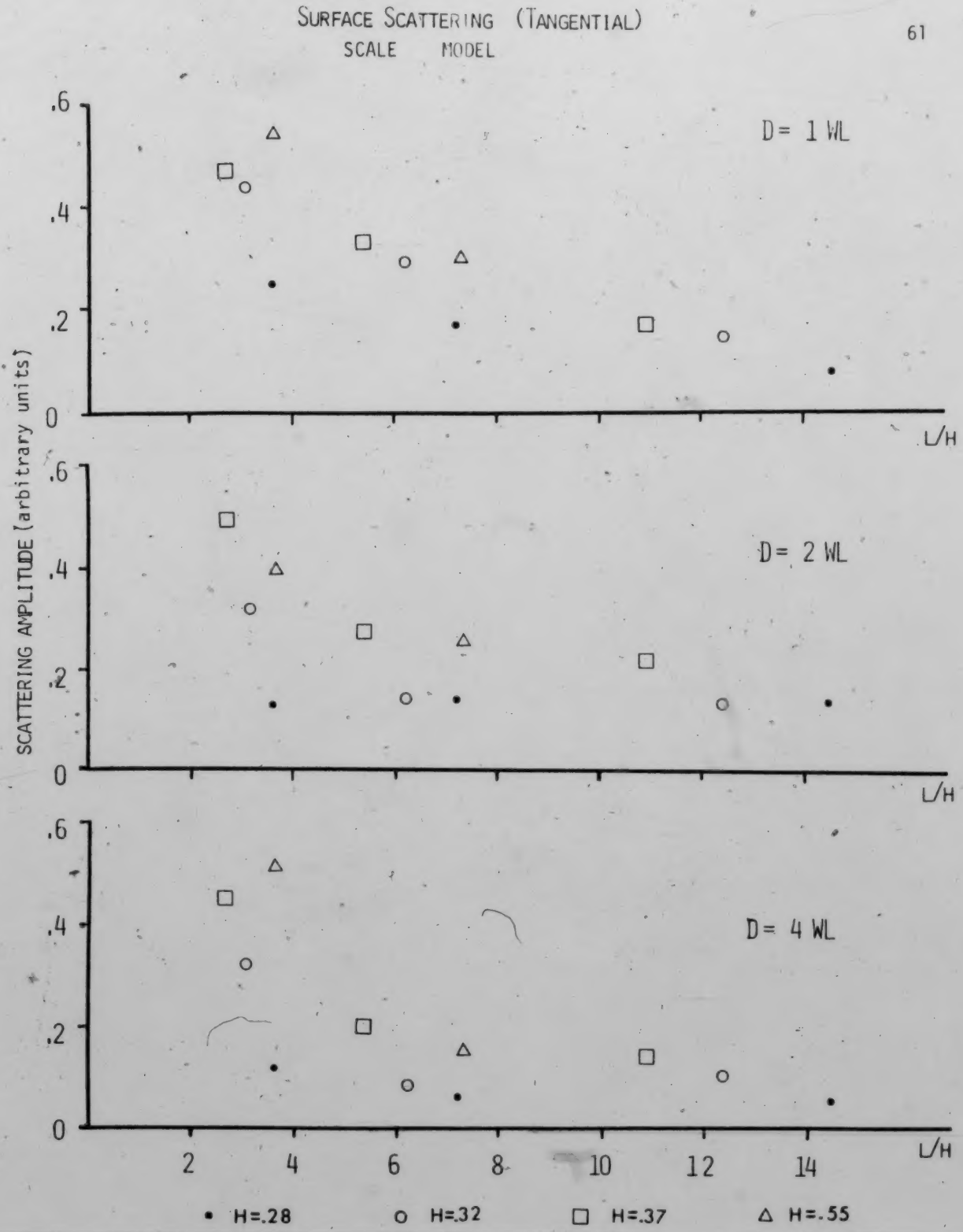

Figure 2-23.
Scattering amplitudes vs roughness for various depths.
Error estimated at ± 25% of each value.

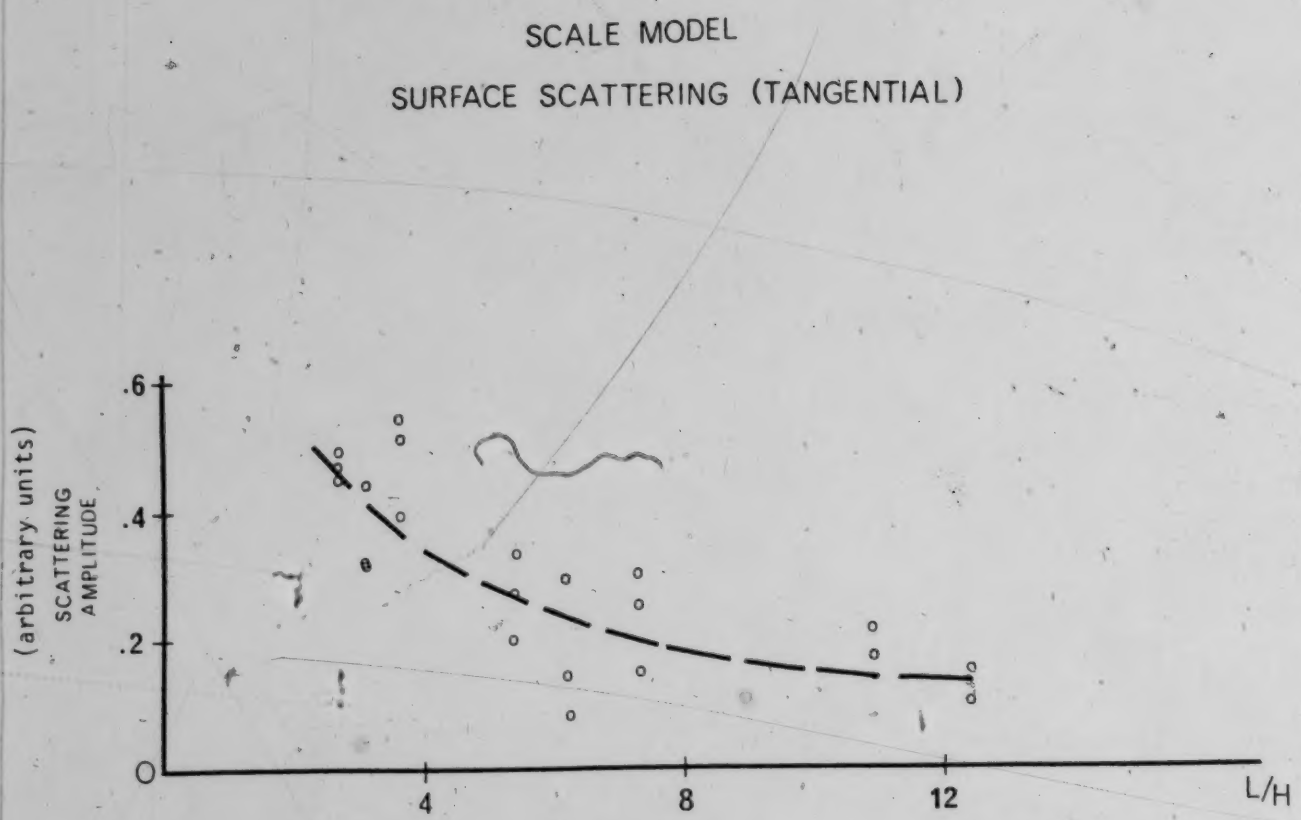

Figure 2-24.

Scattering amplitude vs roughness parameter L/H for all depths, excluding H=0.28 wl_d points. Error estimated at ±25%

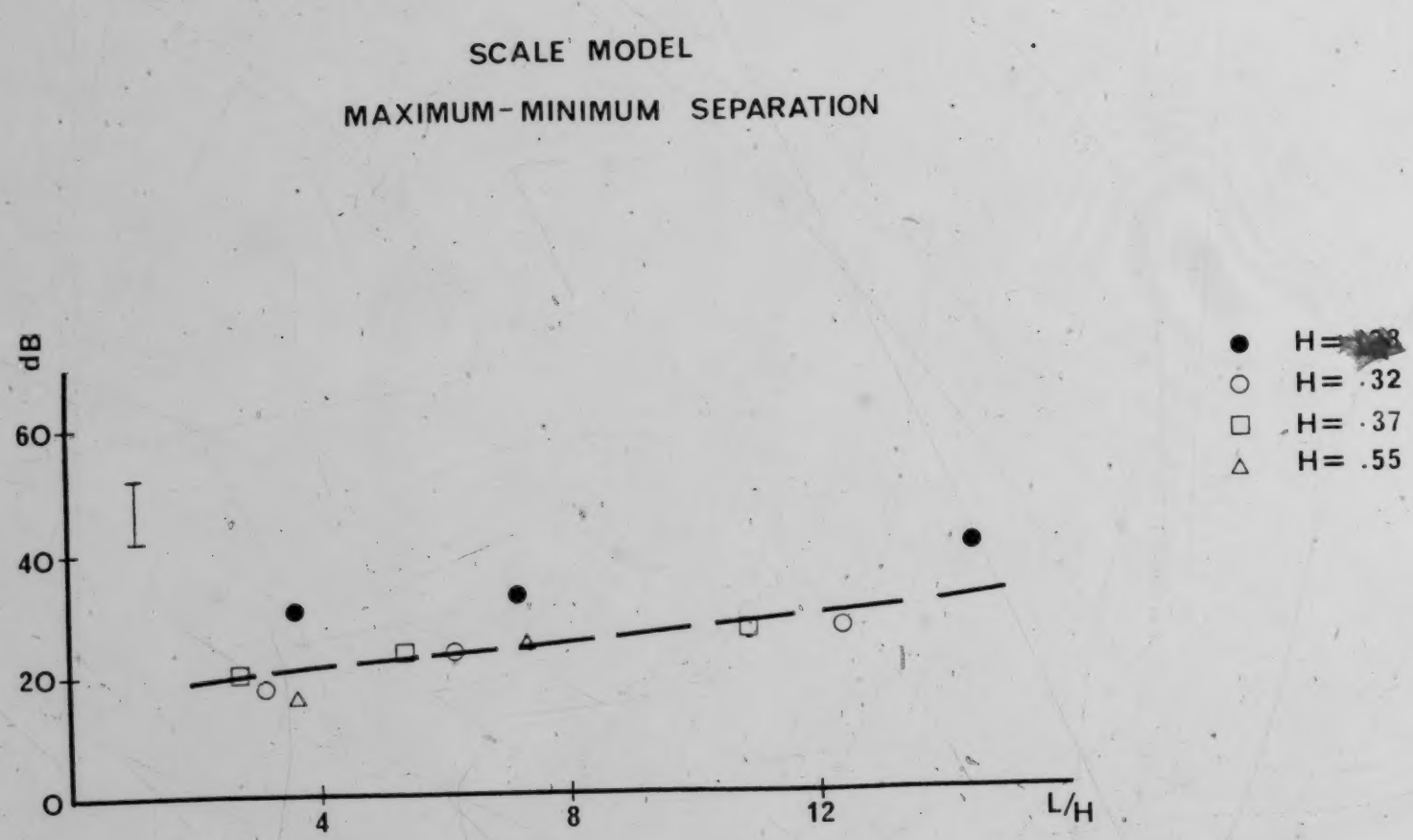

Figure 2-25. Separation vs roughness at all depths. Maximum veriation shown by bar (5 d B)

The scattering level in the model was never great enough to completely randomize the maximum-coupled component, so that the separation was never nil.

Therefore the major effect of random scatterers is to add "noise" to the interference curve over a wide band of spatial frequencies. This incoherent signal can be isolated by high-pass filtering and is indicated by max-min component separation. However, as mentioned in Section 2.2, the latter will also decrease in the presence of lateral inhomogeneities. Hence, it is possible to assign two semi-quantitative parameters to random scattering: the scattering amplitude after high-pass filtering and the max-min component separation. If the scatterers are less than $0.3\ wl_d$ high they are not effective. However, the level of scattering also depends on the number of scatterers per unit area. Therefore, for a narrow distribution of scatterer sizes, once the radio frequency used is high enough to distinguish roughness features as scatterers, the scattering will be essentially frequency-independent.

2.6 Summary of scale model results

The analogue scale model is a convenient way in which to study physical environments which are too complicated to analyze theoretically. In the previous sections four main results have been shown: (a) it is possible to determine the electrical properties and depth of a two-layer structure from the interference pattern that is generated; (b) if the thickness of the layer changes fairly uniformly along the traverse, the dip of the lower reflector can be determined using up- and down-dip traverses; (c) the effect of a single scatterer is only important if the scatterer is greater than 0.3 wl_d in size; and, (d) the effect of an ensemble of scattering objects is much the same as from a single object, although the amount of scattering increases with the number of scatterers.

Therefore, using scale model results as an empirical guide, a number of computational procedures have been developed to extract the parameters of interest from a set of interference curves. In particular, the effect of random scattering can be semi-quantitatively determined by using a number of radio frequencies. Scattering will not be important until the frequency used is high enough that there are scatterers that are at least 0.3 wl_d in size. As higher frequencies are used, the scattering level will not vary much, since both scatterer size and spacing will increase together. However, the level of scattering that is reached roughly indicates the spacing.

In Chapter 4 the procedures developed here will be used to examine field data from a variety of regions. In the next chapter (Chapter 3), a theoretical model of low-level scattering effects will be discussed, which gives a physical basis for the effects of scattering within a two-dimensional waveguide.

CHAPTER 3

THEORETICAL FORMULATION OF VOLUME SCATTERING

3.1 Introduction to volume scattering

The previous chapter showed the effects on interferometry of surface scatterers within a waveguide. It is also possible to have scattering taking place because of inhomogeneity in the medium of propagation, i.e. the dielectric itself. Although the effects may be similar, these two types of scattering are usually treated in quite distinct theoretical ways. Surface scattering is formulated in terms of new boundary conditions which the incident waves must obey (e.g. Beckmann and Spizzichino, 1963; Ince, 1975). Volume scatterers, on the other hand, are usually treated as additional sources within the propagating medium. In a waveguide, however, there is no fundamental difference between the two -- surface scattering can be thought of as a special case of volume scattering in which the inhomogeneity is localized near the walls of the waveguide.

It is not necessary for the volume scatterers to be perfect conductors. Any change in electrical properties will act as a scattering element. It is of interest then to examine what kind of dielectric contrast will be needed in order to produce a scattered signal of comparable amplitude to the incident wave.

The theory of the scattering produced by a dielectric sphere imbedded in a homogeneous dielectric and stimulated by an

incident plane wave is known as Mie theory. Rayleigh scattering is the low-frequency approximation to Mie theory, i.e. the scatterer is very small compared to a wavelength. Essentially the incident wave excites various dipole moments within the sphere, which then re-radiates the scattered field. For small scatterers (Rayleigh limit) only the first excited moment is important, and the re-radiated field is (Stratton, 1941, p. 572) proportional to frequency squared, and therefore the scattered power is proportional to the fourth power of frequency -- the well-known Rayleigh law. However, as shown in Section 2.3, scatterers required for significant interference effects are of the same order of size as a wavelength, and therefore the Rayleigh scattering approximation does not apply. It is easy to show that no improvement can be made by a sufficiently large dielectric contrast, since the dipole moment increases as:

$$\frac{\varepsilon_1 - \varepsilon_2}{\varepsilon_1 - \varepsilon_2} \longrightarrow 1 \qquad \text{for } \varepsilon_1 >> \varepsilon_2$$

where ε_2 and ε_1 are the dielectric constants of the medium and of the scatterer, respectively. Therefore the only improvement can come with larger scatterers.

For large scatterers, dipole moments greater than the first must be considered, even at large distance from the sphere. Watts and England (1976) have evaluated these for $\varepsilon_1 = 81$ and $\varepsilon_2 = 3.3$. Although the scattered field is very irregular (corresponding to resonance conditions of the various excited

modes in a sphere), the mean scattered field rises quickly with increasing sphere size from Rayleigh Law behaviour; to a moderately uniform level when the sphere has a radius of about 0.1 wavelengths.

Hence, as in the case of surface scattering, it appears that once the scatterers become sufficiently large to affect interferometry data, the degree of scattering seen in the data is controlled by the density, not the size, of the scatterers.

It is of interest to examine the total effects that many small random inhomogeneities have on the effective properties of a dielectric. Intuitively there should be two major effects: first, because each inhomogeneity will slightly refract a wave travelling through the dielectric, the path length will slightly increase, and this will be measured as a slight increase in the effective dielectric constant; secondly, since each scattering point will re-radiate energy into all directions, the sum of these contributions will appear as an increase in the loss of the dielectric. In an effort to quantify these effects, even though they may be of secondary importance to interferometry, the effects of small random perturbations in the properties of a dielectric within a two-dimensional waveguide were examined. This theoretical development and its results are the main points of this chapter.

Note: In chapter 3 dielectric constants are denoted by ε, and propagation constants are denoted by k^2. ρ is defined differently (equation 3-39) from the ρ used in Chapter 2 (equation 2-11 ff).

3.2. Perturbation theory

It is, of course, impossible to give an exact description of a wave travelling through a medium that is, by definition, random. However, if the statistics of the properties of the medium are known, it should be possible, in principle, to determine something about the statistics of a wave that traverses the medium. In particular, it should be possible to say something about the mean, or coherent, wave, especially if the random properties of the medium do not differ too greatly from some average value.

We will use a method developed by Keller (1967 , and earlier references therein) for treating linear stochastic equations using perturbation theory. It is assumed that the linear operator can be separated into random and non-random parts, and that the random properties are small compared to the non-random ones -- i.e. the randomness acts as a perturbation on the non-random solution. We will then apply this method to the equation describing waves in a simple two-dimensional waveguide.

Following Keller's development, assume that the equation describing random process is linear, and has the form

$$L\,u = g \qquad (1)$$

where L is a linear operator

u is the unknown, and

g is the known.

Then, if a solution for (1) can be found,

$$u = L^{-1} g. \tag{2}$$

If L is random, then u also will be random, and $\langle u \rangle$ is given by

$$\langle u \rangle = \langle L^{-1} \rangle g, \tag{3}$$

where $\langle\rangle$ indicates the expectation operator.

Multiplying (3) by $\langle L^{-1} \rangle^{-1}$ gives

$$\langle L^{-1} \rangle^{-1} \langle u \rangle = g \tag{4}$$

and, if g = 0 so that (1) is a homogeneous equation,

$$\langle L^{-1} \rangle^{-1} \langle u \rangle = 0 . \tag{5}$$

In order to find $\langle L^{-1} \rangle^{-1}$, let us assume that L can be divided into non-random part M, and a random part V, so that

$$L = M + V . \tag{6}$$

Then, if M is invertible,

$$\begin{aligned} L^{-1} &= \left[M(1 + M^{-1}V)\right]^{-1} \\ &= (1 + M^{-1}V)^{-1} M^{-1} \end{aligned} \tag{7}$$

If $M^{-1}V$ (or its operator norm) is less than one, (7) can be expanded using the binomial theorem:

$$L^{-1} = \sum_{n=0}^{\infty} (-M^{-1}V)^n M^{-1} . \tag{8}$$

Taking expectation values of both sides of (8), and separating the first term,

$$\langle L^{-1} \rangle = \left[1 + \sum_{n=1}^{\infty} \langle (-M^{-1}V)^n \rangle\right] M^{-1} \tag{9}$$

Inverting both sides of (9), again using a binomial expansion,

$$\langle L^{-1}\rangle^{-1} = M \sum_{q=0}^{\infty} \left[\sum_{n=1}^{\infty} \langle (M^{-1}V)^n \rangle \right]^q . \qquad (10)$$

If V is small compared to M, only the first few terms of (10) are important; hence,

$$\langle L^{-1}\rangle^{-1} = M + \langle V\rangle - \langle VM^{-1}V\rangle + \langle V\rangle\ M^{-1}\ \langle V\rangle + O\left[(M^{-1}V)^3\right]. \qquad (11)$$

If $\langle V\rangle = 0$, (11) becomes, dropping terms above second order,

$$\langle L^{-1}\rangle^{-1} = M - \langle VM^{-1}V\rangle . \qquad (12)$$

M^{-1} is often expressed as an integral operator

$$M^{-1}\ u(x) = \int G(x,x')\ u(x')\ dx', \qquad (13)$$

where G(x,x') is the Green's function of M satisfying the boundary conditions of the problem and the equation

$$M\ G\ (x,x') = \delta(x-x'), \qquad (14)$$

in which $\delta(x-x')$ is the Dirac delta function.

Then our equation for $\langle u(x)\rangle$, (5), becomes with (12) and (13):

$$M\ \langle u(x)\rangle - \int \langle V(x)\ G(x,x')\ V(x')\ \langle u(x')\rangle\ dx'\rangle = 0 . \qquad (15)$$

Therefore, to terms of second order, the effects of the perturbations can be represented by a convolution of the random operator, V, with the non-random Green's function, G, as given in (15).

3.3 Homogeneously-filled waveguide

In order to examine the effects of random inhomogeneity relevant to radio interferometry, we will take wave propagation in a plane two-dimensional waveguide, i.e. a layer with randomly inhomogeneous electrical properties. The physical example will be kept as simple as possible within this framework, first, so that the mathematics does not become too cumbersome; and, second, so that the effects due to the inhomogeneities are most apparent.

The layer is set up as shown in Fig. 3-1. The boundaries of the layer are at $z = 0$ and $z = h$, and are assumed to be perfectly conducting. A source is located at z_0 on the z-axis within the layer, and oscillates with time dependence $e^{-i\omega t}$. We will assume that the signal is received within the layer at P (r,z), a large distance from the source, i.e. r large, $0 < z < h$.

The solution for the situation in which the layer is homogeneous is well known (e.g. Budden, 1961; Wait, 1962). We will review quickly the treatment by Brekhovskikh (1960 , Sections 25 and 26).

The source can be represented by a Hertz vector with only a vertical component ψ . From ψ all components of the electrical and magnetic fields can be determined. For transverse magnetic (TM) wave propagation, the vertical electric Hertz vector must be used, and the normal gradient of ψ must vanish at the boundaries since they are perfectly conducting, i.e.

$$\frac{d\psi}{dz} = 0 \text{ at } z = 0,h \qquad (16)$$

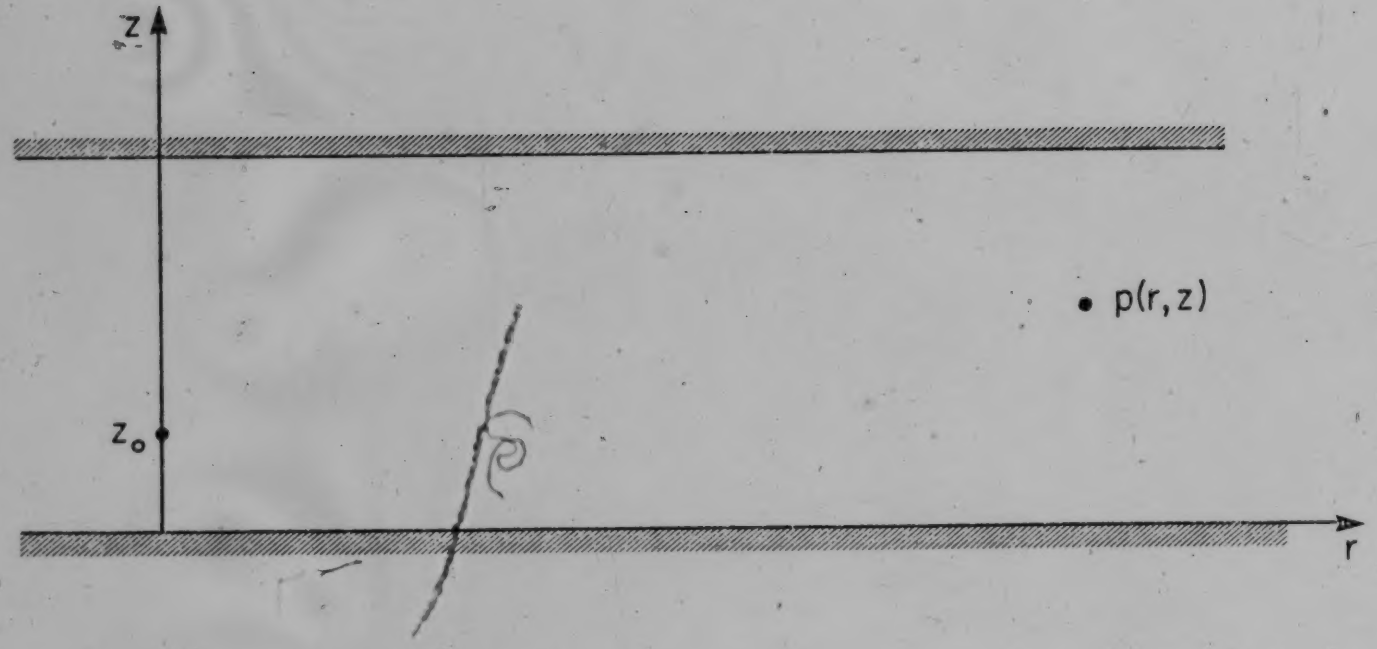

Figure 3-1: Cross-section of two-dimensional waveguide

The reflection coefficient is + 1. Conversely, for transverse electric (TE) propagation, the magnetic Hertz vector is required, and the boundary conditions are

$$\psi = 0 \text{ at } z = 0,h. \tag{17}$$

and the corresponding reflection coefficient is -1. The analysis is identical in both cases.

ψ satisfies the scalar wave equation

$$\nabla^2 \psi + k^2 \psi = 0 \tag{18}$$

where ∇^2 is the Laplacian operator,

and $k^2 = \omega^2 \mu\varepsilon$ is the propagation constant.

For a homogeneous medium the magnetic permeability, μ, and the dielectric constant, ε, are constant, but will have imaginary parts if the medium has magnetic or electric losses, respectively.

The signal received at P will be made up not only of direct spherical waves emanating from z_o, but also waves reflected from the boundaries. These waves appear to be coming from image sources located at $-z_o$ and at $h + (h-z_o)$, for the first reflection. The waves from these image sources are also reflected, so at large distances from the source,

$$\psi = \sum_{n=0}^{\infty} W^{2n} \left[\frac{\exp(ikR_{n1})}{R_{n1}} + W \frac{\exp(ikR_{n2})}{R_{n2}} + W \frac{\exp(ikR_{n3})}{R_{n3}} + W^2 \frac{\exp(ikR_{n4})}{R_{n4}} \right] \tag{19}$$

where $R_{n1} = \left[r^2 + (2nh + z - z_o)^2 \right]^{\frac{1}{2}}$

$R_{n2} = \left[r^2 + (2nh + z + z_o)^2 \right]^{\frac{1}{2}}$

$R_{n3} = \left[r^2 + (2(n+1)h - z - z_o)^2 \right]^{\frac{1}{2}}$

$R_{n4} = \left[r^2 + (2(n+1)h - z + z_o)^2 \right]^{\frac{1}{2}}$

$W = \pm 1$ is the reflection coefficient at the boundaries.

This solution (19), being made up of spherical waves, satisfies the wave equation (18), and it satisfies the boundary conditions, (16), or (17).

After some rather tedious mathematical manipulations (see Brekhovskikh, pp. 332-334), which essentially reduce (19) to an integration of waves travelling at all possible angles with respect to the z-axis, (19) can be written, (for $z < z_o$, and $W = +1$),

$$\psi = \int_{-\infty}^{\infty} \frac{\cosh(bz_o)\ \cosh(h-z)b}{b \sinh(bh)}\ H_o^{(1)}(k_n r)\ k_n dk_n \qquad (20)$$

where $b = (k^2 - k^2)^{\frac{1}{2}}$, (21)

$H_o^{(1)}$ is the Hankel function of the first kind, order 0, and, k_n is a radial wavenumber.

The integration in (20) can be reduced to the sum of the residues of its poles, located at points where

$$\sinh(bh) = 0 \qquad (22)$$

i.e. when $$bh = in\pi, \qquad (23)$$

where n is an integer, and $i = \sqrt{-1}$. From (21) and (23),

$$k_n = \left[k^2 - \left(\frac{n\pi}{h}\right)^2 \right]^{\frac{1}{2}} \tag{24}$$

Therefore, unattenuated radial waves propagate only for a few discrete wavenumber or modes. This situation corresponds physically to standing waves being set up in the z direction, i.e. waves whose path length is an integral number of half-wavelengths between reflections.

If the boundaries are not perfect reflectors, the physical situation does not change greatly; however, instead of (22), the poles are given by the more general expression

$$1 - W_1 W_2 \exp(2ik_z h) = 0 \tag{25}$$

where W_1 and W_2 are the reflection coefficients at the boundaries, and k_z is the vertical wavenumber. The expression (25) can be complicated to evaluate, since the W will be, in general, complex, and different for each of the k_z (i.e. each angle of incidence).

Equation (20) therefore reduces to the summation

$$\psi(r,z) = \frac{2\pi i}{h} \sum_{n=0}^{\infty} a_n \cos\left(\frac{n\pi z}{h}\right) \cos\left(\frac{n\pi z_o}{h}\right) H_o^{(1)}(k_n r) \tag{26}$$

with k_n given by (24),

and $a_n = \begin{cases} \frac{1}{2} & n=0 \\ 1 & n \neq 0. \end{cases}$

In order to evaluate (26), two more approximations will be made that are consistent with fields distant from the source.

First the Hankel function will be replaced by its asymptotic expansion for large argument (Abramowitz and Stegun , 1970, p.364):

$$H_o^{(1)}(\xi) = \frac{2}{\pi\xi} \exp\left[i\left(\xi - \frac{\pi}{4}\right)\right]\left[1 - i\frac{1}{8\xi} + \ldots\right] . \tag{27}$$

Only the first term of the expansion will be used.

Secondly, the summation over n will be limited to the range 1 to N, where N satisfies

$$N < \frac{hk}{\pi} . \tag{28}$$

In effect we are limiting the summation to only real values of k_n, i.e. to propagating waves. The non-propagating waves, with only imaginary wavenumbers, are attenuated exponentially in r, and therefore do not contribute significantly to the field when r is large.

Then, with (27) and (28), (26) becomes

$$\psi(r,x) \approx \frac{2}{h}\sqrt{\frac{2\pi}{r}}\, e^{i\pi/4} \sum_{n=0}^{N} \frac{a_n}{\sqrt{k_n}} \cos\left(\frac{n\pi z}{h}\right) \cos\left(\frac{n\pi z_o}{h}\right) e^{ik_n r} . \tag{29}$$

In order to relate (29) to the actual $\bar{E}$ and $\bar{H}$ fields certain vector operations must be performed on the Hertz vector, given by (e.g. Brekhovskikh, 1960, p. 236):

$$\begin{Bmatrix} \bar{E} \\ \bar{H} \end{Bmatrix} = k^2 \bar{\pi}_m^e + \bar{\nabla}\bar{\nabla}\cdot\bar{\pi}_m^e$$

$$\begin{Bmatrix} \bar{E} \\ \bar{H} \end{Bmatrix} = i\omega \begin{Bmatrix} \mu \\ -\varepsilon \end{Bmatrix} \bar{\nabla} \times \bar{\pi}_m^e \tag{30}$$

where $\frac{-}{\pi}\frac{e}{m}$ represents the electric or magnetic Hertz vector.

As an example, the magnetic field produced from a vertical electric Hertz vector, π_z, with radial symmetry is

$$\bar{H} = -i\omega\varepsilon \bar{\nabla} \times \pi_z$$

$$= i\omega\varepsilon \frac{\partial \pi_z}{\partial r} \bar{a}_\theta . \qquad (31)$$

$\bar{H}$ has only a tangential component for this case, -- hence the term "transverse magnetic". From (31), and (29),

$$H_\theta = \frac{2\sqrt{2\pi}}{h} \omega\varepsilon e^{i\pi/4} \sum_{n=0}^{N} \frac{a_n}{\sqrt{k_n}} \cos\frac{(n\pi z)}{h} \cos\frac{(n\pi z_o)}{h} e^{ik_n r}\left[\frac{k_n}{r^{\frac{1}{2}}} + \frac{i}{r^{3/2}}\right]. \qquad (32)$$

It can be seen from (32) that the field is made up of contributions from a finite number of waves with wavenumbers given by the k_n, which depend on the layer thickness. The waves are unattenuated if the k_n are real, but decay as $r^{-\frac{1}{2}}$ when r is large, corresponding to spreading of spherical waves trapped in a two-dimensional guide.

Examples of fields in the waveguide, calculated from (32), are shown in Fig. 3-2. If only one mode is excited, the field shows a steady decay. As the thickness increases, other modes are possible, and two or more waves interfere with each other (see Annan, et al., 1975).

MODE THEORY - NO SCATTERING

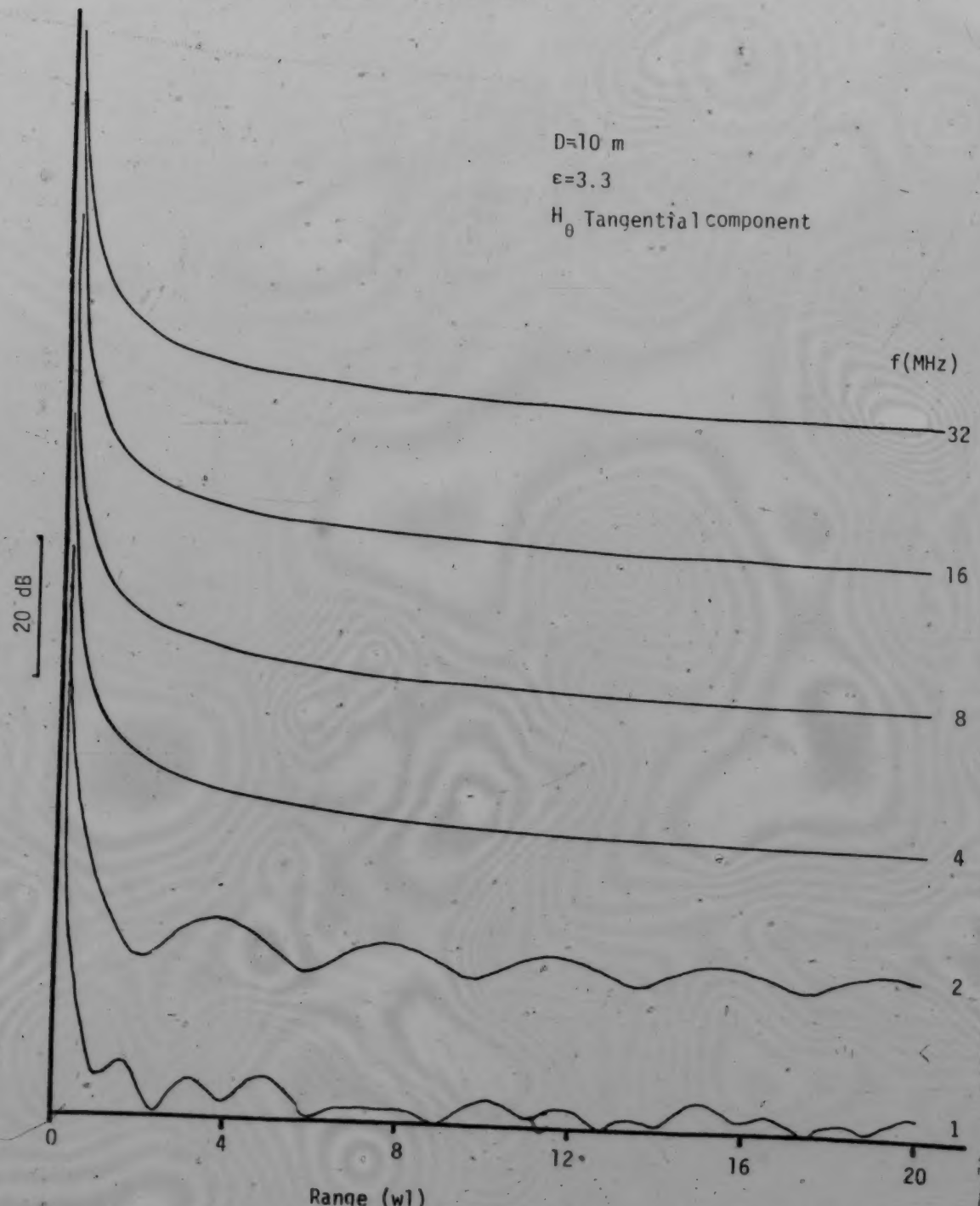

Figure 3-2.

3.4 Inhomogeneously-filled waveguide

The results of the previous two sections can now be combined to determine some properties of waves travelling in a randomly inhomogeneous layer. Taking equation (18),

$$\nabla^2 \psi + k^2 \psi = 0 \qquad (18)$$

where $k^2 = \omega^2 \mu \varepsilon$, now let,

$$\mu = \mu_o, \text{ the permeability of free space,} \qquad (33)$$

$$\text{and } \varepsilon = \varepsilon_o \varepsilon_1 (1 + \eta \varepsilon_2), \qquad (34)$$

where ε_o is the permittivity of free space,

ε_1 is the average relative dielectric constant of the layer, and is a real constant,

η is an explicit small parameter, $\ll 1$, and,

ε_2 is the spatial variation in dielectric constant in the layer, and is a real, normalized random variable, with $\langle \varepsilon_2 \rangle = 0$. It is clear from (33) and (34) that the material in the layer has no intrinsic EM losses.

Substituting (33) and (34) into (18),

$$(\nabla^2 + k_o^2 + \eta k_o^2 \varepsilon_2) \psi = 0 \qquad (35)$$

where $k_o^2 = \omega^2 \mu_o \varepsilon_o \varepsilon_1$, the propagation constant of the unperturbed layer (mode o). Then k_n, the wavenumber for the n^{th} mode, can be found from equation (24).

Equation (35) is now in the form of equations (1) and (6), with

$$L = M + V = (\nabla^2 + k_n^2) + (\eta k_n^2 \varepsilon_2),$$

$$u = \psi, \text{ and,}$$

$$g = 0. \qquad (36)$$

Hence, since $\langle V \rangle = \langle \eta k_n^2 \varepsilon_2 \rangle = 0$, equation (15) applies:

$$(\nabla + k_n^2) \langle \psi(x) \rangle - \int \langle \eta k_n^2 \varepsilon_2(x) \; G(x,x') \; \eta k_n^2 \varepsilon_2(x') \langle \psi(x') \rangle \, dx' \rangle = 0 \tag{37}$$

where x and x' are positions in the waveguide.

The second term of (37) becomes

$$\eta^2 k_n^4 \int \langle \varepsilon_2(x) \; \varepsilon_2(x') \rangle \, G(x,x') \; \langle \psi(x') \rangle \, dx' \tag{38}$$

where $\langle \varepsilon_2(x) \; \varepsilon_2(x') \rangle$ is the correlation function in space of the random variable ε_2, and G(x,x') is the Green's function for the waveguide, given by equation (29).

Hence at point x the mean field, represented by the wave-function $\langle \psi(x) \rangle$, is made up of the first, a non-scattering term, plus the second, a perturbation term. The perturbation term is the total effect at point x of scatterers at all locations x' within the waveguide, each scatterer stimulated by the coherent field at x'.

To evaluate expression (38), we will follow the development given by Karal and Keller (1964). First, we define

$$\underline{\rho} = \underline{x} - \underline{x}' \text{ and } \rho = |x - x'|, \tag{39}$$

the radial distance between point x and a scatterer at x'.

Then, it is clear from equation (29) that the Green's function for the waveguide has the form

$$G(x,x') = G(\rho) \tag{40}$$

for far-field solutions.

We will also assume $\langle \varepsilon_2(x) \; \varepsilon_2(x') \rangle$, the correlation coefficient of the random properties, depends only on ρ, and more specifically

has the form

$$\langle \varepsilon_2(x)\ \varepsilon_2(x') \rangle = e^{-\rho/\rho_0} \qquad (41)$$

where ρ_0 is a correlation length that is a measure of the typical scatterer size.

$\langle \psi(x') \rangle$ can be evaluated by expanding as a sum of plane waves. Then,

$$\langle \psi(x') \rangle = \langle \psi(x) \rangle \psi(\rho). \qquad (42)$$

Developing a mean-value theorem for solutions of the wave equation, the integration in equation (38) can be performed in cylindrical co-ordinates around x:

$$\begin{aligned} \int \psi(\varrho) d\varrho &= \int_0^h dz \int_0^\infty d\rho \int_0^{2\pi} \rho\ e^{ik\rho\ \cos\theta} d\theta \\ &= 2h \int_0^\infty \rho\ d\rho \int_0^\pi e^{ik\rho\cos\theta}\ d\theta \\ &= 2\pi h \int_0^\infty \rho\ \ J_0(k\rho)\ \ d\rho, \end{aligned} \qquad (43)$$

where $J_0(k\rho)$ is the Bessel function of the first kind, order 0 (Abramowitz and Stegun, 1970, p. 360).

Substituting (39), (40), (41), (42) and (43) into (37):

$$(\nabla^2 + k_n^2 - 2\pi h\ n^2\ k_n^4 \int_0^\infty \rho\ e^{-\rho/\rho_0}\ G(\rho)\ \ J_0(k\rho)\ d\rho\ )\ \langle \psi(x) \rangle = 0. \qquad (44)$$

It can be seen that k_n^2, the propagation constant for the n^{th} mode is modified by a scattering correction term, to give a new effective propagation constant, k^2:

$$k^2 = k_n^2 - n^2\ k_n^2 I(k,k_n) \qquad (45)$$

where $I(k,k_n) = 2\pi h\ k_n^2 \int_0^\infty \rho e^{-\rho/\rho_0}\ G(\rho)\ J_0(k\rho)\ d\rho$

Substituting from equation (29) and for $G(\rho)$; and ignoring

distributions of scatterers in z,

$$I(k,k_n) = 4\pi\sqrt{2\pi}\, e^{i\pi/4} a_n k_n \int_0^\infty \sqrt{k_n \rho}\; e^{-\rho/\rho_0}\, e^{ik_n\rho}\, J_0(k\rho)\, d\rho. \tag{46}$$

By letting $k = k_n$ in equation (46), it is possible to solve equation (45) for the new k^2, the effective propagation constant of the waveguide for the nth mode, including the first-order scattering correction. It should be noted that as (46) is written, no effects of scattering from one mode to or from another are accounted for; therefore, it is strictly true only for a waveguide in which a single mode propagates.

3.5 Numerical evaluation

In order to solve equation (45) for k, the new wavenumber that takes into account scattering, the integral in (46) must be evaluated. By setting

$$\rho/\rho_o = \zeta,$$

$$C = 4\pi\sqrt{2\pi}\, e^{i\pi/4}\, a_n ,$$

$$I = C\int_o^\infty k\, e^{-\zeta}\sqrt{k\rho_o\zeta}\; e^{ik\rho_o\zeta}\, J_o(k\rho_o\zeta)\rho_o\; d\zeta \tag{47}$$

and, by further letting $k\rho_o = a$, (47) becomes;

$$I = C\, a\int_o^\infty e^{-\zeta}\sqrt{a\zeta}\; e^{ia\zeta}\, J_o(a\zeta)\; d\zeta. \tag{48}$$

The parameter a is non-dimensional, and relates the mean scatterer size to the wavelength in the dielectric.

Unfortunately, the integral in (48) cannot be evaluated by simple numerical integration for most values of a. For small values of a (<<1), the oscillating terms in the integrand vary slowly, and quadrature integration is successful. However, as a →1, these terms oscillate many times before the exponentially decaying term becomes small. Therefore the integration was broken into two steps (see Fig. 3-3):

$$I = C\, a\left\{\int_o^{\zeta'} e^{-\zeta} F(a\zeta)\, d\zeta + \int_{\zeta'}^\infty e^{-\zeta} F(a\zeta)\, d\zeta\right\}, \tag{49}$$

where $F(a\zeta) = \sqrt{a\zeta}\; e^{ia\zeta}\, J_o(a\zeta)$.

$\int_0^\infty e^{-\zeta} F(a\zeta)\, d\zeta$ evaluation

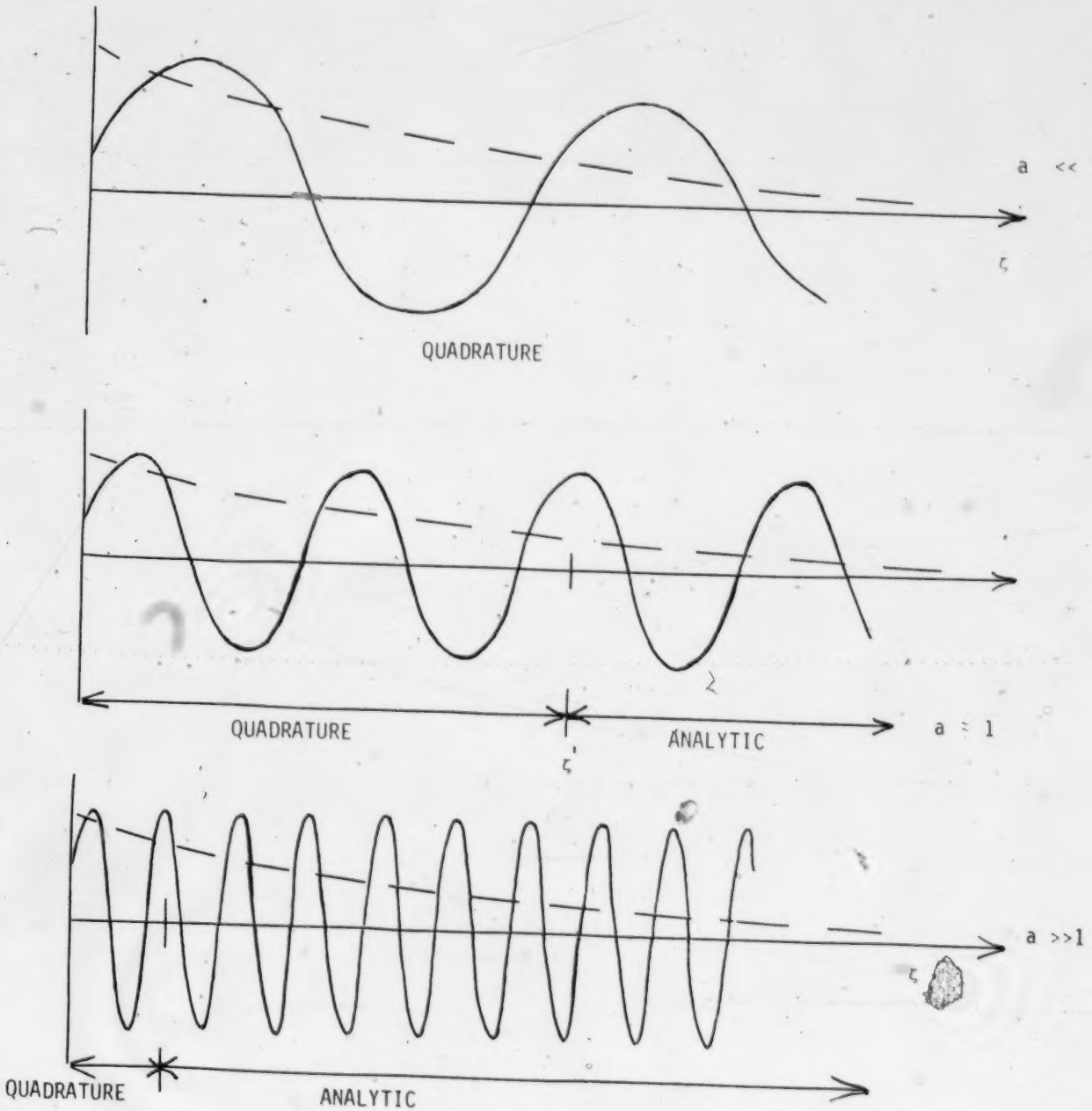

Figure 3-3

The first term in (49) was performed using 32-point Gaussian quadrature. ζ' was set $\approx 33/a$. The second term was evaluated analytically using the asymptotic expansion of J_0 for large argument and Laplace transforms. For large argument (Abramowitz and Stegun, 1970, p. 364):

$$J_0(a\zeta) = \sqrt{\frac{2}{\pi a\zeta}} \cos(a\zeta - \tfrac{\pi}{4}) + O(|a\zeta|^{-1}) \qquad (50)$$

Hence,

$$F(a\zeta) = \sqrt{\frac{2}{\pi}} \left[\cos(a\zeta - \tfrac{\pi}{4})\right]\left[\cos(a\zeta) + i \sin(a\zeta)\right], \qquad (51)$$

and,

$$\int_{\zeta'}^{\infty} e^{-\zeta} F(a\zeta)\, d\zeta = e^{-\zeta'} \mathcal{L}\left[F(a\zeta + a\zeta')\right]. \qquad (52)$$

Multiplying (51) and collecting terms:

$$F(a\zeta + a\zeta') = \sqrt{\frac{2}{\pi}} \sin(\tfrac{\pi}{4}) \times \left[D_1 \cos^2(a\zeta) + D_2 \cos(a\zeta)\sin(a\zeta) + D_3 \sin^2(a\zeta)\right] \qquad (53)$$

where

$$D_1 = (A^2 + AB) + i(B^2 + AB)$$
$$D_2 = (A^2 - B^2 - 2AB) + i(A^2 - B^2 + 2AB)$$
$$D_3 = (B^2 - AB) + i(A^2 - AB)$$
$$A = \cos(a\zeta')$$
$$B = \sin(a\zeta').$$

Substituting (53) into (52) and taking Laplace transforms (Erdélyi, 1954, p. 159):

$$\int_{\zeta'}^{\infty} e^{-\zeta} F(a\zeta)\, d\zeta = e^{-\zeta'} \sqrt{\frac{2}{\pi}} \sin\left(\frac{\pi}{4}\right) \times \left(\frac{1}{1 + 4a^2}\right) \times \left[D_1(1 + 2a^2) + D_2(a) + D_3(2a^2)\right], \quad (\mathrm{Im}(a) < \tfrac{1}{2}) \qquad (54)$$

which can be inserted into the right-hand side of (49).

The result of this evaluation is that both the real and imaginary parts of k^2 increase, corresponding to increases in the effective dielectric constant and loss tangent of the dielectric in the waveguide. A thin waveguide with only a single propagating mode, and a filled with a lossless material with a dielectric constant on of 3.2, is used as an example. The change in the dielectric constant is small, but the loss tangent (shown in Fig. 3-4) increases dramatically from negligible values to ≈ 0.1 when $r/\lambda \to 1$. The parameter n is also highly important -- it roughly corresponds to the product of the perturbation in dielectric constant and the number of scatterers per unit volume. Values of r/λ greater than about 1 are not valid, since the imaginary part of a becomes large, and the iteration procedure becomes unstable.

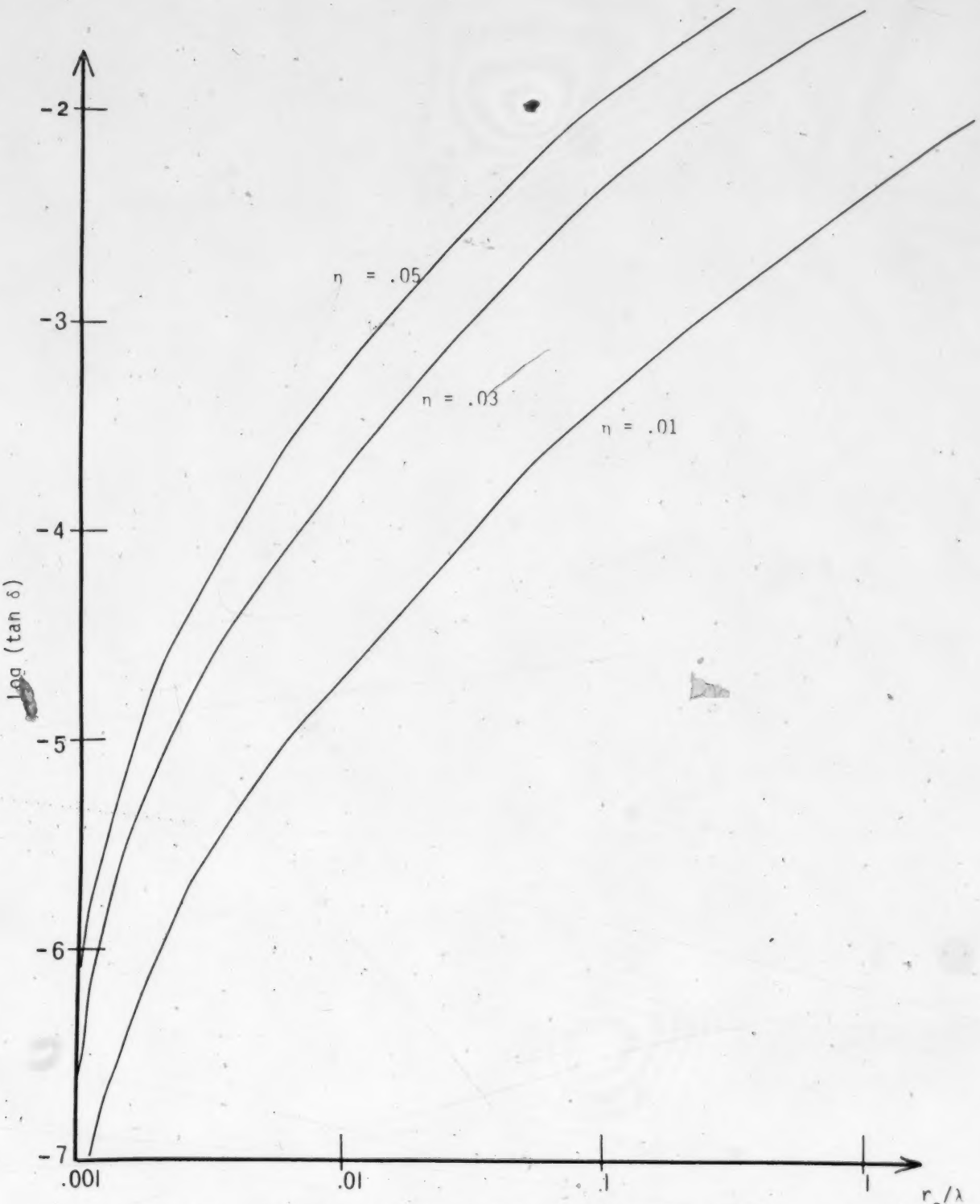

Figure 3-4: Effective loss tangent for lossless scattering dielectric in a waveguide (mode 0), $\varepsilon_r = 3.2$

Theoretical calculation

3.6 Discussion of theoretical results

Although there are several serious limitations to this theoretical solution, which are discussed below, there are several points which can be made. The results shown in Fig. 3-4 can be compared to those of Roth and Elachi (1975), who calculated the effective loss tangent for a low-loss scattering dielectric whole space. Their solutions show a very strong peak in the loss tangent when r_o/λ is between 1 and 10, for values of n between 0.01 and 0.05. Therefore for a distribution of scatterers, their results do not differ qualitatively from those of Watts and England (1976), in which the effects of a spherical scatterer reach a limit when the scatterer size approaches a wavelength. Although the high frequency limit for the waveguide case has not been examined, the effective loss tangent in Fig.3-4 levels off for larger scatterers. It is clear that the effective loss tangent for low-loss dielectrics can be substantially increased by the effects of random scattering.

These results confirm the idea, outlined in Section 3.1, that volume scattering will not greatly affect interferometry data until the scatterers are close to a wavelength in size. This result is also consistent with one set of scale model data, in which about 300 12 mm diameter plastic beads were placed into the oil. A rough estimate of n gives:

$$n \approx \left(\frac{\Delta\varepsilon}{\varepsilon}\right) N\left(\frac{\Delta v}{v}\right) \sim \left(\frac{1}{3}\right)(300)\left(\frac{.02}{1000}\right) = .002, \qquad (55)$$

so that even though the beads had a $r_o/\lambda \approx 0.18$, their total effect would not be expected to be large (see Fig.3-5). In fact no discernible change could be seen in the results.

It is worth summarizing the limitations to the theory presented in this chapter. The most serious limitation is that there is no quantitative analytical or experimental verification of the results. Therefore, the data presented in Figs.3-4 and 3-5 must be considered qualitative, at best.

There are also a number of assumptions implicit in the solution itself. The Green's function that was used is only true for far-field solutions -- i.e. the source is distant from the point of measurement. Therefore it only accurately represents the effect of scatterers that are distant both from the source and from the point of observation. Only inhomogeneities in the radial direction are considered; i.e. the waveguide is homogeneous in the vertical direction. Only small variations in the parameters are allowed, since all high-order scattering terms have been discarded. As the frequency becomes high (corresponding to increasingly large scatterers), the solution presented becomes infinite, which indicates that it must then be solved more accurately for large values of $k\rho_o$.

The results presented have three more implicit restrictions that were avoided by computing values for only the zero mode:
(1) Cross-mode scattering terms were excluded -- i.e. the effects of energy scattering from one mode to another.

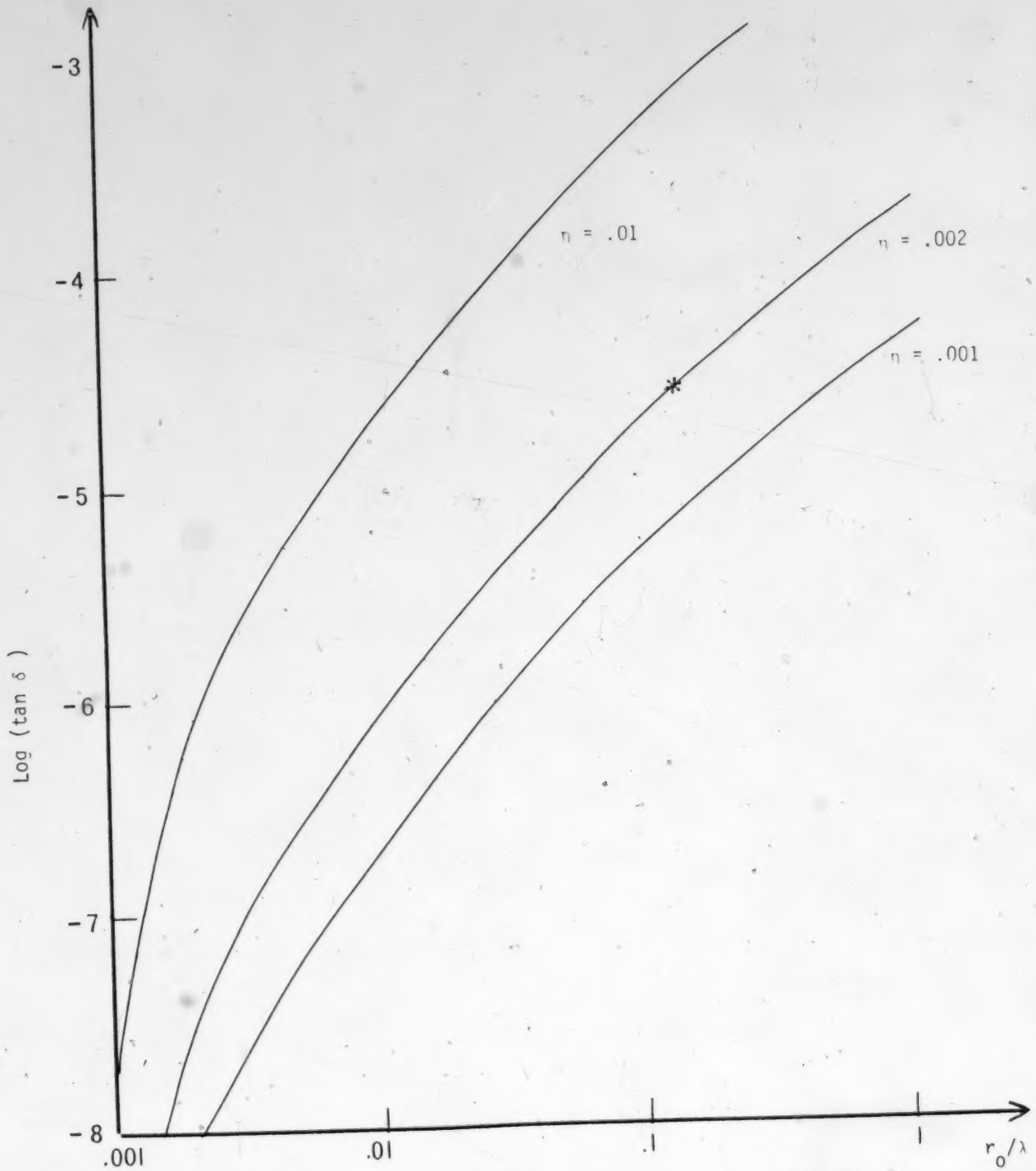

Figure 3-5: Effective loss tangent for lossless scattering dielectric in a waveguide (mode 0), $\epsilon_r = 2.16$
Theoretical calculation

* SCALE MODEL

(2) The perturbation technique becomes quickly invalid for problems in which the dispersion relation allows only discrete values for the wavenumber. Therefore, for a waveguide, if the scattering substantially alters the wavenumber, the effect of the scattering will be constrained by the boundary conditions.

(3) The vertical distribution of scatterers needs to be accounted for. For odd-numbered modes, the total effect of a uniform vertical distribution of scatterers would appear to be zero, with the contribution from the positive portions of the standing wave cancelled by the negative portions. Hence scattering in these modes could be substantially less than otherwise expected.

In spite of these limitations, the perturbation approach is applicable to a wide variety of scattering problems, and leads to a good physical understanding of the scattering process.

CHAPTER 4

INTERPRETATION OF INTERFEROMETRY FIELD DATA

4.1 Introduction and interpretation procedure

Radio interferometry field data have now been collected from a variety of geological regions: two different temperate glacial areas, the surface of the moon, a permafrost area, and a frozen lake. Generally the data from each region show quite distinct features. In this chapter the results from each of these regions will be presented and discussed. Interpretation of the data, both in terms of a layered structure and in terms of the effects of random scattering, will be presented.

Although several initial interpretations of field data have already appeared in the published literature, interpretation based primarily on scale model results (Chapter 2) is presented here for the first time. Hence, it is probably useful to summarize the steps through which the radio interferometry field data were interpreted (Fig.4-1). The procedure was aimed at giving estimates of both the structure and the electrical properties of the subsurface.

Before applying these steps, the data were put into a standard format. The demultiplexing and reformatting procedures were both laborious and exacting (Rossiter, 1975), and they could

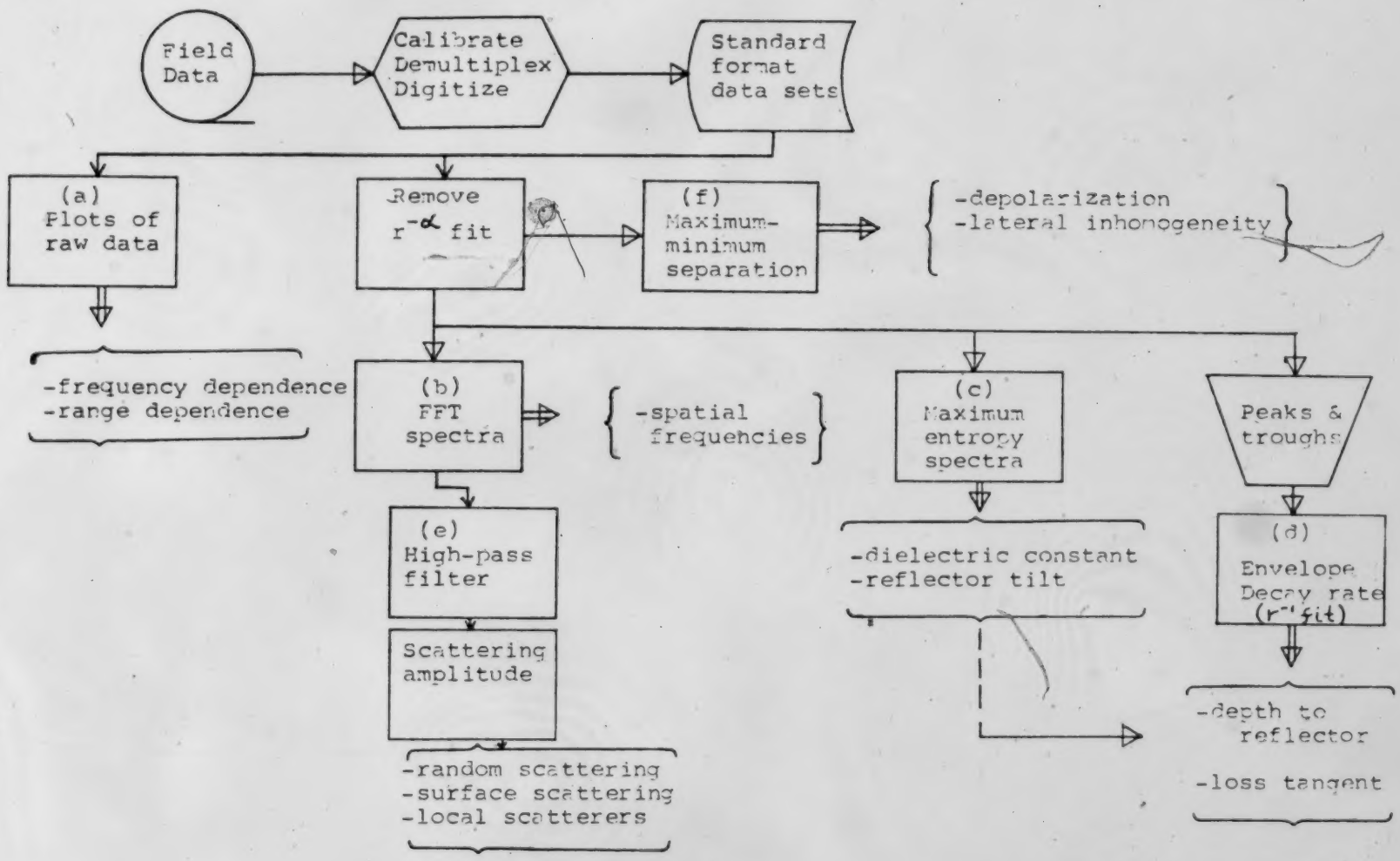

Figure 4-1. Logical flow of interpretation procedure for radio interferometry field data. Major steps are lettered (a) through (f). Major interpretive results are enclosed in curled parentheses.

have been done in many other ways. Each of the 36 components in a run of field data (6 components for each of 6 frequencies) were separated and stored in arrays of dB vs transmitter-receiver distance. Then, after elimination of bad data points, each component was digitized at a rate of 10 samples per free-space wavelength (wl), to the end of the data, or to 20 wl, whichever was less. Tests were done before digitization to ensure that aliasing would not occur during re-sampling. The data were then stored so that any component of any run could be retrieved individually, as well as descriptive information about the run.

(a) Examination of raw data

This is an obvious first step. It can reveal overall trends in the data, anomalies in particular components, or anomalies that occur only at particular distances. Each of the data sets described below have distinct features that can be qualitatively described from examination of properly formatted raw data.

(b) FFT power spectra

Fast Fourier Transform (FFT) power spectra were calculated from field-strengths (instead of dB) vs wl, after $r^{-\alpha}$ had been removed, where r is distance in wl, and α is determined by a least-squares fit to all points in the component (see Appendix 2). The FFT spectra

reveal the overall uniformity of the data. For a homogeneous plane geometry only a few spectral lines should be clear.

(c) Maximum entropy power spectra

Because many of the runs were short--showing only a few interference peaks--maximum entropy spectra were also taken. These gave better resolution to specific spectral lines, and were used to calculate dielectric constant and, in some cases, tilt of the subsurface reflector. Dielectric constant of the upper layer can be estimated by substituting the highest beat frequency into equation 2-2. As shown in Section 2.2, a moderately deep, tilting subsurface reflector will alter this frequency, with a shift (at least for small angles of tilt) that is approximately equal to minus the tilt.

(d) Envelope and decay

An envelope was constructed around the main components by manually picking the major peaks and troughs in a curve, and fitting a piecewise cubic spline to the two sets of selected extrema. The envelope is useful for two estimates: if the envelope has a large peak the position of the peak can indicate the depth to a reflector, even if the reflector is tilting, using equation 2-19 and results from (c) above;

secondly, it is sometimes possible to estimate the loss tangent of the upper layer from the rate of decay of the envelope, using equation 2-8. Both of these estimates are subject to a fair amount of uncertainty; therefore, they are only useful if a consistent picture emerges from several components and frequencies.

(e) High-pass filtering

After removing spatial frequencies due to interference of coherent waves, the resultant is largely due to scattering. This curve is plotted to examine anomalous bursts of energy, due to scattering from a localized object. The background level, due to random scattering, has been called the "scattering amplitude". Since its magnitide is normalized in the interferometry technique to the direct wave, values are independent of output transmitted power. By determining the lowest radio frequency at which random scattering first becomes significant, the typical size of scatterers can be estimated. The rate of onset of scattering is indicative of the range of sizes of the scatterers. If the onset is rapid, the distribution of scatterer sizes is probably fairly limited. If, on the other hand, the effects of scattering appear to grow slowly with increasing radio frequency, then there is probably a large range of scatterer sizes.

The spacing between scatterers can also be estimated, if only crudely, using Figure 2-24. Once a constant scattering level has been reached (i.e. as the radio frequency increases, scattering remains fairly constant), the scattering level depends mainly on the density of scatterers. In Figure 2-24 the L/H parameter is the scatterer spacing to size ratio, based on a two-dimensional spatial distribution of scatterers. L is defined as $(A/N)^{\frac{1}{2}}$, where N is the number of scatterers, and A is the area over which they are spread. Hence L is the mean distance between scatterers spread on a surface.

It is also of interest to be able to estimate the mean distance between scatterers that are uniformly distributed through a waveguide of thickness D. Then,

$$L_3 = (V/N)^{1/3} \qquad (1)$$

where L_3 is the mean scatterer separation in volume V, and N is the number of scatterers. Hence,

$$L_3 = (L^2 \times D). \qquad (2)$$

The number of scattering centres per unit volume, m, is clearly given by

$$m = L_3^{-3} \qquad (3)$$

Therefore, from the data, H can be estimated using the frequency at which scattering becomes intensive, knowing that inhomogeneities less than 0.3 wl_d are ineffective scatterers. Then L/H can be estimated using Figure 2-24 , and L can be determined. Finally, assuming that the scatterers are spread throughout a given volume, L_3 and m can be found using equations (2) and (3).

The H_ϕ endfire component is rather unusual, in that although it is maximum-coupled, it does not show any interference, and therefore does not receive any significant energy from the subsurface. Therefore, if it does not decay smoothly, it is due to irregularities in the upper surface. It has been used as an indicator of surface roughness by examining its scattering amplitude after filtering, in exactly the same way as the other maximum-coupled components. Unfortunately, this component has no analogue in the scale model (in which only electric fields can be measured), and has not yet been rigorously examined analytically. Therefore, it has only been used to qualititatively compare surface roughness from area to area.

(f) Maximum and minimum componentseparation

It is possible to estimate the degree of lateral inhomogeneity and/or scattering by examining the difference in power levels

between the maximum and minimum coupled components. To do this, a power law fit (parameter α, described in (b) above) was made to each component, and the fit intercepts from the various components were compared. In scale model data, differences of up to 40 dB were seen between the two sets of components. The separation is usually less pronounced in field data, but decreases when lateral boundaries are nearby, and when scattering increases, as determined in (e) above.

In the remainder of this chapter, data from each of the different regions studied will be presented in turn. A layered interpretation and the scattering parameters will be determined, using the procedures just outlined, and will be compared to previous interpretations. Finally, the scattering results from all of the regions will be summarized. Plots of the raw data from each region are given in Appendix 4.

4.2 The Athabasca Glacier

The Athabasca Glacier, Alberta, is a temperate valley glacier, about 1200 m wide and several km long (see Fig. 4-2). Near the snout, the glacier increases in thickness from about 70 m to about 300 m, as determined by drilling and seismic work. It was the site of a number of radio interferometry experiments during various stages of equipment development. These results have been discussed elsewhere (Rossiter, 1971; Rossiter et al., 1973; Simmons et al., 1972; and Strangway et al, 1974). Essentially the interferometry data at 1, 2 and 4 MHz can be fitted to a plane two-layer interpretation that is consistent with the known structure of the glacier.

Three runs will be examined in this section (see Appendix 4), all taken during the summer of 1971: run 25, running alongside the eastern side of the glacier, southward away from the snout; run 71, running along the same path, but in the opposite direction; and run 59, also running north, but closer to the centre of the glacier. These are shown in Fig. 4-2.

The most striking feature in the over 70 data sets collected is that at the lower frequencies (1, 2, and 4 MHz) there is a clear separation of 10-20dB between the maximum- and minimum-coupled components, but at 8, 16 and 32 MHz this distinction has totally disappeared. We will examine this point further later in the section. The maximum-coupled components at 1,2, 4 and perhaps 8 MHz are regular, and show distinct interference patterns.

FFT power spectra of run 71 are shown in Fig. 4-3. At the lower frequencies the power is concentrated in the spatial frequencies below 1 cycle/wl, although at the higher frequencies,

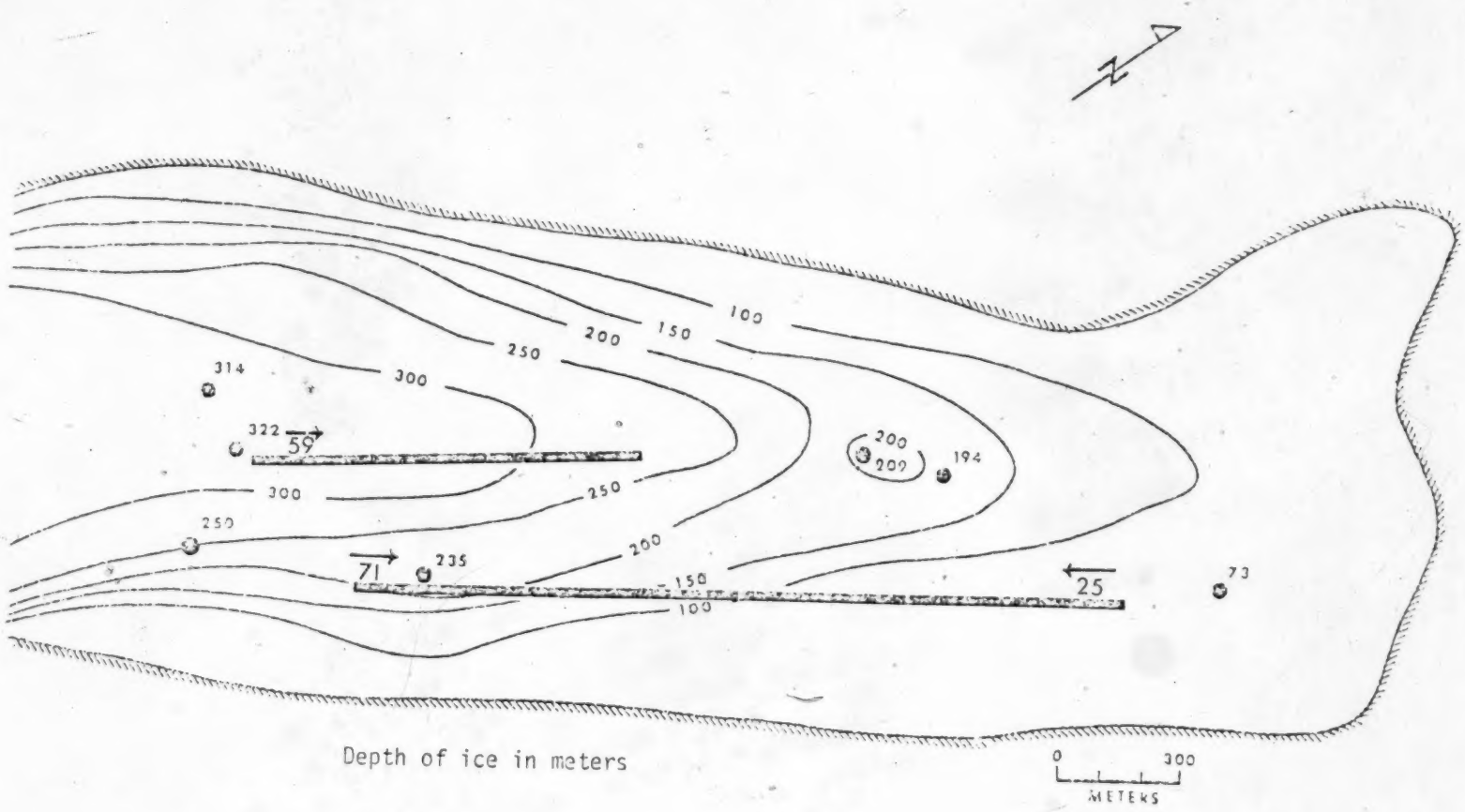

CONTOUR MAP OF DEPTH OF ATHABASCA GLACIER

● Boreholes with depth of ice

Interferometry Traverse Line 59→

Figure 4-2

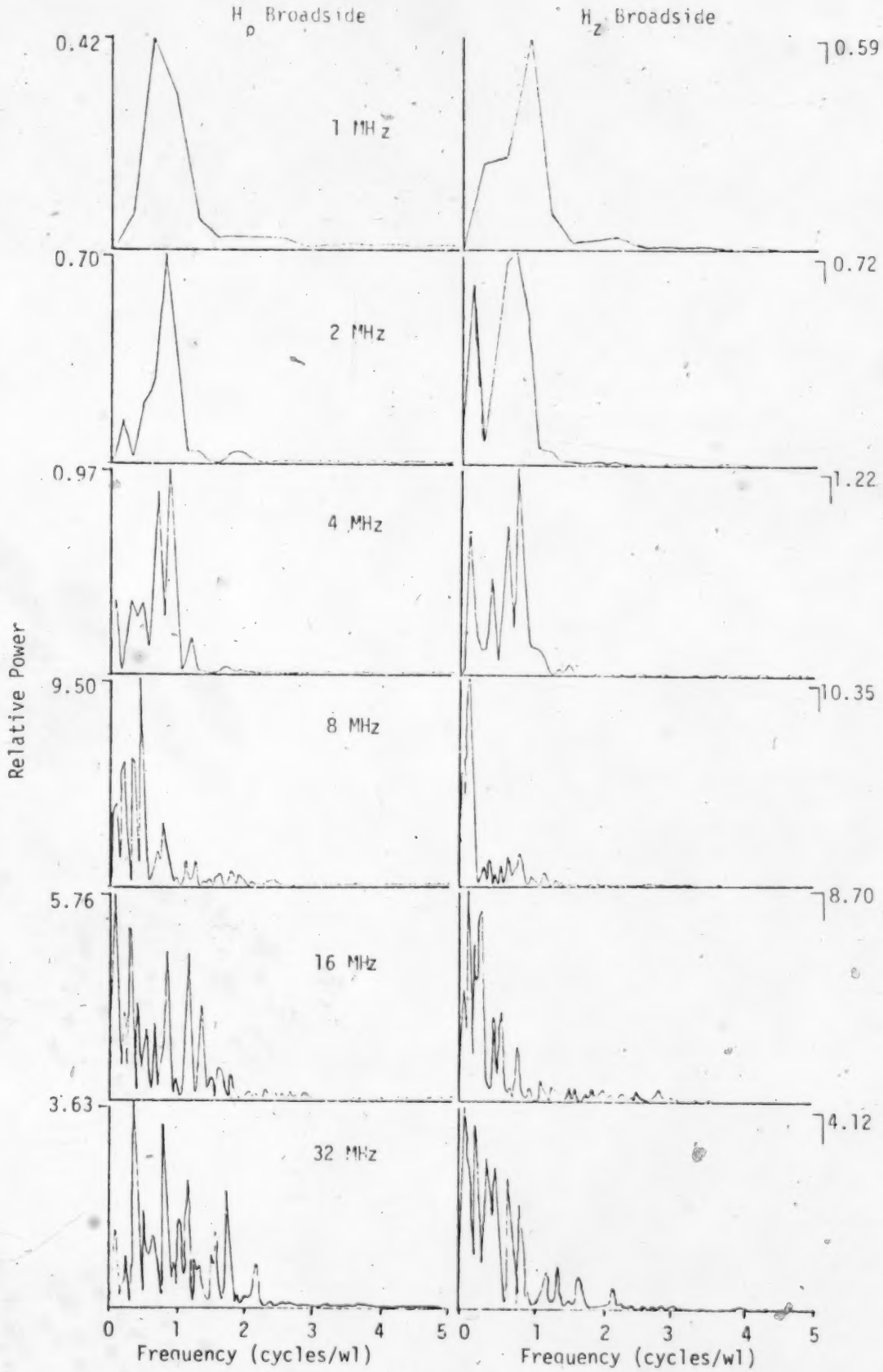

Figure 4-3. FFT power spectra, Athabasca Glacier, run 71. Relative amplitudes are indicated.

the power spreads to higher spatial frequencies. It is difficult to assign a consistent dielectric constant to the ice from the FFT spectra, since the peaks are fairly broad. However, using maximum entropy spectra, the dielectric constants given in Table 4-1 (a) were estimated. There is a systematic difference between the estimated dielectric constants for the up-dip runs (59 and 71) and the down-dip run (25) -- the former are higher than the known value for ice of 3.2 to 3.3, while the latter is lower (Fig.4-4). This difference is attributed to the shift of the beat frequency by the tilted bottom reflector, due to increasing ice thickness up-glacier. Using the rule of thumb developed in section 2.2, a tilt of +.05 to +0.7 would be assigned to run 25, and tilts of about -.03 and -.05 to runs 59 and 71 respectively. Using these values gives a more consistent dielectric constant, as shown in Table 4-1 (a).

Assigning different tilts to runs 25 and 71 is not inappropriate. The tilts represent increasing thickness of ice away from the snout of the glacier. Seismic work shows that this increase is greatest near the snout, whereas further up the glacier the increase becomes relatively small.

Depths to the bottom of the glacier were estimated using equation 2-19, both for no tilt, and for the tilts estimated from the spectral shift. The first major peak in the envelope of the interference curve, as shown in Figure 4-5, was used to interpret the depth. At frequencies below 4 MHz there was usually no clear peak, and at frequencies above 8 MHz the curves became erratic. The results, given in Table 4-1 (b), are reasonable for the

Table 4-1: Athabasca Glacier -- 2-layer interpretation

Frequency (MHz)	Run 25			Run 71		Run 59	
(a) Dielectric Constant (using maximum entropy spectral peaks)							
Tilt:	0.0	+ .05	+ .07	0.0	- .05	0.0	- .03
1 H_ρ	3.4	3.6	3.7	3.2	3.1	3.5	3.4
1 H_z	3.4	3.6	3.6	3.9	3.7	3.8	3.7
2 H_ρ	2.8	2.9	3.0	3.3	3.2	3.2	3.2
2 H_z	3.2	3.4	3.5	3.4	3.2	3.2	3.0
4 H_ρ	2.6	2.8	2.9	3.4	3.2	3.3	3.2
4 H_z	2.8	2.9	3.0	3.6	3.4	3.4	3.2
Average	3.0	3.2	3.3	3.5	3.3	3.4	3.3
(b) Ice thickness (m) (using k_1=3.3 and peaks of envelopes ± 1 wl)							
4 H_ρ ± 40	--	--	--	213	245	--	--
4 H_z	307	266	250	233	268	--	--
8 H_ρ ± 20	219	189	179	264	304	239	260
8 H_z	278	241	227	--	--	239	260
Average	268	232	219	237	272	239	260
(c) Loss tangent (using decay of envelopes)							
2	----			.10 - .20		----	
4	.02 - .06			.06 - .12		.01 - .02	
8	.02			.02 - .04		.07 - .08	
16	.02			.02		.03 - .07	
(MHz^{-1}) Average	----			0.30 ± .10/f		0.45 ± .1/f	

Figure 4-4. Maximum entropy power spectra, Athabasca Glacier, run 71. Arrow indicates peak chosen for dielectric constant estimate.

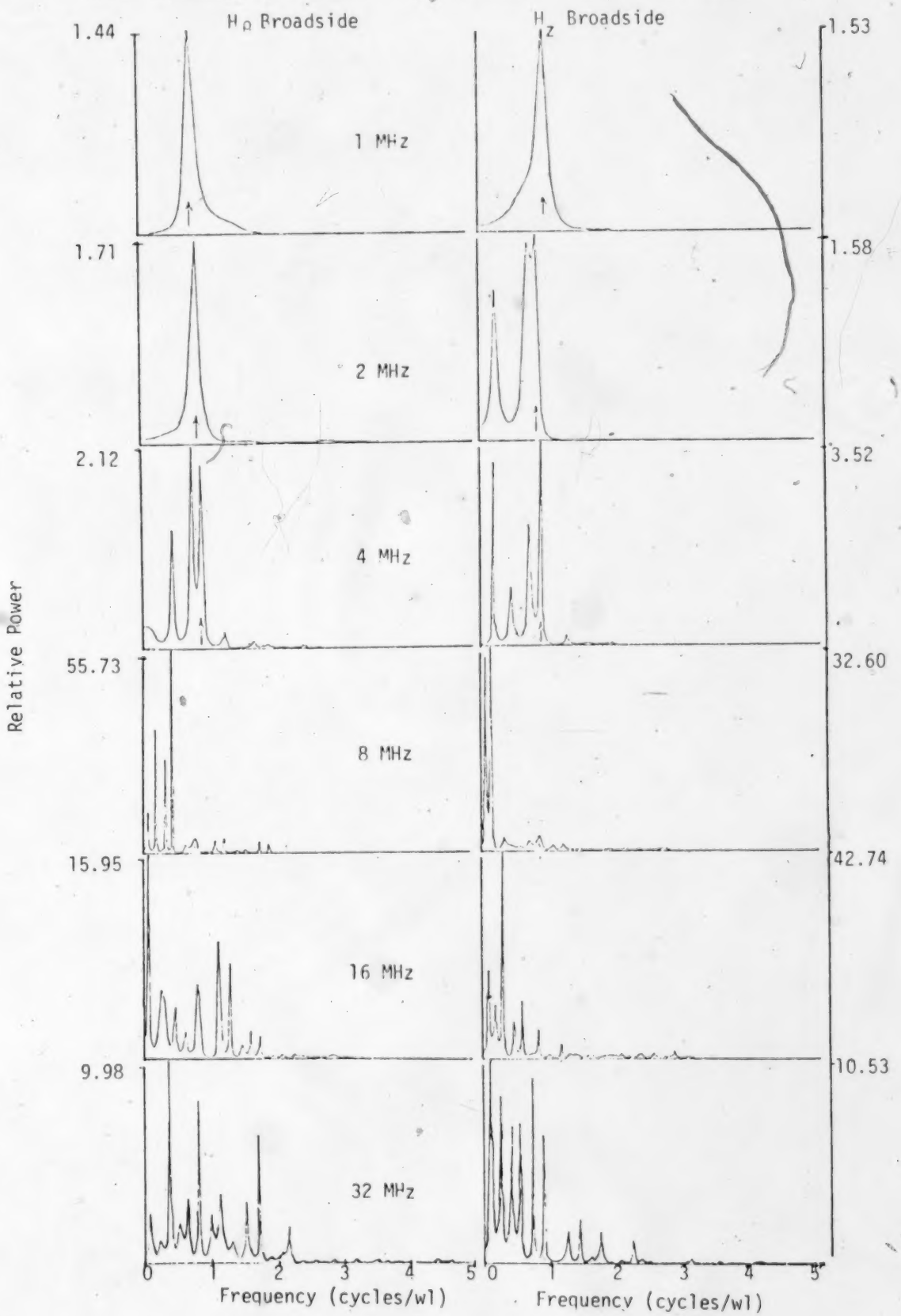

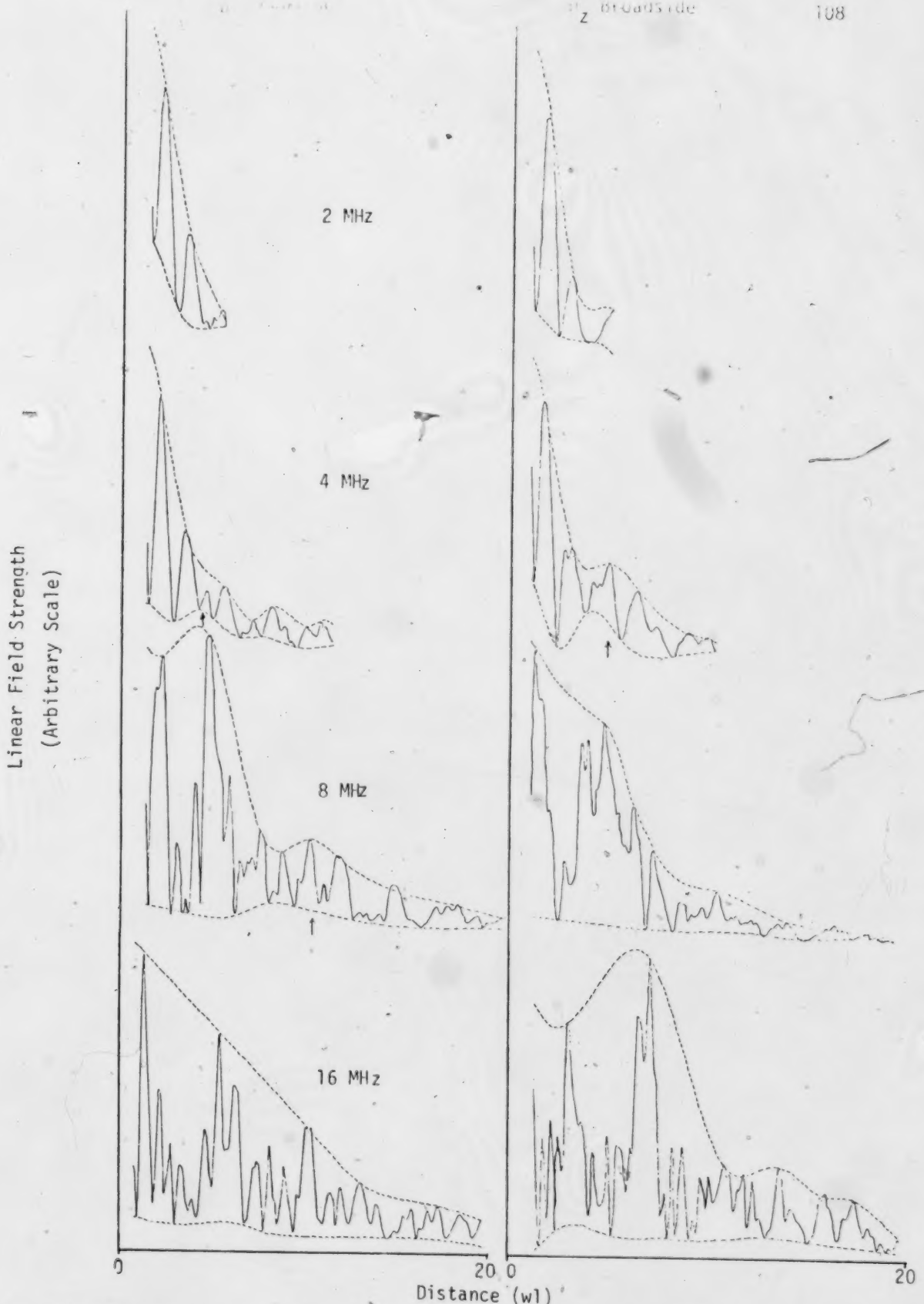

Figure 4-5. Envelopes (---) of interference curves(——), Athabasca Glacier, run 71. Arrow indicates peak used for [illegible]

glacier, and are much more consistent with previous work when the correction for a glacier thinning toward its snout is included. The thickness of ice in the centre of the glacier (from seismic work) is about 300-320 m, considerably greater than the estimate from run 59. However, the peak in the envelope was not very strong for this run, so that the estimated value could be considerably in error.

The loss tangent of the ice was also estimated from the envelope. Previous work (Evans, 1965) has shown that the loss tangent for ice at $0^{o}C$ is given by $\tan \delta = .3/f$, where f is frequency in MHz. At 1 MHz there were not enough data points to adequately form the envelope, and at 16 and 32 MHz the curves did not decay smoothly. There is also quite a bit of variation in the estimates (Table 4-1 (c)), but it is interesting that the losses generally show the expected frequency-dependent behaviour.

The scattering parameters for the Athabasca runs are given in Table 4-2. The overall scattering level, Table 4-2 (a), is low at 1 and 2 MHz, increasing slightly at 4, and markedly at 8 MHz, and is very high at 16 and 32 MHz. The apparent drop-off in the scattering level at 32 MHz is probably due to the fact that using early prototypes of the hardware the highest radio frequencies were insufficiently sampled. Hence, at 32 MHz the full range of spatial frequencies is not present, as seen in Figure 4-3. This loss affects the scattering amplitude which is based on the level of the higher spatial frequencies. (The problem was corrected in later

Table 4-2: Athabasca Glacier -- Scattering Parameters

Frequency (MHz)	Run 25	Run 71	Run 59
(a) Overall scattering amplitude (from H_ρ & H_z broadside) ± 25% 1.0 - 5.0 cycle/wl filter.			
1	.15 - .20	.15 - .17	.14 - .30
2	.16	.16 - .18	.19 - .24
4	.24 - .30	.35 - .38	.31 - .60
8	.47 - .49	.45 - .78	.74 - .90
16	.98 -1.2	1.0 -1.4	.99 -1.2
32	.77 - .91	.91 -1.3	.71 - .85
(b) Surface scattering amplitude (from H_ϕ endfire) ± 25% 1.0 - 5.0 cycle/wl filter			
1	.09	.02	.17
2	.04	.05	.14
4	.09	.03	.08
8	.11	.11	.26
16	.48	.45	.69
32	.74	.57	.70
(c) Separation of maximum and minimum components (dB)			
1	10	9	11
2	13	11	15
4	14	14	17
8	6	13	11
16	4	5	5
32	0	0	2

models of the hardware, and does not appear in data collected after the end of 1972.) See also Fig. 4-6.

The surface scattering level, from the H_ϕ endfire component, Table 4-2 (b), is generally low up to 8 MHz, increasing at 16 and 32 MHz. The surface of the glacier was in fact very rough, with many crevasses with dimensions of 1 to 10 m. Runs 25 and 71 were made along a "road" that had been graded for a commercial snowmobile tour, and many other parts of the glacier were too rough to be accessible to the interferometry vehicle. It is interesting, therefore, that run 59, made in the centre of the glacier where the crevassing was heavy, shows the surface scattering level increasing at 8 MHz, instead of at 16 MHz.

The component separation, Table 4-2 (c), shows considerably lower values than that from the scale model. The level never exceeds 15-20 dB, and drops off to 0 dB at the highest frequencies. The separation decreases fairly smoothly from 1 to 32 MHz, except that at 1 MHz it is slightly smaller. This effect is because the field strength at 1 MHz quickly reaches the receiver background noise level, which is of course about the same for both maximum and minimum components. The overall low separation is attributed to lateral effects from the sides of the glacier, which are clearly not horizontal plane interfaces (Fig.4-2). This interpretation is consistent with the fact that the levels from run 59 are slightly greater. The decrease in the level with increasing frequency is attributed to the increasing effect of random

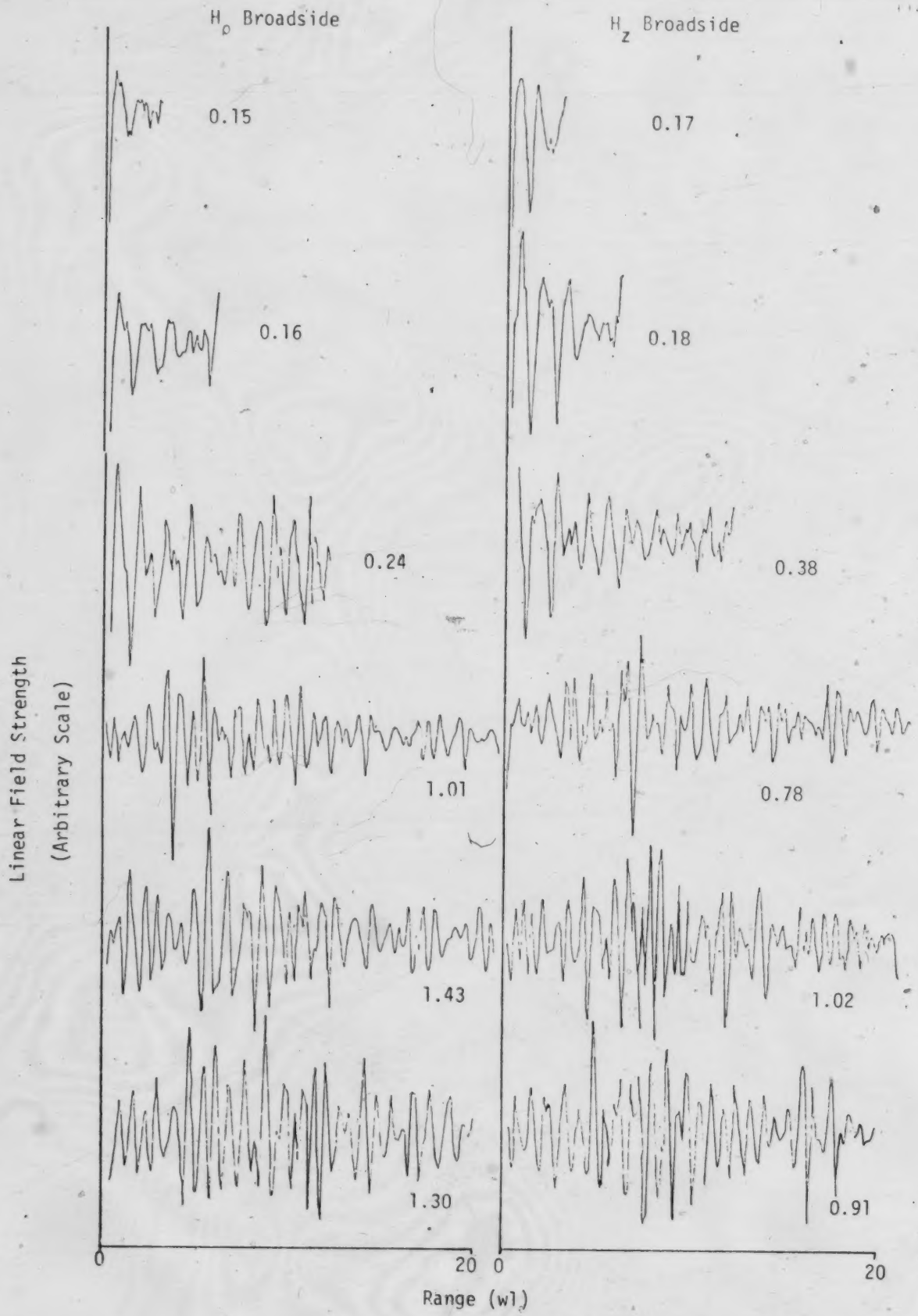

Figure 4-6. Amplitude of interference curves, 1-5 cycle/wl filter. Relative amplitudes are shown. A r^{-2} decay has also been removed.

scattering, as discussed above.

Using 8 MHz as the frequency at which scattering becomes significant, a typical scatterer size of about 6 m is estimated, with some scatterers slightly larger. Comparing the maximum scattering level to those of the scale model, gives a scatterer separation:size ratio of about 1 or 2. Therefore the separation on a plane would be about 6 to 12 m, and if the scatterers were spread throughout the volume of the glacier, they would be separated by about 14 to 33 m. This interpretation is consistent with the observed surface inhomogeneities which have these kinds of dimensions. The question of whether or not these represent all the scattering bodies will be discussed later.

Therefore, the layered model interpretation for the thickness, dielectric constant and loss tangent of the glacier have been determined, at least roughly, directly from the data. The values obtained are consistent with those determined by curve fitting (Strangway et al., 1974), but were obtained in a less subjective manner. Also, ice thickness variation along the traverse has been explicitly accounted for. Random scattering effects are clearly important in the results, and they will be compared to those from another temperate glacier in the following section.

4.3 Juneau Icefield

Radio interferometry measurements were made on the Juneau Icefield, Alaska in 1972. Although this is a huge icefield, made up of many glaciers, three main areas will be examined (shown in Fig.4-7): run 36, made at site 6 in the middle of the Taku Glacier, running approximately north-west; run 92, made from site 25 in the accumulation zone of the Matthes Glacier; and run 84, across Icy Basin from approximately site 22A.

Preliminary results from runs 36 and 92 have been published previously by Rossiter et al.(1975) who discussed an intriguing feature seen in most of the Juneau data -- that there is very little interference at about 4 MHz. This was satisfactorily explained by examining the effect of a snow layer 15 to 20 m thick overlying an infinite half-space of ice. The layer is essentially transparent to the longer wavelengths, but is thick enough to support propagating modes at the higher frequencies. Near 4 MHz there is a transition region in which the snow layer effectively decouples the underlying ice, but at the same time is too thin to support propagation.

However, each of the Juneau runs presents somewhat different data. In run 36, the decoupling is essentially complete at 4 MHz, whereas there is a slight amount of interference seen at 4 MHz in run 92, and considerable interference seen in run 84. These differences are probably due to differing snow-ice properties, and it was postulated by Rossiter et al. (1975) that the snow layer

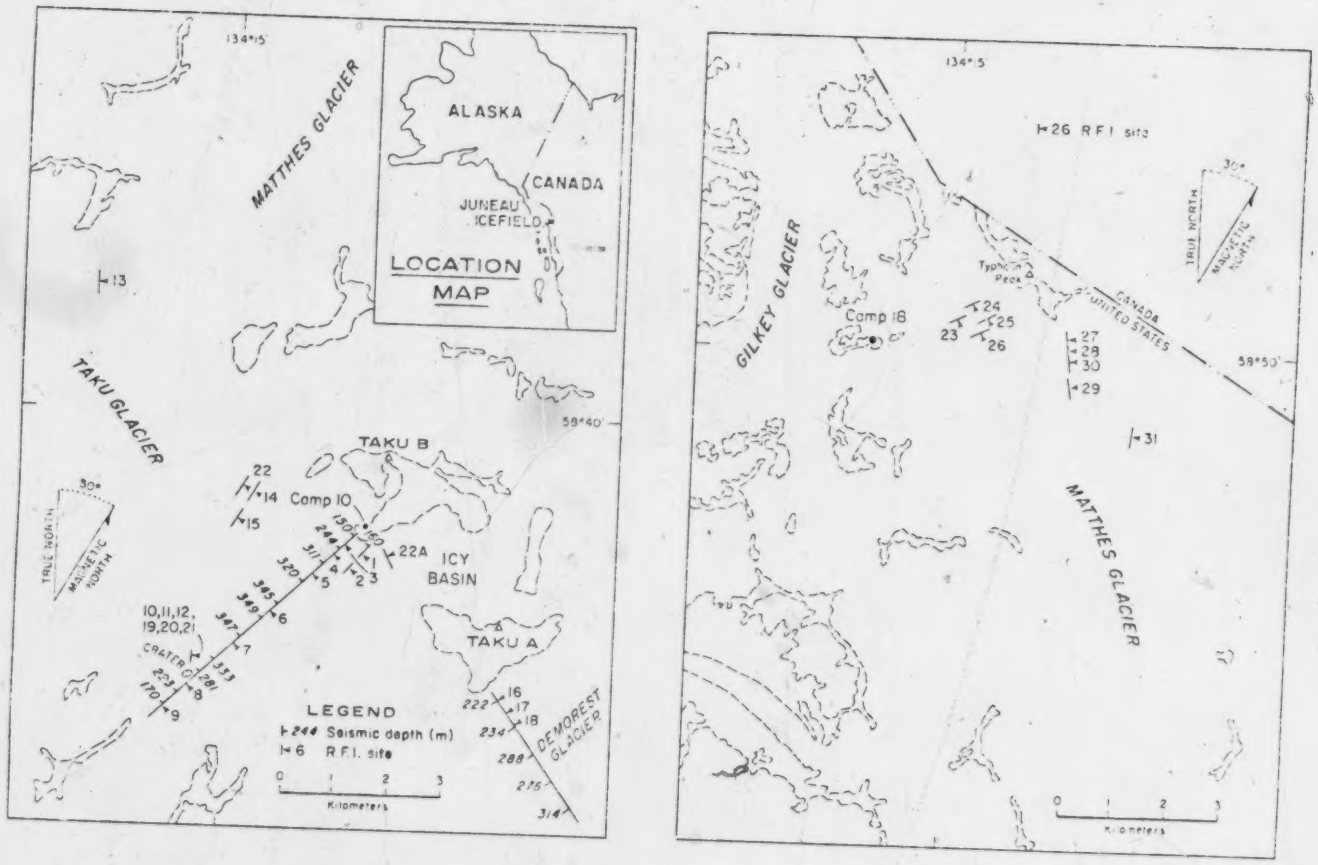

Figure 4-7 Juneau Icefield, Alaska (after Rossiter et al., 1975). Run 36 was made approximately NW from site 6 and run 84 across Icey Basin from site 22A (left). Run 92 was made at site 25 (right). There is a gap of 2 km between the top of the map on the left and the bottom of the map on the right.

graded into ice, giving a fair amount of variability in the estimate of the snow thickness.

The FFT spectra contain much the same information. There is a clear spectral peak between 0.5 and 1.0 cycle/wl at 1 and 2 MHz, little energy at 4 MHz, and several peaks at 8, 16 and 32 MHz, both below 0.5 cycles/wl, due to interfering modes within the snow, and above 1 cycle/wl, due to scattering.

Using maximum entropy spectra, the peaks at the lower frequencies were used to estimate the dielectric constant of the ice (Table 4-3 (a)). For runs 36 and 84 the estimates are somewhat high for ice. Since there are no independent measurements of ice thickness variations, nor are there up and down dip traverses, it is difficult to assign reasonable estimates to the tilt of the glacier bottom. In fact, the overall indication from the vicinity of run 36 (see Fig. 4-7) is that the Taku Glacier increases in thickness toward the north-west. This is contrary to the dip that would be assigned by adjusting the spectral lines in run 36 to give a dielectric constant of 3.2 or 3.3. Moreover, the glacier is quite deep in that location, about 350 m, and it is not likely that the bottom would exert a large influence.

Assuming that the dielectric values are as high as estimated, an alternative explanation is that the glacier ice contains a significant amount of water. The Lichtenecker mixing formula is commonly used to determine the bulk dielectric constant of a mixture of several dielectrics (Von Hippel, 1954, p. 231),

Table 4-3: Juneau Icefield -- layered interpretation

Frequency (MHz)		Run 36	Run 92	Run 84
(a)	Dielectric constant (ice layers) (Tilt =0)		± 0.2	
1	H_ρ	3.06	2.96	3.06
1	H_z	3.88	3.31	3.88
2	H_ρ	3.80	3.03	3.46
2	H_z	3.61	3.39	3.46
4	H_ρ	--	3.20	3.61
4	H_z	--	3.35	3.89
	Average	3.6	3.2	3.6
(b)	Ice thickness (m) (using k_1=3.3 and peaks shown on page 117a)			
2	± 75	375	--	--
4	± 40	330	318 - 330	230 - 240
8	± 20	--	225	200 - 220
(c)	Loss tangent	(using approximate decay of envelopes)		
2		.08	.10 - .15	--
4		--	.09 - .10	--
8		.02	.03 - .05	.04 - .07
16		--	.02 - .03	.03 - .06
32		--	--	.008
Average (MHz^{-1})		0.16/f	.034 ± .06/f	0.5 ± .2/f

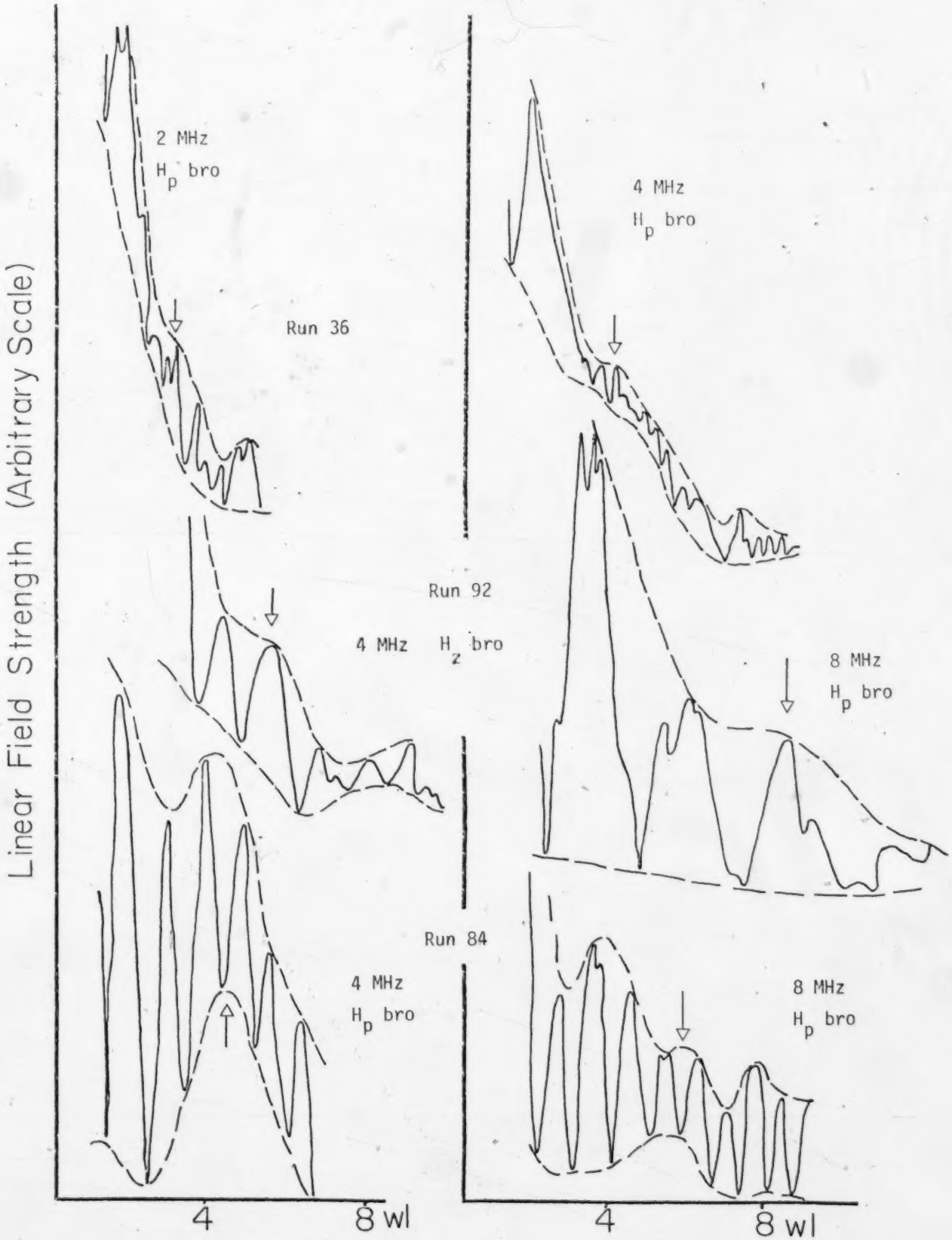

Arrow indicates position of peak used for depth estimates.

$$K_m = \prod_{i=1}^{n} k_i^{V_i} \qquad (4)$$

where K_m is the bulk dielectric constant of a material composed of n different constituents, each with a dielectric constant of K_i and a volume fraction V_i. Using $K_1 = 3.2$ and $K_2 = 81$, for ice and water respectively, only about 3 to 4% water is required to increase the bulk dielectric constant of the glacial ice to 3.5 or 3.6. (The fact that the water might act as a random scattering agent will also tend to increase the effective dielectric constant, as shown in Chapter 3. However, as shown, this effect would be slight compared to the mixing effect.) The addition of a slight amount of liquid water to the ice would also explain the fact that a dielectric constant of 3.3. gave the best overall fits to the data from the Athabasca Glacier.

It is therefore interesting that the results from run 92 do not show a higher dielectric constant. This run was made in a higher and colder region of the Icefield. Rossiter et al. (1975) obtained better fits of theoretical curves to the curves from this run if a lower loss tangent was used, which is consistent with a colder environment and less free water.

Run 84, made across Icy Basin, is unique among interferometry results collected to date. At 4 and 8 MHz there are strong spatial frequencies well above the values that could reasonably be expected for the dielectric constant of ice, as shown in Fig. 4-8. These are

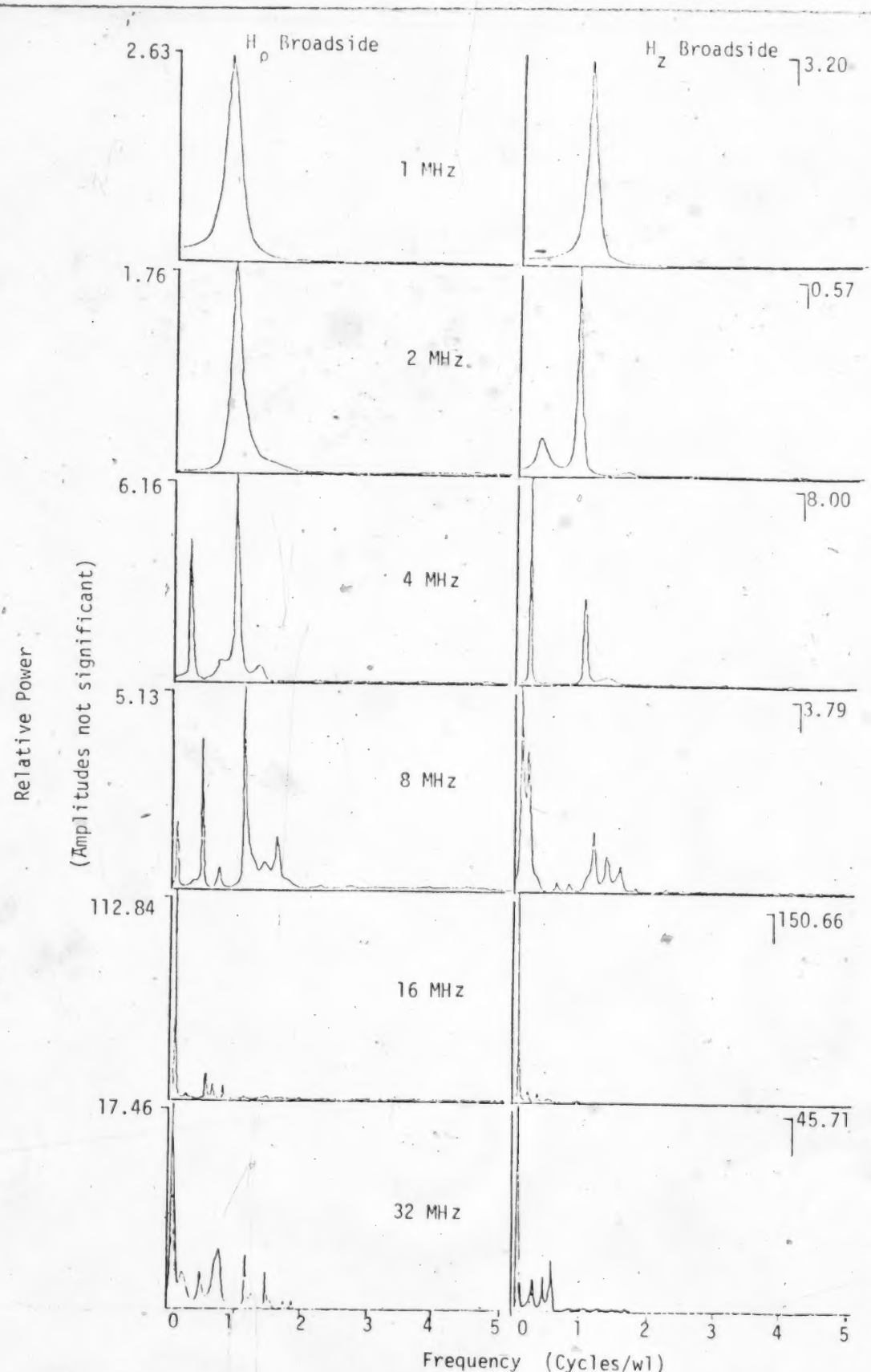

Figure 4-8. Maximum entropy power spectra, Icy Basin, Juneau. Run 84. Note higher spatial frequencies than in Figure 4-4.

not attributed to random scattering, since the interference peaks are very regular (see Appendix 2). It is postulated that this interference is of a rather peculiar nature -- that it is beating between a wave in the snow layer and some of the higher order modes in an ice layer about 200 m thick. This hypothesis remains unproven, since three-layer theoretical solutions are not readily available, but it is conceivable that a relatively thin upper layer favours particular modes in the lower layer.

The rate of beating is given by

$$f_b = \frac{\Delta k}{2\pi} \lambda_o \qquad (5)$$

where f_b is the beating rate (cycles/wl),

Δk is the difference in radial wavenumbers (m^{-1}),

and, λ_o is the free-space wavelength (m).

At 4 MHz, there is a spectral line at about 1.22 cycles/wl, indicating a Δk of 0.102 m^{-1}. A calculation of the possible radial wavenumbers supported by a layer with a dielectric constant of 3.6 and a thickness of 200 m (see Chapter 3) indicates that the highest propagating mode has a wavenumber of 0.025 m^{-1}. A thin layer with a dielectric constant of 2.5 would have a wavenumber of 0.133 m^{-1}, giving $\Delta k = 0.108\ m^{-1}$, very close to that required. At 8 MHz, it is not quite so easy to get the large wavenumber differences required for the high beating rates observed. However, because the waveguide is effectively twice as thick as at 4 MHz, even higher order modes are able to propagate.

Therefore, although this explanation of the rapid beating rates at 4 and 8 MHz in run 84 remains unproven, it does appear to be feasible.

Using the envelopes of the curves to calculate the ice thickness and loss tangent gave the results presented in Table 4-3 (b) and (c). There are only a few estimates because the records are short at the lowest frequencies, are dominated by propagation in the upper snow layer at the higher frequencies, and have little interference at 4 and 8 MHz. However, within these constraints, the values are at least reasonable. For run 36, the ice thickness from seismic sounding is 350 m (Fig. 4-7), but at the other sites there are no independent checks. The loss tangent values follow the pattern of decreasing with increasing frequency typical for ice, but the range of the estimates is fairly large.

The scattering parameters for the Juneau runs are given in Table 4-4. Scattering appears to be low at the lower frequencies, increasing slightly at 8 MHz, and is quite high at 16 MHz. The apparent drop-off at 32 MHz is probably due to low sampling rates (as discussed with the Athabasca Glacier data). The surface scattering also increases with frequency, but not as quickly. The surface of the ice was quite smooth, partly because of the overlying snow layer, but the snow could also have masked crevasses in the top surface of the ice layer.

The separation of the maximum and minimum coupled components

Table 4-4: Juneau Icefield -- Scattering Parameters

Frequency (MHz)	Run 36	Run 92	Run 84
(a) Overall scattering amplitude (from H_ρ & H_z broadside) ± 25% 1.0 - 5.0 cycle/wl filter			
1	.23	.15 - .18	.14 - .21
2	.16 - .17	.21 - .27	.13 - .23
4	.22 0 .24	.17 - .25	.33 - .45
8	.54 - .57	.33 - .36	.42 - .57
16	1.03 -1.67	.66 -1.0	.48 - .82
32	.57 - .86	.50 - .92	.89 -1.0
(b) Surface scattering amplitude (from H_ϕ endfire component) ± 25% 1.0 - 5.0 cycle/wl filter			
1	.19	.25	.21
2	.29	.08	.22
4	.24	.06	.14
8	.15	.14	.32
16	.37	.31	.18
32	.44	.22	.43
(c) Separation of maximum and minimum components (dB)			
1	14	15	15
2	19	20	22
4	22	25	20
8	13	18	20
16	6	12	13
32	6	5	10

also decreases with increasing frequency. Since the ice in the Juneau region appears to be considerably thicker than for the Athabasca Glacier (at least for run 36), and since the region generally was larger, the effects of lateral inhomogeneities are almost certainly less. As a consequence, the component separation is consistently greater, reaching a minimum of 5 to 10 dB. The conclusion is that the decrease with increasing frequency is largely due to depolarization of the components by random scatterers.

Using the rules of thumb from Chapter 2, the mean scatterer size would be about half that of those in Athabasca Glacier, or about 3 m in diameter, with some scatterers somewhat larger. The separation:size ratio for the scatterers would not be much different, so that if they were spread over a plane, they would be about 3 to 6 m apart. If they were uniformly spread over a layer of ice 350 m thick, they would be typically about 15 to 23 m apart.

Without discussing possible features that cause this type of scattering in glaciers, which will be left to the next chapter, it is clear that there are inter-glacier differences. The scattering becomes important at 8 MHz in the Athabasca Glacier results, but at 16 MHz in the Juneau, indicating larger scatterers in the former location. Certainly surface scattering is greater in the former as well, but in probably neither case is it large enough to account for the total amount of scattering seen.

4.4 Taurus-Littrow valley of the Moon

Radio interferometry data were collected by the crew of Apollo 17 on the Taurus-Littrow valley of the Moon in December 1972, as the Surface Electrical Properties (SEP) Experiment. The site is shown in Fig. 4-9. The antennas were laid east-west and north-south on the lunar surface, and the traverse was made during EVA II slightly to the south of west. Although data were collected out to a range of 4.3 km, only the first few hundred meters of data are significant.

Preliminary interpretations of the data were presented by the SEP Team (1973), and have been briefly discussed by Strangway and Olhoeft (1977). A more comprehensive paper is in preparation (Strangway et al., 1977). Essentially the data (Appendix 4) are consistent with a 4-layer model to describe the surface of the moon. All the layers are exceedingly dry, and therefore have low loss tangents(on the order of 0.01), but have dielectric constants increasing with depth, consistent with increasing rock density. The dielectric constant increases from about 3 near the surface to greater than 10 below about 100 m. The layers are interpreted as loose soil, unconsolidated regolith, fractured rock, and unfractured rock, respectively. In addition, the regolith appears to be about 20 m thick near the transmitter, thinning to about 10 m several hundred meters west.

The spectra (Fig. 4-10) show the basic rationale behind this interpretation. The beating rates are higher (1 to 2 cycles/wl) at

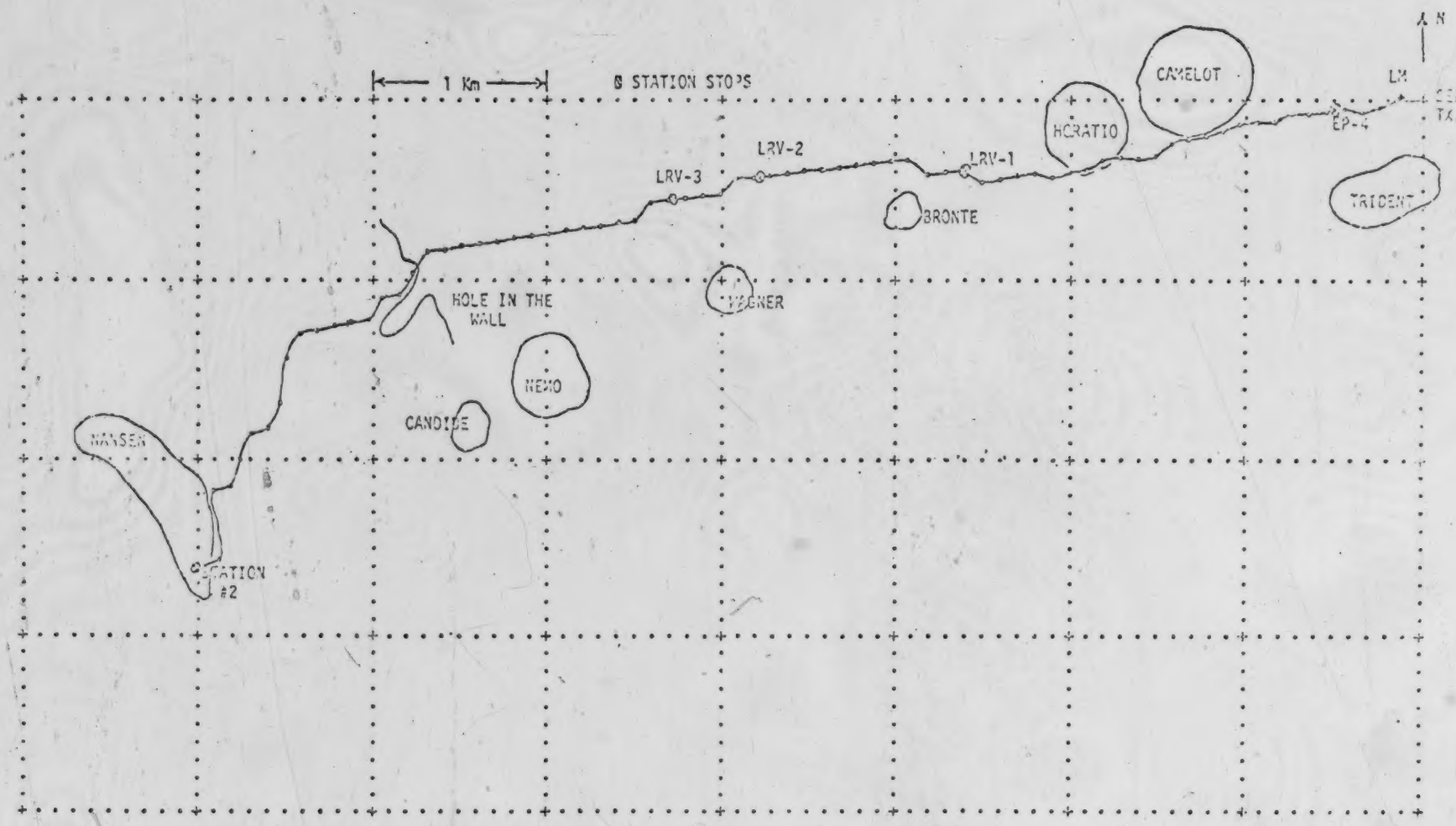

Figure 4-9 : SEP Traverse Reconstruction - Taurus-Littrow valley of the moon (after Strangway et al, 1974(a)).

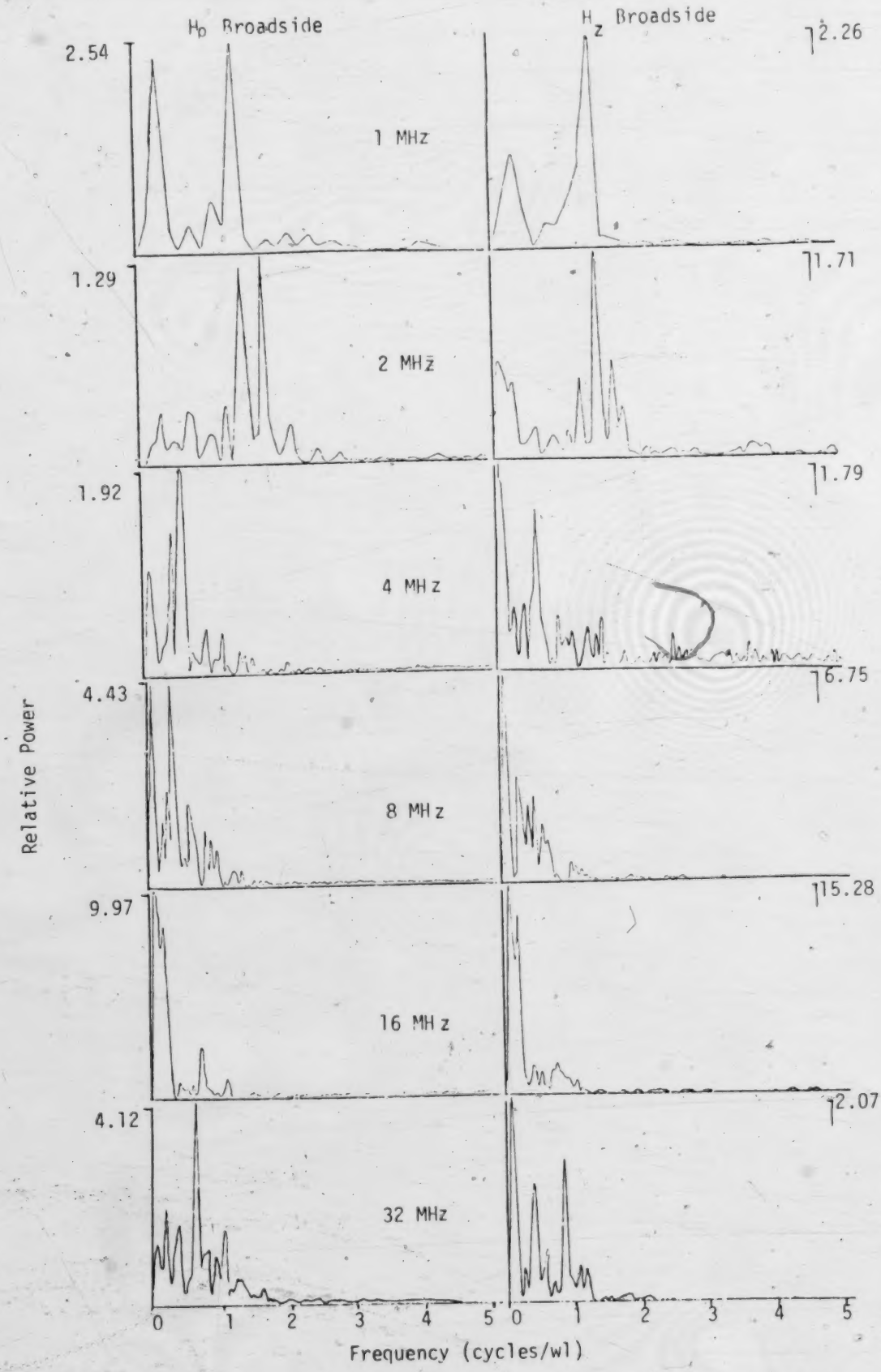

Figure 4-10. FFT power spectra, Taurus-Littrow Valley. Note generally decreasing spatial frequencies for higher radio frequencies. Broad-band response in 4 MHz H Broadside is due to a spike in the raw data curve (see Appendix 4)

the lower frequencies, which penetrate the deeper material. These rates decrease to less than 1 cycle/wl at the lower frequencies, which are most sensitive to the upper material. There are no frequencies at which no interference is seen, as found in some of the Juneau Icefield data.

Clearly the interpretation procedure developed for two-layer models can only be applied in a limited way to this set of data, particularly since there is the possibility of rather complex interactions between modes propagating in different layers. A theoretical solution to the multiple-layer interferometry problem is being formulated by A.P. Annan (private communication), and this will be required to resolve the layered interpretation. However, by doggedly applying the principles developed previously, perhaps we can understand some of the constraints imposed by the data.

The maximum entropy spectra have several distinct lines at virtually all frequencies, so that it is not possible to separate the effects due to dielectric constant interference and inter-layer mode beating. However, using the highest major peak, the dielectric constants presented in Table 4-5 (a) were calculated. The trend is certainly from values of about 6 to 8 at 1 and 2 MHz, to values of about 4 at the 16 and 32 MHz. The dielectric constant at 2 MHz appears to be higher than at 1MHz, and this is probably a spurious result due to a deep reflector.

Examining envelopes of the interference curves (Table 4-5 (b)) gives a reasonably consistent layer 500 to 700 m deep. This is

Table 4-5: Lunar data -- layered interpretation

Frequency (MHz)	H_ρ - broadside	H_z - broadside
(a) Dielectric constant (from highest major spectral line)		
1	5.71 ± 0.3	5.86 ± 0.3
2	7.78	8.18
4	5.81	6.00
8	5.38	5.29
16	4.33	4.08
32	4.16	4.58
(b) Depth to reflector (m). (Using dielectric constants calculated above -- see text.		
1	±150	525	625
2	± 75	695	635
4	± 40	695	--
8	± 20	--	160
16		--	--
32	± 5	39	46
(c) Loss tangent.		
1	.04 - .08	.08 - .12
2	.01 - .04	.05 - .13
4	.01 - .03	.03 - .04
8	.04 - .06	.02
16	.02 - .10	.07 - .10
32	.01 - .02	.04 - .05

considerably deeper than the top of the solid rock interface, postulated by initial fits to the data, and this point needs to be examined with more elaborate theoretical models. At 8 and 16 MHz there are no consistent peaks in the envelope curves from which to make depth estimates. At 32 MHz a reflector about 30 to 45 m deep is indicated, but again this needs to be examined more thoroughly.

The loss tangent estimates are given in Table 4-5 (c). They range from about 0.01 to 0.10, with possibly a slight increase with decreasing frequency. This frequency dependence would most likely be associated with increasing penetration depth, and is therefore consistent with a slightly greater loss in the denser, underlying material (Olhoeft and Strangway, 1975).

In summary, the layered structure does not appear to be simple. Compared to other interpretations, deeper reflectors, both for the solid rock interface and for the bottom of the regolith, are suggested. The large number of distinct spectral lines indicates the importance of full multi-layer solutions for a satisfying interpretation.

The scattering parameters for this run are given in Table 4-6. Because of the higher dielectric constants of the lunar surface material, the filter passband for scattering amplitudes was rather arbitrarily set to 2.0 to 5.0 cycles/wl, so that results are not directly comparable to other runs. If a lower cut-off spatial frequency is used, coherent energy is added into the estimates of the non-coherent energy. However, the results are still internally

Table 4-6: Lunar data -- Scattering parameters

Frequency (MHz)	H_ρ - broadside	H_z - broadside
(a) Overall scattering amplitude: 2 - 5 cycle/wl filter. ± 25%		
1	.39	.26
2	.30	.24
4	.13	.13
8	.21	.20
16	.15	.30
32	.30	.20
(b) Surface scattering (H_ϕ -endfire) 2 - 5 cycle/wl filter. ± 25%		
1	.21	
2	.11	
4	.05	
8	.05	
16	.10	
32	.17	
(c) Separation of maximum and minimum components (dB)		
1	12	
2	13	
4	13	
8	13	
16	11	
32	7	

comparable from frequency to frequency. It appears that there is no significant increase of scattering amplitudes, even to 32 MHz, for both overall and surface scattering. The conclusion is that there must be very few objects of sizes greater than about 1 to 2 m within or on the regolith which act as effective scatterers.

The only hint that scattering might become important at higher frequencies is the slight decrease in the component separation at 32 MHz (Table 4-6 (c)). Hence, it is possible that there are scatterers, such as boulders, that would be important at frequencies above those used in this experiment. It is also interesting that the component separation is not very large in this set of data, being much closer to that from the Athabasca Glacier than to that from the Juneau Icefield. Mixing of the components by the off-axis lunar traverse may explain this low separation, since the traverse was up to 6^{o} south of west, on the average, out to 1 km. This angle could decrease the separation by up to 20 dB, assuming an initial separation of 40 dB. However, the relatively low level of component separation could also be due to lateral inhomogeneity at the Taurus-Littrow site (see Appendix 3).

Taurus-Littrow valley lies to the east of Mare Serenitatis, an old impact basin. The valley is considered to be a graben radial that was formed at the time of the Serenitatis event (Muehlberger et al., 1973). Gravity and seismic data (Talwani et al., 1973; Kovach et al., 1973; Kovach and Watkins, 1973; Cooper et al., 1974) indicate that there is considerable lateral inhomogeneity in the

narrow arm of the valley that leads to Mare Serenitatis, caused both by the walls of the North and South massifs on either side of the valley, and by step-like structure of the basement along the length of the valley. The former structure might explain the SEP component separation, in a very similar way to the Athabasca Glacier results.

It is clear that there are striking differences between the lunar data and the glacier results. The former show a much more complicated layered structure, but negligible scattering, while the latter show relatively simple layered geometries, but considerable scattering within the frequency range used. The lunar data indicate low EM losses for the lunar surface material, whereas the temperate glacier ice has a frequency -dependent loss that limits the ultimate depth of penetration. Lateral inhomogeneity effects are observable in the Athabasca data, and possibly the lunar results, but not in the Juneau data.

4.5 Conductive regions

Interferometry data were collected at two other sites which were essentially conductive half-space earths for the interferometry measurements. The sites were a region of permafrost, near Tuktoyaktuk, N.W.T., and a frozen lake, near Sudbury, Ontario. The received signals from these two areas decay smoothly, with little or no interference (Appendix 4). Since data from these areas should show virtually no scattering, they are limiting full-scale examples to compare with the previous results.

The work in the Arctic was part of a program to examine the usefulness of a number of different EM techniques for studying permafrost. It was originally thought that the permafrost might be resistive enough to allow successful interferometry sounding. Measurements were made at the Involuted Hill test site set up by the Geological Survey of Canada, and runs were made both on the ice-cored Hill (runs 2 and 15) and on the permafrost flats to the south (runs 3 and 19). Measurements were made both in summer (August 1974) and winter (March 1976), in order to be able to isolate effects of the active layer which is unfrozen in the summer.

Although the interferometry sounding results were largely negative, a slight degree of interference can be detected at 16 and 32 MHz in some runs. This fact has been used to estimate the dielectric constant and conductivity of the permafrost (Rossiter et al., 1978), and the values of 6 and 5×10^{-4} S m^{-1} respectively are in agreement with other work (e.g. Wong et al., 1977; Olhoeft, 1977).

The poor penetration appears to be due entirely to the conductivity of the permafrost, and not to the presence of a conductive melted layer on the surface, since the summer and winter curves are similar. This is consistent with impulse radar measurements made at the same site (Annan and Davis, 1976).

Because of the lack of interference, giving very weak spectra and no useful envelopes, further layered interpretations were not attempted. However, the scattering amplitude and component separation were calculated (Table 4-7). The scattering is low, and is comparable to model data with no scatterers. The component separation is not as great as expected, partly because in many cases the signal levels went down to the noise level of the receiver. The high variability in the derived data is apparent.

The other conductive region, Lake McFarlane, near Sudbury, was studied while it was ice-covered during April 1975. Only the higher frequencies were recorded. Again there is very little interference. The run to the south (run 2) went onto the shore, and even this feature is not apparent in the data. No interference was expected due to modes propagating in the ice itself, because the ice was too thin (0.6 to 0.8 m) to support modes even at 32 MHz, for which it would need to be greater than about 2 m thick (Annan et al., 1975). Nor was any interference seen in the data from the water layer before re-digitization at 10 samples/wl. Since water has a dielectric constant of 81, at least 16 samples/wl are required to avoid aliasing (data were collected with very high

Table 4-7: Scattering parameters from conductive regions

Frequency	T02	T03	T15	T19	S01	S02
(a) Overall scattering (H_ρ and H_z broadside) 1.0 - 5.0 cycle/wl filter ±25% *						
1	.07-.25	.07-.18	.23-.28	.13-.36	--	--
2	.37-.56	.11-.38	.37-.39	.10-.42	--	--
4	.23-.56	.06-.11	.19-.32	.08-.28	--	--
8	.31	.02-.11	.11-.30	.04-.09	.06-.07	--
16	.23-.30	.14-.32	.05-.07	.08-.10	.09	.08-.13
32	.24-.30	.30-.34	.10-.26	.07-.14	.11-.14	.11-.13
(b) Surface scattering amplitude (H_ϕ -endfire) ± 25%						
1	.07	--	.18	.27	--	--
2	.10	--	.20	.09	--	--
4	.12	--	.12	.12	--	--
8	.10	--	.07	.07	.07	.12
16	.14	--	.08	.07	.07	.09
32	.16	--	.08	.07	.12	.12
(c) Component separation (dB)						
1	9	5	6	8	--	--
2	15	6	5	12	--	--
4	7	24	5	14	--	--
8	8	15	7	14	21	30
16	4	--	11	11	12	18
32	6	--	--	--	5	6

*(Some larger values caused by poor data quality giving transients.)

NB T = Tuktoyaktuk, N.W.T.
S = Sudbury, Ontario

sampling rates). Two-layer theoretical curves show that a layer with a conductivity of more than 0.1 S will effectively eliminate any interference. For example, a 10 m water layer with a conductivity of more than 0.01 S m^{-1} would suppress interference. These values are possible, although the conductivity and thickness of the lake were not measured.

The scattering parameters for this set of data (Table 4-7) show the same behaviour as for the permafrost case. The scattering amplitudes are low, but the component separation is highly variable. Since the components are well separated (see Appendix 4), this is attributed to poor data quality adversely affecting the fits that are made in calculating the separation.

In conclusion, it appears that the conductive cases do show low scattering as expected. These regions are useful as limiting examples of non-scattering geological environments.

4.6 Summary of scattering results

It is useful to summarize the estimates of random scattering from the various regions that have been studied. The derived scattering parameters from Tables 4-2, 4-4, 4-6, and 4-7 are shown graphically in Figures 4-11, 4-12, and 4-13.

Fig. 4-11 shows clearly that the scattering levels are greatest on the Athabasca Glacier, rising quickly above about 8 MHz. On the Juneau Icefield scattering becomes important near 16 MHz. Both sets of data otherwise show very similar behaviour. The Apollo 17 results contrast sharply, with virtually no scattering seen. The apparent dip in scattering level at 4 MHz is not considered to be significant. The results from Tuktoyaktuk and Sudbury provide a non-scattering reference, which is consistent with results from the scale model.

The upper surface scattering information (Fig. 4-12) shows that each of the three regions are different. Again the lunar data never exceed the region of little or no scattering. The Athabasca Glacier data show large amounts of surface scattering at frequencies above 8 MHz, but the Juneau data show much less surface scattering, except possibly at 16 and 32 MHz. Since the overall scattering behaviour is similar in these two regions, it is quite likely that surface scattering is not the only scattering mechanism on the Athabasca Glacier. Again the conductive regions show little surface scattering.

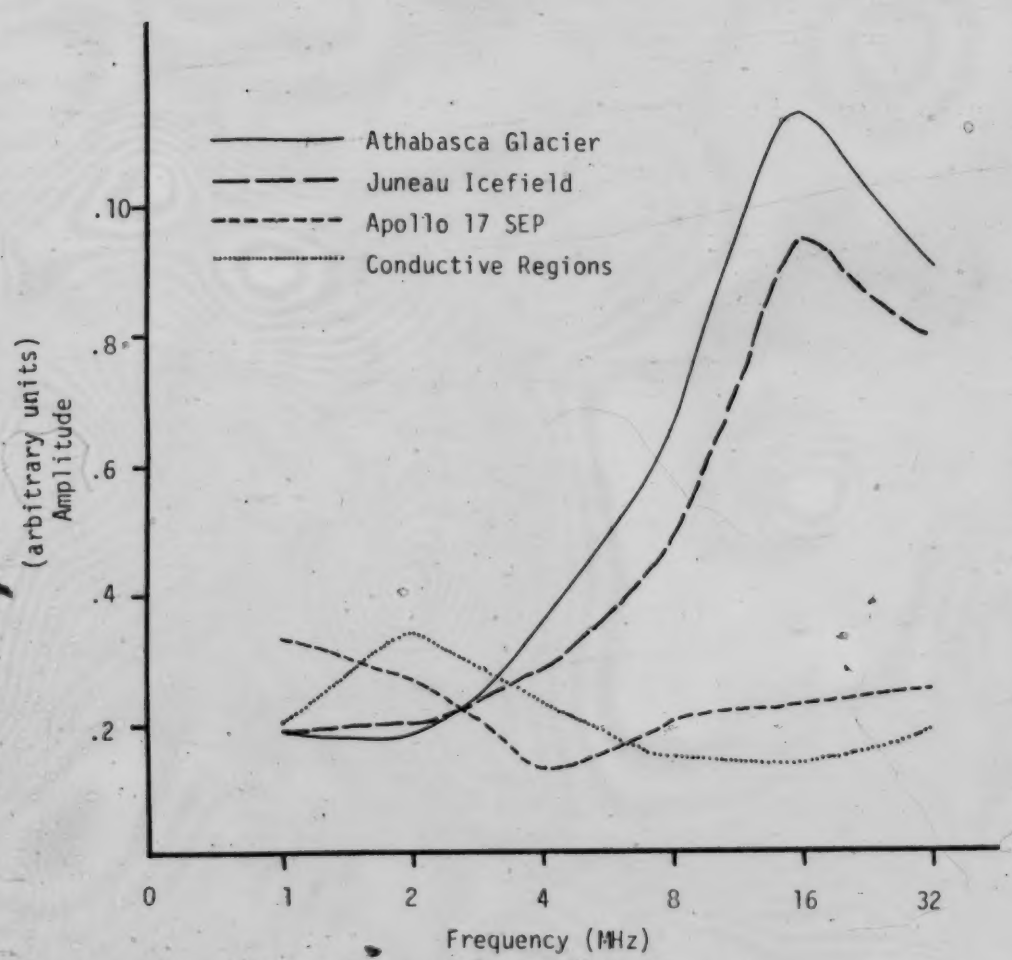

Figure 4-11. Overall Scattering Amplitude

Possible error estimated at ± 25% of value.

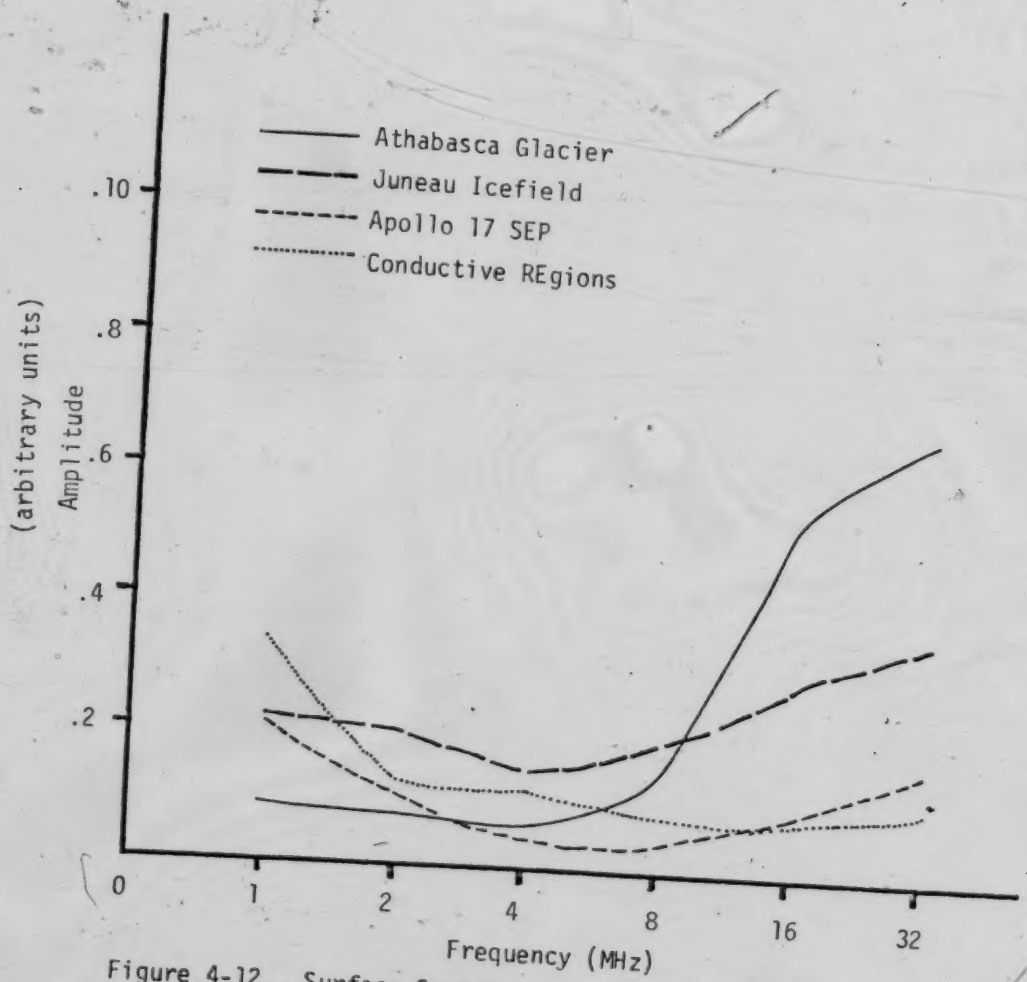

Figure 4-12. Surface Scattering Amplitude
Possible error estimated at ±25% of value

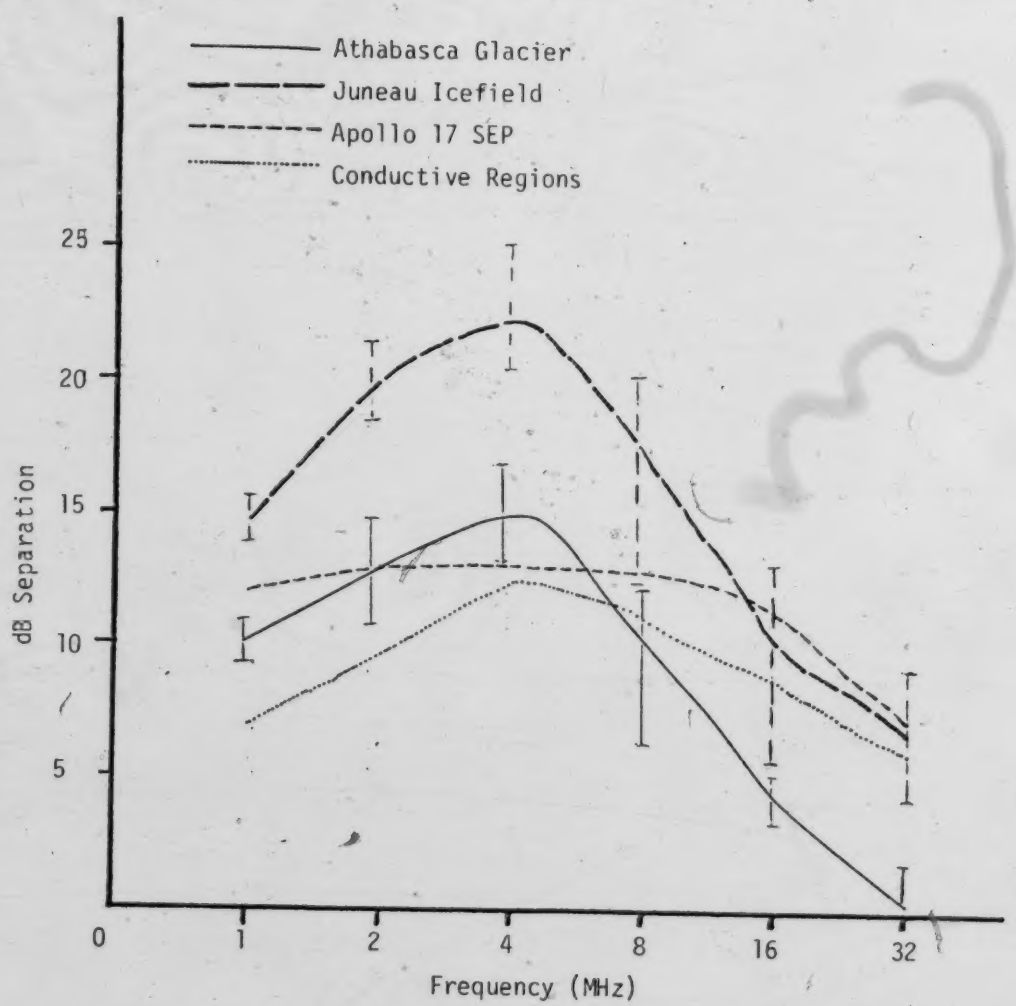

Figure 4-13. Max-min Component Separation. Range of values for Athabasca and Juneau are shown.

The separation of the maximum and minimum components (Fig. 4-13) is rather interesting. The Athabasca and Juneau curves are very similar in their overall shape, but the Juneau components are consistently about 15 dB more separated than their Athabasca counterparts. They both are low at low frequencies, increasing near 4 MHz, and then dropping rapidly at 16 and 32 MHz. The drop is almost certainly due to the increasing effectiveness of random scatterers at the higher frequencies. The difference between the two glacial regions is attributed to a greater degree of lateral inhomogeneity in the Athabasca Glacier region, with reflections from the valley walls. The drop at 1 and 2 MHz is possibly caused by higher losses in ice at low frequencies similar to the Tuktoyaktuk results.

On the lunar surface, the separation is very constant from 1 to 8 MHz. The level is low enough (10 to 15 dB) to suggest lateral inhomogeneity in the sub-surface. At 16 and 32 MHz the separation begins to decrease further, possibly due to increased inhomogeneity nearer the transmitter or nearer the surface.

Using the results of Fig. 4-11, estimates can be made of the maximum scatterer size and the typical separation between them (or the number of scattering centres per unit volume). By assuming that the scatterers are roughly spherical, a very approximate estimate of the total scattering volume fraction can be made. These results are given in Table 4-8.

Table 4-8: Inferred scatterer properties

Region	Dimension of largest scatterers (m)	Separation in a volume (m)	Scatterers per m^3	Volume fraction of scatterers (3)
Athabasca Glacier	~6	14 (1) 33 (2)	4×10^{-4} 3×10^{-5}	4×10^{-2} 3×10^{-3}
Juneau Icefield	~3	15 (1) 23 (2)	3×10^{-4} 8×10^{-5}	4×10^{-3} 1×10^{-3}
Taurus-Littrow valley	<2			

Notes: (1) L/H ratio = 1

(2) L/H ratio = 2

(3) Assuming spherical scattering bodies of largest size

In summary, the temperate ice regions are clearly the most scattering environments of those studied in the frequency range used. In comparison, the lunar surface is essentially non-scattering. Permafrost regions may have scatterers of the sizes of meters, but the permafrost was too conductive for any scatterers to be detected using radio interferometry.

CHAPTER 5

CONCLUSIONS

5.1 Scattering in temperate glaciers

The effects of random scatterers within temperate ice sheets has been a source of frustration to radio echo sounding for some time (Smith and Evans, 1972). However, it was not clearly diagnosed as the problem until relatively recently (Davis, 1973). It is apparent from the preceeding discussion that the effects of random scattering have a major influence on radio interferometry data collected in these regions. This problem is of glaciological interest, and has been discussed by Watts and England (1976). Therefore the implications of the results from Chapter 4 will be considered, and compared to those of Watts and England.

The scattering can be from three possible sources: (a) irregularities in the upper surface of the ice, e.g. crevasses; (b) irregularities in the bed of the glacier; or (c) inhomogenities within the glacier itself. Of course any or all of these may be important.

Upper surface scattering is certainly important on the Athabasca Glacier -- crevasses on the surface were large enough to preclude traverses being made except in certain areas, and the surface scattering amplitude is very high. However, the overall scattering level is also high for the Juneau Icefield (but lower than for the Athabasca Glacier), where the surface was smooth and snow-covered, and

the surface scattering amplitude was relatively low. Hence it is unlikely that surface scattering is the sole source of scattering.

Scattering from the glacier bottom is also not a likely explanation. It is not likely, for example, that a large number of features with sizes of up to 6 m, separated by about 6 to 12 m, are present on the floor of the moving Athabasca glacier. On the Juneau Icefield, it appears that in many of the runs the bottom does not influence the interferometry results to any large extent. Hence this mechanism does not fully explain the data.

It appears that scatterers within the ice itself are important in both the regions studied. In order for voids to be effective scatterers, and in order for them to support the pressures that exist (as pointed out by Watts and England), they must be water-filled. This is consistent with Goodman's (1973) observation of time-varying features on the Athabasca Glacier seen with a pulse radar system. Large amounts of water run into glaciers during the summer melt season, and since the water can co-exist with the ice, it is possible for large water-filled features to be present in temperate glaciers.

Watts and England calculated the effective scattering cross-section for dielectric spheres with a dielectric constant of 81 imbedded in ice with a dielectric constant of 3.2. They obtained scattering cross-sections that increased according to Rayleigh Law behaviour until the radius of the spheres was 0.1 wl_d. At higher frequencies (or larger radii), the scattering cross-section

was essentially constant in level. This is in agreement with the results presented in Chapter 2, except that the scattering in the model did not become effective until the scatterers had a radius of close to 0.15 wl_d. This discrepancy is probably due to the different shape of the scatterers (thick disks instead of spheres). In any case, both treatments indicate that if scatterers are less than 0.1 wl_d in radius, they will be essentially ineffective scattering bodies. Watts and England argue in their paper that scattering power will increase as the radius of the scatterer (or frequency) to the sixth power. However, this is only true when the scattering is in the Rayleigh region. As has been pointed out above, for scattering to be effective the scatterer size must be above this limit, in which case scattering is essentially constant. This error in logic does not seem to have been carried into their detailed calculations.

They go on to calculate the possible scatterer size distribution for the Athabasca Glacier, and conclude that a Gaussian distribution of the scatterers with a mean diameter of 2 m and a standard deviation of 0.4 to 0.8 m, explains the interferometry data. These values are somewhat lower than those calculated in Chapter 4, in which sizes of up to 6 m are suggested. Certainly there are crevasse features that have these dimensions on the Athabasca Glacier, therefore it seems quite possible that there are also inhomogeneities within the glacier of this size. Perhaps, given the diversity of the approaches taken to tackle this rather complex problem, these two estimates are in very good agreement.

Watts and England do not suggest a scatterer density for the Athabasca Glacier, but, based on hot-point drill results from the South Cascade Glacier, Washington, they calculate that for 2 m diameter spherical scatterers, the spacing would be about 11 m. Using the same data, but 6 m diameter spheres, the spacing would be about 22 m. These results are remarkably close to the typical spacing calculated, using interferometry data, in Chapter 4. It must be pointed out, however, that these numbers are only very approximate.

It is interesting to summarize the data on size and spacing of the scatterers, and to calculate the volume fraction that they represent, as shown in Table 5-1. Although, as pointed out earlier, there are certainly inter-glacier differences, the scattering properties of the various temperate glaciers studied are reasonably similar. The upper bound for the volume fraction of water in the Athabasca Glacier is probably too high, since it is clear that some of the scattering there is from surface crevasses. However, water volume fractions of up to several percent do not seem unlikely. This implies that the bulk dielectric constant of the ice would be significantly increased by the water, as shown. Hence, depth estimates from radar sounding of ice based on a dielectric constant of 3.2 will possibly be over-estimated. The fact that the Juneau results do not indicate large volume fractions of water is not consistent with the high dielectric constants estimated in Chapter 4. Perhaps the conclusion is that the scatterers are not uniformly

Table 5-1: Water-filled spherical scatterers in temperate glaciers

Region		Diameter (m)	Spacing (m)	Volume Fraction (%)	K_b (2)
Athabasca Glacier	R	6	14-33 (1)	0.3-4.0	3.2-3.6
	W&E	2	--	--	--
Juneau Icefield	R	3	15-23 (1)	0.1-0.4	3.2-3.3
South Cascade Glacier	W&E	2 (assumed)	11	0.3	3.2
		6 (assumed)	22	1.0	3.3

Notes:

R - Rossiter (Chapter 4); W & E - Watts and England (1976)

(1) Assuming all scattering is due to spheres spread uniformly through the volume of the ice.

(2) Bulk dielectric constant of the ice using a Lichtenecker mixing formula and the volume fraction indicated.

spread through the volume of the glacier.

The nature of the scatterers in temperate glaciers is important not only for radar work, but is critical to the understanding of the mass transport and thermal behaviour within glaciers (Paterson, 1972). Although water-filled cavities appear to be common to most temperate glaciers, there are clearly inter-glacier differences that are possibly significant. One approach to understanding this problem better is now being examined using a high-frequency, high-gain radar system that may be able to examine the scatterers themselves (Narod, 1975; Goodman, et al., 1977).

5.2 Scattering from the lunar surface

It is clear from Chapter 4 that there are few scatterers near the surface of the moon at the Apollo 17 site that have dimensions greater than about 2 m, and that scattering is therefore not highly effective for frequencies below 30 MHz(wavelengths greater than 10 m). This conclusion is in agreement with the observations from earth using various radar frequencies, in which the limb of the moon is dark with respect to the centre of the lunar disk (Hagfors, 1970). However, limb darkening decreases with increasing frequency, and it is generally agreed that scattering from the lunar surface increases with increasing frequency, largely due to the roughness of the surface itself.

The terrestrial and orbital radar studies of the moon have been very successful in estimating the properties of lunar surface material (Strangway and Olhoeft, 1977). But the question of whether the thickness of the regolith, or the nature of the regolith-rock boundary, can be deduced from these types of data is still controversial. The reflection coefficient of radar returns at different frequencies from the lunar surface show a reasonably smooth increase with increasing wavelength (Fig. 5-1). The increase has been attributed to increasing reflection from solid rock below the regolith at lower frequencies. However, it has been suggested by Strangway and Olhoeft (1977) that these results cannot be easily fitted to a simple two or three layer model of the lunar surface. Gold et al. (1976) state that the generally low

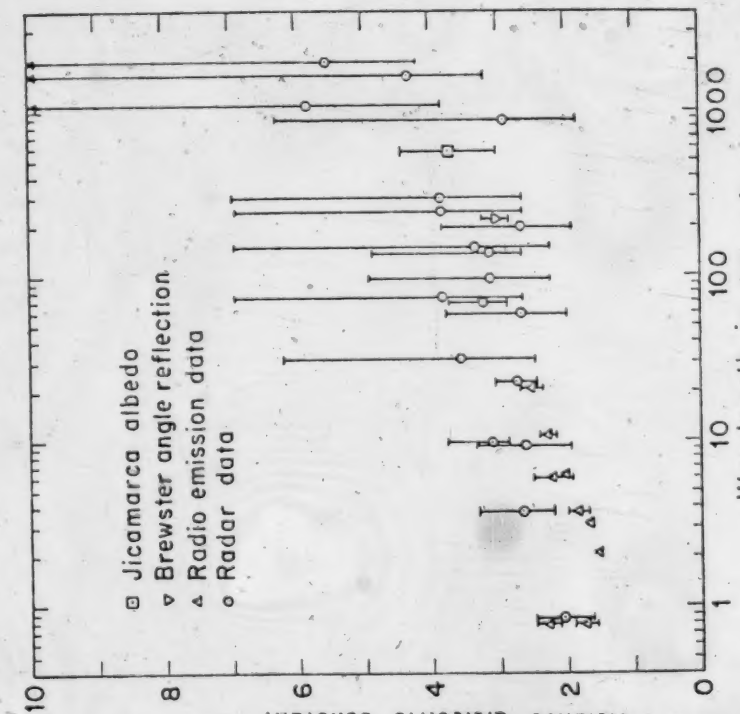

Figure 5-1: Summary of inferred dielectric constant of the lunar surface from various radar measurements (after Hagfors, 1970).

reflection coefficient, along with limb darkening (and hence little scattering), imply either a thick regolith and/or a very smooth, non-cratered bedrock. These latter deductions conflict with other evidence of regolith properties (e.g. Watkins and Kovach, 1973).

Since the SEP results do in fact show low scattering up to 32 MHz for the lunar surface, this problem was examined theoretically in somewhat more detail. The complex reflection coefficient for plane waves normally incident on a multi-layer, lossy dielectric was calculated, using the expressions contained in Ward et al. (1968). Results for plane layered models, even with reasonably high losses, show very great variations in the reflection coefficient with frequency, due to interference effects between the layers. In any event, this model is unrealistic, since a radar resolution cell for the moon, even from orbiting platforms, is on the order of kilometers. Hence, some variation in the thickness of the layers over the area of the illumination footprint is to be expected.

A two-layer theoretical model was examined: an upper layer with a dielectric constant of 2, overlying a lower layer with a dielectric constant of 7, representing the regolith and solid rock, respectively. The mean thickness of the upper layer was 5m, but it was allowed to vary. Also several loss tangents, typical of the known properties of returned lunar samples were used. After the complex reflection was calculated, its amplitude was used to

deduce an implied effective dielectric constant in order to be directly comparable to the results in Fig. 5-1.

Results of the calculations are shown in Figs. 5-2, 5-3, and 5-4. In Fig. 5-2, the upper layer varies by ± 10%, i.e. the area illuminated has a regolith thickness that varies from 4.5 to 5.5 m, in 11 equally-contributing facets. The deduced dielectric constant still shows large variations with frequency. Increasing the variation in thickness to ± 50%, i.e. 2.5 to 7.5 m (Fig. 5-3), reduces the oscillations, and increasing the number of facets from 11 to 51 (Fig. 5-4) reduces them still further. The slope of the curves depend rather slightly on losses, and the fit to the experimental data was not improved by invoking three layer models.

The interesting feature that remains in all cases, even allowing for the highest reasonable losses and large variations in upper surface thickness, is the deep null near 10 MHz. This null is the result of destructive interference between the reflection from the upper surface of the top layer and from the upper surface of the underlying layer. The exact position of the null depends on the mean thickness of the regolith in the illuminated area. Unfortunately, there are very few data points at such low frequencies. The Apollo Lunar Sounder Experiment operated at 5 and 15 MHz (Porcello et al., 1974), but no quantitative reflection coefficient data have been published. However, there is a mention of extreme fading of the 5 MHz signal over some mare regions (Brown et al., 1974), which could be due to this interference effect. The implication

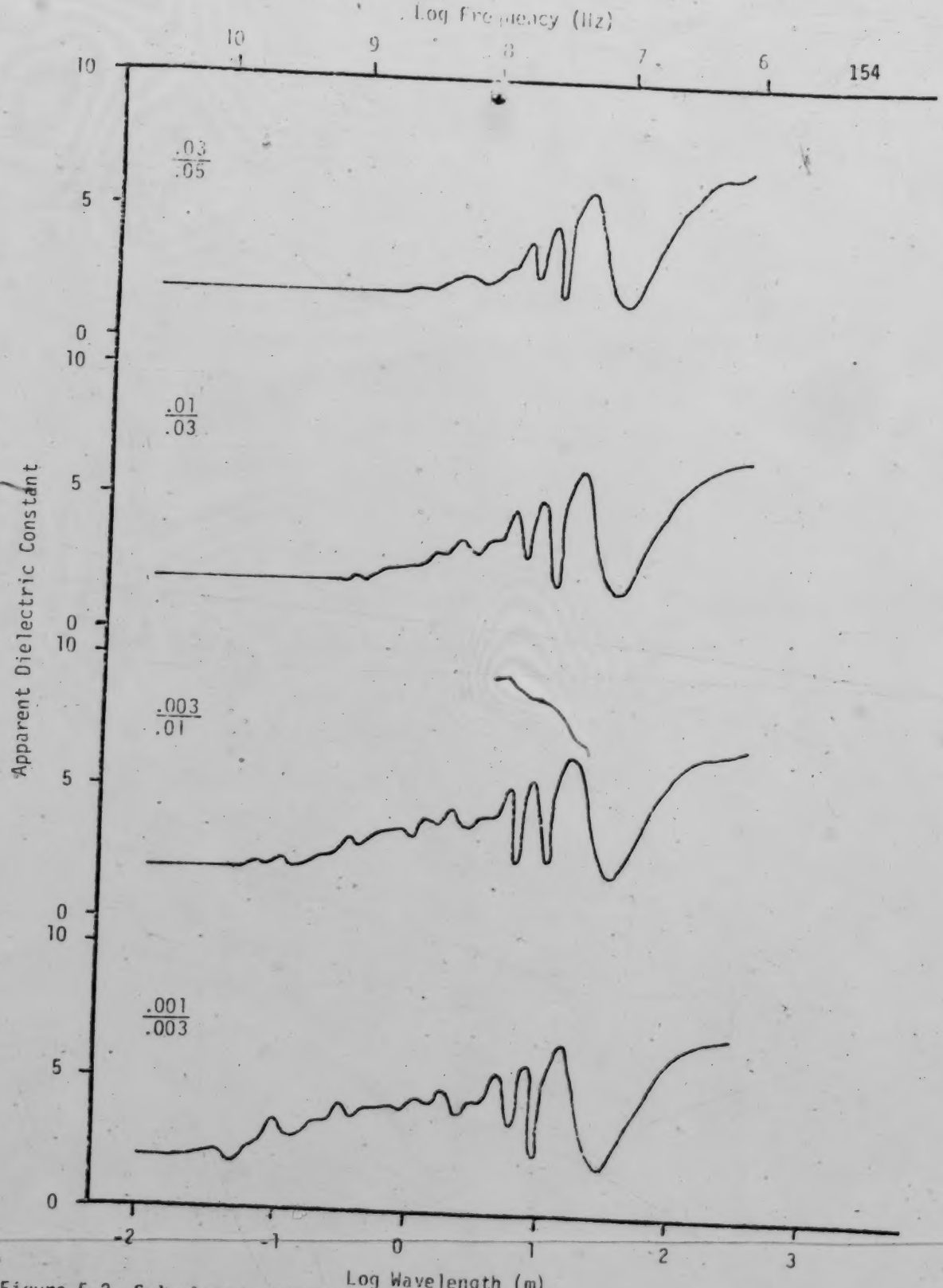

Figure 5-2 Calculated effective dielectric constant from plane two-layer moon at normal incidence. Upper layer has dielectric constant of 2, lower layer, 7. Loss tangents are shown. Thickness 5m ± 10%, 11 points.

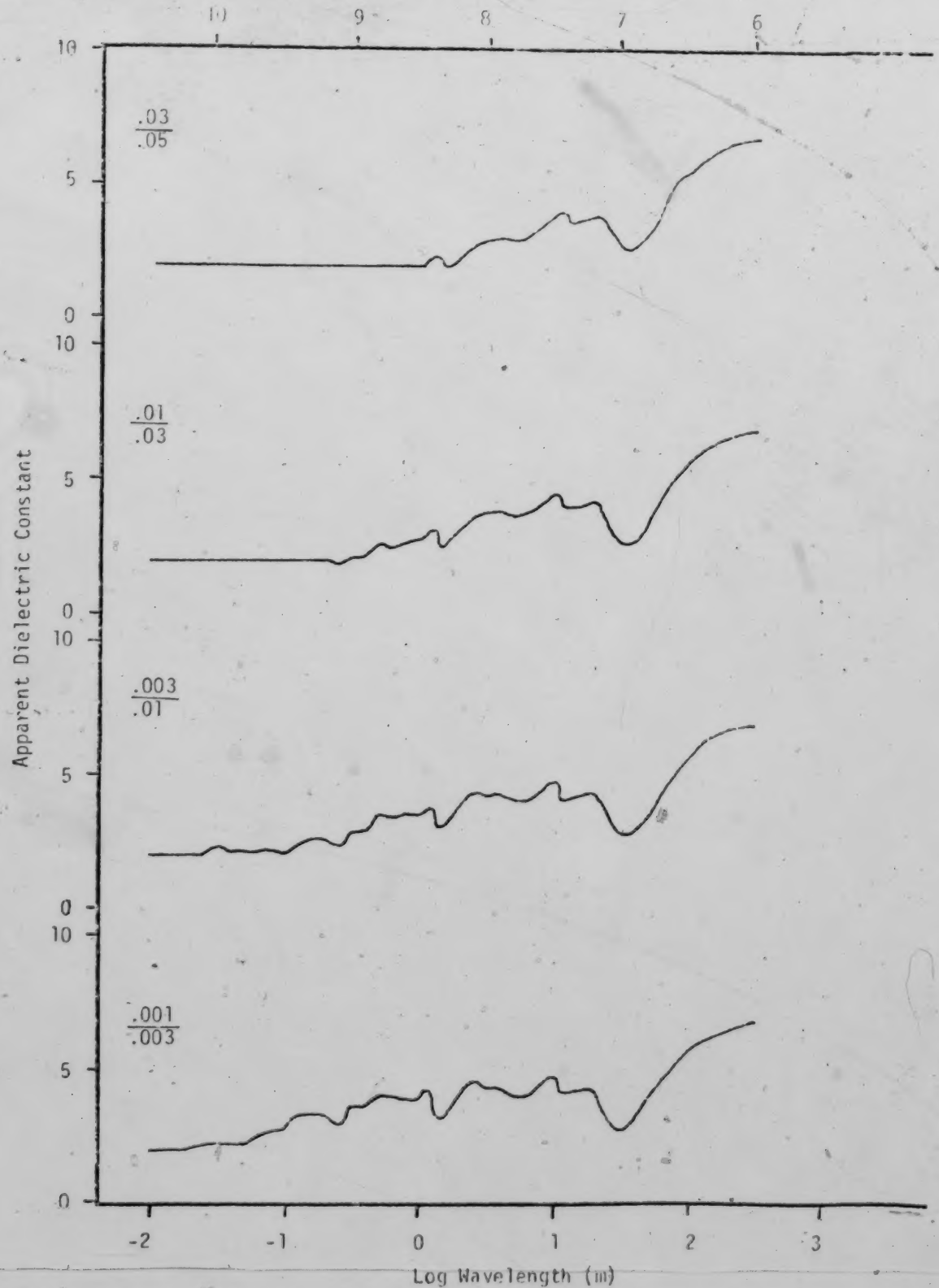

Figure 5-3 Calculated effective dielectric constant from plane two-layer moon at normal incidence. Upper layer has dielectric constant of 2, lower layer, 7. Loss tangents are shown. Thickness 5m + 50%, 11 points.

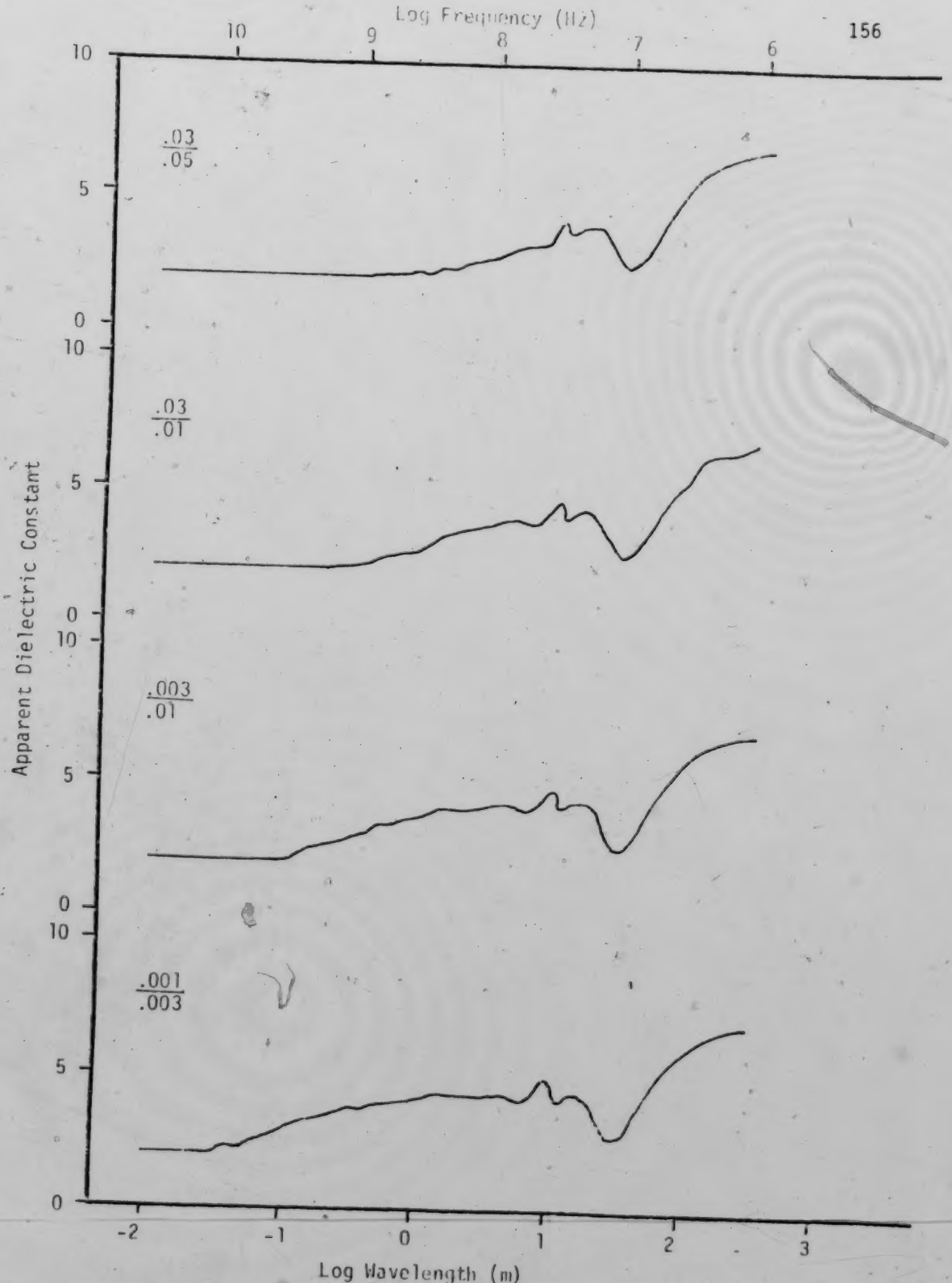

Figure 5-4 Calculated effective dielectric constant from plane two-layer moon at normal incidence. Upper layer has dielectric constant of 2, lower layer, 7. Loss tangents are shown. Thickness 5m + 50%, 51 points.

of these results is that the mean regolith thickness could be deduced by careful measurement of the reflection coefficient from the lunar surface over a frequency range from about 1 to 50 MHz.

The large variability of the reflection data (e.g. Tyler and Howard, 1973) may be due to interference effects within the regolith. Even for a moderately thin regolith thickness, the reflection coefficient does not increase to that of the lower layer until very low frequencies are used (less than 1 MHz).

In conclusion, many of the radar results from the moon are consistent with a very simple model: a low dielectric, low loss, regolith layer a few meters thick, overlying a higher dielectric rock layer. The lower layer need not be rough, but probably has undulations which have horizontal dimensions that are many times those of the vertical dimensions. Undoubtedly there are objects such as boulders in and on the regolith which become effective scatterers at higher frequencies (as seen in the limb darkening data). These inhomogeneities might increase the effective loss tangent of the upper layer, as described in Chapter 3, but it is not necessary to invoke a complex scattering model to satisfy the existing data.

This conclusion of a powder regolith several meters thick and generated by impact processes is basically confirmed by the interpretation of SEP data from the Apollo 17 site (Strangway et al., 1977). A more complex four-layer model was needed to explain all the details of the response at that particular location, because

of the high sensitivity of the interferometry method to small differences in the relevant parameters. Therefore, it appears that once again the earth- and satellite-based radar results have provided a remarkably accurate picture of the nature of the lunar surface.

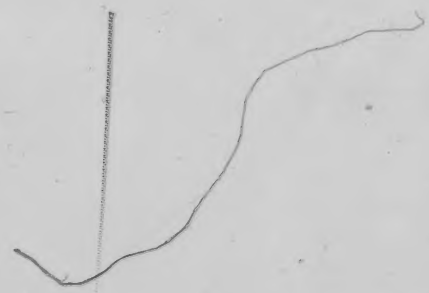

5.3 Overall Summary

In this thesis random scattering has been included as an integral part of interpretation of radio interferometry sounding data. A means of separating scattering parameters using filtering techniques has been presented, using results from an analogue scale model as a guide. As well, more automated techniques for two-layer interpretation of interferometry data have been developed, which include the effects of along-traverse changes in the thickness of the upper layer.

It has been shown that for inhomogeneities to be effective scatterers, they must have dimensions greater than about 0.3 wl_d. Larger objects do not scatter much more appreciably, but the total effect of scattering increases with the total number of scatterers.

Scattering features tend to de-polarize the interferometry signal, but this can also be accomplished by lateral boundaries that are not necessarily rough. Hence de-polarization is the sum of these two processes.

The interpretive procedures have been applied to interferometry from all the regions studied to date. In locations where there is a two-layer structure, the layered interpretations are in agreement with other results. Scattering is important in data from temperate glaciers, but is not important, up to 32 MHz, in data from the lunar surface. Two relatively conductive regions are examples of low scattering geological enviroments, and the results from them are

similar to those from the scale model with no scatterers present.

A physical theoretical model of small random inhomogeneities in a two-dimensional waveguide was developed using perturbation theory. Although the assumption of small variations in properties was not consistent with the necessity of large scattering objects to scatter interferometry data, the effects of scatterers in increasing the effective dielectric constant and loss tangent of the scattering medium were observed. This work could be extended in several ways, for example, to examine mode-to-mode scattering, or to take into account more completely the rather particular boundary conditions of a waveguide.

Scattering effects are very important in the data from both temperate glacial regions. It is concluded that although some of the scattering is caused by crevasses on the upper surface of the Athabasca Glacier, substantial contributions are also from water-filled cavities within the glacier. There are differences in scattering between this glacier and the Juneau Icefield, and these differences may be important in understanding the hydrology of temperate ice sheets. Therefore, further studies of these features are highly recommended.

The near-surface of the moon at the Apollo 17 landing site does not appear to have significant numbers of scatterers with dimensions greater than about 2 m. It has been shown that a two-layer model of the lunar surface is able to satisfy much of the lunar radar data, without resorting to complicated scattering

mechanisms. However, interference effects within the upper layer will tend to give highly variable responses, even when a distribution of thicknesses are illuminated.

Future interpretation of interferometry data should include estimates of the effects of random scattering. Although the major conclusions reached here, i.e. that there is high scattering in temperate ice and low scattering on the moon at radio frequencies, are not novel, it has been possible to assign quantitative estimates to the properties of the scatterers in both cases.

REFERENCES

Abramowitz, M. and Stegun, I., editors: Handbook of Mathematical Functions, Dover Publications, New York, 1970.

Annan, A.P.: "Radio Interferometry Depth Sounding," M.Sc. Thesis, Dept. of Physics, University of Toronto, NASA Report, Grant No. NGL 22-009-257, 1970.

Annan, A.P.: "Radio Interferometry Depth Sounding: Part I -- Theoretical Discussion," Geophys., v.38, no.3, pp.557-580, 1973.

Annan, A.P. and Davis, J.L.: "Impulse Radar Sounding in Permafrost," Rad. Sci., v.11, no.11, pp.383-394, 1976.

Annan, A.P.; Waller, W.M.; Strangway, D.W.; Rossiter, J.R.; Redman, J.D.; and Watts, R.D.: "The Electromagnetic Response of a Low-loss, 2-layer, Dielectric Earth for Horizontal Electric Dipole Excitation," Geophys., v.40, pp.285-298, 1975.

Beckmann, P. and Spizzichino, A.: The Scattering of Electromagnetic Waves from Rough Surfaces, MacMillan, New York, 1963.

Brekhovskikh, L.: Waves in Layered Media, Academic Press, New York, 1960.

Brown, W.S.; Adams, G.F.; Eggleton, R.E.; Jackson, P., Jordan, R.; Kobrick, M.; Peeples, W.J.; Phillips, R.J.; Porcello, L.J.; Schaber, G.; Sill, W.R.; Thompson, T.W.; Ward, S.H.; and

Zelenka, J.S.: "Elevation Profile of the Moon," Proc. 5th Lun. Sci. Conf., Suppl. 5, Geochim. Cosmochim. Acta, v.3, pp.3037-3048 , 1974.

Budden, K.G.: The Wave-guide Mode Theory of Wave Propagation, Prentice-Hall, Englewood Cliffs, 1961.

Chan, W.-C.M.; Kong, J.A.; and Tsang, L.: "Geophysical Sub-surface Probing with a Horizontal Magnetic Dipole," IEEE Trans. Ant. Prop., v. AP-24, pp.877-879, 1976.

Cooper, M.R.; Kovach, R.L.; and Watkins, J.S.: "Lunar Near-surface Structure," Rev. Geophys. Sp. Phys., v.12, pp.291-308, 1974.

Davis, J.L.: "The Problem of Depth Sounding Temperate Glaciers," unpublished M.Sc. Thesis, Trinity College, Cambridge, 1973.

Erdélyi, A., editor, Bateman Manuscript Project, "Tables of Integral Transforms," v.1, McGraw-Hill, 1954.

Evans, S.: "Dielectric Properties of Ice and Snow -- A Review," J. Glaciol., v.5, no.42, pp.773-792, 1965.

Gold, T.; Bilson, E.; and Baron, R.L.: "Electrical properties of Apollo 17 Rock and Soil Samples and a Summary of the Electrical Properties of Lunar Material at 450 MHz Frequency," Proc. Lunar Sci. Conf. 7th pp.2543-2603, 1976.

Goodman, R.H.: "Time-Dependent Intraglacier Structures," J. Glaciol., v.12, no.66, pp.512-513, 1973.

Goodman, R.H.; Outcalt, E.; Narod, B.B.; and Clarke, G.K.C.: "Radar Techniques for the Measurement of Floating Ice Thickness," Proc. 4th Canadian Symposium on Remote Sensing, Quebec, May 16-18, 1977.

Hagfors, T.: "Remote Probing of the Moon by Infrared and Microwave Emissions and by Radar," Rad. Sci., v.5, pp.189-227, 1970.

Ince, A.N., editor, "Electromagnetic Wave Propagation involving Irregular Surfaces and Inhomogeneous Media", AGARD Conference Proceedings No. 144, The Hague, 25-29 March, 1974, 1975.

Karal, F.C. and Keller, J.B.: "Elastic, Electromagnetic and Other Waves in a Random Medium," J. Math. Phys., v.5, pp.537-547, 1964.

Keller, J.B.: "The Velocity and Attenuation of Waves in a Random Medium," in Electromagnetic Scattering, Rowell, R.L. and Stein, R.S., editors, Gordon and Breach, New York, 1967, Proc. 2nd Interdisciplinary Conf. on Electromagnetic Scattering, held at the University of Massachusetts at Amherst, June, 1965.

Kong, J.A.: "Electromagnetic Fields due to Dipole Antennas over Stratified Anisotropic Media," Geophys., v.37, no.6, pp.985-996, 1972.

Kong, J.A.; Tsang, L.; and Simmons, G.: "Geophysical Sub-surface Probing with Radio-Frequency Interferometry," IEEE Trans. Ant. Prop., v. AP-22, pp.616-620, 1974.

Kovach, R.L.; and Watkins, J.S.: "The Structure of the Lunar Crust at the Apollo 17 Site," Proc. 4th Lunar Sci. Conf, Suppl.4, Geochim.Cosmochim. Acta, v.3, pp.2549-2560, 1973.

Kovach, R.L.; Watkins, J.S.; and Talwani, P.: "Lunar Seismic Profiling Experiment," Apollo 17 Preliminary Science Report, NASA SP-330, pp.10-1 --10-12, 1973.

La Torraca, G.A.: "Half Wavelength Dipole Antennas over Stratified Media," unpublished report CSR-T-72-1, Center for Space Research, Mass. Inst. Technology, 1972.

Muehlberger, W.R.;Batson, R.M.; Cernan, E.A.; Freeman, V.L.; Hait, M.H.; Holt, H.E.; Howard, K.A.; Jackson, E.D.; Larson, K.B.; Reed, V.S.; Rennilson, J.J.; Schmitt, H.H.; Scott, D.H.; Sutton, R.L.; Stuart-Alexander, D.; Swann, G.A.; Trask, N.J.; Ulrich, G.E.; Wilshire, H.G.; and Wolfe, E.W.: "Preliminary Geological Investigation of the Apollo 17 Landing Site," Apollo 17 Preliminary Science Report, NASA SP-330, Washington, pp.6-1 --6-91, 1973.

Narod, B.B.: "Ultra High Frequency Radio Echo Sounding of Glaciers," unpublished M.Sc. Thesis, Dept. of Geophysics and Astronomy, University of British Columbia, 1975.

Olhoeft, G.R.: "Electrical Properties of Natural Clay Permafrost," Can. J. Earth Sci. , v.14, pp. 16-24, 1977.

Paterson, W.S.B.: "Temperature Distribution in the Upper Layer of the Ablation Area of the Athabasca Glacier, Alberta, Canada," J. Glaciol., v.11, pp.31-41, 1972.

Porcello, L.J.; Jordan, R.L.; Zelenka, J.S.; Adams, G.F.; Phillips, R.J.; Brown, W.E.Jr.; Ward, S.H.; and Jackson, P.L.: "The Apollo Lunar Sounder Radar System," Proc. IEEE v.62, no.6, June 1974.

Rossiter, J.R.: "Interferometry Depth Sounding on the Athabasca Glacier -- Development of the Interferometry Technique for Lunar Exploration," unpublished M.Sc. Thesis, University of Toronto, Dept. of Physics, 1971.

Rossiter, J.R.: "SEP Mark II Data Processing," unpublished internal memo, Depts. of Physics and Geology, University of Toronto, 1975.

Rossiter, J.R.; La Torraca, G.A.; Annan, A.P.; Strangway, D.W.; and Simmons, G.: "Radio Interferometry Depth Sounding: Part II -- Experimental Results," Geophys., v.38, no.3. pp. 581-599 , 1973.

Rossiter, J.R.; Strangway, D.W.; Annan, A.P.; Watts, R.D.; and Redman, J.D.: "Detection of Thin Layers by Radio Interferometry," Geophys. v.40, pp.299-308, 1975.

Rossiter, J.R.; Strangway, D.W.; Koziar, A.; Wong, J.; and Olhoeft, G.R.: "Electromagnetic Sounding of Permafrost, N.W.T., Canada, in Summer and Winter," Proc. 3rd. Int'l. Conf. on Permafrost, Edmonton, July 10-13, 1978 (in press).

Roth, L.E.; and Elachi, C.: "Coherent Electromagnetic Losses by Scattering from Volume Inhomogeneities," IEEE Trans. Ant. Prop,. v. AP-23, PP.674-675, 1975.

SEP Team: "Surface Electrical Properties Experiment," Apollo 17 Preliminary Science Report, NASA SP-330, Washington, pp. 15-1 --15-14, 1973.

Simmons, G.; Strangway, D.W.; Bannister, L.; Baker, R.; Cubley, D.; La Torraca, G.; and Watts, R.: "The Surface Electrical Properties Experiment," in Kopal, Z. and Strangway, D. editors, Lunar Geophysics, Proc. of a conference at the Lunar Science Institute, Houston, Texas, Oct. 18-21, 1971, Dordrecht, D. Reidel, pp.258-271, 1972.

Smith, B.M.E.; and Evans, S.: "Radio Echo Sounding - Absorption and Scattering by Water Inclusion and Ice Lenses," J. Glaciol., v.11, pp.133-146, 1972.

Strangway, D.W.; Annan, A.P., Redman, J.D.; Rossiter, J.R.; Rylaarsdam, J.C.; and Watts, R.D.: "Final Technical Report on the Surface Electrical Properties Experiment," unpublished report submitted by University of Toronto for NASA contract NAS 9-11540, 1974.

Strangway, D.W.; Annan, A.P.; Redman, J.D.; Rossiter, J.R.; and Watts, R.D.: "Electrical Structure at Taurus-Littrow," in preparation, 1977.

Strangway, D.W.; and Olhoeft, G.R.: "Electrical Properties of Planetary Surfaces," Phil. Trans. R. Soc. Lond., v. A285, pp.441-450, 1977.

Strangway, D.W.; Simmons, G.; La Torraca, G.; Watts, R.; Bannister, L.; Baker, R.; Redman, J.D.; and Rossiter, J.R.: "Radio-Frequency Interferometry -- A New Technique for Studying Glaciers," J. Glaciol., v.13, no. 67, pp.123-132, 1974.

Stratton, J.A.: Electromagnetic Theory, McGraw-Hill, New York, 1941.

Talwani, M.; Thompson, G.; Dent, B.; Kahle, H.G.; and Buck, S.: "Traverse Gravimeter Experiment," Apollo 17 Preliminary Science Report, NASA SP-330, Washington, PP. 13-1 --13-13, 1973.

Tsang, L.; Brown, R.; Kong, J.; and Simmons, G.: "Numerical Evaluation of Electromagnetic Fields due to Dipole Antennas in the Presence of Stratified Media," J. Geophys. Res., v.79, pp.2077-2080, 1974.

Tsang, L.; and Kong, J.A.: "Electromagnetic Fields due to a Horizontal Electric Dipole Antenna Laid on the Surface of a Two-layer Medium," IEEE Trans. Ant. Prop., v. AP-22, pp.709-711, 1974.

Tsang, L.; Kong, J.A. and Simmons, G.: "Interference Patterns of a Horizontal Electric Dipole over Layered Dielectric Media," J. Geophys. Res., v.78, no.17, pp.3287-3300, 1973.

Tyler, G.L.; and Howard, H.T.: "Dual-Frequency Bistatic-Radar Investigations of the Moon with Apollos 14 and 15," J. Geophys. Res., v.78, no.23, 1973.

Ulrich, T.J.; and Bishop, T.N.: "Maximum Entropy Spectral Analysis and Autoregressive Decomposition," Rev. Geophys. and Space Phys., v.13, no.1, pp.183-200, 1975.

von Hippel, A.R.: Dielectrics and Waves, M.I.T. Press, Cambridge, 1954.

Wait, J.R.: Electromagnetic Waves in Stratified Media, MacMillan, New York, 1962.

Waller, W.M.: "Surface Electrical Properties Simulation Model," Lockheed Electronics Co., (Final Report, unpublished, LED/PESD 634-TR-139) for Contract NAS 9-12200, NASA-JSC, Houston, 1973.

Ward, S.H.; Jiracek, G.R. and Linlor, W.I.: "Electromagnetic Reflection from a Plane-Layered Lunar Model," J. Geophys. Res.,v. 73, pp.1355-1372, 1968.

Watkins, J.S.; and Kovach, R.L.: "Seismic Investigation of the Lunar Regolith," Proc. 4th Lunar Sci. Conf., Suppl.4, Geochim. Cosmochim. Acta, v.3, pp. 2561-2574, 1973.

Watts, R.D.; and England, A.W.: "Radio-echo Sounding of Temperate Glaciers: Ice Properties and Sounder Design Criteria," J. Glaciol., v.17, no.75, pp.39-48, 1976.

Wiggins, R.A.: and Miller, S.P.: "New Noise-reduction Technique Applied to Long-period Oscillations from the Alaskan Earthquake," Bull. Seis. Soc. Am., v.62, pp.471-479, 1972.

Wong, J.; Rossiter, J.R.; Olhoeft, G.R.; and Strangway, D.W.: "Permafrost: Electrical Properties of the Active Layer in situ," Can. J. Earth. Sci., v.14, pp.582-586, 1977.

APPENDIX 1

ANALOGUE SCALE MODEL

The analogue scale model, used to collect experimental interferometry data in a controlled environment, has been well described elsewhere by Waller (1973) and by Annan et al. (1975). Therefore the following description will be brief, and the details will not be repeated except where they have changed.

A sketch of the model is shown in Figure A1-1. It is basically a fiberglass tank filled with dielectric transformer oil (Voltesso-35). The inside of the tank is lined with Eccosorb microwave absorbing material to reduce reflections from the walls of the tank. The transmitter is a horizontal half-wave electric dipole antenna fixed just above the surface of the oil, and powered at 5.9 GHz by a microwave source. The receiver is another half-wave electric dipole, but is suspended from a mobile carriage so that it can traverse along the length of the tank, again just above the surface of the oil. At 5.9 GHz, the tank is approximately 30 wl x 15 wl x 15 wl (60 x 30 x 30 inches).

The transformer oil, forming the upper layer of a two-layer model, typically has a dielectric constant of 2.16, and a loss tangent of about 0.002. The lower layer is a perfect reflector, formed by an aluminum plate, which is suspended in the oil by movable wooden supports. It can be placed at various depths in the oil, both horizontally and with various angles of tilt.

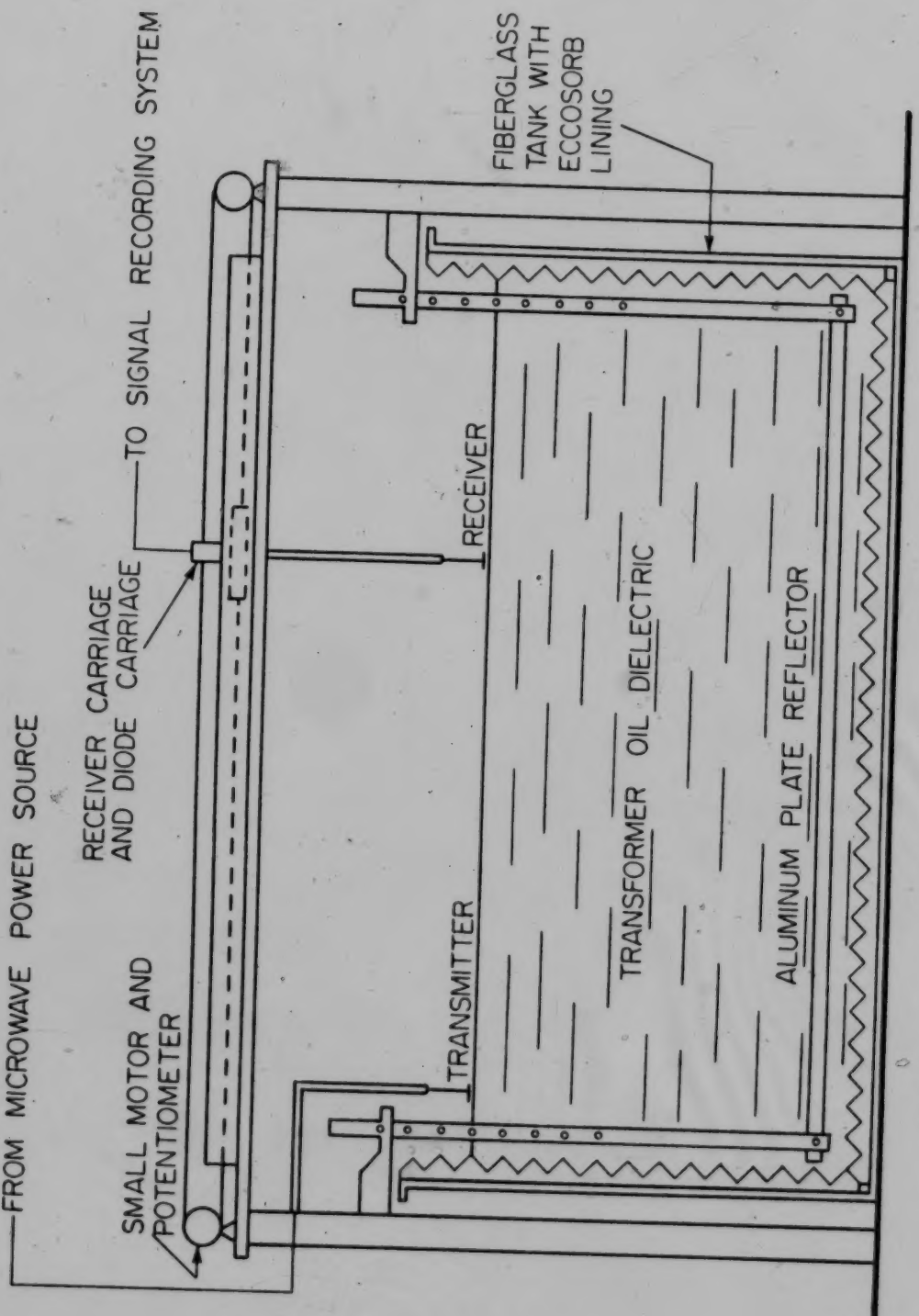
FROM MICROWAVE POWER SOURCE
SMALL MOTOR AND POTENTIOMETER
RECEIVER CARRIAGE AND DIODE CARRIAGE
TO SIGNAL RECORDING SYSTEM
TRANSMITTER
RECEIVER
TRANSFORMER OIL DIELECTRIC
ALUMINUM PLATE REFLECTOR
FIBERGLASS TANK WITH ECCOSORB LINING

Figure A1-1

Scatterers can be either placed on the plate surface, or suspended within the oil layer with threads.

An important aspect of the scale model is the ability to automatically record data, complete with range information, both on paper, for real-time inspection, and on magnetic tape, for computer processing. A schematic of the model set-up is shown in Figure A1-2. For direct plots of the data, the output from the diode is log-amplified and recorded on an x-y plotter. Range information is determined by the voltage across a potentiometer which is controlled by the carriage position.

In order to record data on magnetic tape, the signal level is fed into the S.E.P. Data Acquisition System (see SEP Final Report, 1974). The output from the log amplifier is 20 mv/dB, from 0 to 800 mv, taking into account the square-law output behaviour of the diode detector. On its x1000 scale, the Wavetek voltage-controlled generator changes frequency by 2 Hz/mv . Therefore the correct scaling factor is 2 x 20 = 40 Hz/dB. This signal is put into the VCO channel of the Data Acquisition System.

Position information is determined by pulses generated when a toothed wheel, rotating with the carriage control motor, operates a microswitch. There are 194 $\pm$ 2 pulses per traverse of 25 wl. These go into the Acquisition System TCD channel. Finally, a 5200 Hz reference signal is entered into the REF channel.

Data are digitized in the same manner as field data, althouth several small changes are necessary in the set-up because there are no synch pulses in the data stream. 186 samples of field

SCALE MODEL SCHEMATIC

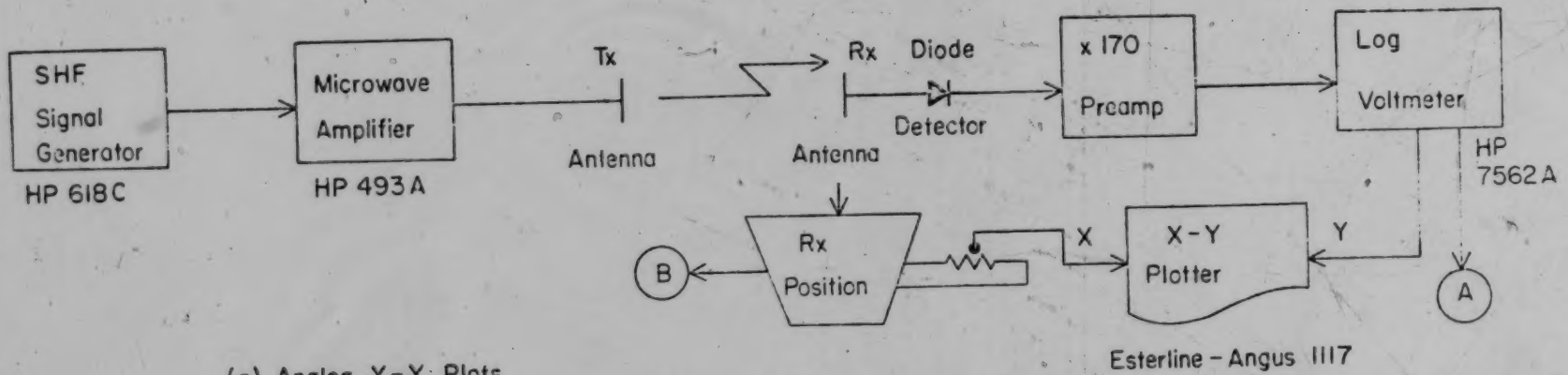

(a) Analog X-Y Plots

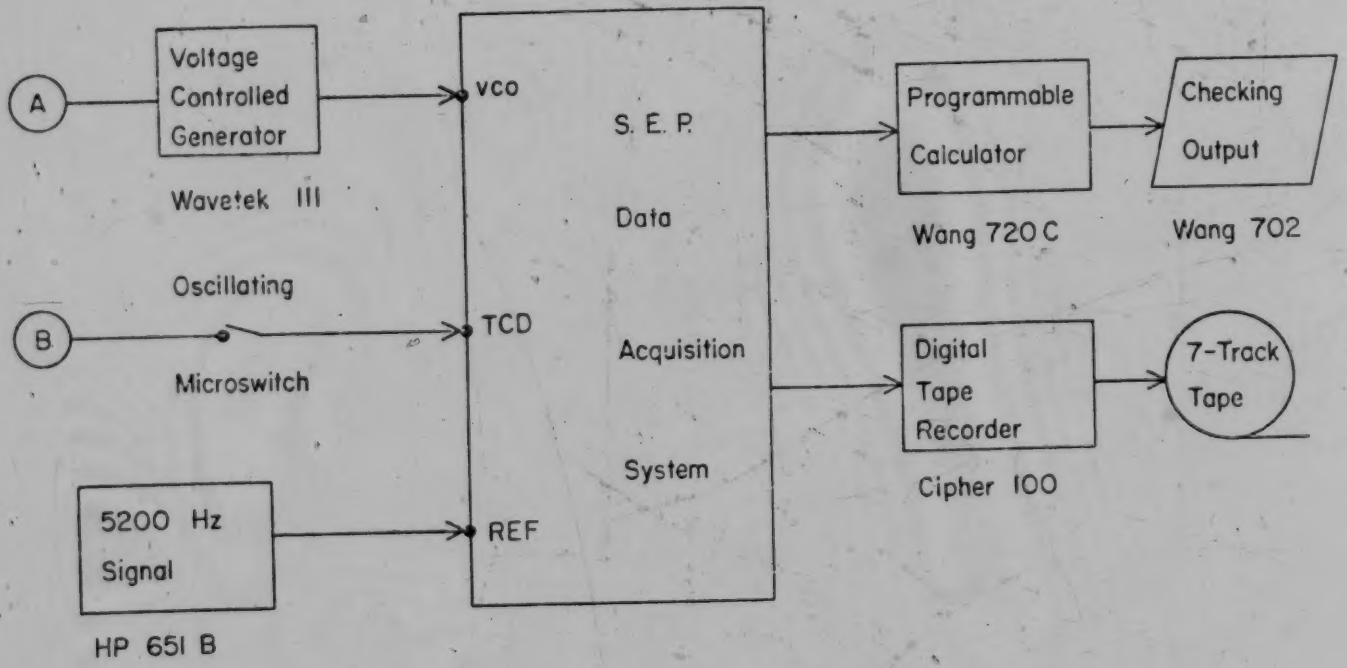

(b) Analog to Digital

Figure A1-2

strength data are collected every 6.48 seconds. A traverse of 25 wl (from 2 to 27 wl from the transmitter) takes about 40 seconds, giving approximately 1100 points, or 45 points/wl (well above the number for the standard interpolation at 10 points/wl).

The data, both signal level and odometer pulses, are recorded on a 7-track, computer-compatible tape in BCD format. Selected data for checking are also printed by a Wang calculator in real-time. The intricacies of converting the raw data on tape back into the original dB vs. wl readings are done on the IBM 370/165-II computer. The procedure followed is essentially the same as that for field data, as documented in a memo by Rossiter (1975). However, since the model data is not multiplexed, and since odometer information is similar from run to run, several simplifications were made. A set of 36 runs is usually processed and stored on disk in a single job.

Reproducibility of scale model data is shown in Fig. A1-3, in which two runs, measured on Oct. 17, 1975 and Dec. 1, 1975 respectively, are presented. The oil is 1 wl deep and the interference is relatively weak, so that perturbations due to set-up differences are most apparent. As can be seen, the reproducibility is accurate to better than $\pm$ 1 dB. The maximum possible position (range) error is $\pm$ 2 pulses, i.e. $\pm$ 1% of total range.

Although reflections from the walls of the tank are minimized by use of absorbing material, there are reflections from the end of the tank. Those only become apparent for ranges greater than 22 wl (Fig. A1-3). Since data were only examined in the thesis to 20 wl, this does not appear to be a limitation.

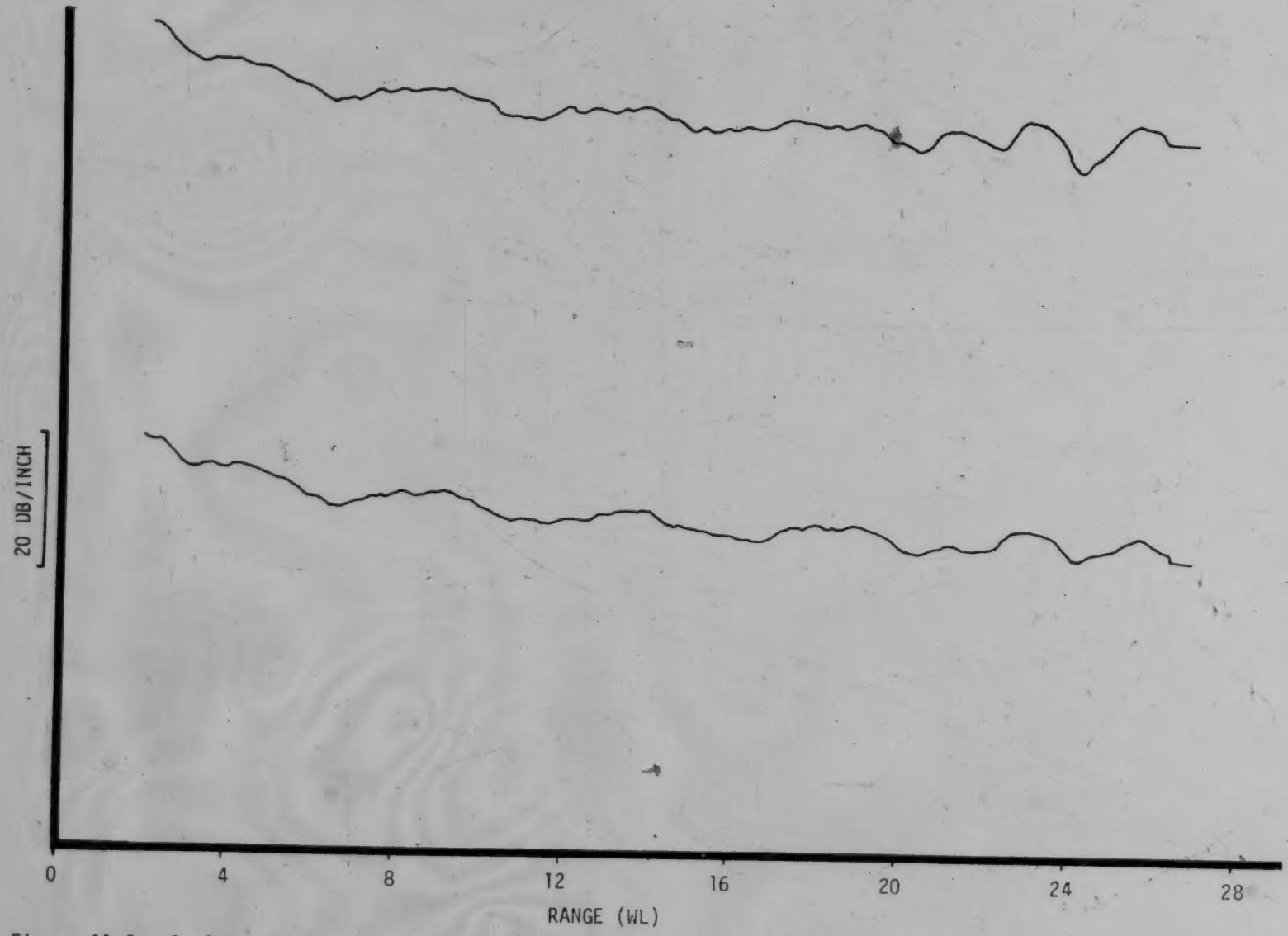

Figure A1-3. Scale model runs for oil 1 wl thick (max component). Upper run was made on Oct 17, 1975; lower, on Dec. 1, 1975. Note reproducibility of the data.

The small ripple with a spatial frequency near 1 cycle/wl is due to standing waves set up between the transmitter and receiver (see Chapter 2, and Annan, 1970). This represents a systematic error in the model, but since this ripple has a typical amplitude of less than 2 dB, its overall effect is quite small.

APPENDIX 2

$r^{-\alpha}$ DECAY PARAMETER

In order to filter the interferometry data it was first necessary to remove a decay from each curve. This was done by evaluating in a least-squares sense, a curve of the form $c\ r^{-\alpha}$, where c and α are constants, and r is distance between the transmitter and receiver. This procedure was done by a linear least-squares regression fit to all the points in the interference curve (after sampling at 0.1 wl intervals).

The constant, c, is indicative of the overall level of the curve, and although its absolute value is not important, it was used to compare maximum and minimum coupled components. The decay parameter, α, is given in Table A2-1 for scale model data, and in Table A2-2 for field data.

As can be seen in the tables, the scale model data curves have decay rates generally between -0.5 and -0.1. This is in rough agreement with theory, in which the far-field approximation in a 2-dimensional waveguide has components with $r^{-3/2}$ and $r^{-1/2}$ decay rates (Chapter 3).

The field data appear to decay more quickly, with decay rates of generally between -1.0 and -2.0. The difference between the field data and the scale model results is probably due to the lack of near-source data from the scale model experiment, due to constraints imposed by the traversing equipment.

There do not appear to be any systematic decay differences, either in the scale model data or in the field data, for variations in layer thickness, scattering level, or conductivity of the subsurface material. There is, however, a fairly large variation in this parameter from curve to curve, since the curves themselves are highly variable due to interfering waves.

Table A2-1: Decay Parameter, Scale Model Data

Values as averaged over runs made at 1, 2, and 4 wl thick oil.

No Scatterers: Max: -0.7; min, -0.2

$H\ (wl_d)$		L = 4		L = 2		L = 1	
		max.	min.	max.	min.	max.	min.
0.28	radial	-0.7	-0.5	-0.7	-0.5	-0.7	-0.9
	tangential	-0.7	-0.2	-0.6	-0.5	-0.6	-0.2
0.32	radial	-0.7	-0.7	-0.7	-0.5	-0.8	-1.0
	tangential	-0.7	-0.6	-0.7	-0.5	-1.0	-0.9
0.37	radial	-0.8	-0.7	-0.8	-0.7	-0.9	-1.1
	tangential	-0.9	-0.7	-0.9	-0.7	-1.4	-1.1
0.55	radial	-0.8	-0.5	-0.1	-0.8	-	-
	tangential	-0.9	-0.6	-0.2	-0.9	-	-

max = maximum - coupled E_ϕ broadside component

min = minimum - coupled E_ρ broadside component

Table A2-2: Decay Parameter, Field Data

Frequency (MHz)	Endfire Hρ	Endfire Hφ	Endfire Hz	Broadside Hρ	Broadside Hφ	Broadside Hz
			Athabasca Run 25			
1	-1.2	-1.6	-1.5	-1.8	-1.1	-2.1
2	-1.3	-1.7	-1.3	-1.8	-1.3	-1.9
4	-1.5	-1.8	-1.3	-2.0	-1.5	-1.9
8	-1.9	-1.9	-2.0	-2.2	-2.0	-2.2
16	-2.2	-2.5	-2.1	-1.9	-1.6	-1.9
32	-1.1	-1.3	-1.4	-1.5	-1.8	-1.6
			Athabasca Run 71			
1	-1.7	-1.4	-1.8	-1.7	-0.6	-2.0
2	-1.6	-1.5	-1.6	-1.9	-0.9	-2.0
4	-1.5	-1.7	-1.4	-1.9	-1.4	-1.9
8	-1.6	-1.8	-1.7	-2.1	-2.2	-2.4
16	-1.5	-2.0	-1.7	-1.8	-1.9	-1.8
32	-1.6	-1.8	-1.7	-1.6	-1.8	-1.5
			Athabasca Run 59			
1	-1.5	-1.7	-2.6	-1.7	-1.0	-2.5
2	-1.5	-1.7	-2.2	-2.1	-1.9	-2.3
4	-1.7	-1.8	-1.7	-2.3	-1.9	-2.7
8	-1.9	-2.0	-1.8	-2.3	-1.8	-2.2
16	-2.0	-2.3	-1.9	-2.0	-2.2	-2.1
32	-1.7	-2.0	-1.9	-1.5	-1.7	-1.7

Table A2-2 Continued

frequency (MHz)	Endfire Hρ	Endfire Hφ	Endfire Hz	Broadside Hρ	Broadside Hφ	Broadside Hz
			Juneau Run 36			
1	-0.7	-1.5	-0.9	-1.7	-0.4	-2.0
2	-1.0	-1.7	-1.1	-1.8	-0.7	-2.0
4	-1.2	-1.8	-1.4	-1.7	-1.1	-2.0
8	-1.8	-1.8	-2.0	-2.1	-1.6	-2.3
16	-1.9	-1.7	-1.9	-1.8	-1.5	-2.0
32	-1.2	-1.2	-1.1	-1.1	-1.1	-1.2
			Juneau Run 92			
1	-1.3	-1.7	-1.3	-1.7	-0.8	-2.1
2	-1.5	-1.7	-1.3	-1.7	-1.0	-2.0
4	-1.6	-1.8	-1.3	-1.8	-1.2	-2.1
8	-1.8	-1.9	-1.7	-1.9	-1.6	-2.0
16	-1.6	-1.6	-1.4	-1.7	-1.6	-1.7
32	-1.2	-1.0	-1.1	-1.0	-1.0	-1.0
			Juneau Run 84			
1	-1.5	-1.8	-1.5	-1.5	-0.6	-2.0
2	-1.6	-1.7	-1.6	-1.5	-1.2	-1.6
4	-1.4	-1.5	-1.4	-1.5	-1.1	-1.6
8	-1.6	-2.0	-1.6	-1.6	-1.6	-1.8
16	-1.8	-1.6	-1.9	-2.1	-1.5	-2.1
32	-1.5	-1.6	-1.3	-1.2	-0.9	-1.4

Table A2-2 Continued

frequency (MHz)	Endfire Hρ	Endfire Hφ	Endfire Hz	Broadside Hρ	Broadside Hφ	Broadside Hz
			SEP Lunar Data			
1	-1.6	-1.7	-1.5	-1.8	-1.3	-1.8
2	-1.8	-1.8	-1.5	-2.0	-1.6	-2.1
4	-1.8	-1.7	-1.7	-2.0	-1.8	-2.3
8	-1.8	-1.7	-1.8	-2.2	-1.8	-2.3
16	-1.8	-1.6	-1.9	-2.1	-1.8	-2.3
32	-1.6	-1.6	-1.9	-1.9	-1.7	-2.0
			Tuk Run 2			
1	-1.3	-1.1	-0.7	-2.1	-1.5	-1.6
2	-0.9	-1.4	-	-1.9	-1.3	-1.2
4	-1.5	-1.5	-1.8	-2.1	-1.5	-2.1
8	-1.6	-1.5	-1.7	-2.1	-1.6	-2.1
16	-1.5	-1.5	-1.7	-2.4	-1.7	-1.8
32	-2.0	-1.8	-2.0	-2.0	-1.6	-1.6
			Tuk Run 3			
1	-	-	-	-1.7	-1.1	-1.6
2	-	-	-	-1.8	-0.9	-1.1
4	-	-	-	-1.9	-0.5	-2.0
8	-	-	-	-2.0	-1.3	-1.8
16	-	-	-	-1.8	-1.4	-1.9
32	-	-	-	-1.9	-1.4	-0.9

Table A2-2 Continued

frequency (MHz)	Endfire Hρ	Endfire Hφ	Endfire Hz	Broadside Hρ	Broadside Hφ	Broadside Hz
			Tuk Run 15			
1	-1.3	-1.3	-2.0	-2.3	-1.9	-2.0
2	-1.0	-1.0	-1.5	-2.0	-1.4	-1.9
4	-1.6	-1.5	-1.8	-2.1	-1.4	-2.0
8	-1.9	-1.8	-1.9	-2.1	-1.8	-2.1
16	-1.9	-1.8	-2.1	-1.9	-1.9	-2.0
32	-2.2	-1.8	-1.6	-1.9	-1.6	-1.8
			Tuk Run 19			
1	-0.6	-1.1	-0.9	-2.0	-0.8	-o.7
2	-1.0	-1.0	-1.0	-2.1	-1.3	-1.5
4	-1.4	-1.5	-1.5	-2.3	-1.5	-1.8
8	-1.8	-1.6	-1.7	-2.1	-1.5	-2.1
16	-1.7	-1.8	-1.7	-1.9	-1.8	-2.0
32	-2.5	-2.2	-2.7	-1.7	-1.3	-1.6
			Sudbury Run 1			
8	-1.0	-1.0	-1.3	-2.1	-0.9	-1.9
16	-1.1	-1.2	-1.1	-2.1	-1.1	-2.2
32	-3.4	-2.7	-2.4	-1.8	-1.9	-1.9
			Sudbury Run 2			
8	-1.6	-1.1	-2.5	-	-	-
16	-1.0	-1.1	-1.0	-2.3	-	-2.3
32	-2.7	-2.9	-3.5	-1.8	-2.6	-1.9

APPENDIX 3

OFF-AXIS TRAVERSES

If the traverse is not along an extension of one of the legs of the transmitting dipole, there will be mixing of the endfire and broadside components. Of course for a traverse at 45°, the endfire and broadside terminology becomes meaningless. For small off-axis angles, however, the mixing can still be severe.

Let the average level of fits to the maximum and minimum components respectively be represented by:

$$R_{max} = S + N$$

and $$R_{min} = N, \qquad (1)$$

where S is the maximum-coupled signal level, and N is the minimum-coupled background signal level.

Then the component separation for a traverse along the axis is:

$$Sep = 20 \log_{10} \frac{(R_{max})}{(R_{min})} \text{ dB.} \qquad (2)$$

If Sep = 40 dB, which is typical for non-scattering areas, then:

$$S = 99N. \qquad (3)$$

For traverses at angle θ,

$$R'_{max} = S \cos \theta + N$$

$$R'_{min} = S \sin \theta + N \qquad (4)$$

$$Sep' = 20 \log_{10} \frac{(R'_{max})}{(R'_{min})}$$

$$= 20 \log_{10} \frac{99 \cos \theta + 1}{99 \sin \theta + 1} \qquad (5)$$

for Sep = 40 dB.

Using equation (5):

θ =	Sep^1 =
5°	20 dB
10°	15
20°	9
30°	5

Hence the separation between maximum and minimum components decreases markedly for traverses run at small angles off the antenna axis. This result is in contrast to small rotations, at a given point, of the receiver. A component mixing occurs, but one component grows cosinisoidally as the other decreases. This behaviour was observed on the lunar surface, and is reported by Strangway et al, (1974 a).

APPENDIX 4

PLOTS OF RADIO INTERFEROMETRY FIELD DATA

In this appendix full plots of all the field data that are discussed in the thesis are presented. The format is as follows: each page contains two frequencies, 1 and 2, 4 and 8, or 16 and 32 MHz, in the upper and lower half of the page respectively. On the left of each page are endfire components, and on the right, broadside components. In some places blank spaces are left where no data were collected.

The field-strength level of the reference line is marked in dBm, and the scale of the ordinate (in dB) is shown. The abscissa is marked in free space wavelengths for all frequencies. Titles indicate the area from which the data were collected, and the site, run, frequency, and component are given explicitly to the right of each curve. Maximum-coupled components are H_ϕ endfire, H_ρ and H_z broadside; the other three are minimum-coupled to a plane layered geometry (see Fig. 1-3).

Order of plots

Athabasca Glacier, Alberta. Summer 1971.

Run 25 -- side of glacier, up-glacier

Run 71 -- side of glacier, down-glacier

Run 59 -- centre of glacier, down-glacier

Juneau Icefield, Alaska. Summer 1972.

Run 36 -- mid-Taku Glacier

Run 92 -- Matthes Glacier

Run 84 -- Icy Basin

Apollo 17, Surface Electrical Properties Experiment. December 1972.

Taurus-Littrow valley of the Moon, EVA 2.

Tuktoyaktuk, N.W.T., Involuted Hill Test Site.

Run 2 -- Summer 1974, on hill

Run 3 -- Summer 1974, off hill

Run 15 -- Winter 1976, on hill

Run 19 -- Winter 1976, off hill

Lake McFarlane, Sudbury, Ontario. April 1975.

Run 1 -- away from shore

Run 2 -- toward shore

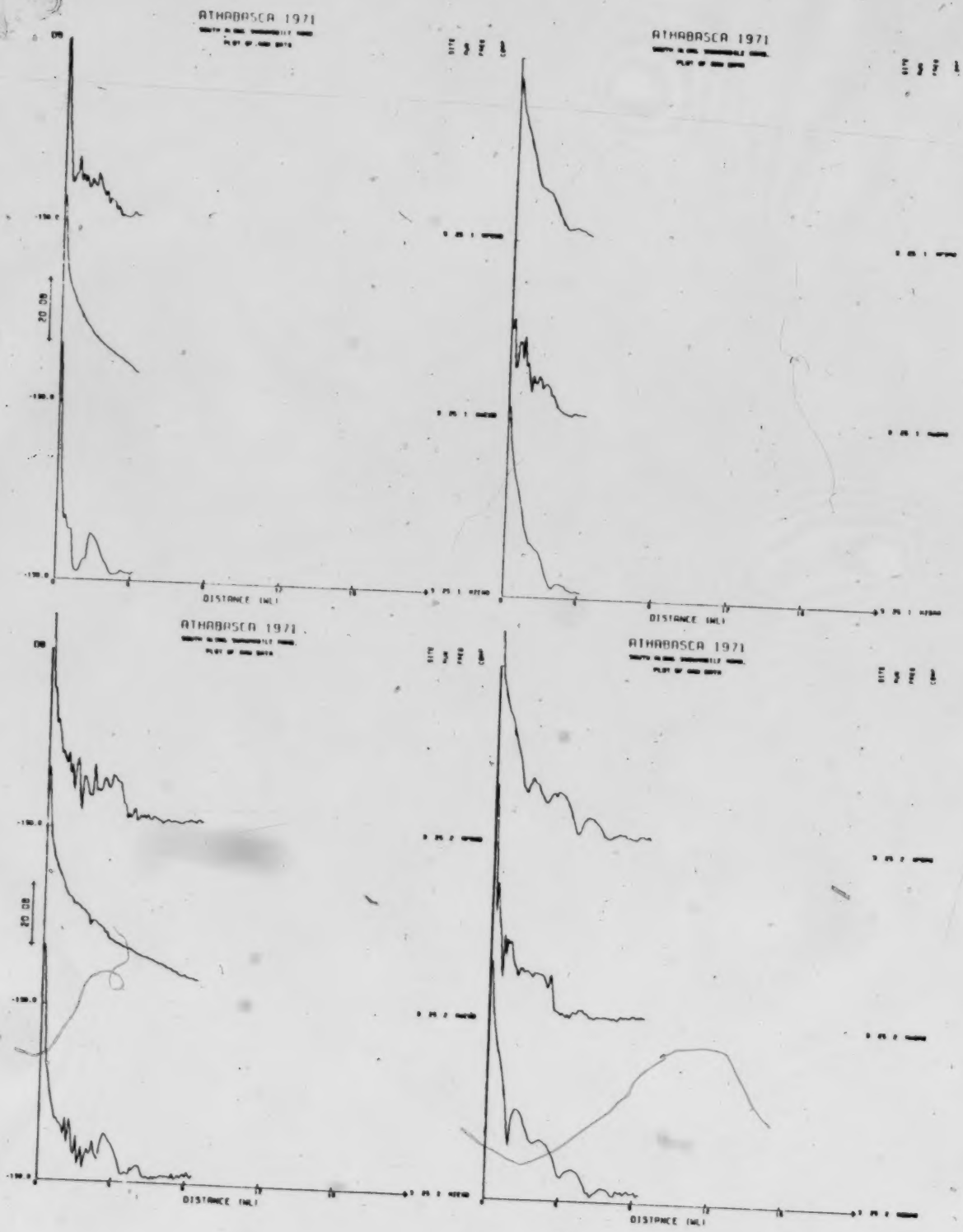
ATHABASCA 1971
ATHABASCA 1971
ATHABASCA 1971
ATHABASCA 1971
20 DB
20 DB
DISTANCE (MI)
DISTANCE (MI)
DISTANCE (MI)
DISTANCE (MI)

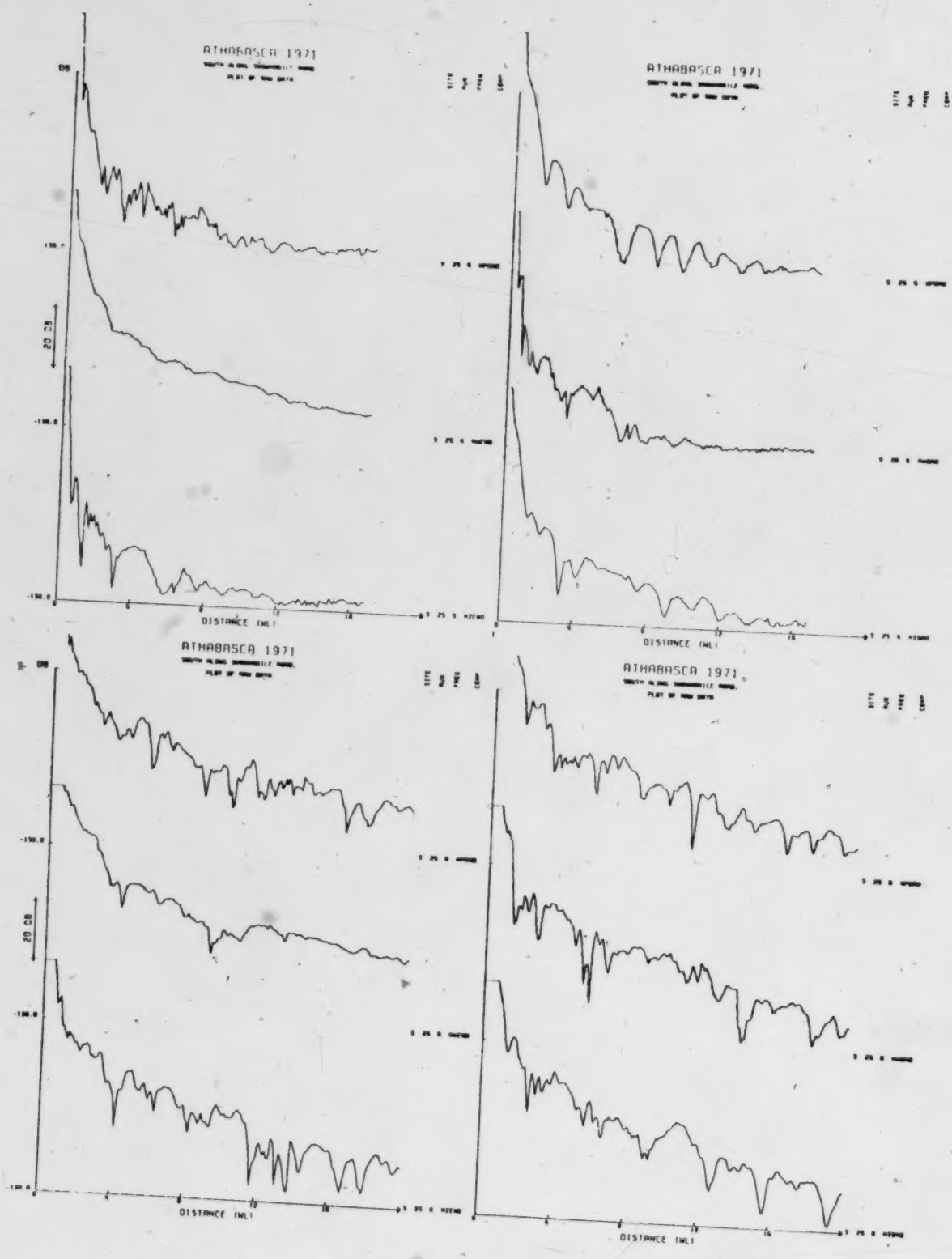
ATHABASCA 1971
DB
20 DB
DISTANCE (MI.)
ATHABASCA 1971
DISTANCE (MI.)
ATHABASCA 1971
DB
20 DB
DISTANCE (MI.)
ATHABASCA 1971
DISTANCE (MI.)

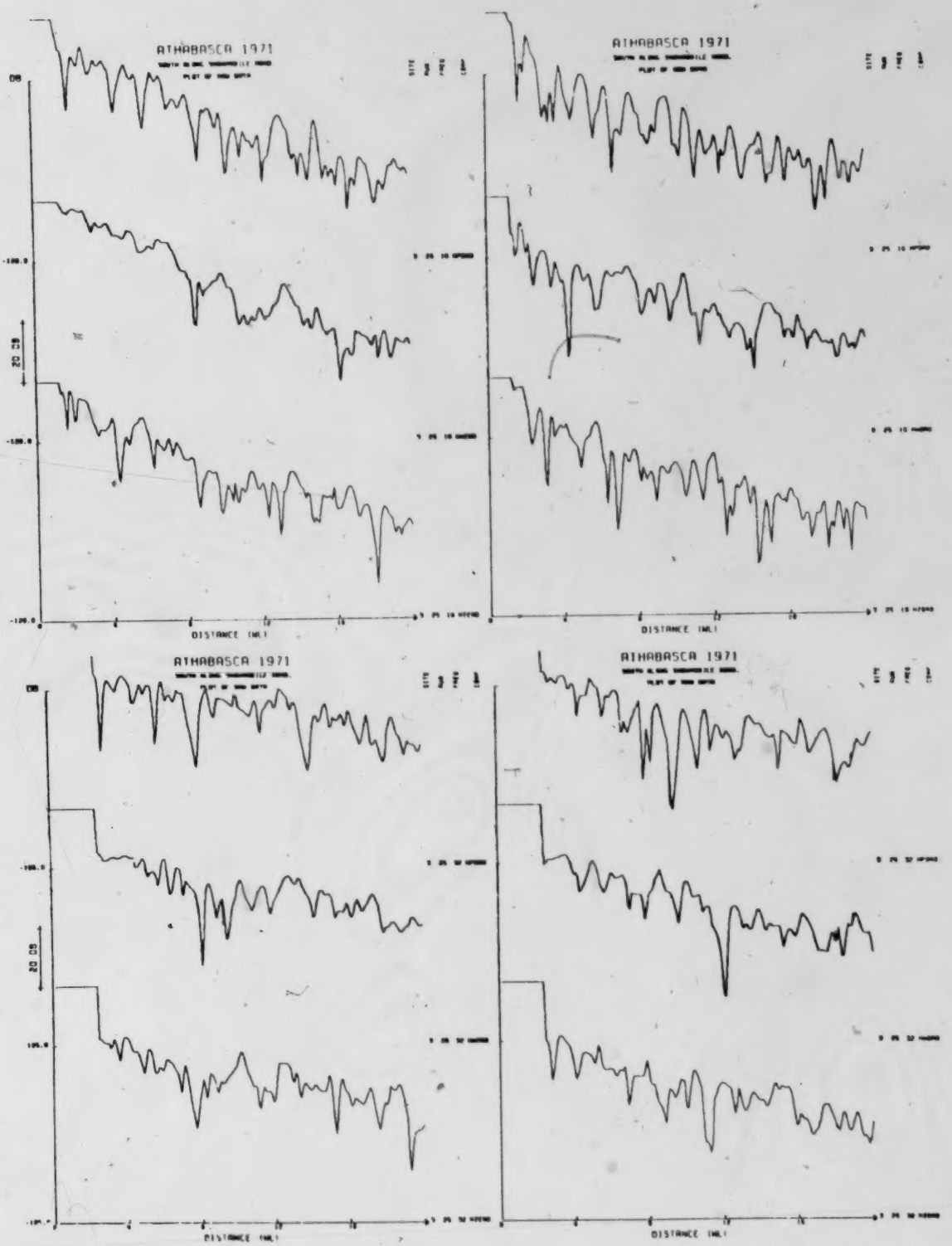
ATHABASCA 1971
DISTANCE (MI)
ATHABASCA 1971
DISTANCE (MI)
ATHABASCA 1971
DISTANCE (MI)
ATHABASCA 1971
DISTANCE (MI)

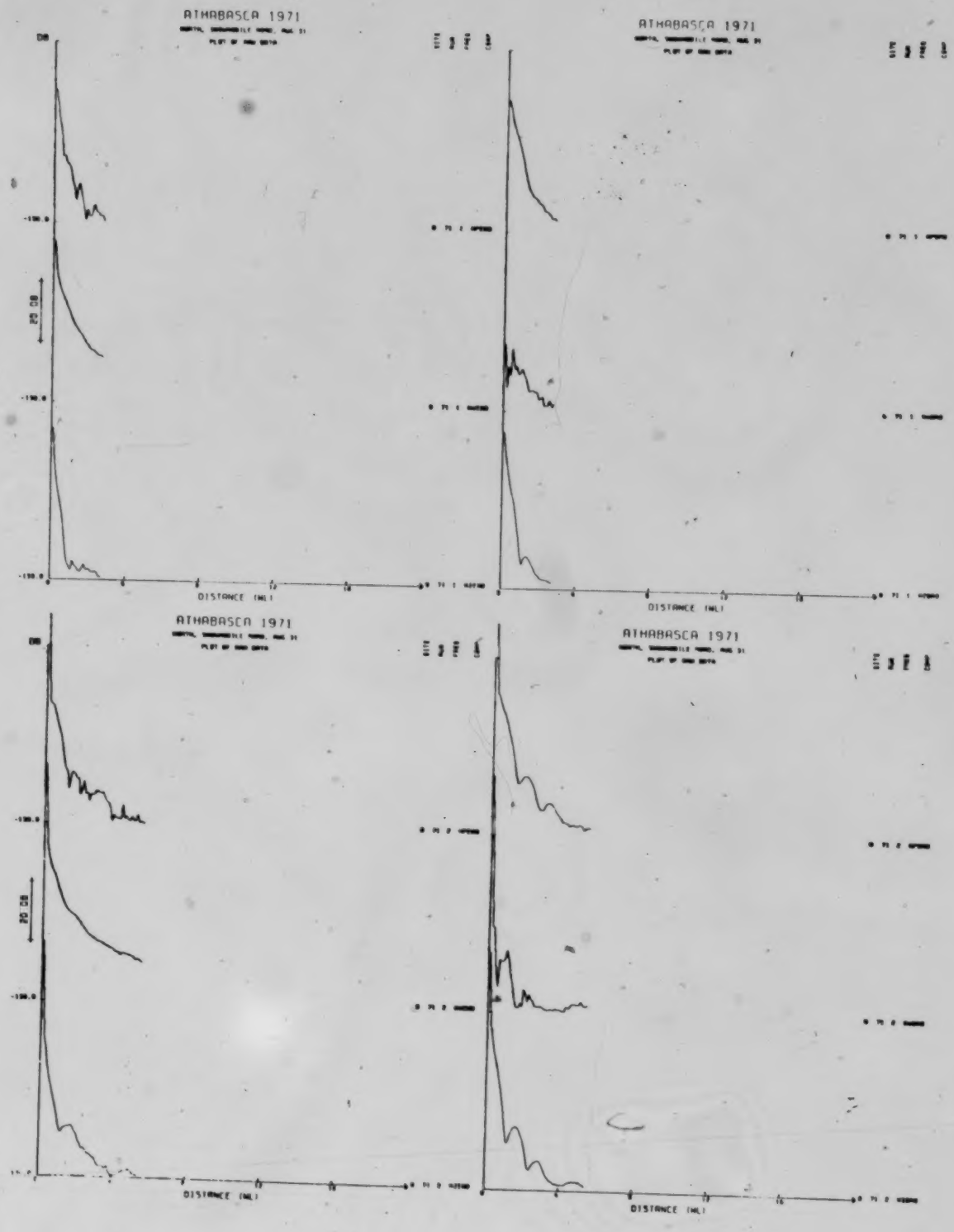
ATHABASCA 1971
DISTANCE (KL)
ATHABASCA 1971
DISTANCE (KL)
ATHABASCA 1971
DISTANCE (KL)
ATHABASCA 1971
DISTANCE (KL)

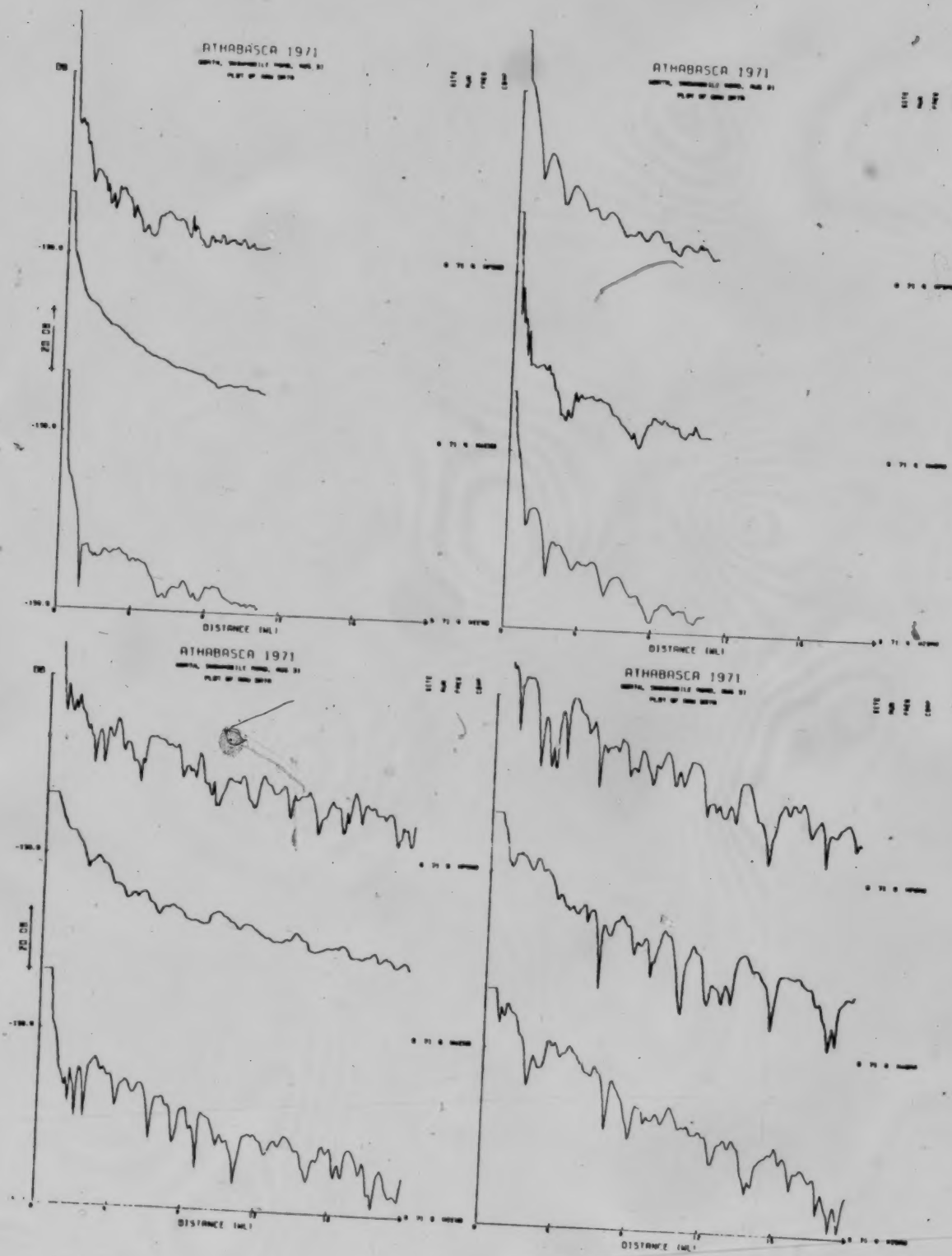
ATHABASCA 1971
ATHABASCA 1971
ATHABASCA 1971
ATHABASCA 1971
DISTANCE (MI)
DISTANCE (MI)
DISTANCE (MI)
DISTANCE (MI)

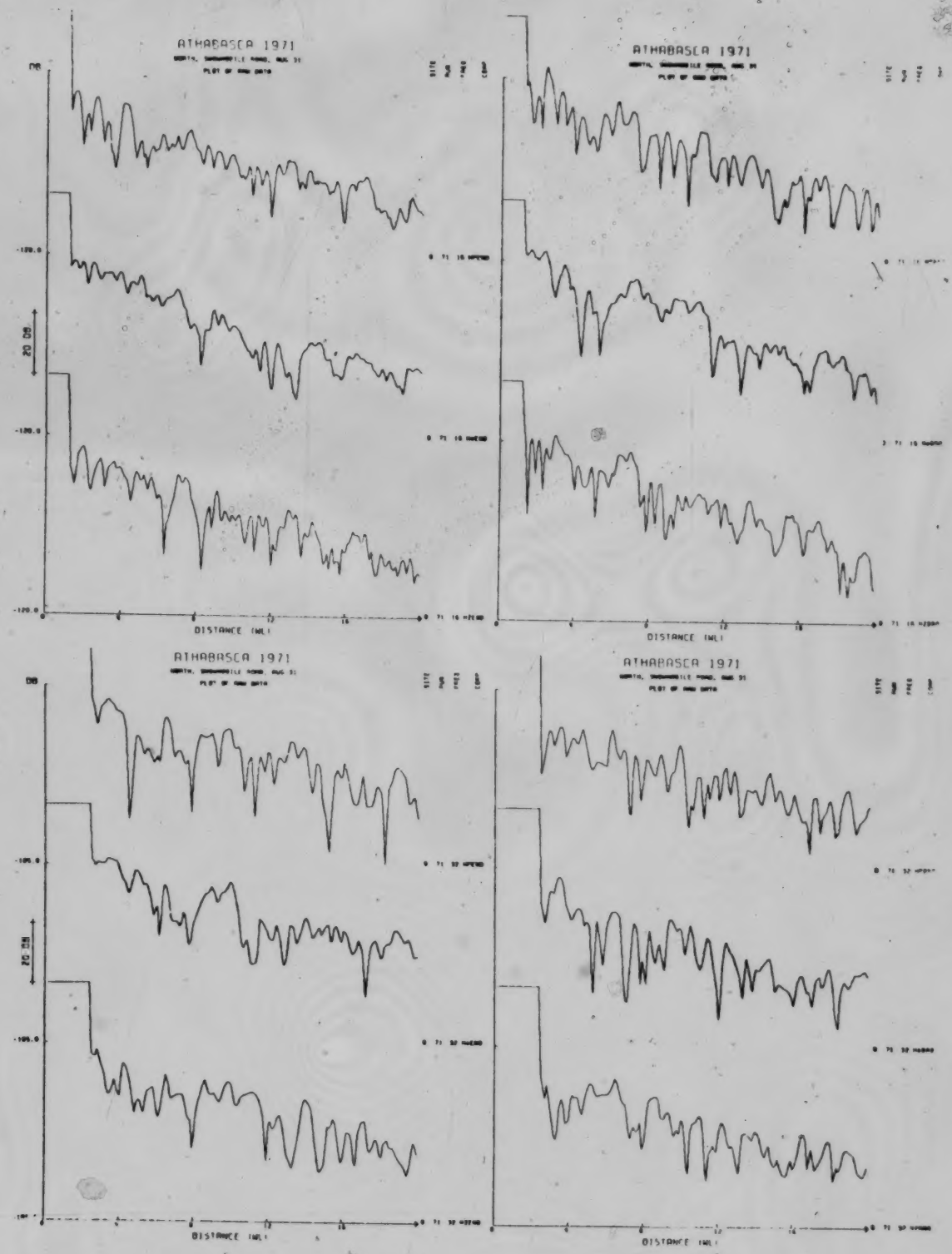
ATHABASCA 1971
DB
20 DB
DISTANCE (MI.)
ATHABASCA 1971
DISTANCE (MI.)
ATHABASCA 1971
DB
20 DB
DISTANCE (MI.)
ATHABASCA 1971
DISTANCE (MI.)

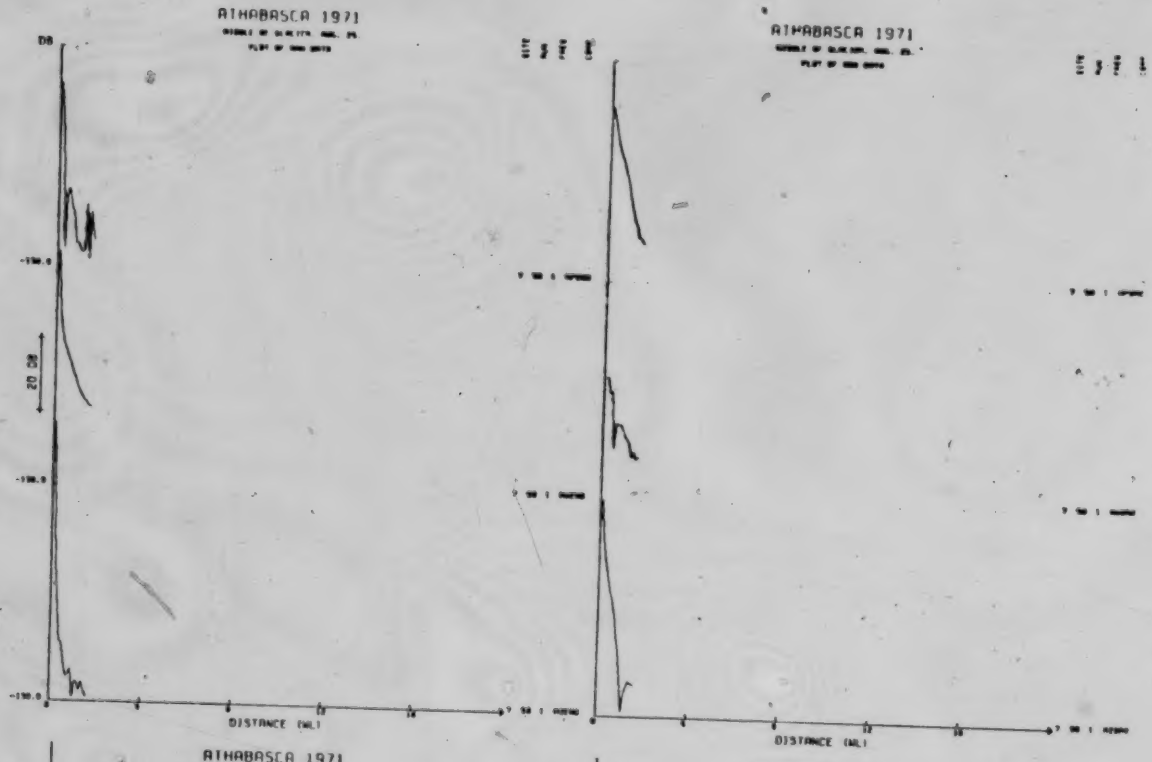
ATHABASCA 1971
DB
DISTANCE (MI)

ATHABASCA 1971
DISTANCE (MI)

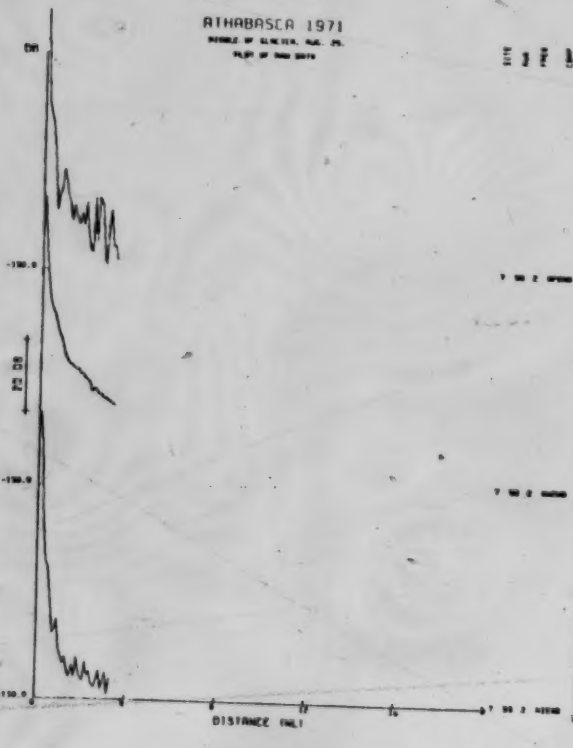
ATHABASCA 1971
DB
DISTANCE (MI)

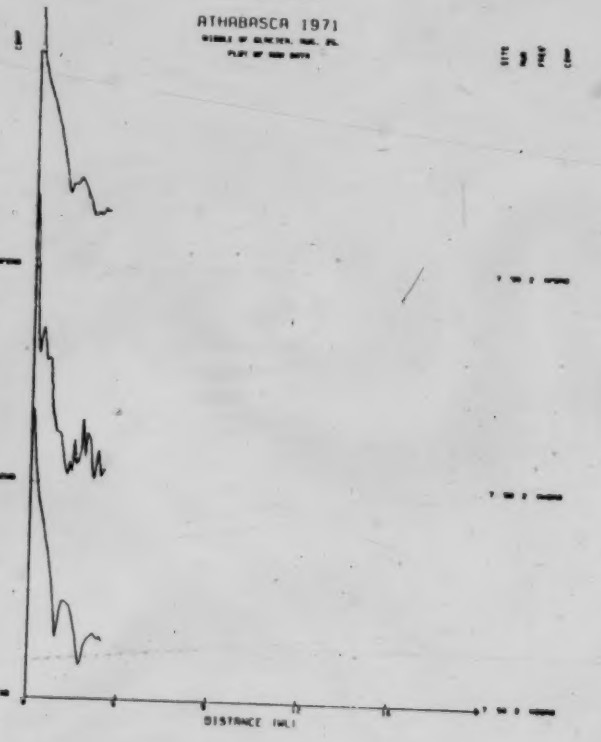
ATHABASCA 1971
DISTANCE (MI)

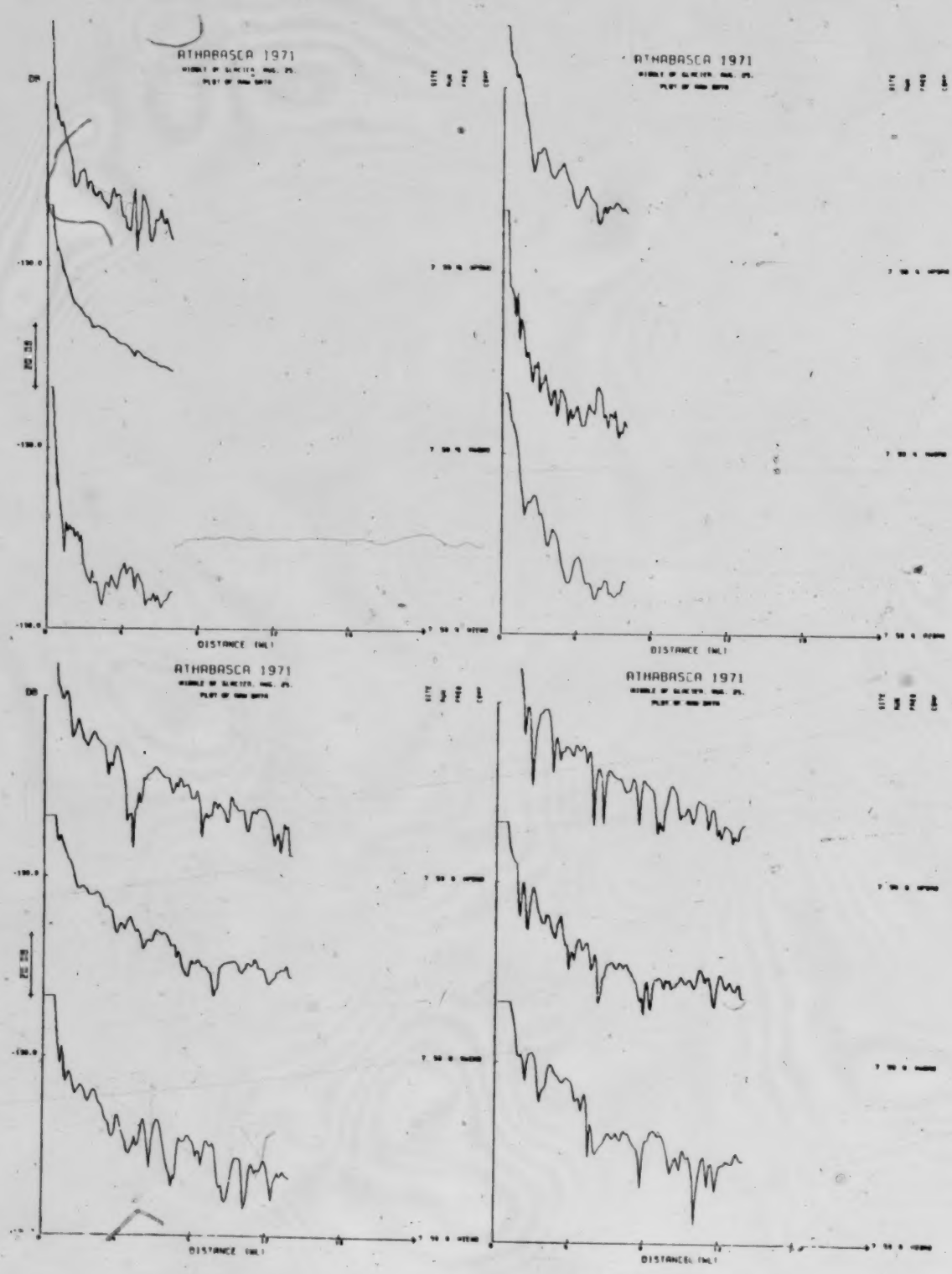
ATHABASCA 1971
DISTANCE (KM.)
ATHABASCA 1971
DISTANCE (KM.)
ATHABASCA 1971
DISTANCE (KM.)
ATHABASCA 1971
DISTANCE (KM.)

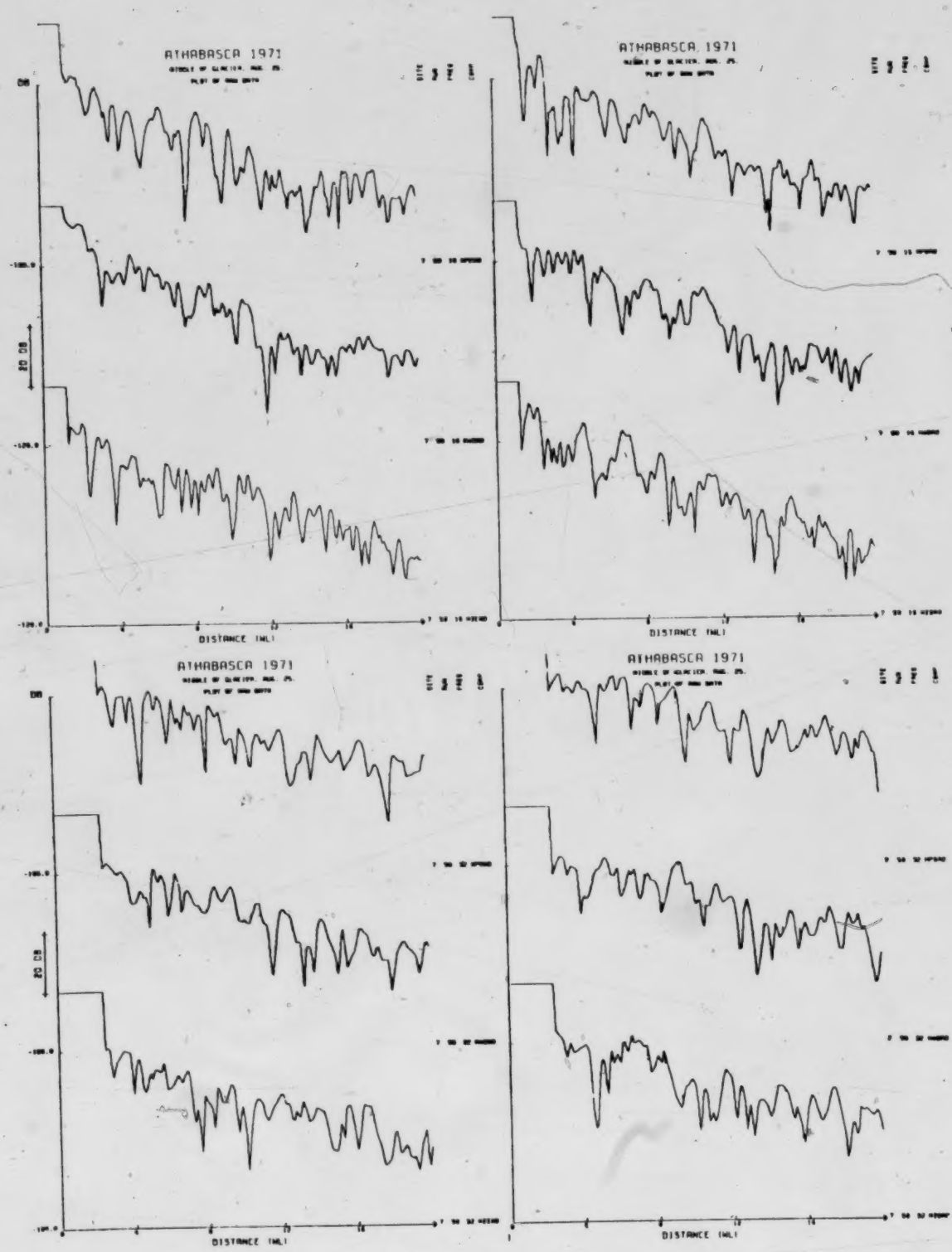
ATHABASCA 1971
DB
20 DB
DISTANCE (MI.)
ATHABASCA 1971
DISTANCE (MI.)
ATHABASCA 1971
DB
20 DB
DISTANCE (MI.)
ATHABASCA 1971
DISTANCE (MI.)

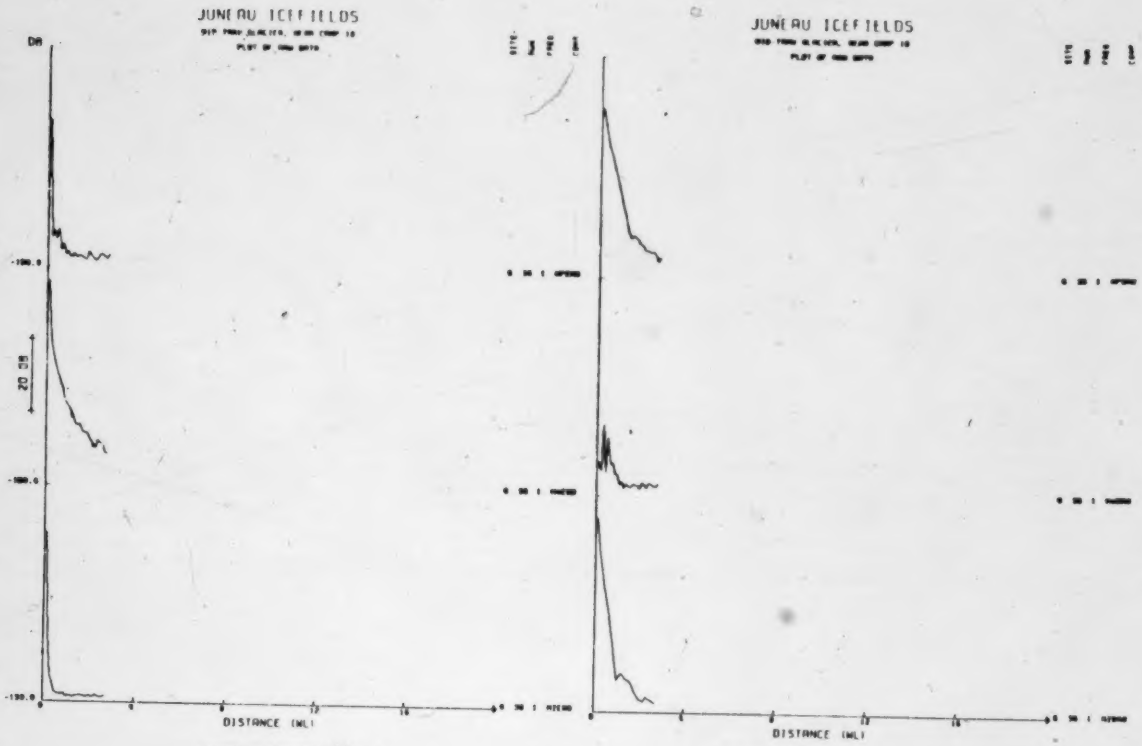
JUNEAU ICEFIELDS
DB
20 DB
DISTANCE (KL)

JUNEAU ICEFIELDS
DISTANCE (KL)

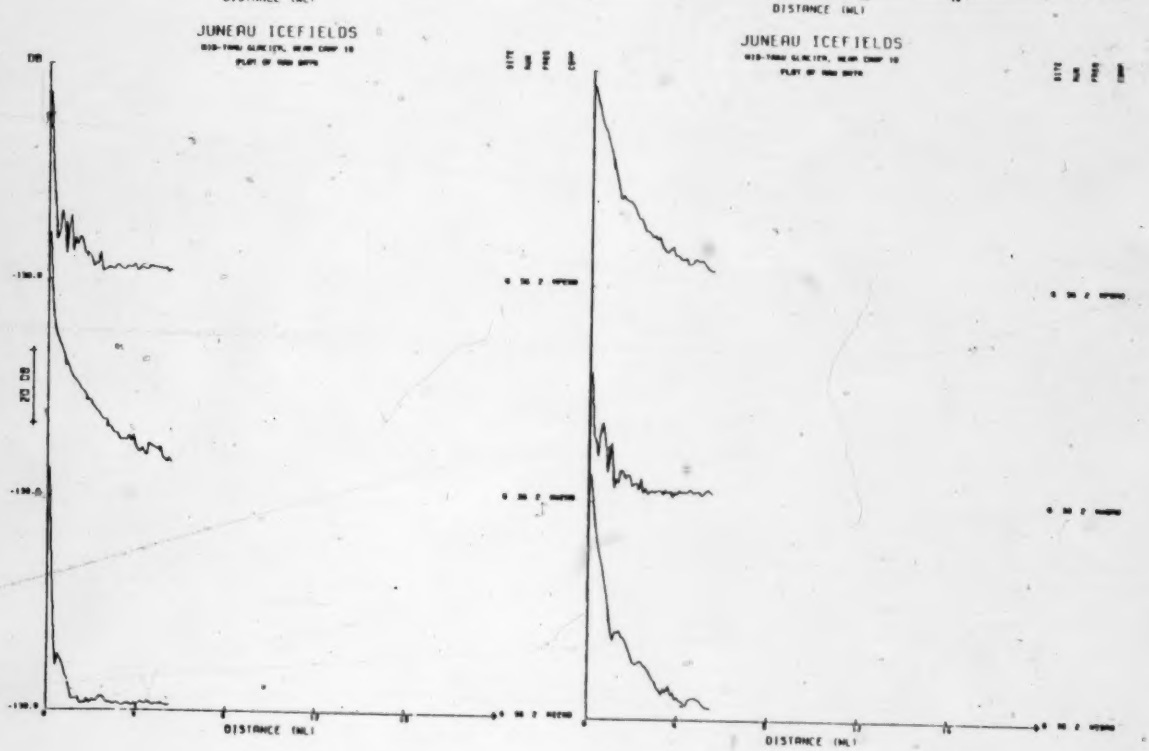
JUNEAU ICEFIELDS
DB
20 DB
DISTANCE (KL)

JUNEAU ICEFIELDS
DISTANCE (KL)

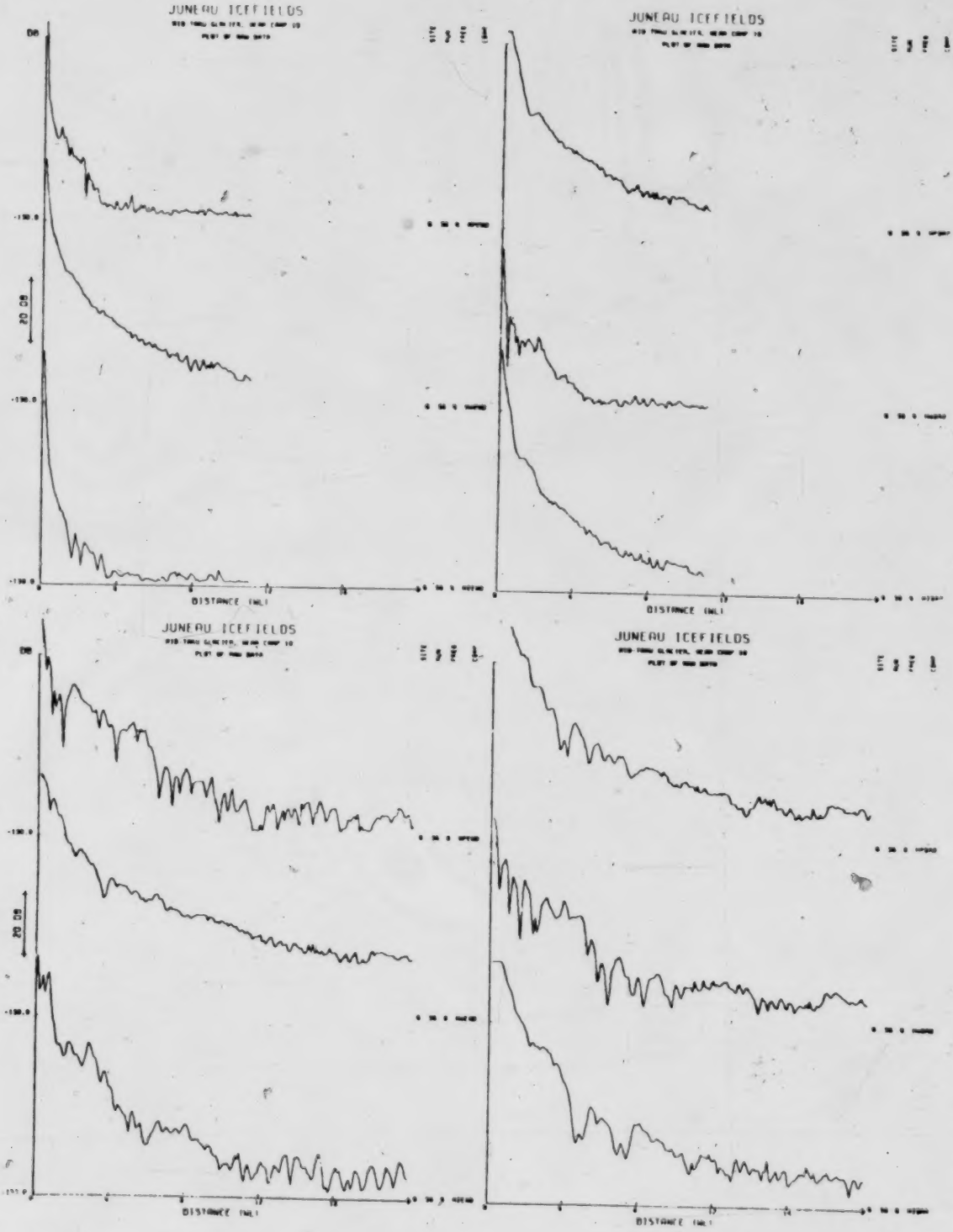
JUNEAU ICEFIELDS
JUNEAU ICEFIELDS
JUNEAU ICEFIELDS
JUNEAU ICEFIELDS
DISTANCE (MI)
DISTANCE (MI)
DISTANCE (MI)
DISTANCE (MI)

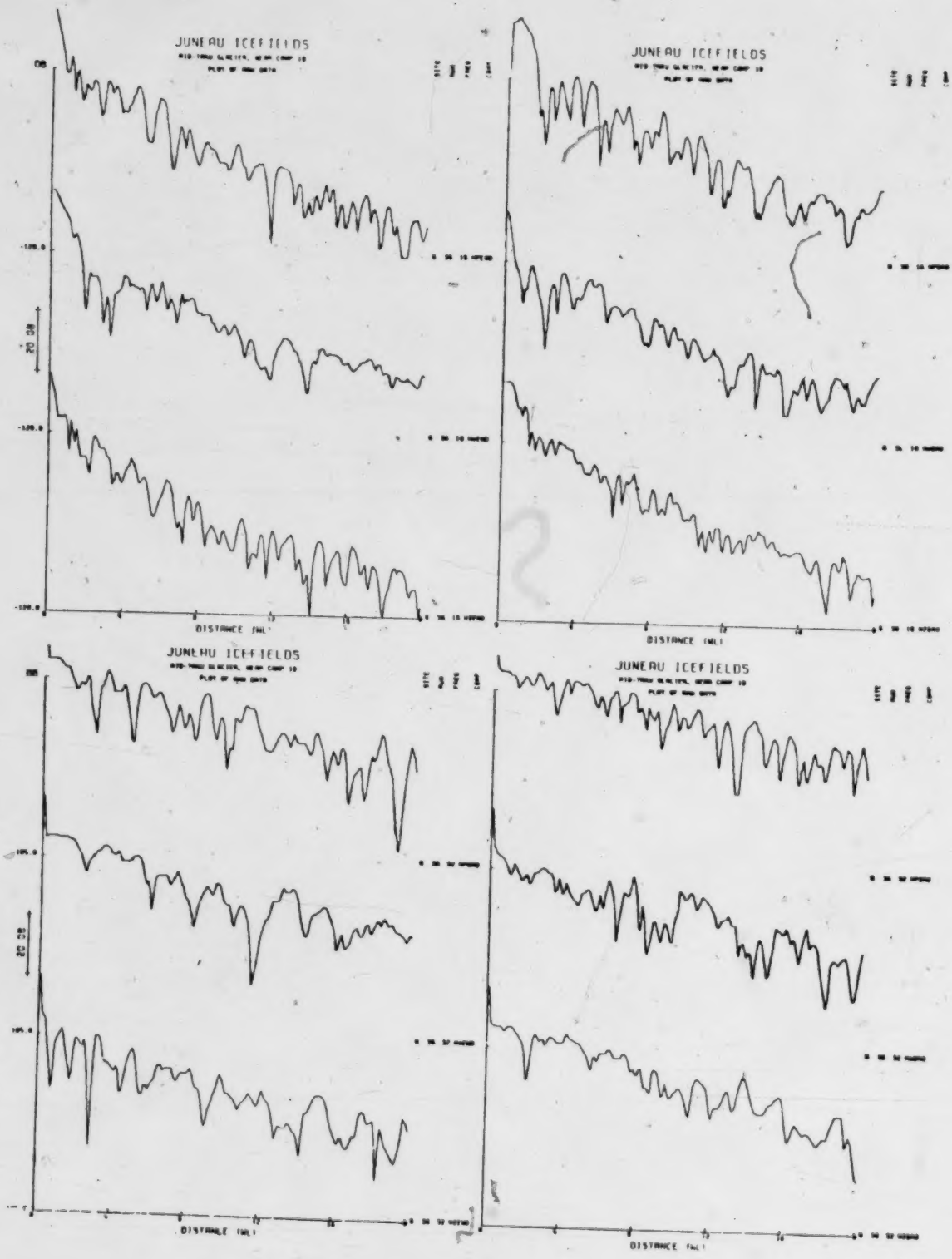
JUNEAU ICEFIELDS
JUNEAU ICEFIELDS
JUNEAU ICEFIELDS
JUNEAU ICEFIELDS
DISTANCE (MI)
DISTANCE (MI)
DISTANCE (MI)
DISTANCE (MI)

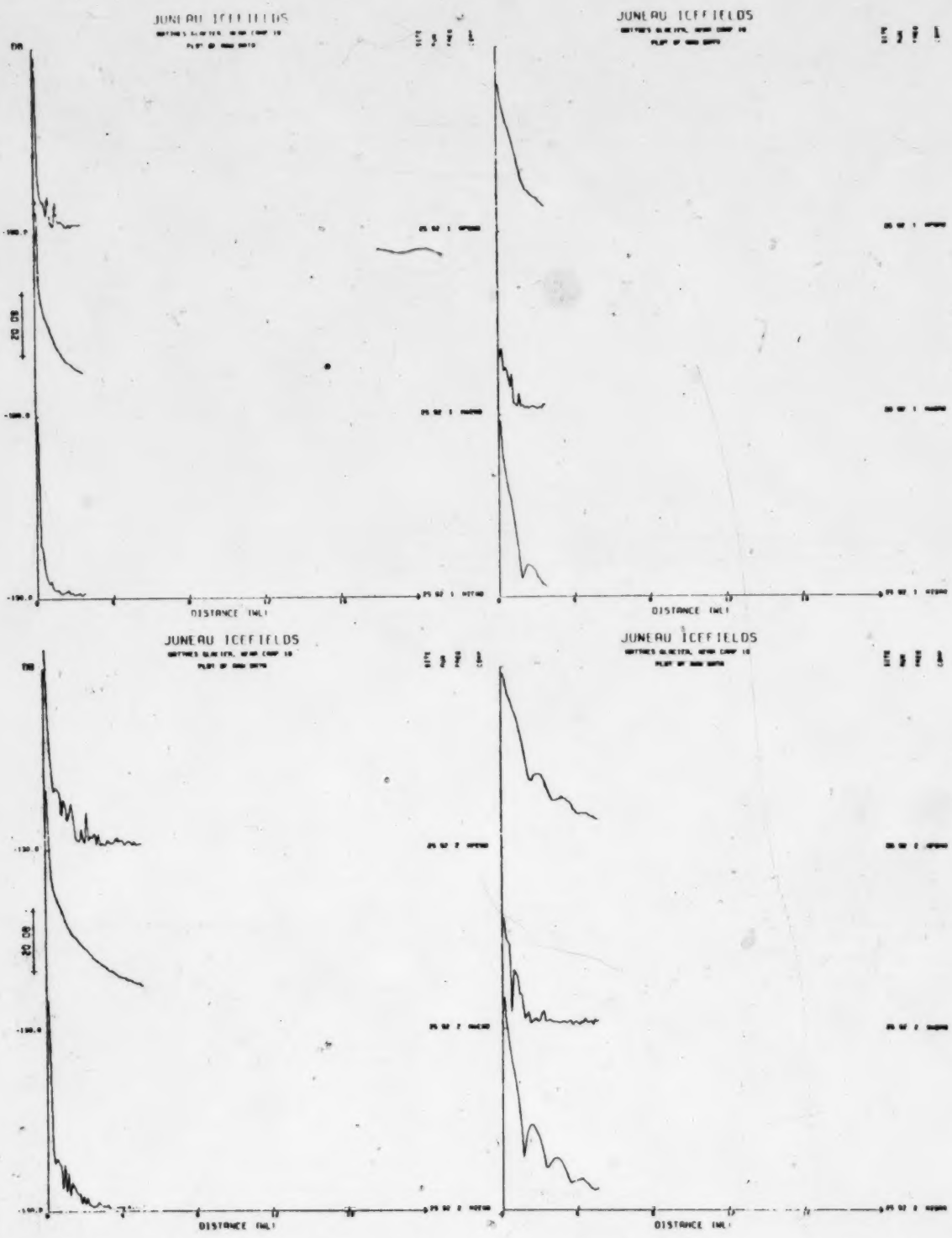
JUNEAU ICEFIELDS
JUNEAU ICEFIELDS
JUNEAU ICEFIELDS
JUNEAU ICEFIELDS
DISTANCE (MI)
DISTANCE (MI)
DISTANCE (MI)
DISTANCE (MI)

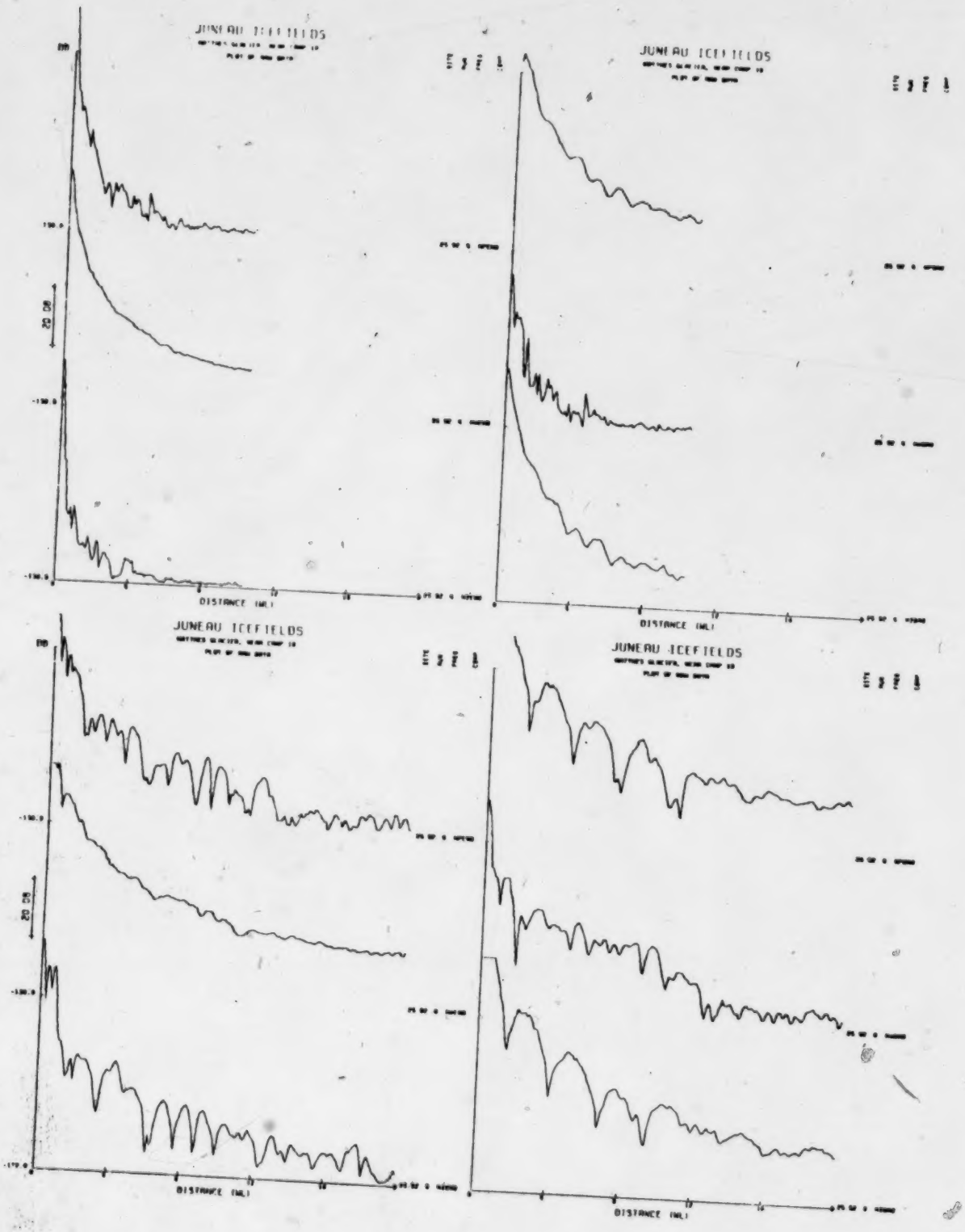
JUNEAU ICEFIELDS
DISTANCE (MI.)
JUNEAU ICEFIELDS
DISTANCE (MI.)
JUNEAU ICEFIELDS
DISTANCE (MI.)
JUNEAU ICEFIELDS
DISTANCE (MI.)

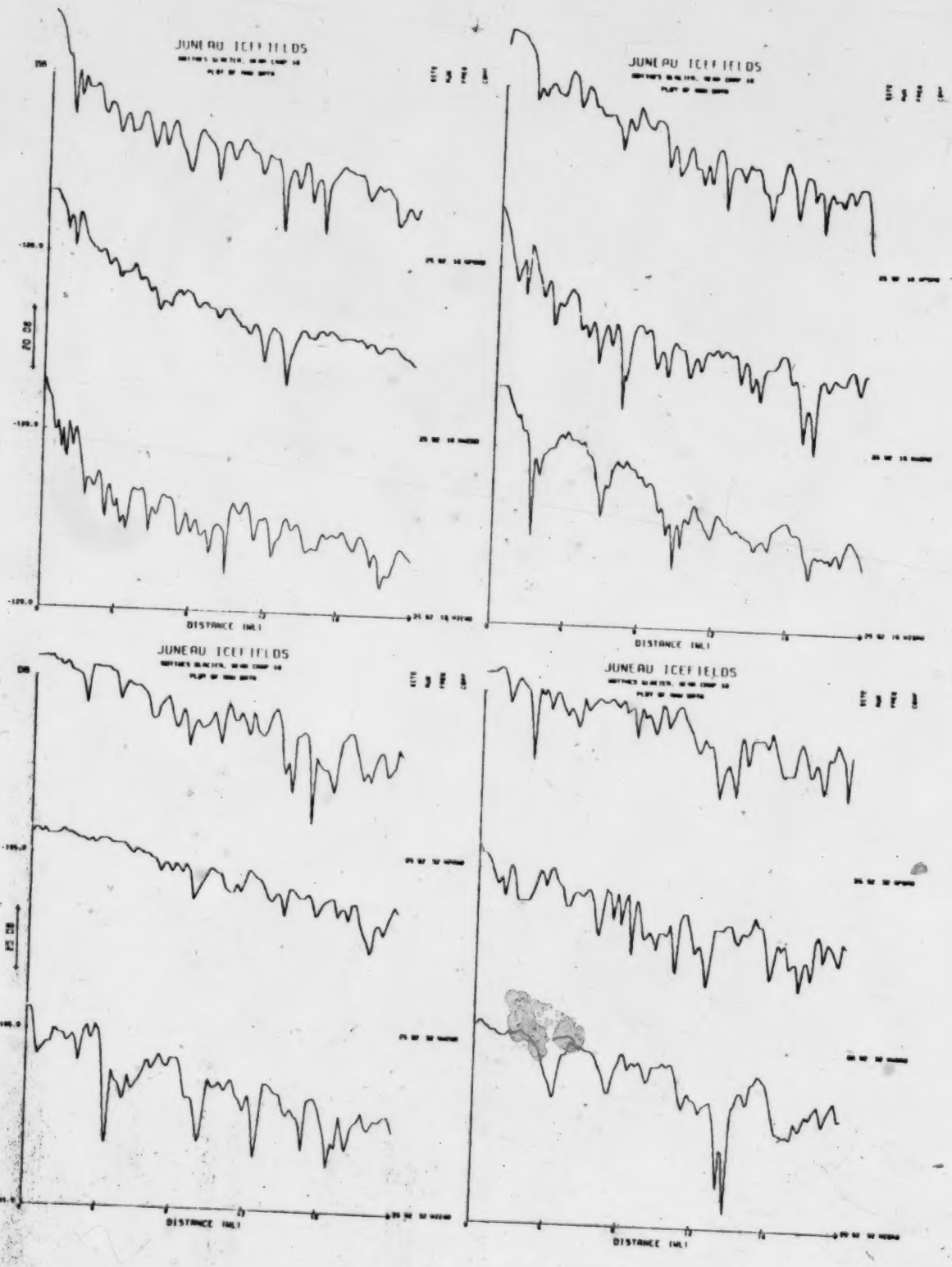
JUNEAU ICEFIELDS
JUNEAU ICEFIELDS
JUNEAU ICEFIELDS
JUNEAU ICEFIELDS
DISTANCE (MI)
DISTANCE (MI)
DISTANCE (MI)
DISTANCE (MI)

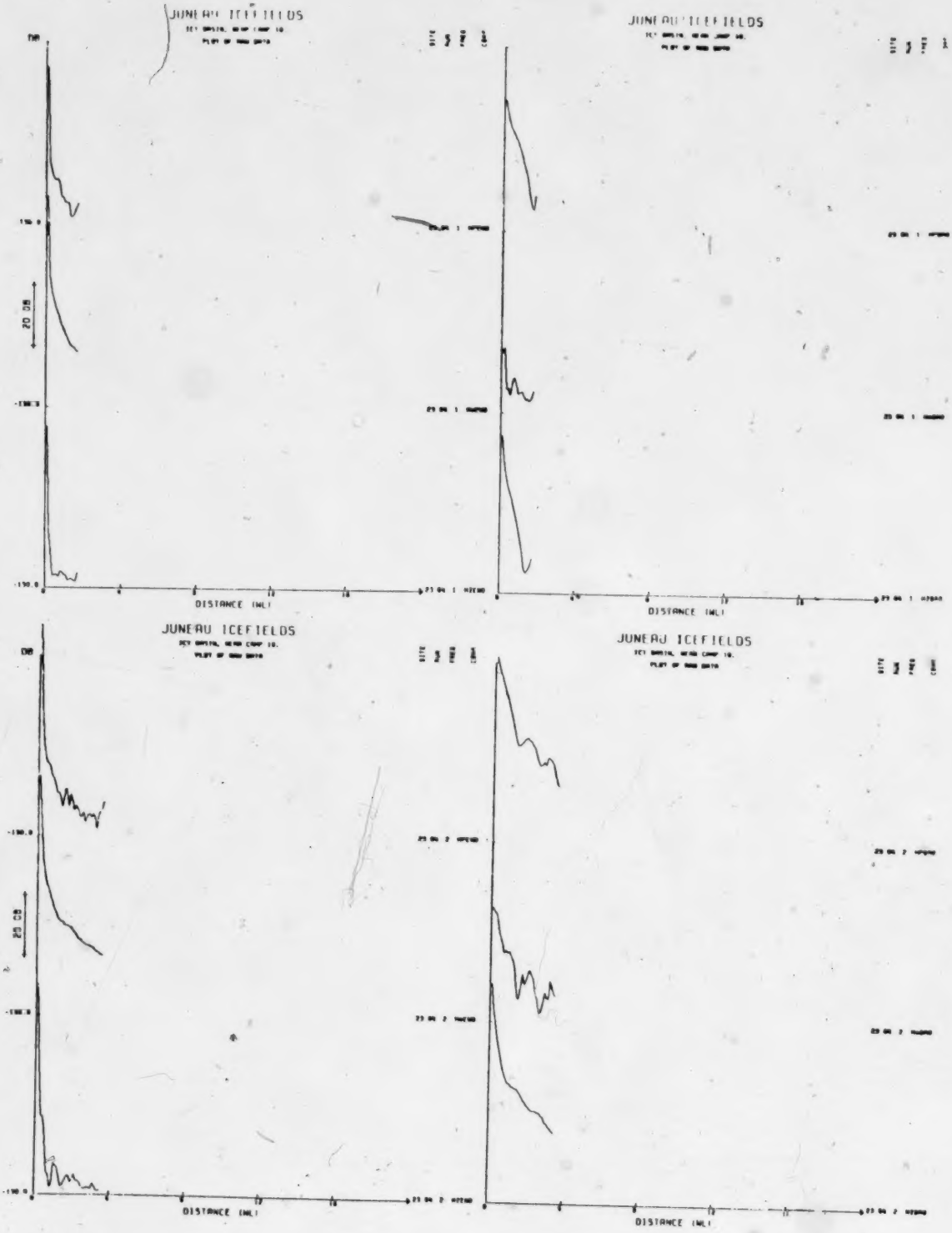
JUNEAU ICEFIELDS
JUNEAU ICEFIELDS
JUNEAU ICEFIELDS
JUNEAU ICEFIELDS
DISTANCE (MI)
DISTANCE (MI)
DISTANCE (MI)
DISTANCE (MI)

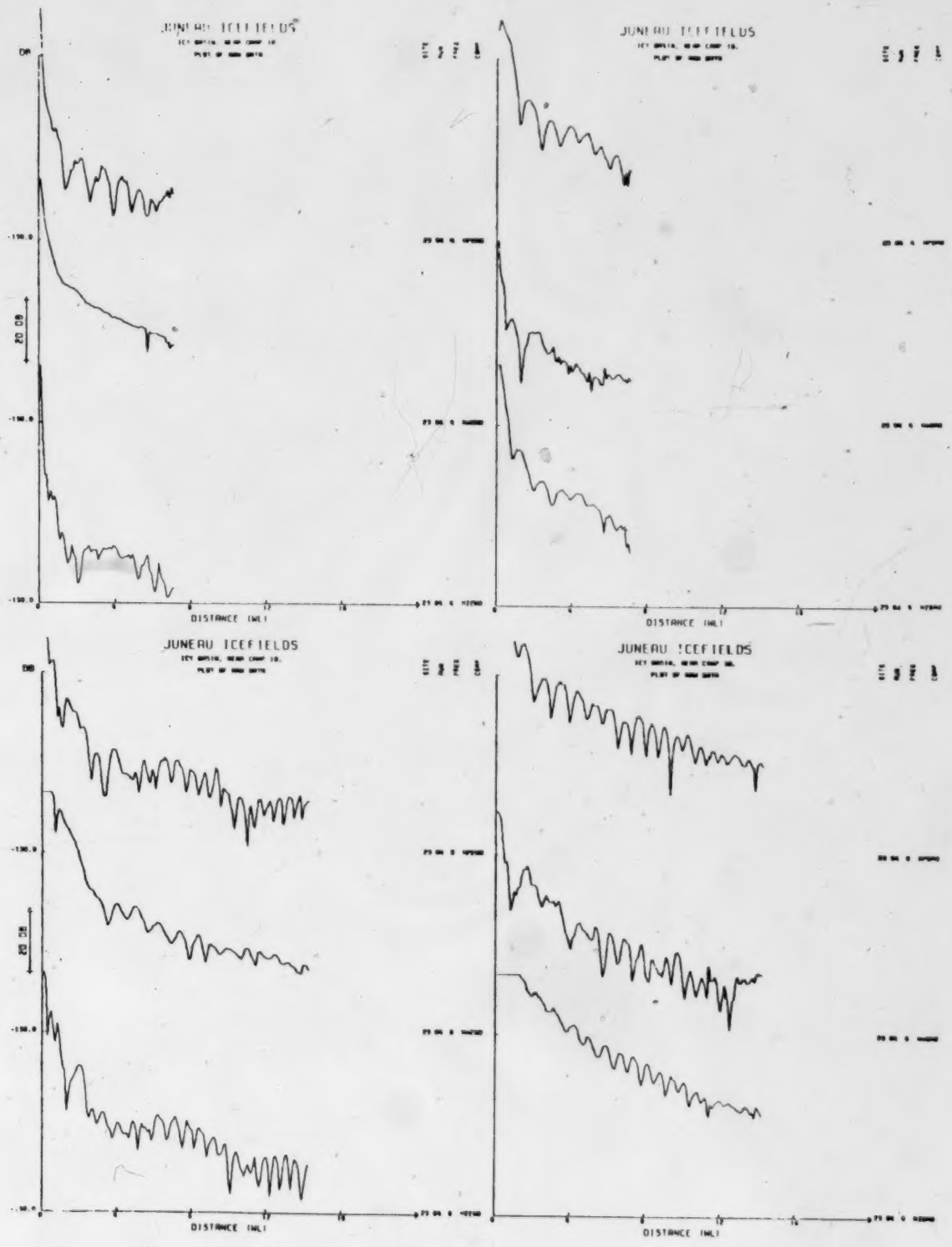
JUNEAU ICEFIELDS
DB
-130.0
20 DB
-150.0
DISTANCE (MI)
JUNEAU ICEFIELDS
DISTANCE (MI)
JUNEAU ICEFIELDS
DB
-130.0
20 DB
-150.0
DISTANCE (MI)
JUNEAU ICEFIELDS
DISTANCE (MI)

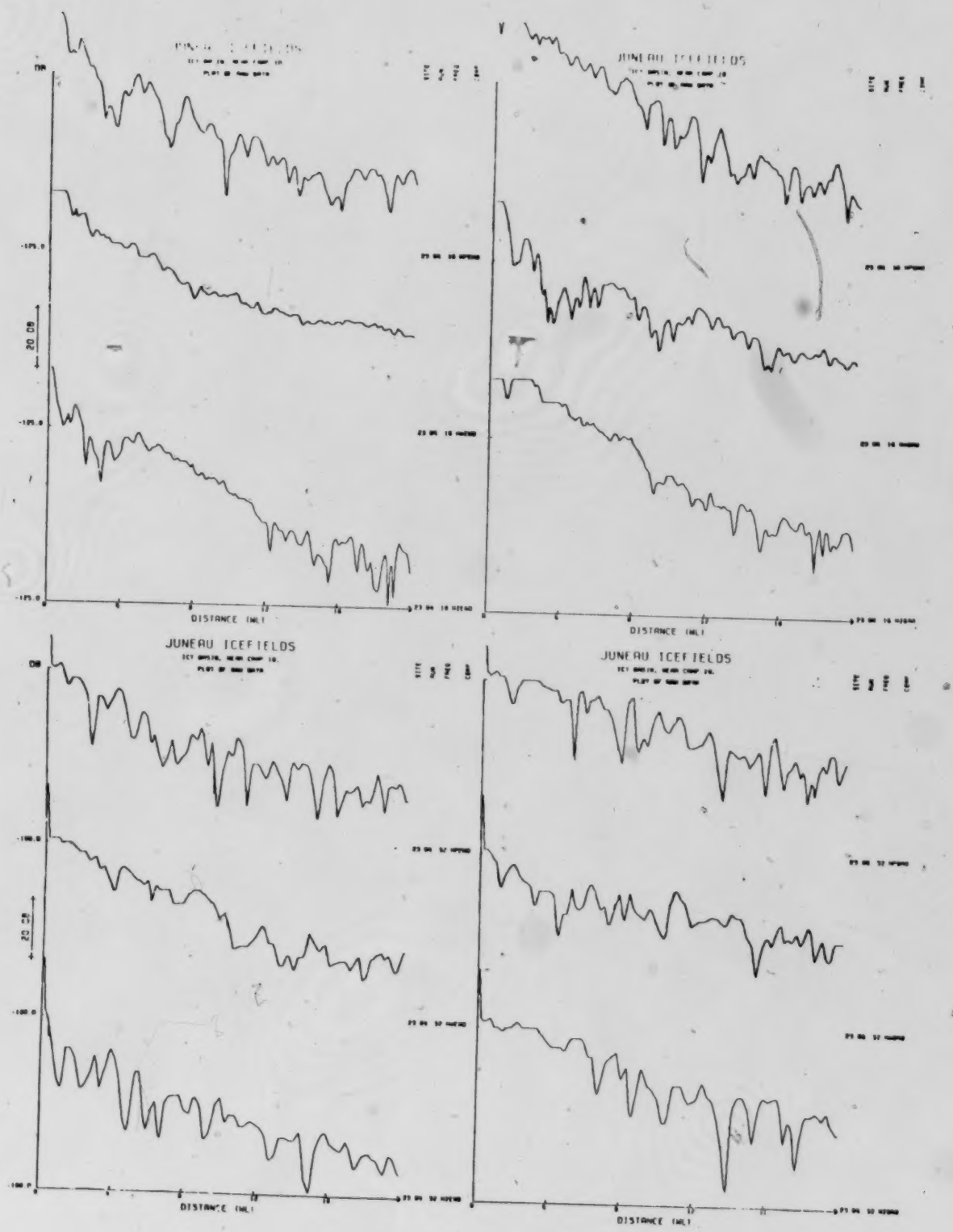
JUNEAU ICEFIELDS
DISTANCE (NI)
JUNEAU ICEFIELDS
DISTANCE (NI)
JUNEAU ICEFIELDS
DISTANCE (NI)
JUNEAU ICEFIELDS
DISTANCE (NI)

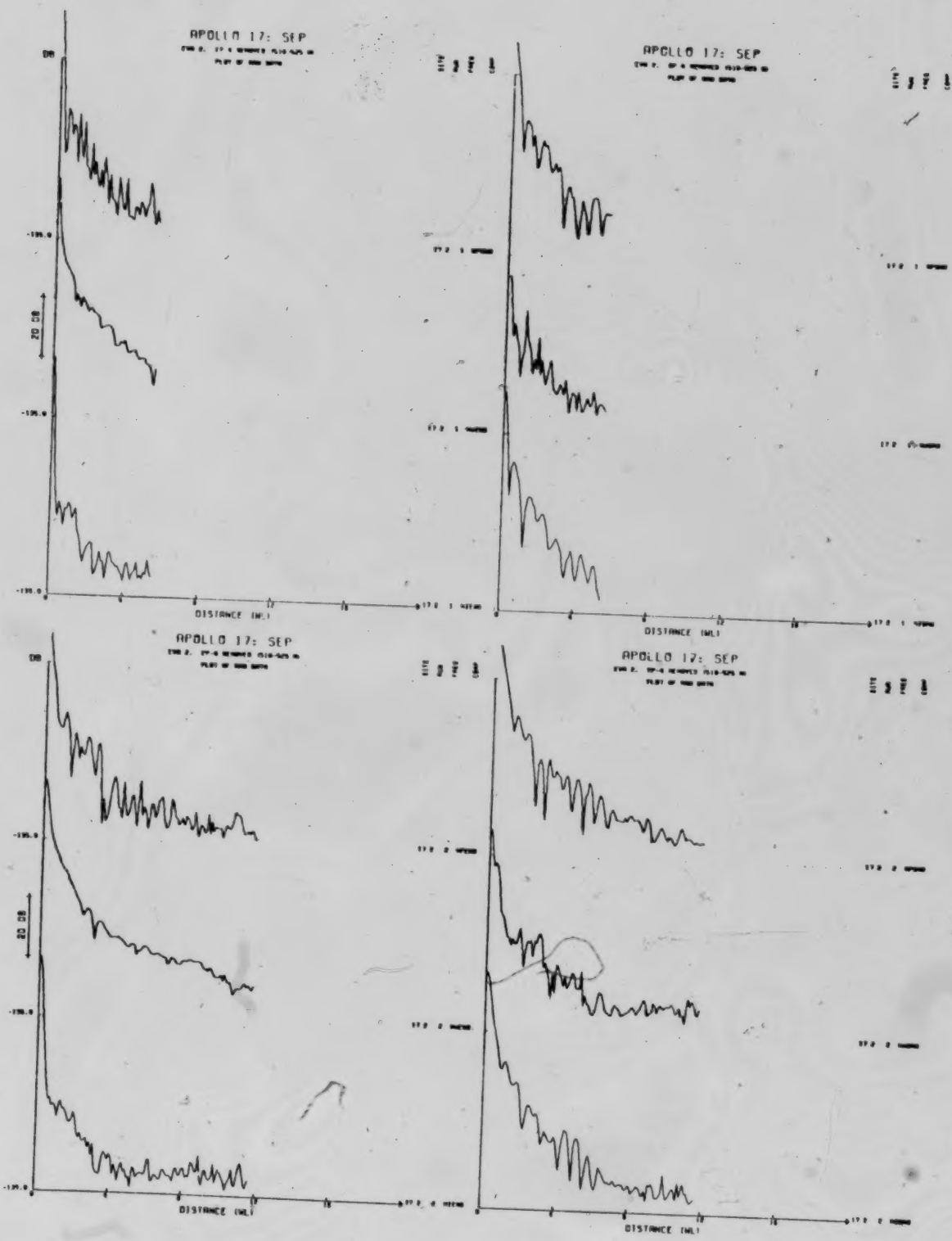
APOLLO 17: SEP
APOLLO 17: SEP
APOLLO 17: SEP
APOLLO 17: SEP
20 DB
DISTANCE (NI)

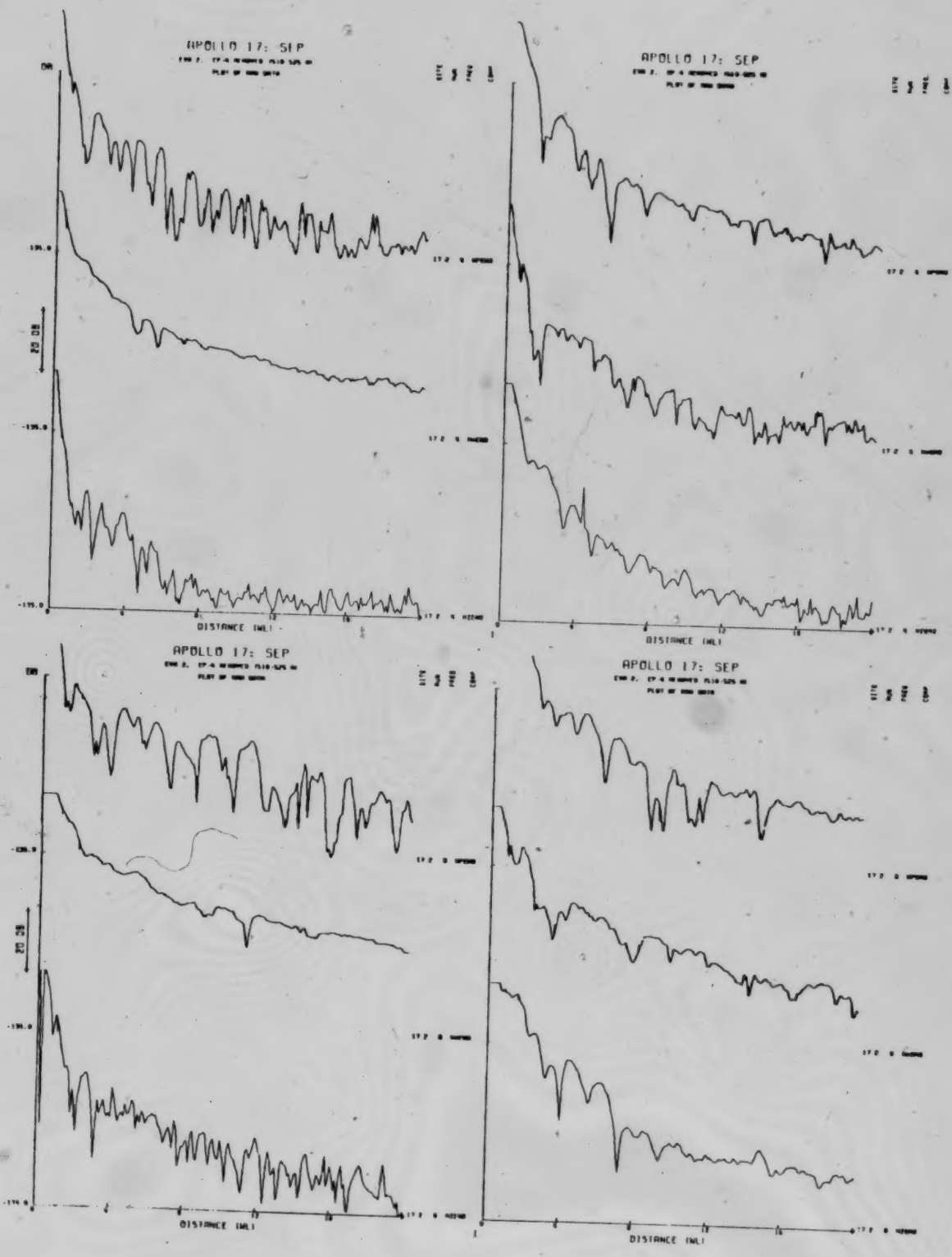
APOLLO 17: SEP
DISTANCE (AU)
APOLLO 17: SEP
DISTANCE (AU)
APOLLO 17: SEP
DISTANCE (AU)
APOLLO 17: SEP
DISTANCE (AU)

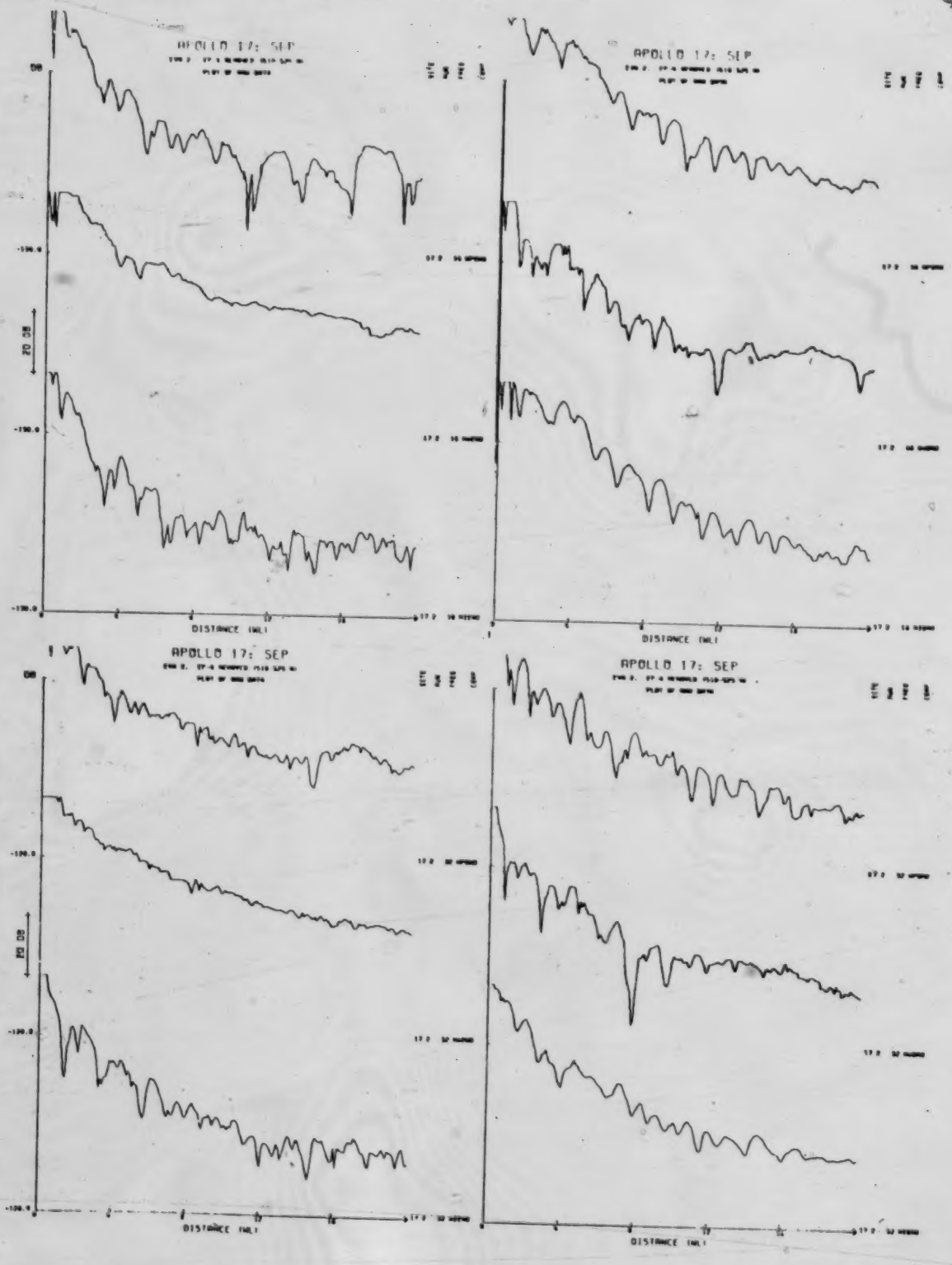
APOLLO 17: SEP
APOLLO 17: SEP
APOLLO 17: SEP
APOLLO 17: SEP
DISTANCE (KM)
DISTANCE (KM)
DISTANCE (KM)
DISTANCE (KM)

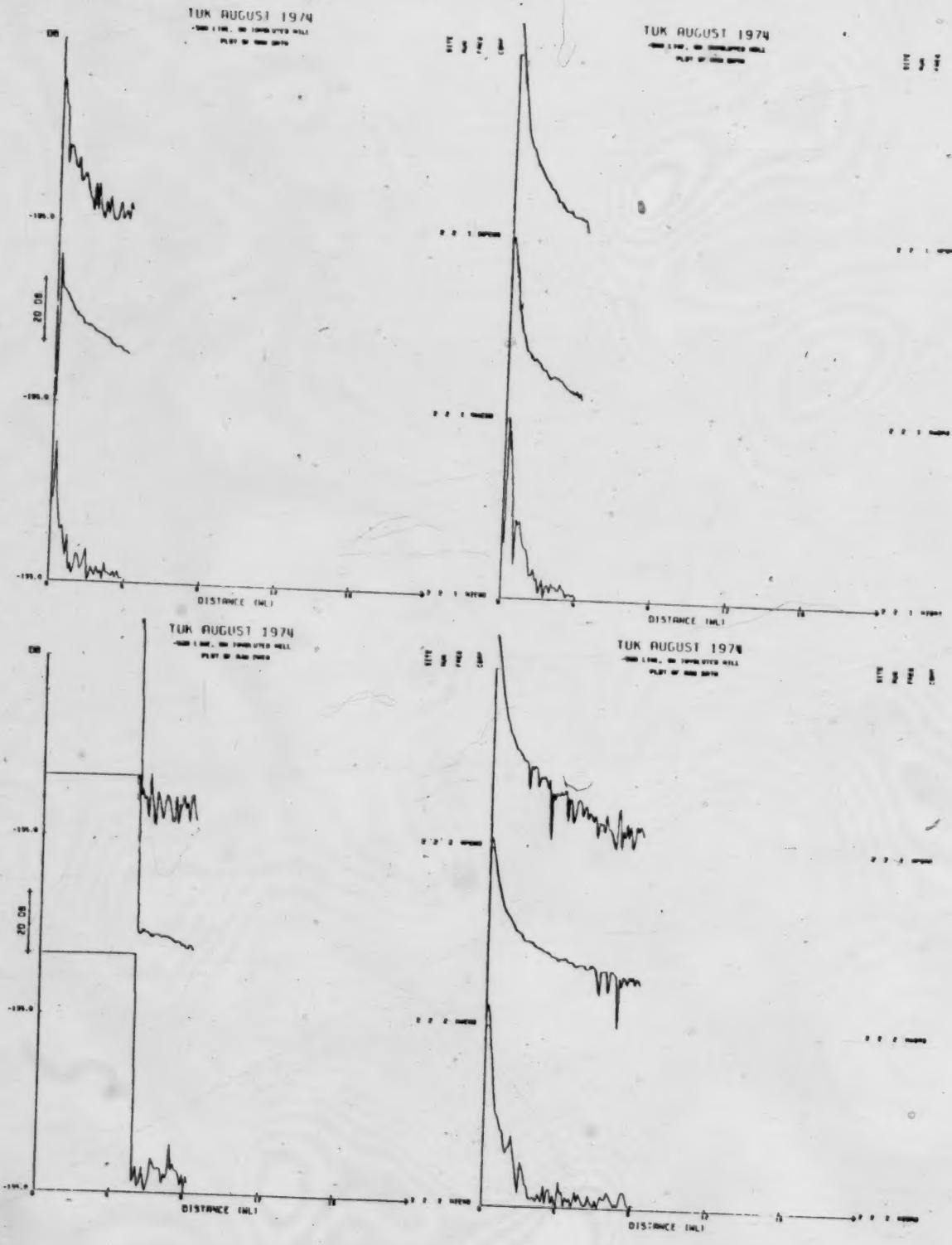
TUK AUGUST 1974
TUK AUGUST 1974
TUK AUGUST 1974
TUK AUGUST 1974
20 DB
DISTANCE (MI)
DISTANCE (MI)
DISTANCE (MI)
DISTANCE (MI)

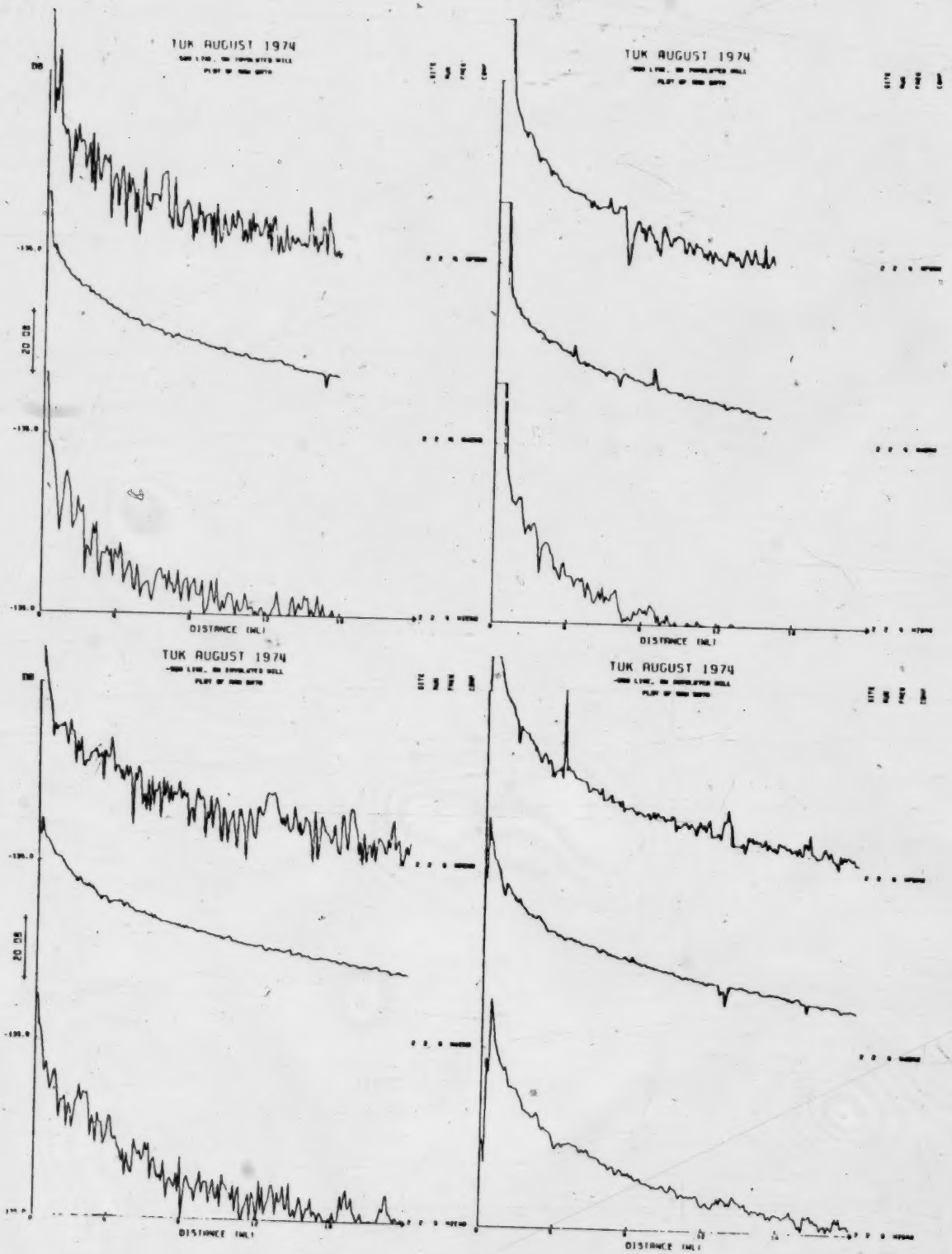
TUK AUGUST 1974
20 DB
DISTANCE (MI)
TUK AUGUST 1974
DISTANCE (MI)
TUK AUGUST 1974
20 DB
DISTANCE (MI)
TUK AUGUST 1974
DISTANCE (MI)

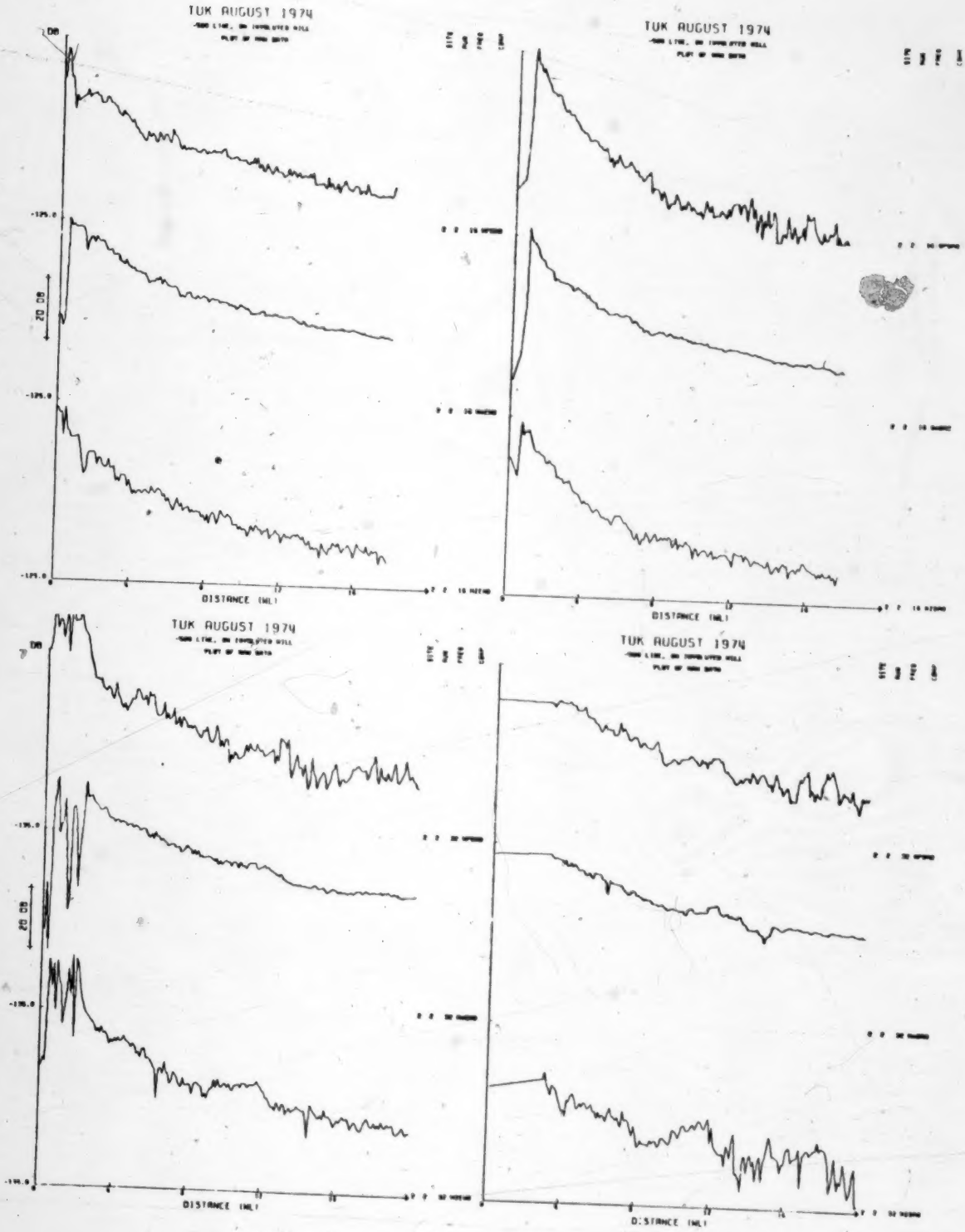
TUK AUGUST 1974
DB
20 DB
DISTANCE (MI.)
TUK AUGUST 1974
DISTANCE (MI.)
TUK AUGUST 1974
DB
20 DB
DISTANCE (MI.)
TUK AUGUST 1974
DISTANCE (MI.)

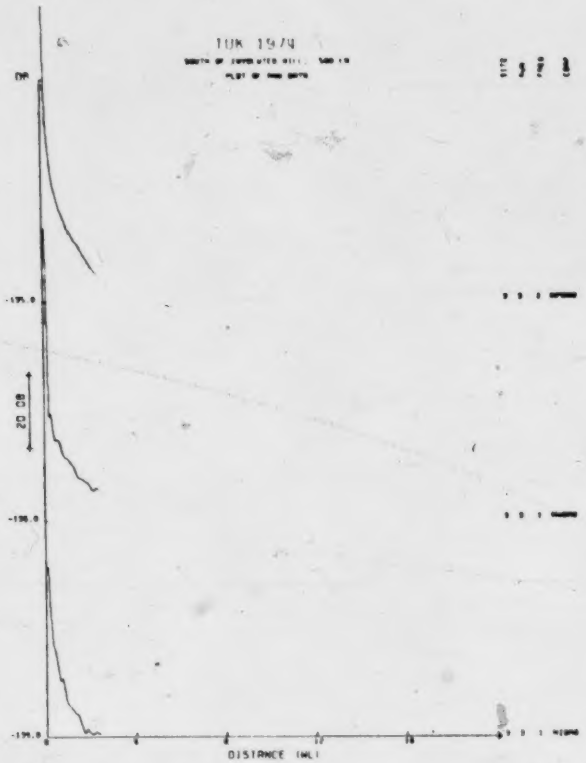
TUK 1974
DB
20 DB
DISTANCE (MI.)

TUK 1974
DB
20 DB
DISTANCE (MI.)

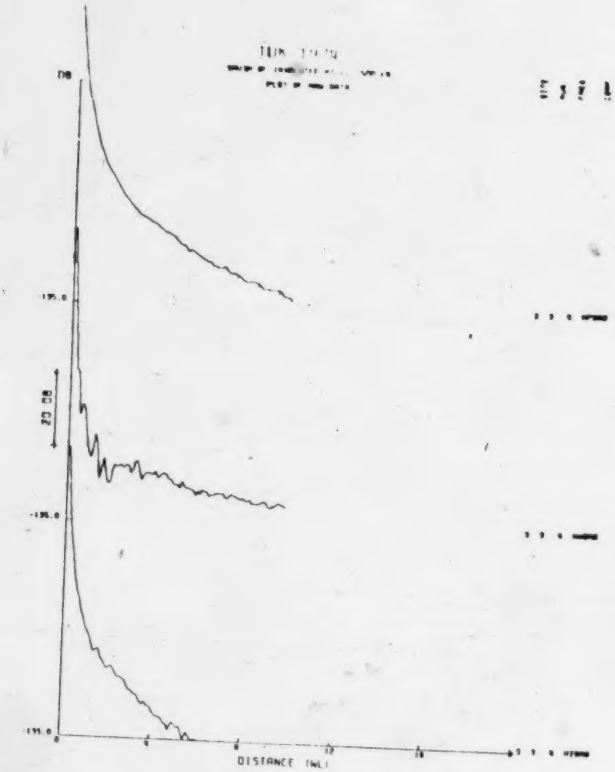
DB
20 DB
DISTANCE (MI)

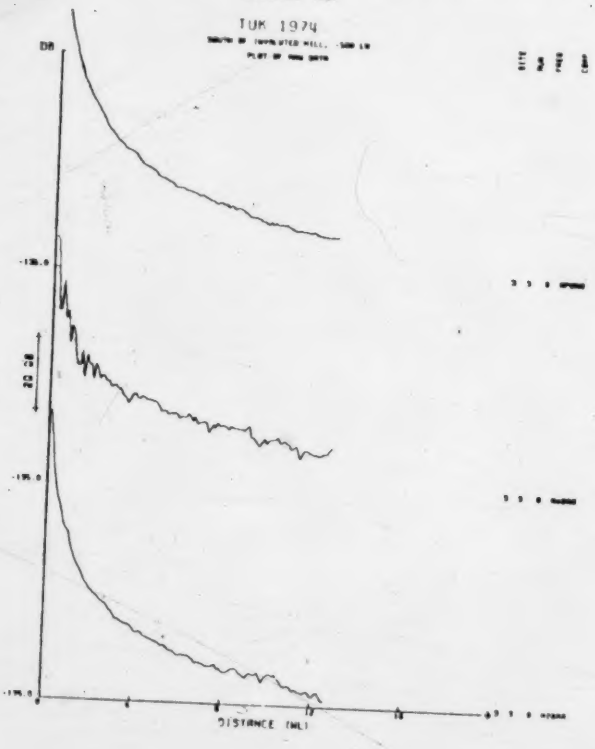
TUK 1974
DB
20 DB
DISTANCE (MI)

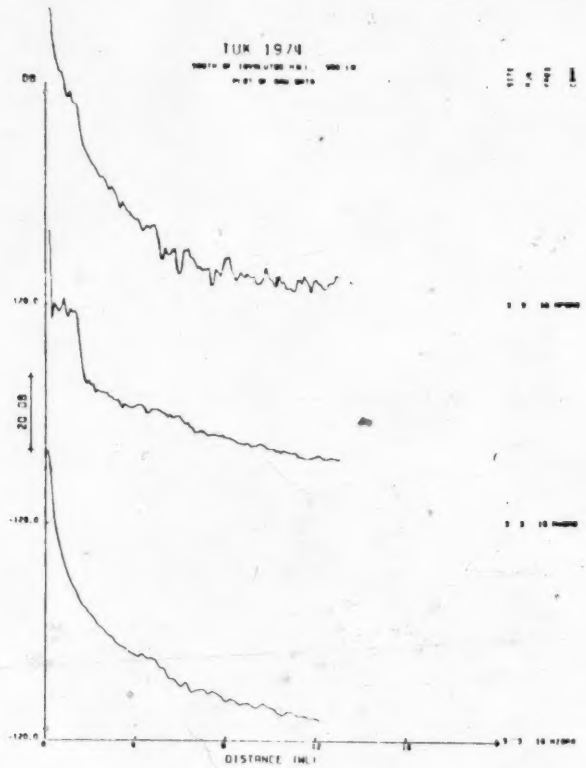
TUK 1974
DB
20 DB
DISTANCE (MI.)

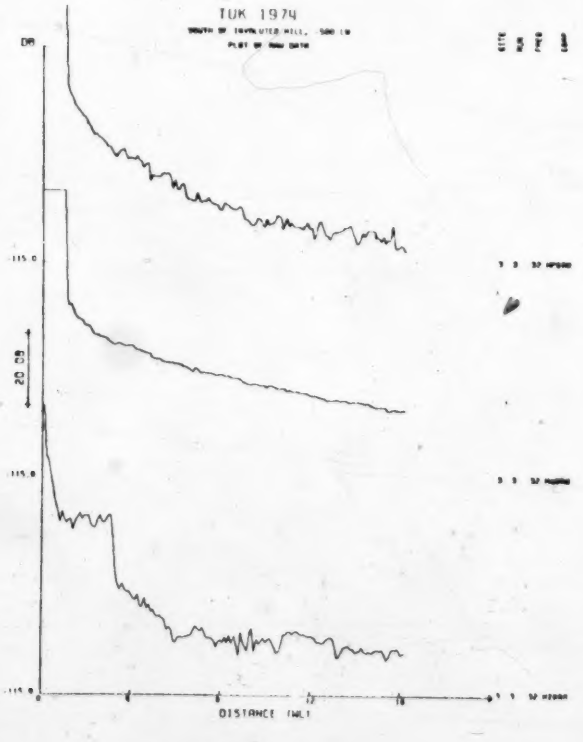
TUK 1974
DB
20 DB
DISTANCE (MI.)

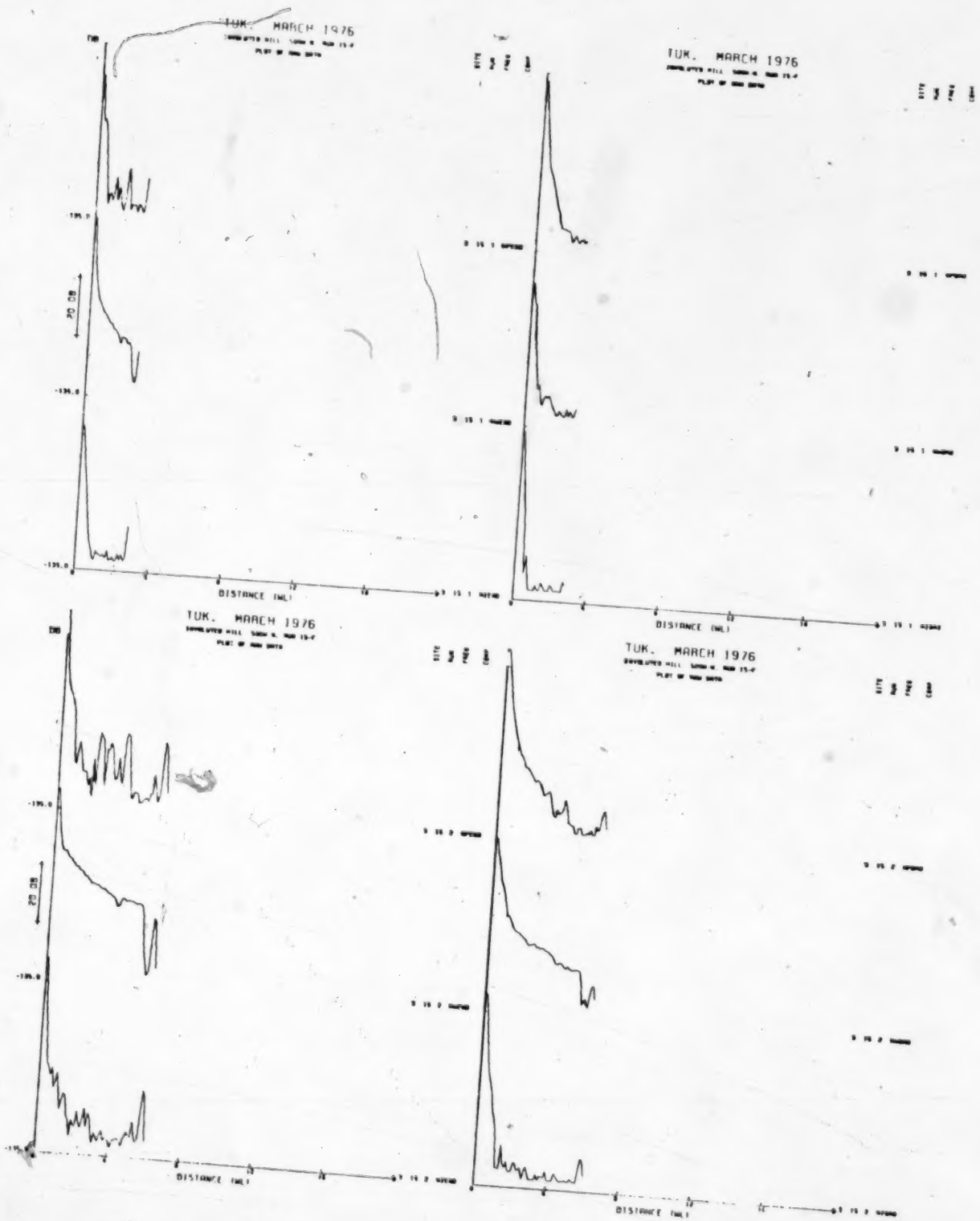
TUK. MARCH 1976
DB
20 DB
DISTANCE (MI)
TUK. MARCH 1976
DISTANCE (MI)
TUK. MARCH 1976
DB
20 DB
DISTANCE (MI)
TUK. MARCH 1976
DISTANCE (MI)

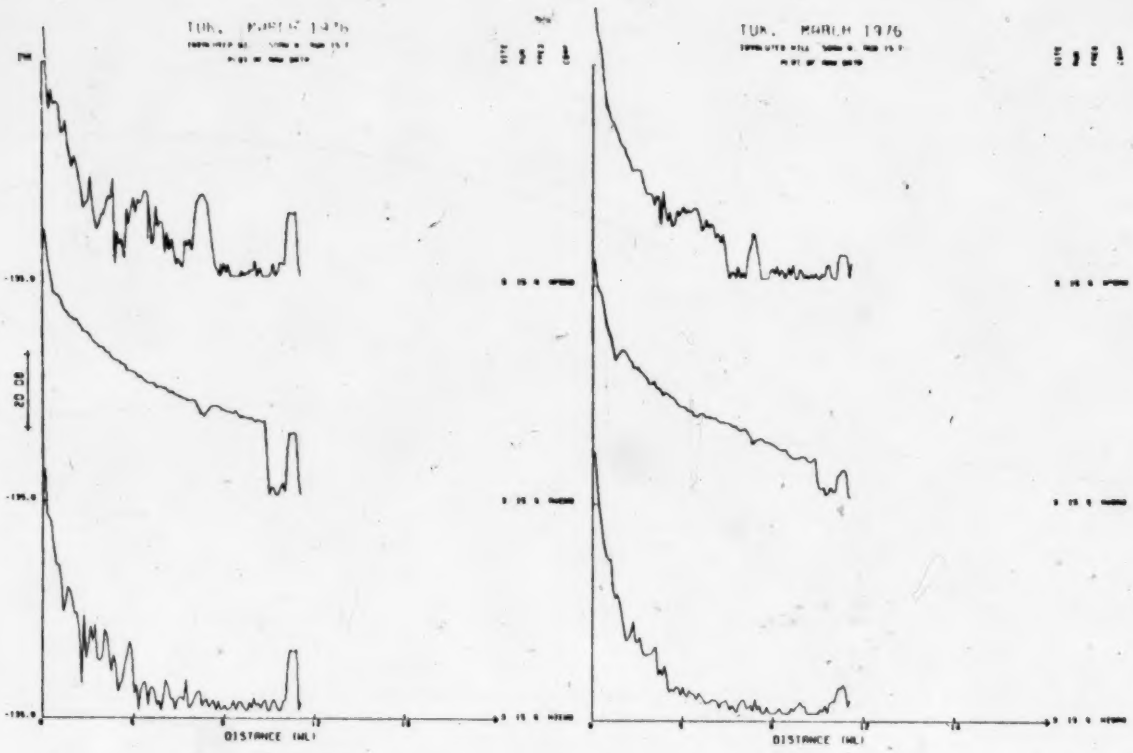
TUK. MARCH 1976
DISTANCE (NL)

TUK. MARCH 1976
DISTANCE (NL)

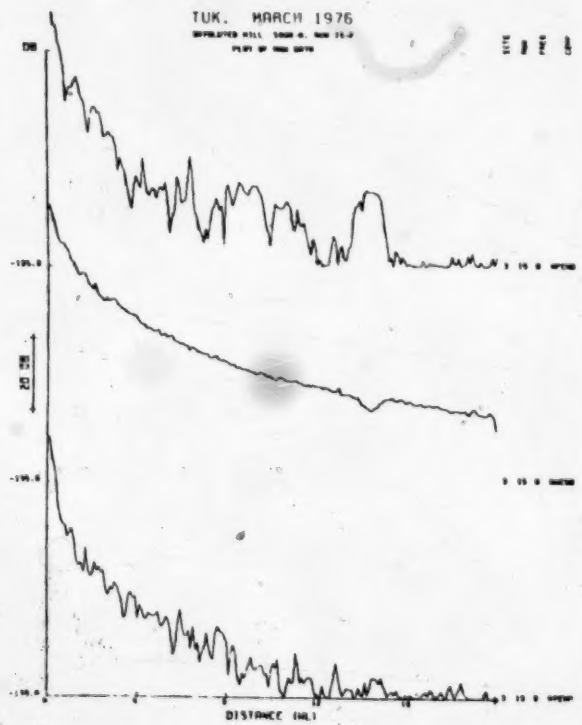
TUK. MARCH 1976
DISTANCE (NL)

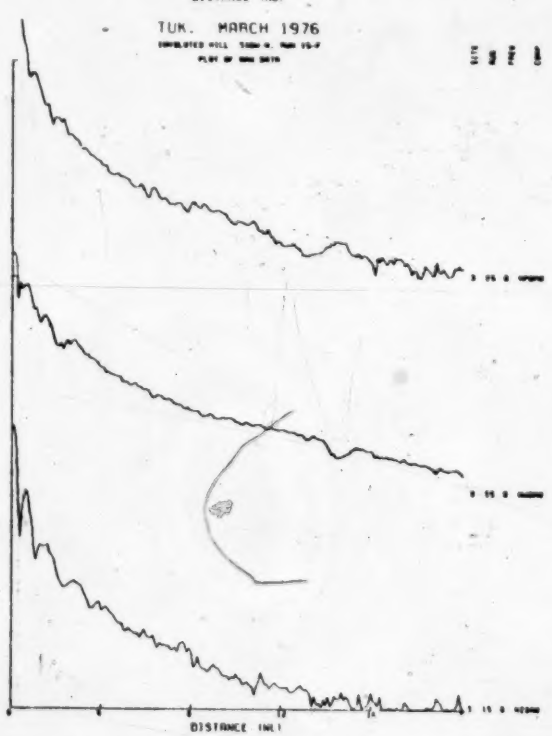
TUK. MARCH 1976
DISTANCE (NL)

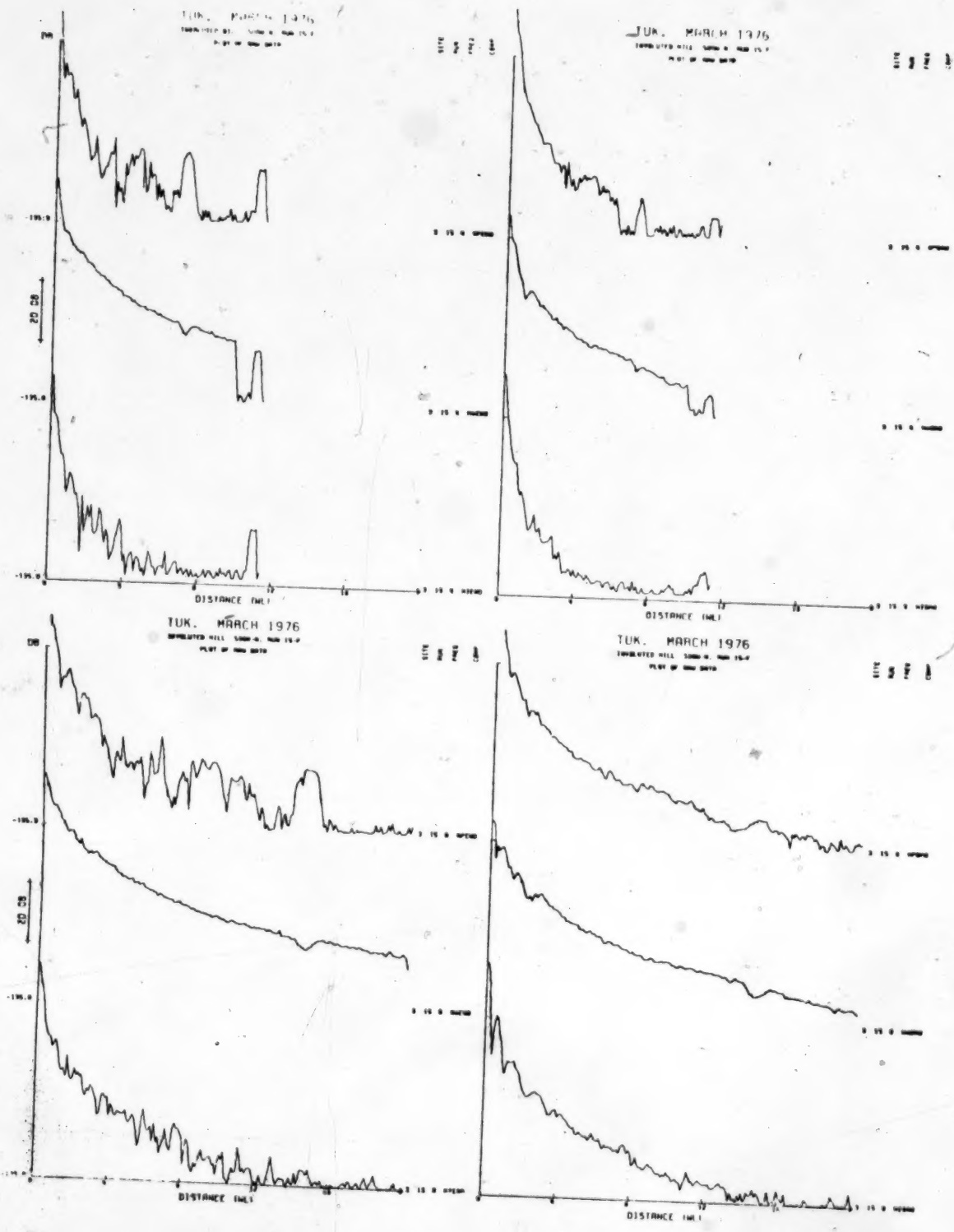
TUK. MARCH 1976
DISTANCE (MI)
TUK. MARCH 1976
DISTANCE (MI)
TUK. MARCH 1976
DISTANCE (MI)
TUK. MARCH 1976
DISTANCE (MI)

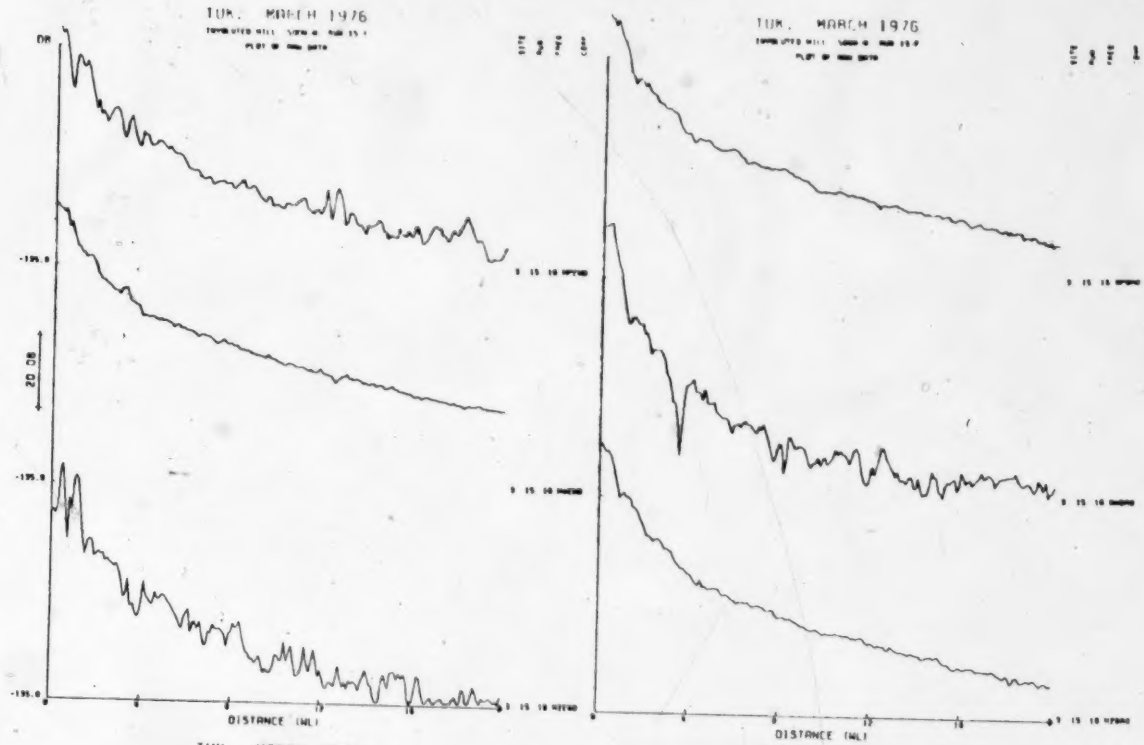
TUK. MARCH 1976
DB
-135.0
20 DB
-135.0
-135.0
DISTANCE (NL)

TUK. MARCH 1976
DISTANCE (NL)

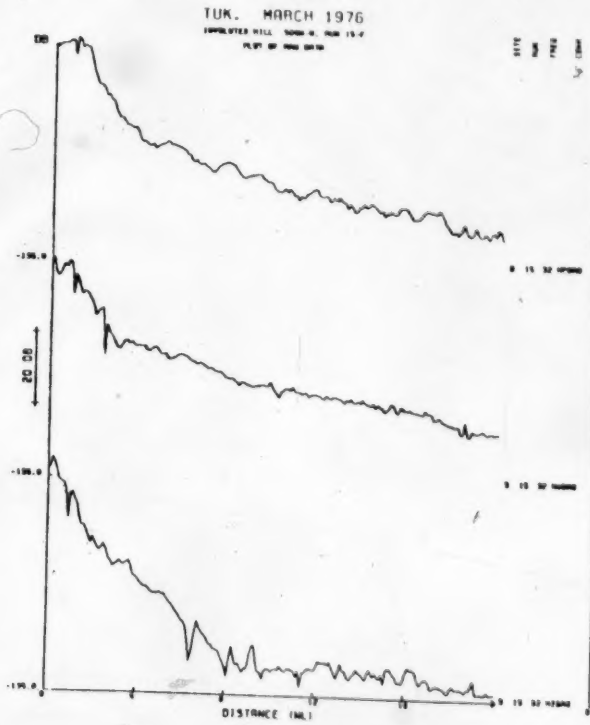
TUK. MARCH 1976
DB
-135.0
20 DB
-135.0
-135.0
DISTANCE (NL)

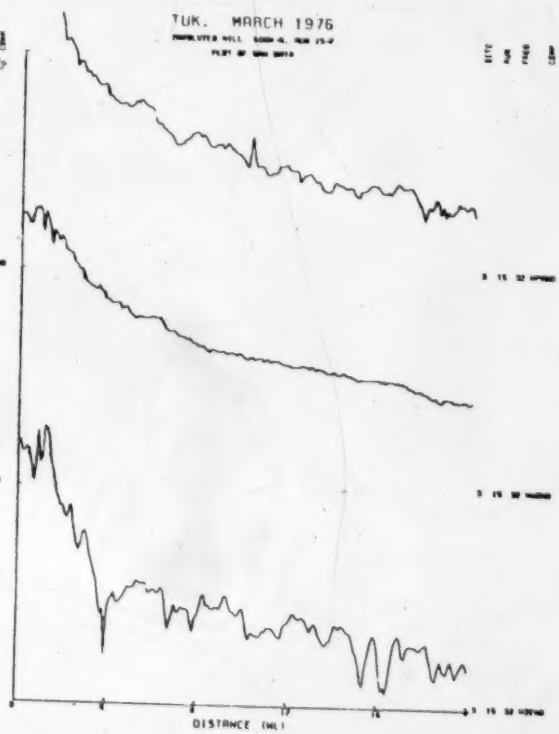
TUK. MARCH 1976
DISTANCE (NL)

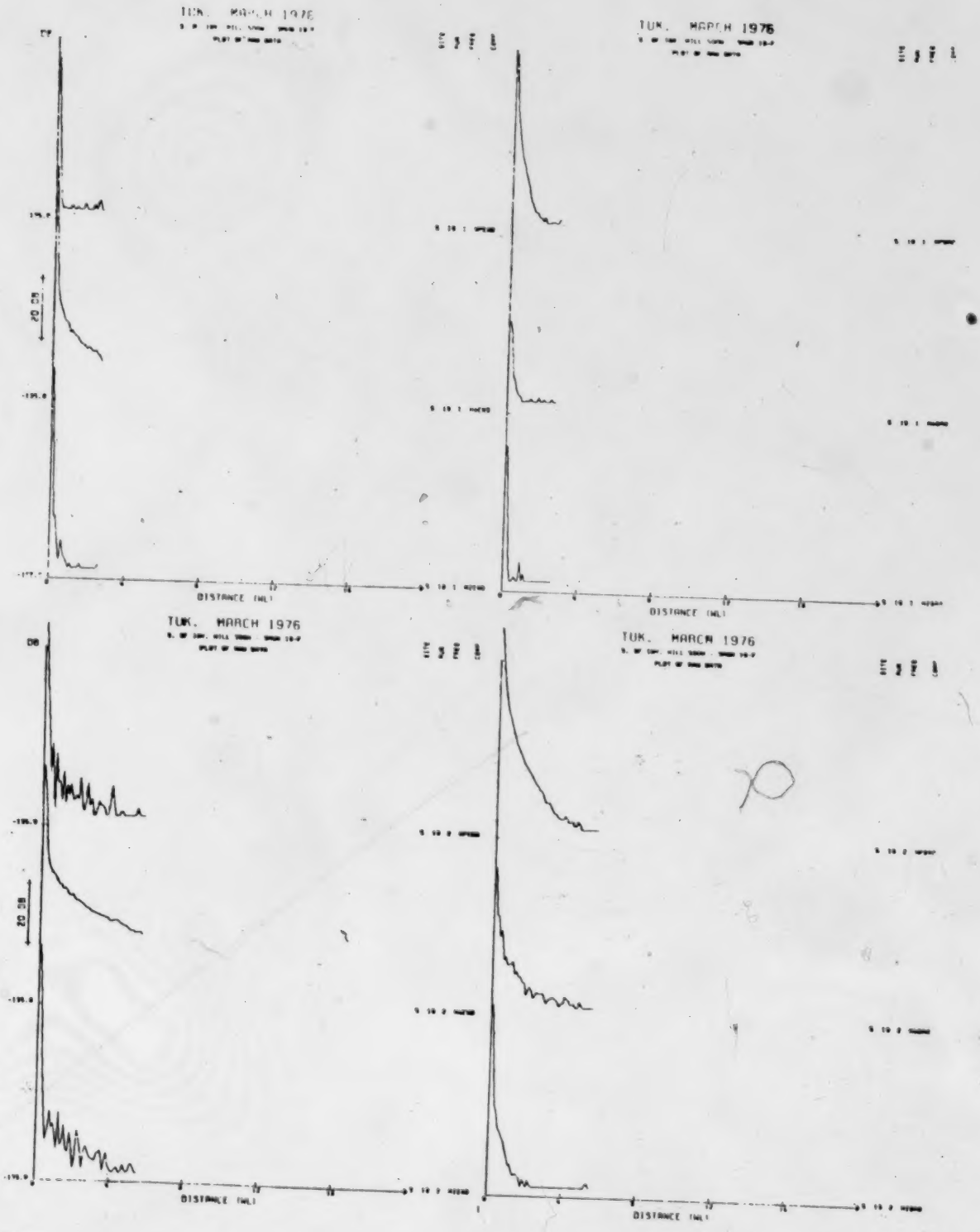
TUK. MARCH 1976
DB
20 DB
DISTANCE (MI)
TUK. MARCH 1976
DISTANCE (MI)
TUK. MARCH 1976
20 DB
DISTANCE (MI)
TUK. MARCH 1976
DISTANCE (MI)

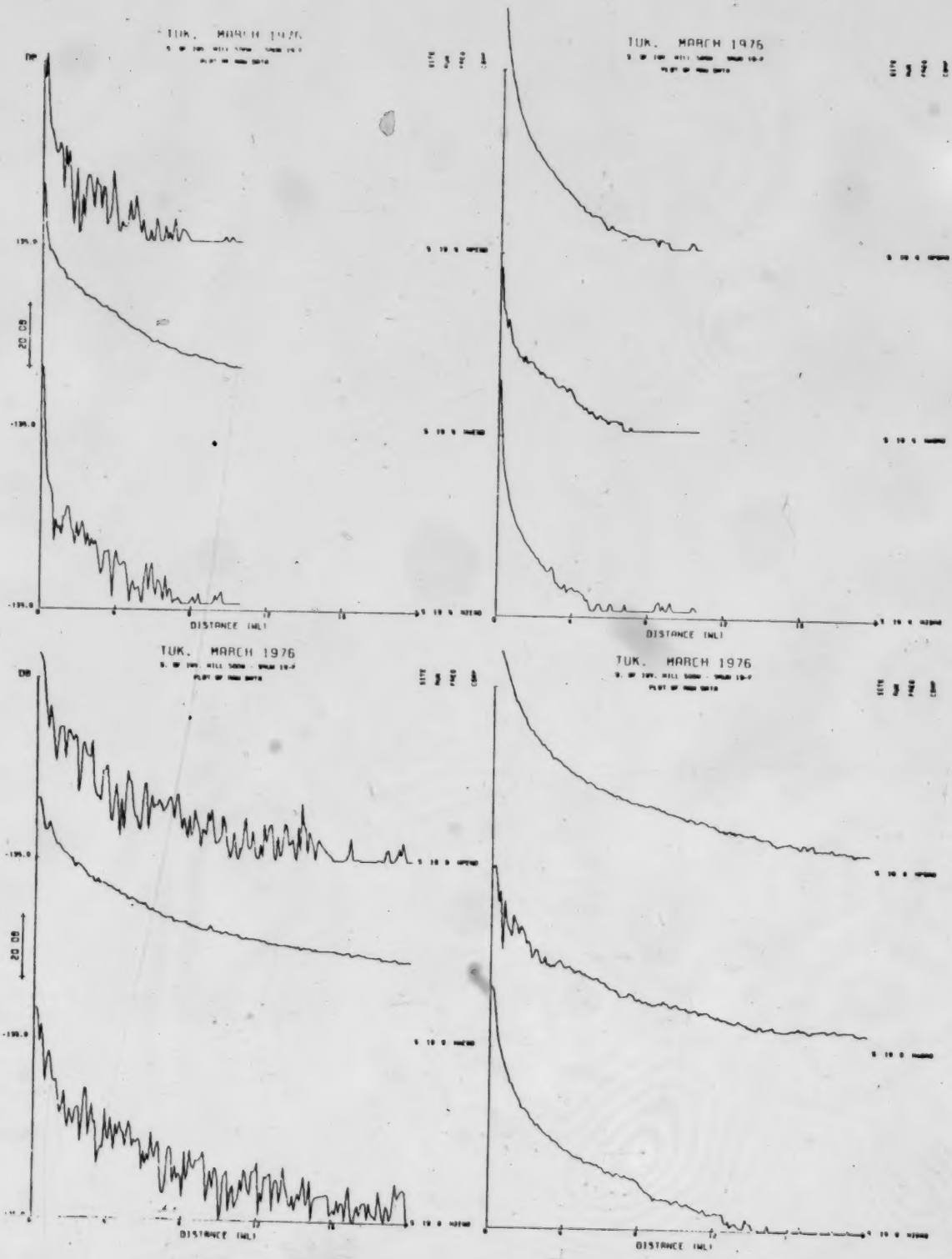
TUK. MARCH 1976
TUK. MARCH 1976
TUK. MARCH 1976
TUK. MARCH 1976
DISTANCE (NL)
DISTANCE (NL)
DISTANCE (NL)
DISTANCE (NL)

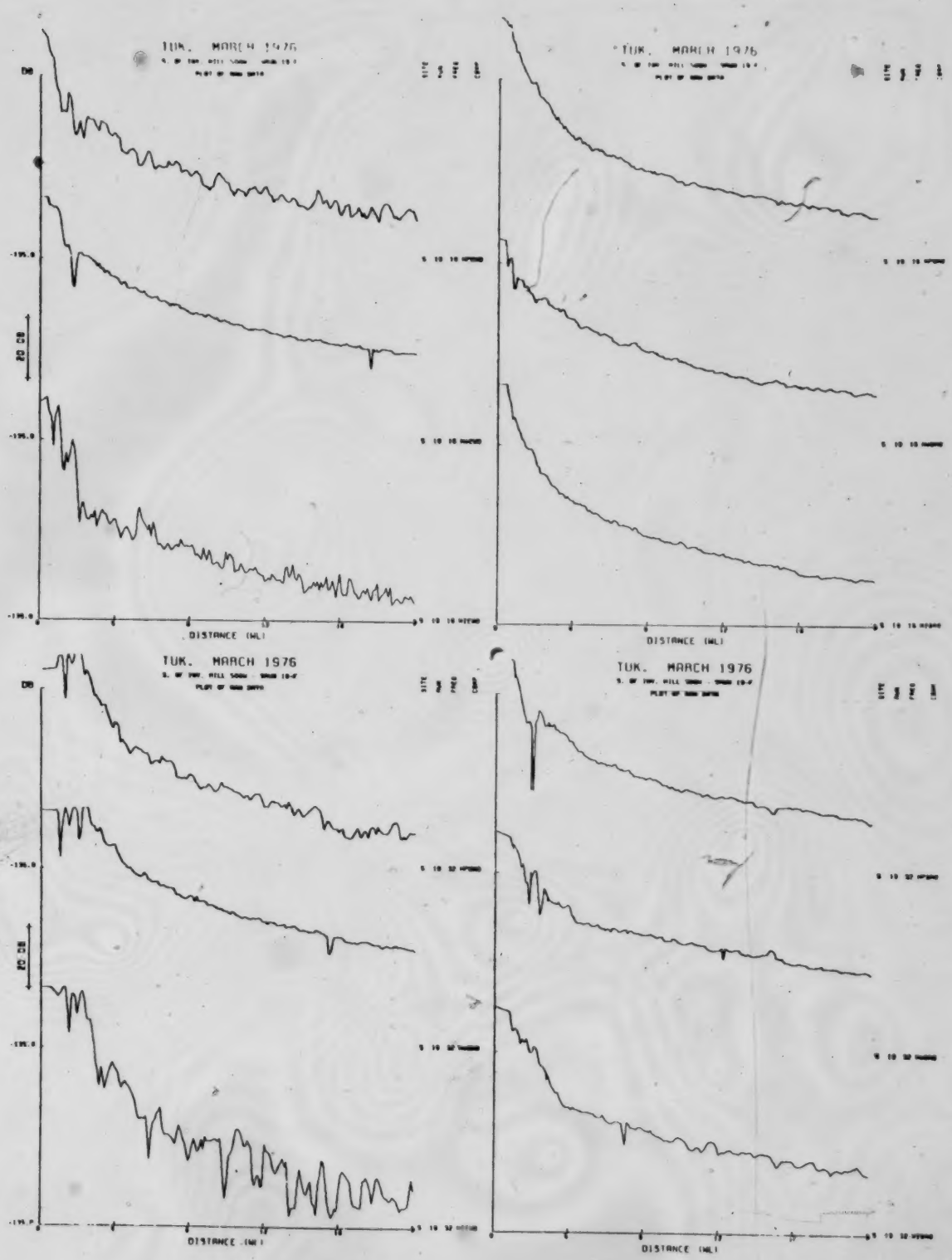
TUK. MARCH 1976
DB
20 DB
DISTANCE (NL)
TUK. MARCH 1976
DISTANCE (NL)
TUK. MARCH 1976
20 DB
DISTANCE (NL)
TUK. MARCH 1976
DISTANCE (NL)

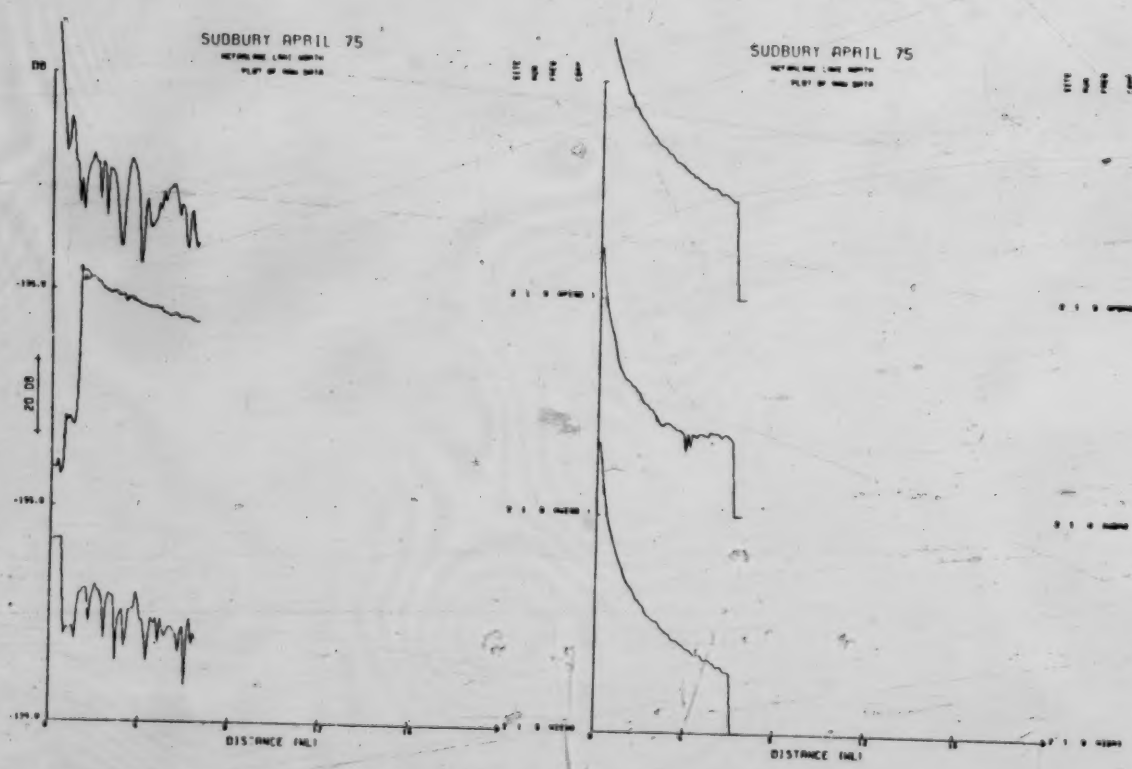
SUDBURY APRIL 75
DB
20 DB
DISTANCE (MI)
SUDBURY APRIL 75
DISTANCE (MI)

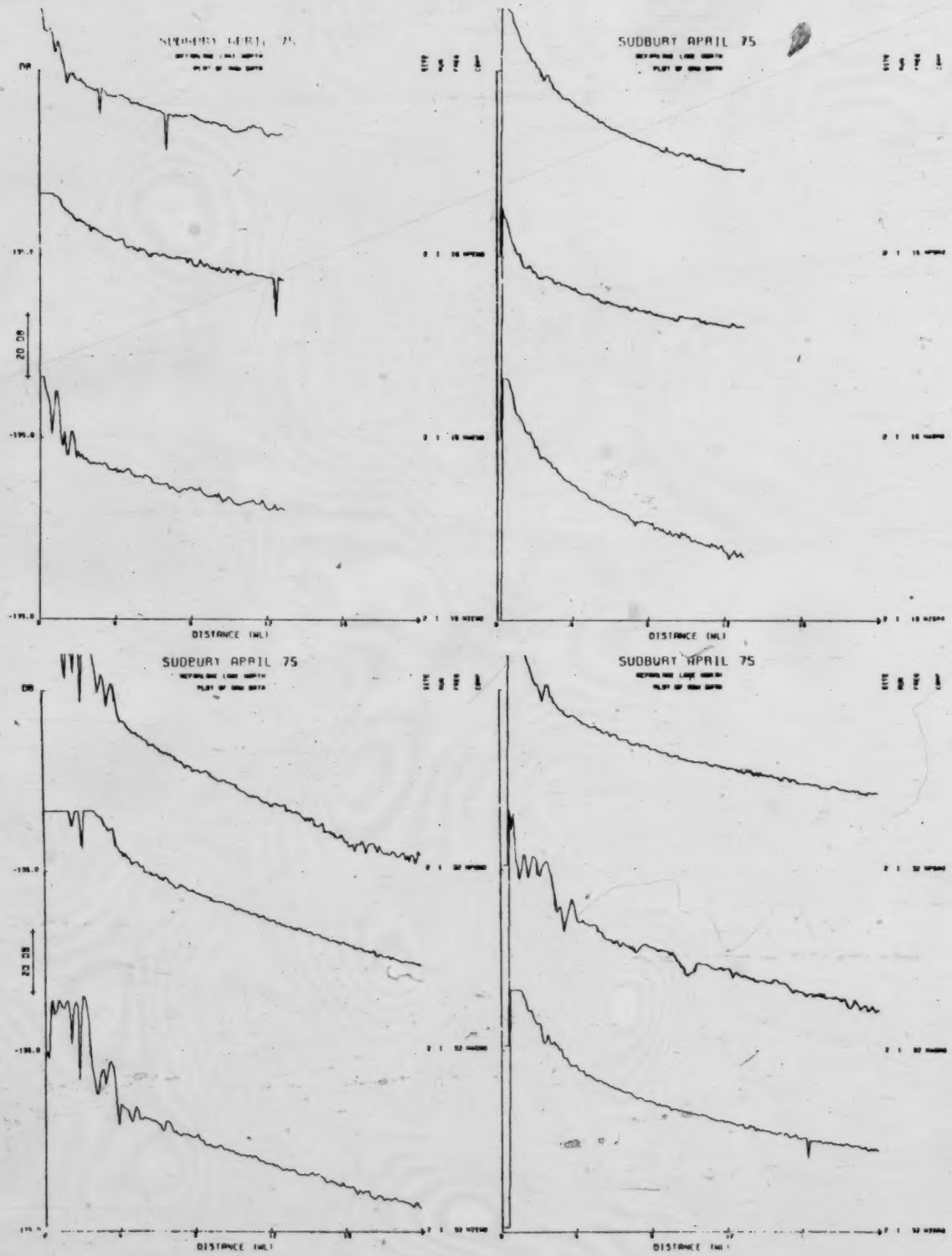
SUDBURY APRIL 75
SUDBURY APRIL 75
SUDBURY APRIL 75
SUDBURY APRIL 75
20 DB
20 DB
DISTANCE (MI)
DISTANCE (MI)
DISTANCE (MI)
DISTANCE (MI)

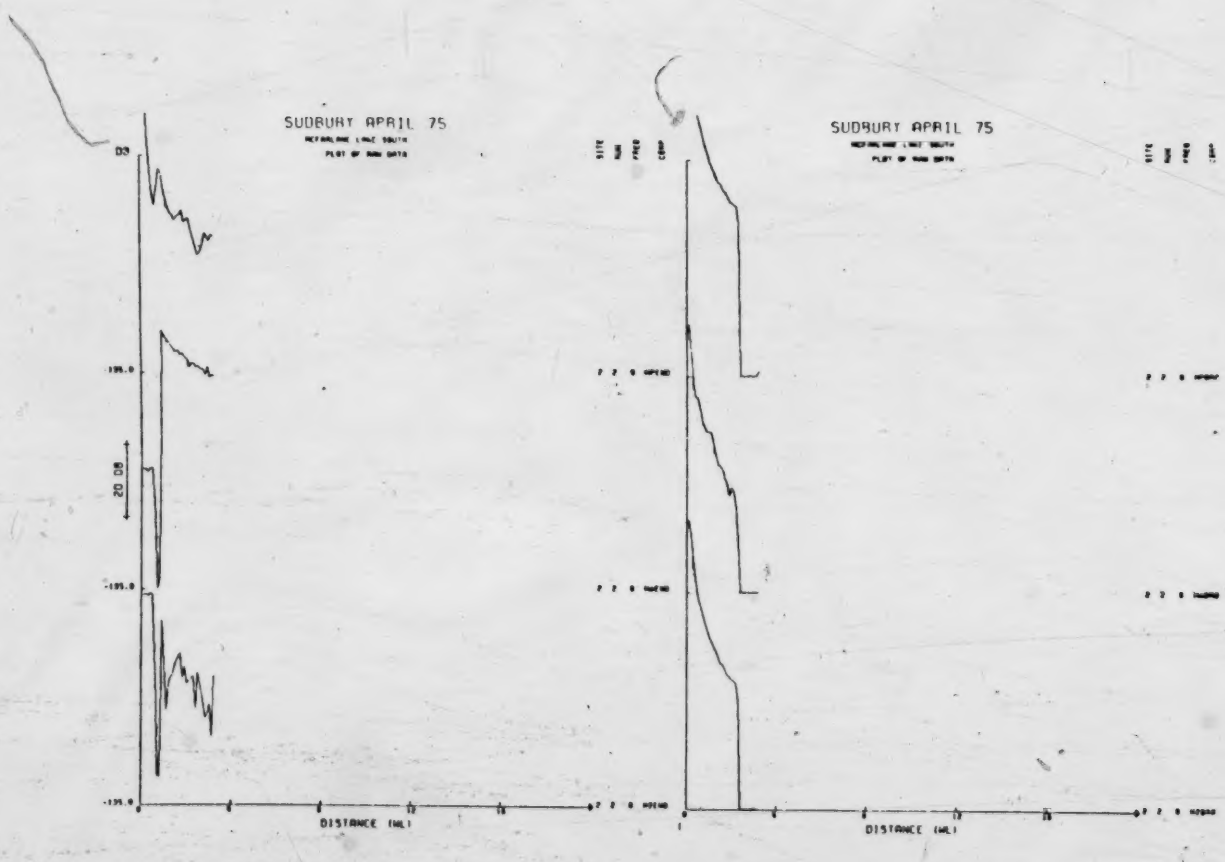
SUDBURY APRIL 75
20 DB
DISTANCE (MI)
SUDBURY APRIL 75
DISTANCE (MI)

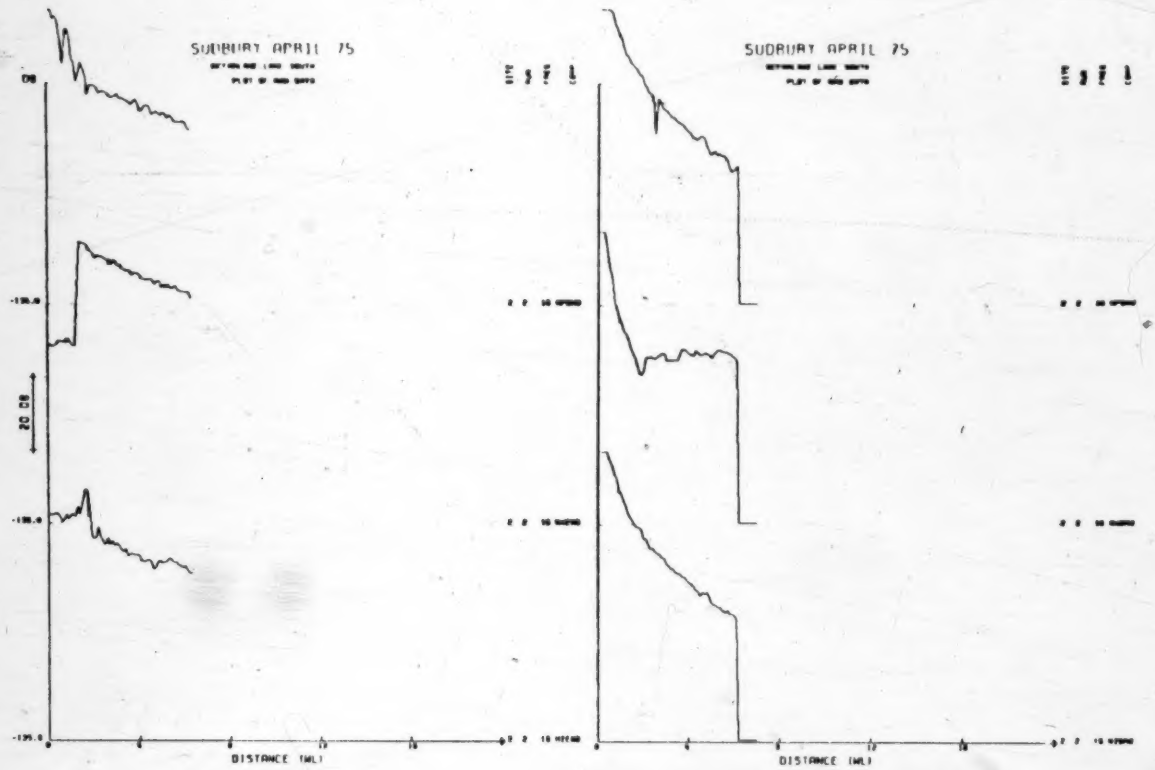
SUDBURY APRIL 75
20 DB
DISTANCE (MI)

SUDBURY APRIL 75
DISTANCE (MI)

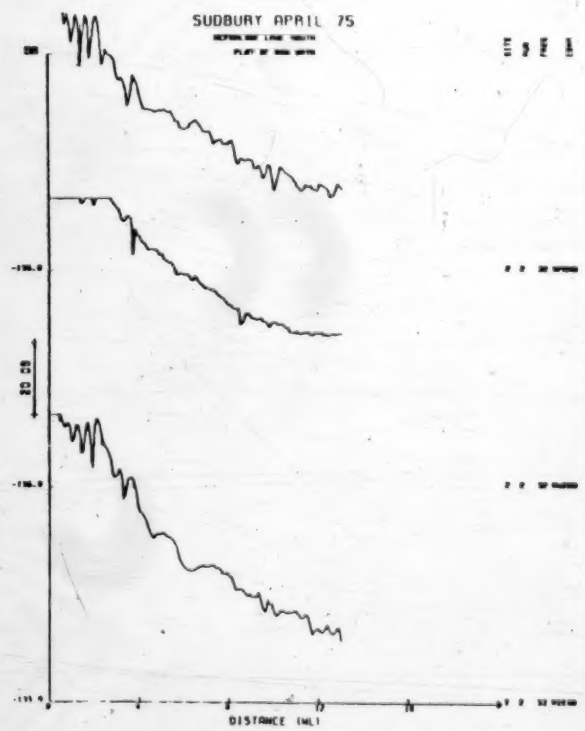
SUDBURY APRIL 75
20 DB
DISTANCE (MI)

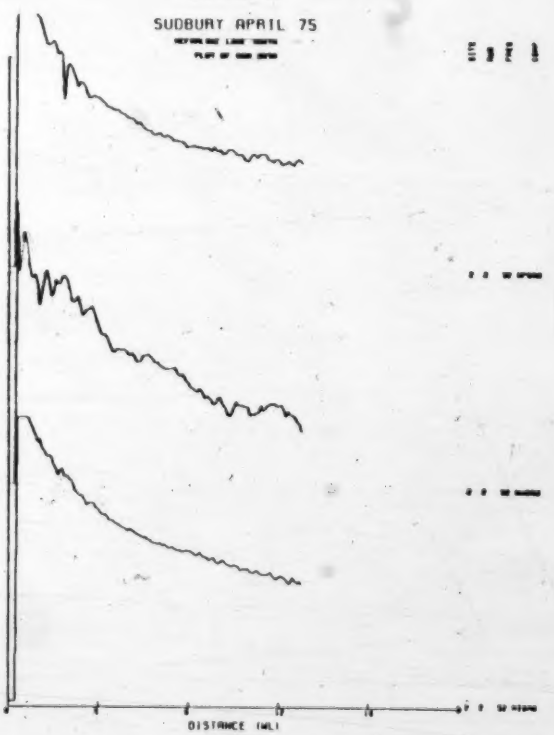
SUDBURY APRIL 75
DISTANCE (MI)